

Development and Multi-Scale Characterization of a Self-Consolidating High-Strength Concrete for Quasi-Static and Transient Loads

By

William Franklin Heard

Dissertation

Submitted to the Faculty of the

Graduate School of Vanderbilt University

in partial fulfillment of the requirements

for the degree of

DOCTOR OF PHILOSOPHY

in

Civil Engineering

May 2014

Nashville, Tennessee

Approved:

Prodyot K. Basu, D.Sc.

Sankaran Mahadevan, Ph.D.

Caglar Oskay, Ph.D.

Thomas Slawson, Ph.D.

James Wittig, Ph.D.

To my wife Leigh Anne, your support and sacrifices made this possible. To Nathan,
Emmy and Clara, thank you for reminding me of what really matters.

ACKNOWLEDGEMENTS

I would like to thank my advisor, Dr. P. K. Basu for the countless hours he invested in this research and for guiding me through the process. I am also grateful for Dr. Thomas Slawson, whose input and advice often refocused my attention on the “forest” instead of the “trees”. I would also like to thank my committee members, Dr. Sankaran Mahadevan, Dr. Caglar Oskay and Dr. James Wittig for their support and useful suggestions.

I am very thankful for the support from the U.S. Army Engineer Research and Development Center (ERDC). I am grateful for the opportunity provided through the “Long Term Training” program. I especially want to thank Mr. James Davis, my supervisor and branch chief of the Survivability Engineering Branch. Mr. Davis provided encouragement, supervision and support to keep me moving forward through the obstacles.

I would like to thank my coworkers at the ERDC. Mr. Brett Williams, Mr. Jamie Stevens, Mr. Richard Magee, Mr. Don Nelson, Mr. Nicholas Boone, Dr. Jesse Sherburn, Mr. Sam Graham and Mr. Thomas McGill all contributed to this research. I am very grateful for their help and their friendship. I would also like to thank my classmates, Dr. Catherine Stephens and Dr. Nikolas Nordendale for help with classwork and projects in the early years, and for the research advice and suggestions in the years that followed. I am also extremely thankful for the contributions from Dr. Xu Nie and Dr. Bradley Martin. I appreciate their time devoted to this research and value the friendship developed through many hours of Kolsky bar experiments.

TABLE OF CONTENTS

DEDICATION	ii
ACKNOWLEDGEMENTS	iii
LIST OF TABLES	vii
LIST OF FIGURES	viii
Chapter	
1. INTRODUCTION	1
1.1 Motivation	1
2. BACKGROUND	5
2.1 High Performance Concrete: What is HPC and why is it important?	5
2.2 Enhancing Compressive Strength: Superplasticizers	7
2.3 Enhancing Compressive Strength: Cement Microstructure	12
2.4 Enhancing Compressive Strength: Supplementary Cementitious Materials	18
2.5 HPCs with Enhanced Compressive Strength	21
2.5.1 DSP cement and Reactive Powder Concrete	22
2.5.2 HSPC, VHSC and CorTuf	23
2.6 HPC with Enhanced Compressive Strength and Ductility: HSHDC	29
2.7 Summary	33
3. DEVELOPMENT OF A SCHSC	35
3.1 Introduction	35
3.1.1 Background of Self-Consolidating Concrete	35
3.1.2 Fresh-state properties of a SCC	37
3.2 Developing a SCC	41
3.2.1 Overview	41
3.2.2 Fly Ash and GGBFS	42
3.3 Materials	46
3.3.1 VMA (Purified Palygorskite Nanoclay)	46
3.3.2 Cement	51
3.3.3 Fly Ash and GGBFS (Slag Cement)	51
3.3.4 Fine Aggregate	51
3.3.5 HRWRA	51
3.4 Mixture Proportions	53
3.5 Mixing and Casting of Specimens	54
3.6 Specimen Preparations and Experimental Procedure	56
3.6.1 MicroCT	56
3.6.2 Compressive Strength	58
3.6.3 Flexure	58
3.6.4 Single Fiber Pull-Out	60
3.7 Results	61
3.7.1 Flow and Flow Rate Results	61

3.7.2 Micro-CT Results	63
3.7.3 Compressive Strength Results	75
3.7.4 Flexure Results	77
3.7.5 Single Fiber Pull-out Results	79
3.7.6 Stability Results	80
3.8 Summary & Conclusions	82
4. CHARACTERIZATION OF A SCHSC	86
4.1 Introduction	86
4.2 Preparation of Specimens	89
4.3 Experimental Approach (Methodology).....	91
4.3.1 Constitutive Models.....	91
4.3.2 Pressure-Volume Response	92
4.3.3 Deviatoric Response	97
4.3.4 Direct Tension Response	100
4.4 Results	102
4.4.1 Pressure-Volume Results.....	102
4.4.2 Deviatoric Results	107
4.4.3 Direct Tension Results	117
4.5 Summary and Conclusions	125
5. HIGH-STRAIN RATE RESPONSE OF A SCHSC	128
5.1 Background and Introduction	128
5.2 Experimental Procedure	136
5.3 Pulse Shaping Technique	138
5.3.1 Radial Inertia in Pulse Shapers.....	138
5.3.2 Annulus Pulse Shapers	144
5.4 Results	146
5.4.1 Mechanical Properties of SCHSC at High Rates	146
5.4.2 Effect of Specimen Inertia.....	152
5.5 Summary and Conclusions	155
6. BALLISTIC EVALUATION OF THE SCHSC	157
6.1 Introduction	157
6.2 Experimental Approach.....	161
6.3 Results	165
6.3.2 SCHSC 25mm panel: No fibers (Test# 1-8).....	167
6.3.3 SCHSC 25mm panel: Fibers (Test #2-6).....	172
6.3.4 SCHSC 50mm panel: No fibers (Test #3-4).....	175
6.3.5 SCHSC 50mm panel: Fibers (Test #4-2).....	179
6.4 Summary and Conclusions	182
7. SUMMARY AND FUTURE WORK	185
7.1 Summary.....	185
7.2 Future Work.....	188

Appendix

A.	BALLISTIC REPORTS	191
B.	PHOTOS OF BALLISTIC RESULTS	195
	B.1 Test Series 1 - SCHSC 25mm: No fibers	195
	B.2 Test Series 2 - SCHSC 25mm: Fibers	197
	B.3 Test Series 3 - SCHSC 50mm: No fibers	201
	B.4 Test Series 4 - SCHSC 50mm: Fibers	204
C.	UC RESULTS OF P3S15W37	206
	References	207

LIST OF TABLES

Table 2.1 PCA classification for concrete strengths & typical water to cement ratios	6
Table 2.2 Summary of WR & HRWR and potential water reducing capability	12
Table 2.3 Component materials and mass proportions relative to mass of cement.....	29
Table 2.4 Properties of HSHDC fiber	32
Table 3.1 Mix proportions for example SCC, HSC and baseline control mix	45
Table 3.2 Chemical and physical properties of materials used in the mix	52
Table 3.3 Gradation analysis of fine aggregate	52
Table 3.4 Proportions of the concrete mixtures.....	54
Table 3.5 Results for flow and flow rate for each mix	62
Table 3.6 Overview of findings from the micro-CT analysis	67
Table 3.7 Summary of results from flexure experiment.....	79
Table 3.8 Summary of results from the single-fiber pull-out experiments	80
Table 3.9 Summary of findings.	85
Table 4.1 Test matrix for hydrostatic and triaxial compression experiments	100
Table 6.1 Individual results for each panel tested in the ballistic evaluation.....	166
Table 6.2 Overall results of the ballistic evaluation of the SCHSC	182
Table 7.1 SCHSC elastic properties	186
Table 7.2 Rate sensitivity of the SCHSC	187
Table 7.3 Ballistic limit and corresponding failure mode for each panel test series.....	188
Table A.1 Ballistic report from Test series 1 (25mm thick: No fibers)	191
Table A.2 Ballistic report from Test series 2 (25mm thick: Fibers)	192
Table A.3 Ballistic report from Test series 3 (50mm thick: No fibers)	193
Table A.4 Ballistic report from Test series 4 (50mm thick: Fibers)	194

LIST OF FIGURES

Figure 2.1 Schematic of a Polycarboxylate HRWRA molecule	11
Figure 2.2 Steric hindrance prevents re-agglomeration of cement grains	11
Figure 2.3 Development of UHPCs at the ERDC	26
Figure 2.4 Direct Tension of HSHDC and CorTuf	32
Figure 2.5 HSHDC loaded in flexure	33
Figure 3.1 Workability Continuum	37
Figure 3.2 Methods of achieving self-consolidation	38
Figure 3.3 J-ring test measuring passing ability of SCC	40
Figure 3.4 Effect of variation of water content of slump flow of SCC mixes	40
Figure 3.5 PPNC	47
Figure 3.6 (Left) Dispersed non-PPNC particles; (right) PPNC agglomerates	48
Figure 3.7 Mixing with Eibenstock 21 S twin paddle concrete mixer	55
Figure 3.8 Casting cubes, single fiber pull-out specimens and beams	56
Figure 3.9 Concrete specimen mounted in the SkyScan 1173 X-ray micro-CT device....	57
Figure 3.10 (Left) 19mm diameter specimen; (right) 6.35mm diameter specimen	58
Figure 3.11 Flexure with third point loading.....	59
Figure 3.12 Single fiber pull-out to investigate PPNC affect on ITZ	61
Figure 3.13 Flow for mix PxS0W32, P6S0W32_2 and PxS0W40	62
Figure 3.14 Flow rates for mixtures PxS0W32, P6WS0W32_2 and PxS0W40	63
Figure 3.15 Total porosity for mix PxS0W32, P0S0W40 and P6SW32.....	67
Figure 3.16 (Left) P0S0W32 (10.0 μ m); (right) P3S0W32 (10.0 μ m).....	68
Figure 3.17 (Left) P6S0W32 (10.0 μ m); (right) P6S15W32 (10.0 μ m).....	68
Figure 3.18 (Left) P0S0W32 (5.36 μ m); (right) P3S0W32 (5.36 μ m).....	69
Figure 3.19 (Left) P6S0W32 (5.36 μ m); (right) P6S15W32 (5.36 μ m).....	69
Figure 3.20 Pore size distribution.....	70
Figure 3.21 Number of pores for a given pore diameter	71
Figure 3.22 Percent of pore volume for a given range of pore diameter.....	72
Figure 3.23 Volume of pores for a given pore size diameter	73
Figure 3.24 Histogram indicating the number of pores for range of pore diameter.....	74
Figure 3.25 Relative frequency of pores in mixes with a w/cm=0.32.....	75

Figure 3.26 Effect of PPNC on compressive strength.....	76
Figure 3.27 Summary of compressive strengths for all mixtures.....	77
Figure 3.28 Effect of PPNC on flexure strength	78
Figure 3.29 Load versus displacement curve for single fiber pull-out experiment.....	80
Figure 3.30 Specimen to evaluate fiber distribution using MicroCT	81
Figure 3.31 3D MicroCT image of fiber reinforcement.....	82
Figure 4.1 Coring, sectioning and grinding.....	90
Figure 4.2 (Left) Direct uniaxial tension; (right) specimen for DIC.....	90
Figure 4.3 Axes and sign convention for cylindrical specimen	94
Figure 4.4 Specimen mounted with instrumentation ready for testing	94
Figure 4.5 Schematic diagram of the 600 MPa capacity pressure vessel.....	95
Figure 4.6 Pressure-volume relationship during hydrostatic compression	96
Figure 4.7 Boundary conditions for UXC experiment	97
Figure 4.8 (Left) DT specimen in loading fixture; (right) DIC setup	102
Figure 4.9 Pressure time history for the HC experiment.....	103
Figure 4.10 Comparison of radial and axial strain with HC.....	104
Figure 4.11 Pressure volume response	104
Figure 4.12 Specimen after HC experiment	105
Figure 4.13 Stress versus strain response for two UXC experiments	106
Figure 4.14 Pressure-volume responses for two UXC and HC experiments	106
Figure 4.15 UXC specimens: before and after	107
Figure 4.16 UC: PSD vs axial strain	108
Figure 4.17 UC: PSD vs volumetric strain.....	109
Figure 4.18 UC: PSD vs radial strain	109
Figure 4.19 Specimens at failure for UC test	110
Figure 4.20 TXC: PSD vs axial strain for 0 MPa to 50 MPa	112
Figure 4.21 TXC: PSD vs axial strain for 100 MPa to 400 MPa	112
Figure 4.22 TXC: PSD vs axial strain for 0 MPa to 400 MPa	113
Figure 4.23 TXC: PSD vs radial strain for 0 MPa to 50 MPa.....	113
Figure 4.24 TXC: PSD vs radial strain for 0 MPa to 400 MPa.....	114
Figure 4.25 TXC specimens after testing.....	114
Figure 4.26 TXC: PSD vs volumetric strain for 0 MPa to 50 MPa.....	115
Figure 4.27 TXC: PSD vs volumetric strain for 100 MPa to 400 MPa.....	115

Figure 4.28 TXC: PSD vs volumetric strain for 100 MPa to 400 MPa.....	116
Figure 4.29 TXC and UC failure points and surface for SCHSC material	116
Figure 4.30 UXC: PSD vs MNS with TXC failure points and surface	117
Figure 4.31 Load vs displacement results from the DT external LVDTs	120
Figure 4.32 Location of three virtual DIC extensometers	120
Figure 4.33 Load vs displacement responses from LVDT and DIC extensometer.....	121
Figure 4.34 Load vs displacement responses of the DIC extensometers	121
Figure 4.35 DIC displacement contours	122
Figure 4.36 Load vs displacement plot showing the location of microcracks	123
Figure 4.37 DIC displacement contours along the Z-axis	123
Figure 4.38 Location of extensometers to evaluate crack opening displacements.....	124
Figure 4.39 Load vs time and crack opening displacement vs time.....	124
Figure 5.1 Schematic of a Kolsky compression bar	129
Figure 5.2 Differential element with an applied dynamic stress	130
Figure 5.3 Gas gun and 50mm diameter Kolsky incident and transmission bars	137
Figure 5.4 Incident pulse waveforms using a 25mm solid copper pulse shaper	143
Figure 5.5 Incident pulse waveforms using a 9mm solid copper pulse shaper	143
Figure 5.6 Stress and strain rate histories of the solid copper pulse shaper specimen	144
Figure 5.7 Incident pulse generated by annulus copper pulse shaper	146
Figure 5.8 Pulse shaper mounted on impact face of incident bar.....	149
Figure 5.9 Stress waveforms from 100s^{-1} experiment.....	150
Figure 5.10 Stress waveforms from 240s^{-1} experiment.....	150
Figure 5.11 Dynamic stress equilibrium check at 240s^{-1}	151
Figure 5.12 Engineering stress-strain curves for SCHSC under different strain rates	151
Figure 5.13 Strength increase factor for a given strain rate for the SCHSC	152
Figure 5.14 Strain rate acceleration for a typical SCHSC specimen.....	155
Figure 6.1 Failure modes in impacted plates.....	160
Figure 6.2 Failure modes for concrete targets	160
Figure 6.3 Experimental setup for ballistic evaluation of SCHSC.....	163
Figure 6.4 SCHSC panel mounted with witness panel for ballistic evaluation.....	163
Figure 6.5 Cartridge with plastic sabot and 12.7mm spherical projectile	165
Figure 6.6 Impact and exit side of test #1-8 at the various time intervals indicated	169
Figure 6.7 Impact side and exit side showing damage from Test #1-8	170

Figure 6.8 Witness panel for Test #1-8 to indicate a PP	171
Figure 6.9 Cross section showing overlap of impact and exit craters	171
Figure 6.10 Impact and exit side of test #2-6 at the various time intervals indicated	174
Figure 6.11 Impact side and exit side showing damage from Test #2-6	174
Figure 6.12 Witness panel for Test #2-6 showing a small breach to indicate a CP	175
Figure 6.13 Impact and exit side of test #3-4 at the various time intervals indicated	177
Figure 6.14 Impact side and exit side showing damage from Test #3-4	178
Figure 6.15 Intersection of impact and exit craters	178
Figure 6.16 Impact and exit side of test #4-2 at the various time intervals indicated	180
Figure 6.17 Impact side and exit side showing damage from Test #4-2	181
Figure 6.18 Projectile lodged in the tunnel of a Test series #4 panel	181
Figure B.1 Test 1-1 impact side (left) exit side (right)	195
Figure B.2 Test 1-2 impact side (left) exit side (right)	195
Figure B.3 Test 1-3 impact side (left) exit side (right)	195
Figure B.4 Test 1-4 impact side (left) exit side (right)	196
Figure B.5 Test 1-5 impact side (left) exit side (right)	196
Figure B.6 Test 1-6 impact side (left) exit side (right)	196
Figure B.7 Test 1-7 impact side (left) exit side (right)	196
Figure B.8 Test 1-8 impact side (left) exit side (right)	197
Figure B.9 Test 2-1 impact side (left) exit side (right)	197
Figure B.10 Test 2-2 impact side (left) exit side (right)	197
Figure B.11 Test 2-3 impact side (left) exit side (right)	198
Figure B.12 Test 2-4 impact side (left) exit side (right)	198
Figure B.13 Test 2-5 impact side (left) exit side (right)	198
Figure B.14 Test 2-6 impact side (left) exit side (right)	198
Figure B.15 Test 2-7 impact side (left) exit side (right)	199
Figure B.16 Test 2-8 impact side (left) exit side (right)	199
Figure B.17 Test 2-9 impact side (left) exit side (right)	199
Figure B.18 Test 2-10 impact side (left) exit side (right)	199
Figure B.19 Test 2-11 impact side (left) exit side (right)	200
Figure B.20 Test 2-12 impact side (left) exit side (right)	200
Figure B.21 Test 2-13 impact side (left) exit side (right)	200
Figure B.22 Test 3-1 impact side (left) exit side (right)	201

Figure B.23 Test 3-2 impact side (left) exit side (right).....	201
Figure B.24 Test 3-3 impact side (left) exit side (right).....	201
Figure B.25 Test 3-4 impact side (left) exit side (right).....	202
Figure B.26 Test 3-5 impact side (left) exit side (right).....	202
Figure B.27 Test 3-6 impact side (left) exit side (right).....	202
Figure B.28 Test 3-7 impact side (left) exit side (right).....	202
Figure B.29 Test 3-8 impact side (left) exit side (right).....	203
Figure B.30 Test 3-9 impact side (left) exit side (right).....	203
Figure B.31 Test 3-10 impact side (left) exit side (right).....	203
Figure B.32 Test 3-11 impact side (left) exit side (right).....	203
Figure B.33 Test 4-1 impact side (left) exit side (right).....	204
Figure B.34 Test 4-2 impact side (left) exit side (right).....	204
Figure B.35 Test 4-3 impact side (left) exit side (right).....	204
Figure B.36 Test 4-4 impact side (left) exit side (right).....	205
Figure B.37 Test 4-5 impact side (left) exit side (right).....	205
Figure B.38 Test 4-6 impact side (left) exit side (right).....	205
Figure B.39 Test 4-7 impact side (left) exit side (right).....	205
Figure C.1 Principal stress difference vs. Axial strain for P3S15W37	206

CHAPTER 1

INTRODUCTION

1.1 Motivation

The Geotechnical and Structures Laboratory (GSL) of the U.S. Army Engineer Research and Development Center (ERDC) serves as the science and technology lead to the Department of Defense (DOD) in the areas of survivability and protective structures. As the lead organization, the GSL provides innovative engineering and scientific solutions to protect the U.S. warfighter and critical facilities[1]. In recent years, shifts toward nontraditional threats and tactics from terrorists engaged in asymmetric warfare have presented new challenges to providing force protection for U.S. troops in foreign theaters of operation. During ‘Operations Enduring Freedom and Iraqi Freedom’, a significant threat to the U.S. warfighter was from direct and indirect fire weapons such as mortars, artillery, shoulder-fired rockets, suicide bombings, and small-arms fire [2].

Physical protection from such threats is typically provided by hardened structures, large soil-filled revetment walls or concrete barriers, or simply put, mass. Although these protective solutions are proven, these traditional approaches are often not practical or desirable, as it requires significant time, manpower, equipment, and other valuable resources. Furthermore, constructing massive concrete structures with limited or poor quality in-situ construction materials often require transporting better quality raw materials from neighboring countries or from the United States. This presents many logistical challenges and is often not cost effective. Moreover, hardened structures and

massive walls or barriers are not practical for many operating conditions. For example, U.S. troops operating in close-engagement conditions such as contingency outposts and outside-the-wire construction or repair operations are often left vulnerable to terrorist attacks. In this typical scenario, the warfighter may occupy an area for very short periods of time until the task is completed—typically hours or days, rather than months or years.

Given this scenario, recent Army research programs have focused on developing high performance concrete (HPC) mixtures for creating lightweight, rapidly deployable protective structures. A major goal of the Army research focus is to develop protective options that depend more on system ductility and enhanced material properties to provide protection from blast and weapon fragmentation, rather than mass alone [3]. Examples of such research programs include the “Modular Protective System for Future Force Assets” (MPS) and “Defeat of Emerging Adaptive Threats” (DEFEAT) [4,5]. For the MPS program, a primary objective was to develop a lightweight structure that could be rapidly constructed and positioned without heavy equipment or significant manpower while providing the required level of protection from specific threats. The lightweight structure, developed by the author and coworkers at ERDC, was clad with multiple layers of thin HPC panels that were prefabricated at a U.S. manufacturing facility and shipped into theater [2,4,5]. The panels were developed to provide protection from blast and weapon fragmentation at a considerably reduced thickness than that required by a more traditional concrete mixture, thus reducing mass. Full-scale field experiments validated the lightweight structure and prototype HPC armor panels and showed initial success of the approach [6]. To build on this success and better understand the micromechanics of cementitious composites, a component of the DEFEAT program emphasized multiscale

material property characterization to further investigate the performance of HPC armor panels [7-9].

The MPS and DEFEAT research programs produced successful prototypes that validated the concept of using engineered high performance materials to provide physical protection from current threats in theater. Though these programs were successful, the research identified new criteria for an alternative HPC armor, and an additional need for more accurate material characterization at the micro and meso length scales.

Specifically, U.S. troops need a HPC mix design that can be cast and cured in the field quickly using semi-skilled efforts, rather than the controlled environment of a stateside prefabrication facility or laboratory. Casting the HPC armor panel in the field would give the soldier flexibility with armor panel dimensions as the impending threat dictates or changes from region to region. A pre-mixed HPC mixture that only needs the addition of water with a simplified casting and curing procedure using common construction tools would allow the soldier to make the armor panel in austere environments under less than ideal conditions. Furthermore, an understanding of the characteristics of matrix, fiber, interface and porosity of the HPC would not only foster improvements to the overall material response to load, but facilitate better models for simulation as the threat changes and adapts to force protection techniques.

In view of the aforementioned scenario, the proposed research identifies two impending needs: a) developing a cementitious material that a soldier can mix and cast in the field with common construction tools, and b) characterize the developed material at the macro, meso and micro length scales to facilitate modeling and simulation under quasi-static, and extreme impulse loads which can be distributed (as in blast effect) or

localized (as in ballistic impact). As an offshoot of this effort, the findings may also lead to methods to better protect buildings and other structures subjected to extreme events.

CHAPTER 2

BACKGROUND

2.1 High Performance Concrete: What is HPC and why is it important?

HPC is a special subset of concrete, the single most widely used material in the world (more than ten billion tons a year) comprising generally of inert filler, cementitious binder and water. The American Concrete Institute defines the term “HPC” as “Concrete meeting special combinations of performance and uniformity requirements that cannot always be achieved routinely using conventional constituents and normal mixing, placing, and curing practices” [10]. Others have used “HPC” to refer to a concrete that satisfies certain criteria that conventional concrete cannot. Examples of such criteria may be strength, durability, toughness, increased structural capacity, or even resistance to environmental influences [11]. With respect to force protection, a HPC is typically distinguished as a concrete mixture with a high, very-high or ultra-high compressive strength with small maximum particle size of inert aggregates, typically less than 1mm. To define such vague terms as “high-strength”, “very-high strength” and “ultra-high strength”, Table 2.1 shows typical values published by the Portland Cement Association [12]. These values present helpful ranges of concrete components and the resulting unconfined compressive strengths, providing a frame of reference for the terminology used in this research.

Table 2.1 PCA classification for concrete strengths & typical water to cement ratios

Characteristic	Conventional Concrete	High-strength Concrete	Very-high-strength concrete	Ultra-high-strength concrete
Strength	< 50 MPa	50 – 100 MPa	100 – 150 MPa	> 150 MPa
Water to cement ratio	> 0.45	0.45 – 0.30	0.30 – 0.25	< 0.25
Chemical Admixtures	Not necessary	WR / HRWR	HRWR	HRWR
Mineral Admixtures	Not necessary	Fly ash	Silica fume	Silica fume

Researchers have focused on attaining high, very high, or ultra high unconfined compressive strength as the criterion for achieving improved ballistic resistance of a HPC. Studies [13-15] have reported that an increase in compressive strength resulted in improved ballistic resistance, but it was also noted that an increase in compressive strength did not necessarily produce a corresponding increase in such resistance. For example, one penetration study [14] with a 20 mm diameter, conical-nose projectile against a 100-mm-thick concrete slab showed that increasing the unconfined compressive strength from 41.4 MPa to 116.7 MPa resulted in a 20% increase in ballistic limit. Similarly, increasing the compressive strength of a second concrete mixture from 84.4 MPa to 196.6 MPa also increased the ballistic limit by the same 20%. Though the unconfined compressive strength was increased more than 100% for both concrete mixtures, the ballistic limit was increased only by 20%. The ballistic limit is defined as the average of the fastest impact velocity without producing perforation and the slowest impact velocity producing complete perforation. Thus, a higher ballistic limit is advantageous and beneficial in mitigating weapon fragmentation. Some studies have, however, shown that the resulting benefit may be less than 20% [16]. In investigating the depth of penetration of a 12.6 mm projectile into high-strength concrete, Zhang et al. [13] reported that the penetration depth was reduced by 42% as the water-to-cement ratio was

decreased from 0.55 to 0.40 causing an increase in the unconfined compressive strength from 46.3 MPa to 111.6 MPa. Also, Zhang et al. noted that penetration depth and crater diameter reductions were minimal when the unconfined compressive strength was increased beyond a certain level, which was observed to be approximately at 100 MPa. Though the specific ballistic results vary according to projectile shape and size or range of impact velocities, the literature suggests a gain in ballistic performance of various HPCs with an increase in unconfined compressive strength. As stated in the previous chapter, an important aspect of this research is to develop a HPC that a soldier can easily mix and cure in the field and use for creating physical protection against various threat weapons. Since there is a correlation between compressive strength of concrete and ballistic performance, it is important to comprehend more recent as well as historical achievements that have contributed to the improvement of compressive strengths of modern high performance concretes. Understanding these advancements and intelligent use of some, may aid in tailoring a HPC with desired attributes. The following sections identify key factors that have influenced recent developments in HPC mix design. The sections focus on the importance of superplasticizers, cement microstructure and supplementary cementitious materials to enhance the compressive strength of HPCs.

2.2 Enhancing Compressive Strength: Superplasticizers

High-strength concrete in the U.S. was first used in significant quantities to construct columns of high-rise buildings in Chicago during the mid sixties and early seventies. Prior to this time, compressive strengths were typically specified as 15 to 30 MPa, but Chicago concrete producers and designers were able to achieve much higher

strengths. Concrete of 50 MPa compressive strength was used for the columns of the Lake Point Tower in Chicago in 1965. Likewise, 60 MPa concrete columns were constructed for the 79-story Water Tower Place in the same city [17,18]. This sudden increase in concrete compressive strength was attributed to the first generation water reducing (WR) admixtures, which were lignosulfonate-based. Lignosulfonate molecules, obtained as a by-product of the pulp and paper mill industry, act as a dispersing agent by neutralizing the electrical charges present at the surface of cement particles (i.e. electrostatic repulsion), thus reducing the tendency to flocculate [17]. The amount of water required to achieve reasonable workability exceeds the amount required to fully hydrate the cement. The excess water not used to hydrate the cement generates porosity and weakens the mechanical properties of the hardened cement. Electrostatic repulsion reduces the water required for ideal workability, thus reducing porosity.

As high-strength concrete became more common in high-rise buildings and construction of platforms for off-shore exploitation of petroleum, higher dosages of lignosulfonate-based water reducing admixtures were needed to reduce the water-to-binder ratio and improve fluidity. However, higher dosages resulted in significant increases in set retardation, entrapped air and cohesiveness of the mix. This dilemma spurred an interest in the next generation of highly efficient water reducers or high-range water reducing admixtures (HRWR), commonly referred to as “superplasticizers” [17,19,20].

The arrival of HRWR admixtures in the U.S. in 1976 played a significant role in the development of high-strength, to ultra high-strength concretes of today. As a leading researcher in the field of concrete testing and development, V.M. Malhotra made the

following statement in 1981, “There have been very few major developments in concrete technology in recent years. The concept of air entrainment in the 1940’s was one – it revolutionized concrete technology in North America. It is believed that development of superplasticizers is another major breakthrough which will have a very significant effect on the production and use of concrete in years to come” [21]. Research and development efforts in the concrete industry over the last 30 years would strongly suggest that Malhotra’s prediction has proven to be true.

Superplasticizers were developed concurrently in Japan (sulfonated naphthalene formaldehyde (SNF) condensates) and in West Germany (sulfonated melamine formaldehyde (SMF) condensates) during the late 1960s and early 1970s for different reasons. Superplasticizers developed in Japan were intended to lower the water to binder ratio, thus increasing the compressive strength of concrete, whereas the initial objective in West Germany was to increase fluidity of the mix. It was soon discovered that these new superplasticizers offered both increased fluidity and increased compressive strength without the adverse secondary effects of the type created by the first generation lignosulfonate-based water reducing admixtures [19,21]. Similar to lignosulfate-based WR admixtures, SMF and SNF based HRWR admixtures rely on electrostatic repulsion as the dominant dispersing mechanism of cement particles.

Japanese researchers reported findings of a new “advanced superplasticizer” (polycarboxylate ether) in 1996 with “high dispersibility, long-term dispersion stability, excellent flowability, and segregation resistance” [22]. Polycarboxylate ether (PCE) based superplasticizers are “comb polymers”. A comb polymer molecule is characterized by a long chain (backbone of the comb) with multiple linear side chains (teeth of the

comb). This is depicted in Figure 2.1. Similar to SNF and SMF HRWR admixtures, PCE superplasticizers also use electrostatic repulsion to prevent flocculation of cement grains. Electrostatic repulsion is accomplished through carboxyl groups that create negatively charged binding sites along the backbone of the comb polymer (carboxyl functional groups are acidic, they will therefore release a hydrogen ion in water, thus leaving a negative charge) [23]. As the binding sites of the PCE molecule get adsorbed to the cement grain, the cement grains are repelled from one another due to like charges on their surfaces. The same mechanism (electrostatic repulsion) was used by previous generations of superplasticizers. However, electrostatic repulsion is not the only or primary means of dispersing cement grains. PCE superplasticizers also disperse cement grains through steric hindrance. Whereas electrostatic repulsion is a mechanism utilizing electrostatic charges, steric hindrance is a physical mechanism. The long ethylene oxide (EO) side graft chains (depicted in Figure 2.1) create a physical barrier that hinder re-agglomeration of the cement grains. Steric hindrance is illustrated in Figure 2.2 [24]. These two dispersing mechanisms compliment each other, resulting in a more efficient superplasticizer that isn't prone to workability retention issues and dosage inefficiencies [25-27]. However, some researchers have reported that dosage inefficiencies of PCE superplasticizers occur at very high dosage rates. Lee et al reported a 13% reduction in compressive strength when the dosage was increased from 0.84% to 1.61% (percent of superplasticizer to cement) [28]. This dosage rate is comparable to amounts required for HPC.

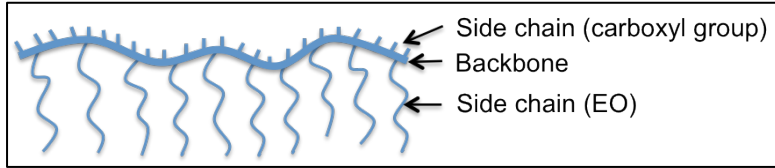


Figure 2.1 Schematic of a Polycarboxylate HRWRA molecule

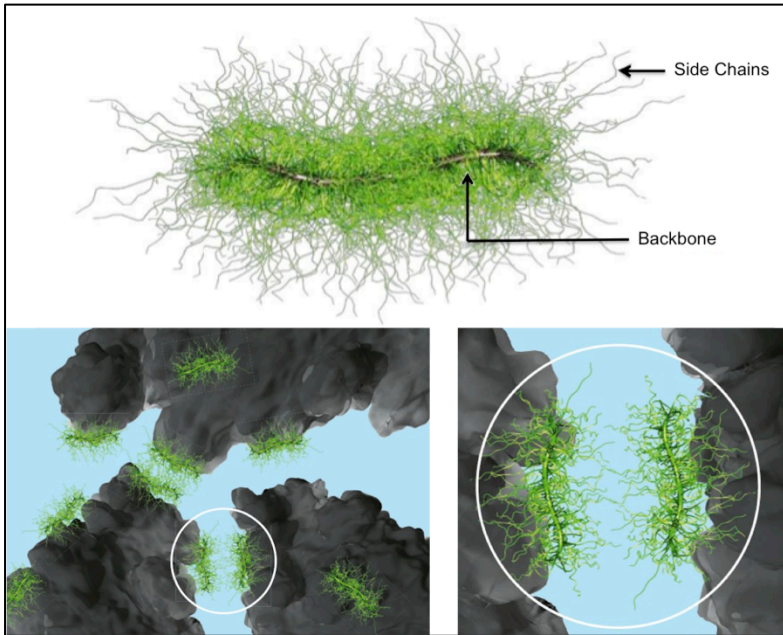

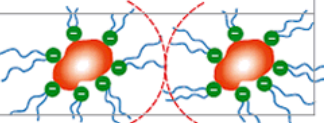


Figure 2.2 Steric hindrance prevents re-agglomeration of cement grains

PCE superplasticizers offered significant advantages over previous HRWR admixtures. Altering the length, density and molecular weight of the side chain and backbone, and the bond between the backbone and side chains, allowed cement chemists to design the PCE superplasticizers to achieve a specific performance. Slump retention, setting time, more substantial water reduction and system fluidity are examples of specific performance achieved by manipulating the molecule [29-32]. These advantages are particularly helpful in designing HPC mixtures. Table 2.2 shows the potential water

reducing capability and primary dispersion mechanism as reported by one of the leading manufacturers of chemical admixtures for cement [33].

Table 2.2 Summary of WR & HRWR and potential water reducing capability

Type of Water Reducer	Chemical Base	Water Reduction Potential	Effect
WR	Carbohydrate / Lignin sulfonate	5 – 10 %	Electro statical forces: 
HRWR	Naphthalene (SNF) & Melamine (SMF)	5 – 25 %	
	Polycarboxylate (PCE)	10 – 40 %	Steric repulsion: 

2.3 Enhancing Compressive Strength: Cement Microstructure

The water-cement (or water-binder) ratio is the major variable influencing the strength of concrete. This principle was presented over a century ago by Feret and later supported by the works of Abrams [34]. Though the principle is well known, it is important to understand some fundamental aspects of the cement hydration process and the resulting microstructure of a hardened cement paste to appreciate the relationship between the water-binder ratio and compressive strength. This section presents an explanation of why there is a correlation between strength and water-binder ratio. To clarify, the term “microstructure” refers to the type, amount, size and distribution of phases present in a solid that are not visible to the human eye (typically taken to be less than 200µm) [35]. A “phase” is defined as “any part of the system which is physically homogeneous and bounded by a surface so that it is mechanically separable from other parts of the system” [36]. This section will focus on five phases of cement

microstructure: calcium sulfoaluminates, calcium hydroxide, calcium silicate hydrate, unhydrated clinker and voids. It should also be noted that cement chemists use abbreviations that correspond to the following: C=CaO; S=SiO₂; A=Al₂O₃; F=Fe₂O₃; \bar{S} =SO₃; H=H₂O [35,36]. These abbreviations are used in the section that follows.

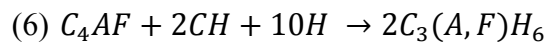
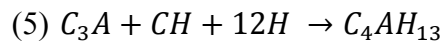
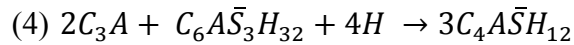
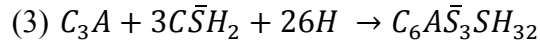
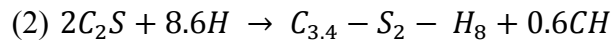
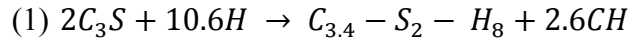
Anhydrous Portland cement is comprised of finely ground clinker and a small amount of calcium sulfate (gypsum). Calcium sulfate is added to control setting time of the cement. Clinker is a heterogeneous mixture of several high-temperature reactions between calcium oxide (CaO, or often referred to as “quicklime”), silica (S), alumina (A), and iron oxide (F). The finely ground clinker particles typically range in size from 1 to 50 μm. The principal compounds in clinker are tricalcium silicate (C₃S), dicalcium silicate (C₂S), aluminate (C₃A), and aluminoferrite (C₄AF). The percentages of these calcium compounds in ordinary anhydrous Portland cement typically range between 45 and 60 percent, 15 and 30 percent, 6 and 12 percent, and 6 and 8 percent, respectively [35].

As the Portland cement dissolves in water, calcium sulfate and the clinker calcium compounds begin to go into solution. As a result, needle shaped crystals of calcium trisulfoaluminate hydrate (C₆A \bar{S} ₃H₃₂), called ettringite, begin to form. The calcium trisulfoaluminate often becomes unstable and may eventually decompose to form monosulfoaluminate (C₄A \bar{S} H₁₈). Nevertheless, calcium sulfoaluminates only occupy approximately 15 to 20 percent of the hardened paste volume, and therefore do not play a significant role in the microstructure [35]. Formation of ettringite is followed by the formation of large prismatic crystals of calcium hydroxide (CH, or more accurately denoted as Ca(OH)₂), also called portlandite. Calcium hydroxide crystals occupy approximately 20 to 25 percent of the hardened paste volume [35]. Due to the relatively

large calcium hydroxide crystal size and low surface area, the strength contributing potential is limited. Hewlett reports that calcium hydroxide crystals can measure up to several tens of micrometers in diameter [36]. Formation of calcium hydroxide crystals is dependent upon the water-binder ratio and local environment, but form during hydration of C_3S . Though it contributes minimally to strength, calcium hydroxide crystals react with various silicates through pozzolanic activity to produce a much more desirable hydrate that is commonly referred to as calcium silicate hydrate (C-S-H). This is key to enhancing the microstructure and is fundamental to developing a HPC mix design. The topic is covered in detail in the section on supplemental cementitious materials and also in Chapter 3.

Calcium silicate hydrate (C-S-H) is the main product of hydration of portland cement. It occupies 50 to 60 percent of the hardened paste volume. The general formula is $CaO_x \cdot SiO_2 \cdot H_2O_y$ where “x” and “y” vary over a wide range. Although it varies, the ratio of C/S is reported to be between 1.4 and 2.0, but most often is reported to be 1.7 [36]. Because of the varying values of the molecular formula, it is most commonly referred to as “C-S-H” without the subscripts. The exact structure of C-S-H is unknown. Material scientist have proposed and debated various models for many years [35,37-39]; therefore, the structure of C-S-H at the nanoscale (between 1 and 100 nm) has not been modeled precisely. Investigative techniques in the last twenty years have only provided qualitative results, thus leaving cement researchers to debate quantitative measurements at the nanoscale. Attempts to characterize important C-S-H microstructure properties, such as pore size distribution and specific surface area at the nanoscale, are unfortunately dependent upon the technique used to measure these properties. Leading researchers

suggest the concept of C-S-H building blocks which are roughly spherical and flocculate to form clusters with a radius of 2.5 nm or less [40]. Pore space between clusters is typically referred to as the “interlayer space” in C-S-H, and range in size from 0.5 to 2.5 nm [35,38,39]. Recalling that C_3S is the most abundant calcium compound in clinker and noting that the molar ratio of C/S in C-S-H is typically taken to be 1.7, which is less than the molar ratio of C_3S , hydration of C_3S is always accompanied by the formation of calcium hydroxide. This is seen in formulas 1 and 2 below showing current theories on cement hydration [41]. Formulas 1 and 2 are the most important reactions for enhancing cement strength, controlling the formation of C-S-H from C_3S and the subsequent formation of calcium hydroxide. This research will focus primarily on formulas 1 and 2.



The preceding discussion identifies calcium sulfoaluminate hydrate, calcium hydroxide and calcium silicate hydrate as the three principal solid phases in a hydrated cement paste. A fourth phase can also exist at very low water-binder ratios with certain cements having larger grain size clinker particles. If the water-binder ratio is not sufficient to hydrate all of the clinker, the smaller clinker particles dissolve first and larger particles may only partially dissolve leaving a clinker particle of reduced size in the microstructure [35]. Some researchers have taken advantage of this technique and

purposefully maintain a very low water-binder ratio to minimize voids and allow unhydrated clinker particles to occupy space in the hardened cement paste [42].

In addition to the solid phases of hydrated cement, it is important to understand the detrimental role of pores, or voids, in the hardened paste. Voids significantly influence the properties of the hardened paste. Mehta [35] categorizes voids in hydrated cement paste into three groups: interlayer space in C-S-H (often referred to as “gel pores”), capillary voids/pores, and air voids [35]. As presented before, interlayer voids within calcium silicate hydrate typically vary in size from 0.5 to 2.5 nm [38,39]. Interlayer space in C-S-H is independent of the water-binder ratio, and given their relative size to other voids in the hardened paste, do not significantly affect strength of the paste [43,44]. These small voids are typically considered an integral part of the hydrated material [35,36].

Capillary pores are a second type of void found in hardened cement paste. Unlike interlayer space in C-S-H, there is a clear relationship between capillary pores, strength and the water-binder ratio. The water-binder ratio determines the porosity of the hydrated paste, as the water-binder ratio increases, porosity increases reducing the compressive strength [36]. Some studies suggest that the relationship between strength and porosity is linear [43,44]. It has also been suggested that the pore size distribution is more important than the total capillary porosity. Macropores (capillary pores larger than 50 nm) are more detrimental to strength, whereas micropores (capillary pores typically ranging from 10 to 50 nm) have less influence on strength but affect creep and drying shrinkage. A well-hydrated cement paste with a low water-binder ratio may have micropores, while a paste with a relatively higher water-binder ratio may have macropores. [35]. Mehta describes

the hydration process in a way that helps illustrate the influence of the water-binder ratio and formation of voids. To summarize, he concludes that the bulk density of hydrated cement is considerably lower than that of anhydrous cement. Approximately 1 cm³ of anhydrous cement requires about 2 cm³ of space once fully hydrated. There is minimal volume change between a freshly mixed paste (cement and water) and the completely hydrated paste; therefore, the hydration process can be viewed as voids within the freshly mixed paste being slowly replaced with solids, or hydration products. Since a higher water-binder ratio results in a larger volume to be filled within the hardened paste, the volume not filled by hydration products will remain as capillary pores in the hardened paste, thus reducing strength [35].

Voids introduced into the fresh mixture, either purposefully or unintentionally, are the third type of void found in hydrated cement. Entrained air may range from 50 to 200 μm, and entrapped air may be as large as 3mm. Since both entrained and entrapped air reduce the strength of the HPC, entrained air would not purposefully be incorporated into the mixture. Therefore, this research only addresses voids unintentionally introduced into the mixture. Developing a HPC that can be mixed in the field with standard construction tools would create a potential environment for entrapping air. A simplified mixing process will be used and entrapped air will be quantified when the procedure is properly followed. A low water-binder ratio will enhance strength by reducing capillary pores in the hardened paste. However, a low water-binder ratio complicates the mixing process. A balance between rheology and strength is required for a HPC that can be cast in the field without the benefit of a controlled laboratory environment. This topic is

investigated thoroughly in Chapter 3 covering the development of a self-consolidating high strength concrete (SCHSC).

2.4 Enhancing Compressive Strength: Supplementary Cementitious Materials

Though high strength can be achieved with superplasticizers and a low water-binder ratio with Portland cement as the only binder, replacing some of the Portland cement with supplementary cementitious material (SCM) offers several advantages. ACI defines “SCM” as “inorganic material such as fly ash (FA), silica fume (SF), metakaolin (MK), or ground-granulated blast-furnace slag (GGBFS) that reacts pozzolanically or hydraulically” [10]. Many other materials are used as SCMs, but the ACI definition lists those most widely used in the concrete industry. Though the definition of SCM is somewhat vague, all of these materials have one significant feature in common - they contain some form of vitreous reactive silica that will react with quicklime (CaO) and water to form additional C-S-H. This process is referred to as a “pozzolanic reaction”. A pozzolan is “a siliceous or silicaceous and aluminous material that in itself possesses little or no cementitious value but that will, in finely divided form and in the presence of moisture, chemically react with calcium hydroxide at ordinary temperatures to form compounds having cementitious properties” [10]. Thus, pozzolanic materials require Ca(OH)_2 to form C-S-H, whereas Portland cement contains enough CaO to exhibit self-cementitious (hydraulic) behavior, but also provides a source of Ca(OH)_2 to aid pozzolanic reaction. Recalling that Ca(OH)_2 typically occupies 20 to 25% of the hardened paste and offers minimal contribution to strength, adding pozzolans to a cement mixture that converts Ca(OH)_2 to C-S-H during secondary hydration can significantly

refine pore structure and improve material microstructure. In addition to the chemical reaction, pozzolans finely divided particle size contribute to mechanical advantage as well. Unreacted pozzolans can serve as fillers within voids to further refine the microstructure and enhance strength and durability. This is particularly advantageous for the interfacial zone between paste and aggregate or reinforcement, which often serves as a weak link in the matrix [45,46].

Pozzolans are commonly referred to as “mineral admixtures” in cement and are categorized as “natural” (e.g. volcanic tuff, calcined clay) or “artificial” (e.g. silica fume, fly ash). Natural pozzolans are inorganic minerals typically of volcanic origin or sedimentary rocks with suitable chemical and mineralogical compositions. A detailed investigation of natural pozzolans is presented in Chapter 3.

Artificial pozzolans also originate from minerals, but are by-products of various manufacturing industries [10,36]. For example, the smelting process for certain silicon metals and ferrosilicon alloys generates fume containing a high concentration of silicon monoxide (SiO) that oxidizes in air during condensation forming silicon dioxide (SiO₂). The fume, typically containing more than 90% SiO₂ and an average particle size of 0.1 μm, is filtered from the gas escaping the furnace and is known as SF. SF was first used in concrete in Norway in the early 1950s, but is now commonly used as an artificial pozzolan in HPC. With an average particle diameter that is less than one-hundredth of that for ordinary Portland cement (OPM), SF is a highly effective pozzolan that imparts many advantages to HPC (i.e. improved rheology due to spherical shape, reduced porosity, enhanced strength and durability due to Ca(OH)₂ consumption) that cement researchers have thoroughly investigated since the early 1980s [36,45,47,48]. An optimum

theoretical amount of SF replacement for OPC was reported to be approximately 20% to 25%. The study reported that at 15% replacement, SF reacted fully with the available Ca(OH)_2 produced from OPC hydration. The pozzolanic reaction rate was governed by the rate at which SF can react with available Ca(OH)_2 . However, as the SF replacement reached 30%, the reaction rate was controlled by availability of Ca(OH)_2 produced by hydration of the cement. Thus, at higher replacement rates, SF served more as inert filler in the hardened paste [49]. A similar experimental study reported that 16% SF replacement for OPC would react fully at water-binder ratios of 0.4, 0.3 and 0.2 [50]. However, due to the significant rise in cost of SF in comparison to the cost of OPC, Aitcin suggests a SF replacement of OPC in HPC should be 8% to 10% [17].

It is important to note that pozzolans are often used as SCM, but not all SCMs are pozzolans. GGBFS (a term still used by cement researchers but now considered obsolete by ACI and ASTM and replaced by the term “slag cement”) is an example of this. Slag cement is a derivative of blast furnace slag (BFS), which is a by-product of producing pig iron. ASTM defines blast furnace slag (BFS) as “the non-metallic product, consisting essentially of silicates and aluminosilicates of calcium and other bases that is developed in a molten condition simultaneously with iron in a blast furnace” [51]. If molten BFS is rapidly chilled by immersion in water, a glassy, granular material is formed and called GBFS. Cooling methods other than quenching of the molten BFS (i.e. air-cooled, expanded) do not result in cementitious properties. If the GBFS is ground to the same fineness as Portland cement, it is called “slag cement”. Slag cement is used as a SCM, but it isn’t a pozzolan. Slag cement can react hydraulically, so it does not require the presence of Ca(OH)_2 to react with water to form additional C-S-H. However, without

Ca(OH)₂, it does not form enough cementitious products, and the rate of reaction is not sufficient for structural applications [35]. Slag cement is covered more thoroughly in Chapter 3 in developing a SCHSC.

Cement researchers have pursued a wide variety of by-products from various industries to evaluate pozzolanic reactivity with Portland cement. Ground corn cob ash, wheat straw ash, sugarcane bagasse ash, rice husk ash and volcanic tuff are examples of such pozzolans investigated by cement researchers [52-56]. For these examples, researchers concluded that the pozzolans either improved material strength, or did not have an adverse effect on material strength when the material contained a minimum of 70 percent SiO₂ + Al₂O₃ + Fe₂O₃, as required by ASTM C618 [57]. In general, pozzolanic reactions are secondary reactions that occur slowly at room temperature. The process can take several months or even continue over several years. The reaction time increases with pozzolans that are more vitreous and have finer particle sizes [17].

2.5 HPCs with Enhanced Compressive Strength

There are many examples of HPCs with enhanced compressive strength in the literature. However, most are not developed for use as armor or force protection. Some of the more significant achievements in recent history are presented in this section. Whether the high, very high or ultra high strength HPC was developed for force protection purposes or not, researchers generally employ the ideas presented in the previous sections: superplasticizers to achieve a low water-to-binder ratio, and SCM to refine the cement microstructure via secondary hydration while minimizing porosity and increasing density.

2.5.1 DSP cement and Reactive Powder Concrete

With the arrival of HRWRs in 1976, water to binder ratios were reduced, but typically not below the threshold of 0.25 to 0.30 until results by H.H. Bache [58] reported findings of his 280 MPa concrete with a water to binder ratio of 0.16. Bache achieved these strengths with a very high dosage of superplasticizer, SF, calcined bauxite, and special external vibration and curing requirements [17,58]. Bache's approach was to simply reduce porosity of concrete by using "densely packed particles of size ranging from 0.5 to 100 μm " with "homogeneously arranged, ultra-fine particles ranging in size from about 0.050 to 0.5 μm " (SF), "made possible by superplasticizers" [58]. Bache patented his material and method for producing the material, which was named "Densified systems containing homogeneously arranged ultrafine particles" and referred to as "DSP" [59]. DSP required heavy external vibration and 280 MPa strength was achieved only when cured in water at elevated temperatures (80 degrees Celsius). Though the material was only producible in the laboratory and was very expensive, it was a benchmark in successfully reaching lower water-binder ratios and using supplementary cementitious material to enhance the microstructure of cement, both resulting in increased compressive strength of concrete [17]. The mix design for DSP is shown in Table 2.3.

Richard and Cheyrezy [60] published findings in 1995 of their "Reactive Powder Concrete" (RPC) that achieved between 170 MPa (RPC 200) and 800 MPa (RPC 800) depending on the curing environment and type of aggregate. The basic principles of RPC were: 1) enhancement of homogeneity by eliminating coarse aggregates, 2) enhancement of compacted density by application of pressure (50 MPa) before and during setting, 3)

enhancement of microstructure through post-set heat treatment, 4) strict mixing and casting procedures. RPC 200 achieved 240 MPa when cured at 90 degrees Celsius for 3 days and RPC 800 achieved 800 MPa when cured at 400 degrees Celsius with a 50 MPa confining pressure, and steel fibers at 1.5% to 3% by volume (3 mm length). Both RPC 200 and RPC 800 required 25% replacement of cement with SF and had a water to cement ratio from 0.15 to 0.19. The authors reported that the SF served three primary functions: 1) filling voids between the next larger class particles (cement), 2) improving rheology by the lubrication effect from the perfect spherical shape of SF, and 3) secondary hydrates by pozzolanic reaction. Table 2.3 presents the mix design for RPC 200.

It should be noted that the curing condition (heat cured under a confining pressure) had a significant impact on the range of compressive strength in RPC, as seen in the strength variation between RPC 200 and RPC 800. Richard and Cheyrezy reported that heat curing (after initial concrete set) accelerated pozzolanic reaction and modified the microstructure of the hydrates [60]. Curing UHPC in a heated and controlled environment is a common technique in attaining substantial strength gain in concrete research. However, these conditions are not realistic for a soldier mixing concrete in the field in a contingency environment.

2.5.2 HSPC, VHSC and CorTuf

The preceding section presented two key materials that were benchmark achievements in developing HPCs with ultra high compressive strength. DSP and RPC are commonly cited in the literature as significant accomplishments in elevating concrete

compressive strengths to new levels. Both DSP and RPC used the key principles presented in the preceding sections, namely, that of lowering water to binder ratios with superplasticizers and refining the cement microstructure with finely graded pozzolans. In addition to this, DSP and RPC utilized specialized aggregate and strict casting and curing conditions at elevated temperatures.

In the 1990s, DSP and RPC served as a blueprint for ERDC researchers while developing concrete with enhanced compressive strength for the Army. The projects were very successful and lead to several research programs that are still active. This section summarizes the development of High Strength Portland Cement (HSPC) Concrete, Very High Strength Concrete (VHSC), CorTuf and High-Strength High-Ductility Concrete (HSHDC). All of these HPCs with high to ultra high compressive strengths were developed as candidate protective materials or targets for the Army.

HSPC Concrete

In 1989, researchers at Waterways Experiment Station (renamed as the ERDC in 1999) developed HSPC concrete for use in projectile penetration studies to enhance the survivability of hardened facilities [61]. A primary objective of the research program was to develop as high an unconfined compressive strength as convenient using available materials. The research investigated 36 concrete mixtures using varying proportions of components including: Type I, II, III and Class H cement, *Class F* and *Class C* fly ash, HRWR admixtures, as well as SF. Water to cementitious material (cement + FA + SF) ratios varied between 0.20 and 0.27. SF ranged between 7.7 to 16.7 percent by weight of cement, and FA varied between 0 to 16.7 percent by weight of cement. Type III and

Type I cements were found to yield the highest strengths, while Type II and *Class H* yielded lower strengths. Ultimately, Type I cement was selected over Type III cement because of the propensity for thermal cracking with Type III cement given the massive size of the targets. The higher amounts (16.7%) of *Class F* FA yielded lower early strengths (7 days), but eventually would prove to yield the highest strengths at 56 days. *Class F* FA yielded higher strengths than *Class C* FA. Test beams and cylinders were cast to verify flexure and compressive strengths. All test specimens required “extended external mechanical vibration” on a laboratory-vibrating table before specimens were “adequately free of large voids” [61]. Immediately after casting HSPC concrete, the concrete slabs were insulated with 8 inches of fiberglass roll insulation wrapped around the perimeter and two layers of $\frac{3}{4}$ ” double foil-backed board and sealed with plastic sheeting, test specimens were cured for 56 days in a humidity controlled curing room [62]. The final optimized design had a slump of 7 inches [63] and reached a crushing strength of 103.5 MPa at 56 days.

VHSC and CorTuf

During this same period, ERDC researchers were also developing VHSC. The mix design for VHSC is shown in Table 2.3. Neeley and Walley [64] used Type V cement to minimize the C_3A content, thus maximizing the amount of C_3S and C_2S available for developing C-S-H. Type V cement also has a relatively moderate grain size, thus reducing the total surface area of cement particles leading to lower water demand. SF and silica flour were used in VHSC for their ideal particle size and shape for achieving dense particle packing, but the authors also acknowledged the added benefit of

potential pozzolanic reaction when cured in heat, as well as the hardness of these materials. O’Neil [42] reports that Walley and Neeley used a powder form of SNF HRWRA and water to cementitious material (cement + SF) ratio of 0.20. To date, very little has been published on VHSC, but the work served as a foundation for second generation VHSC.

Building on the findings of Walley and Neeley, O’Neil further developed and optimized VHSC. The work was published in a PhD dissertation [42] and was patented [65]. Though O’Neil’s dissertation also refers to the material as VHSC, the second generation of VHSC was eventually renamed “CorTuf”. A unique aspect of CorTuf was the use of *Class H* cement. *Class H* cement has a high silica content and a larger grain size as compared to other types of cement. These attributes are helpful in minimizing the water demand and maximizing C-S-H. Larger cement grain size particles will result in less surface area of cement in the matrix, thus, less water is needed to hydrate the cement. In theory, the smaller cement particles would hydrate fully, while the larger cement particles would hydrate only partially, leaving an inner-core of unhydrated cement serving a function similar to a strong aggregate in the matrix. The sequence of development of UHPCs at ERDC is depicted in Figure 2.3.

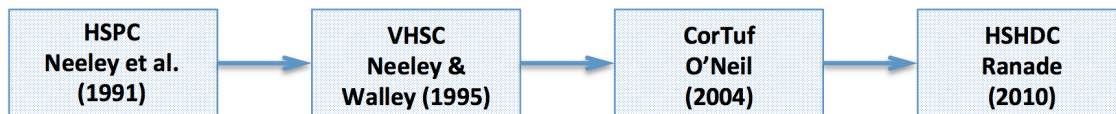


Figure 2.3 Development of UHPCs at the ERDC

O'Neil's underlying principles for enhancing compressive strength in CorTuf were listed as [42]:

- Minimization of flaws in the matrix
- Improvement of matrix homogeneity
- Maximization of the silica content for conversion to C-S-H
- Maximization of the density of the matrix
- Improvement of the microstructure
- Enhancement of matrix ductility

O'Neil's principles are very similar to the ideology shared by many cement researchers. Five of the six principles listed above follow the fundamental approach summarized in the preceding sections of this chapter. His approach emphasized the importance of dense particle packing to minimize flaws (voids) in CorTuf. Dense particle packing was achieved through careful selection of constituent material ranging in particle sizes from 0.1 μm (SF) up to 600 μm (silica sand). Table 2.3 summarizes the mix design of CorTuf and the particle sizes of each constituent material. CorTuf was reported to have a compressive strength of 236 MPa when cured following the regime stated below.

- Twenty four hours in a steam chamber
- Seven days in a lime water bath at ambient temperatures
- Four days submerged in hot bath at 90 degrees Celsius
- Two days in an oven at 90 degrees Celsius

O'Neil reported that CorTuf specimens cured as described above may achieve compressive strengths ranging from 245 MPa to 266 MPa; however, the same specimens would produce compressive strengths ranging from 160 MPa to 180 MPa if cured in 20 degree Celsius lime water solution (specimens had steel fiber reinforcement).

The CorTuf mix proportions shown in Table 2.3 were reported to have a flow number of 71.5 [42]. ASTM C1437 describes the flow number as the “resulting increase in average base diameter of the mortar mass, expressed as a percentage of the original base diameter” when the mortar mass (1 inch thick tamped and troweled into calibrated mold) is dropped 25 times in 15 seconds over a distance of 13 mm on a standard flow table [66]. O’Neil describes the material as “sticky” and notes that oil must be used to coat the mold and help the material flow. HPCs with enhanced compressive strength commonly suffer from such workability limitations due to the higher content of cement than typical concrete (which increases the cost and cohesive properties of the matrix), as well as a low water to binder ratio. Often, this presents a problem for the material to flow around tightly spaced reinforcement or hardware inserts for handling or connecting other structural components.

Table 2.3 Component materials and mass proportions relative to mass of cement

Component	DSP ^(a,b)	RPC 200 ^(a)	VHSC ^(c)	CorTuf ^(d)	HSHDC ^(d)
Cement	1.00	1.00	1.00 ^(e)	1.00 ^(f)	1.00 ^(f)
Aggregate	2.88 ^(g)	n/a	n/a	n/a	n/a
Sand	1.77 ^(h)	1.10 ⁽ⁱ⁾	1.20 ⁽ⁱ⁾	0.967 ^(k)	0.70 ^(k)
Silica Fume	0.33	0.25	0.24	0.389 ^(l)	0.389 ^(l)
Silica Flour	n/a	n/a	0.34	0.277 ^(m)	0.277 ^(m)
HRWRA	0.03 ⁽ⁿ⁾	0.016	0.04 ⁽ⁿ⁾	0.0171 ^(o)	0.0177 ^(o)
Water	0.25	0.15	0.25	0.208	0.208
F'c (MPa)	150	170	239	236	166

Table Notes:

- (a) Water cured 20°C
- (b) External vibration with applied compacting load for consolidation
- (c) Cured 56 days 83°C
- (d) Cured 7 days 20°C, 4 days 90°C hot bath, 2 days 90°C oven
- (e) Type V cement
- (f) Class H cement (20 to 100µm)
- (g) Crushed granite 8 to 16mm
- (h) Quartz sand 0.25 to 4µm
- (i) Crushed Quartz: 150 to 600µm
- (j) Chert sand: 200µm to 6.4mm
- (k) Silica Sand: 100 to 600µm
- (l) 0.1 to 1µm
- (m) 5 to 100µm
- (n) SNF
- (o) Polycarboxylate ether

2.6 HPC with Enhanced Compressive Strength and Ductility: HSHDC

Five of O'Neil's CorTuf principles were the criteria for compressive strength improvements; the sixth principle addressed a common problem with HPCs. Increasing the compressive strength of concrete improves ballistic performance, but it also tends to

increase matrix brittleness and reduce tensile capacity. A study on the brittleness and fracture properties of high-strength concrete showed that increasing the compressive strength by 160% resulted in a 25% increase in fracture toughness, but more than a 200% increase in brittleness number (determined by the size effect method to obtain fracture properties that are size- and shape-independent for brittle heterogeneous material) [67]. Whereas, conventional strength concrete has a tensile capacity that is normally 10% to 15% of the compressive strength, Williams et al reported the CorTuf matrix had a tensile capacity that was 4.2% of the compressive strength [68]. Others have characterized the tensile properties of HPCs with high to ultra high compressive strength and found similar results [69].

Though compressive strength is important for ballistic performance, ductility is another important material property for protection against extreme loads. In general, an increase in material ductility increases material toughness, or energy dissipation potential. This is an important attribute for a material resisting severe loading, such as blast load. In a high compressive strength HPC with a brittle matrix, ductility is achieved through an optimized selection of fiber reinforcement. Randomly distributed short fibers are the preferred method for HPC reinforcement because conventional continuous reinforcement is not practical for thin panels, especially for applications stated in the introduction of this research. Since the brittle matrix has very low tensile strength, appropriate fibers must be selected to enable successful bridging of crack openings. If this process is properly engineered and optimized, additional energy is consumed as the fiber partially pulls out of the matrix before arresting the crack, mobilizing another crack to repeat the process. In order

for this progressive cracking condition to exist, a balanced mix of fiber, matrix and interface is necessary.

This quantitative link between material properties and material microstructures (i.e., fiber, matrix, and interface) is termed “micromechanics” [70]. An investigation of micromechanics provides a more thorough understanding of the interaction between the constituents of cementitious material and fiber reinforcement. Researchers at the University of Michigan successfully developed and implemented this approach with “Engineered Cementitious Composites” (ECC). Though it has low strength, ECC was developed to be highly ductile to absorb energy from extreme load / displacement events such as earthquakes [70]. Researchers at the ERDC partnered with University of Michigan to develop a new high strength high ductility concrete (HSHDC). HSHDC is supposed to combine most of the desirable attributes of CorTuf (160 MPa compressive strength) and ECC (average tensile strain capacity of 3.5%) [8,9]. The research is ongoing, but HSHDC has shown very promising results under quasi-static loads. Air blasts experiments have also been conducted at the ERDC in the blast load simulator (BLS) to determine strain rate sensitivity of the performance-based design HPC. The mix design and curing requirements for HSHDC are very similar to CorTuf. External vibration for material consolidation during casting is preferred and heat curing is required. The mass proportions of components (relative to cement mass) are shown in Table 2.3 and mechanical and physical properties of the polyethylene fiber optimized for HSHDC are shown in Table 2.4. Figure 2.4 compares HSHDC to CorTuf when loaded in direct tension and Figure 2.5 shows the ductile response under flexure. Though the development of HSHDC was a significant achievement, the cost of the polyethylene fiber

resulted in a HPC that is three times more costly than CorTuf, which was already an order of magnitude more expensive than standard ready mix concrete. Nonetheless, for specific applications, achieving ultra-high strength and ductility in cementitious material was an accomplishment and step in the right direction for the ERDC and future research programs. A micromechanics approach to optimize the fiber, matrix and interface to improve ductility and toughness of a high strength, field cast and cured HPC is investigated thoroughly in Chapter Five.

Table 2.4 Properties of HSHDC fiber

Fiber Properties	Values
Diameter (μm)	28
Length (mm)	12.7
Volume fraction	2%
Tensile strength (MPa)	3000
Young's Modulus (GPa)	100
Specific Gravity	0.97
Fiber mass / Cement mass	0.0214

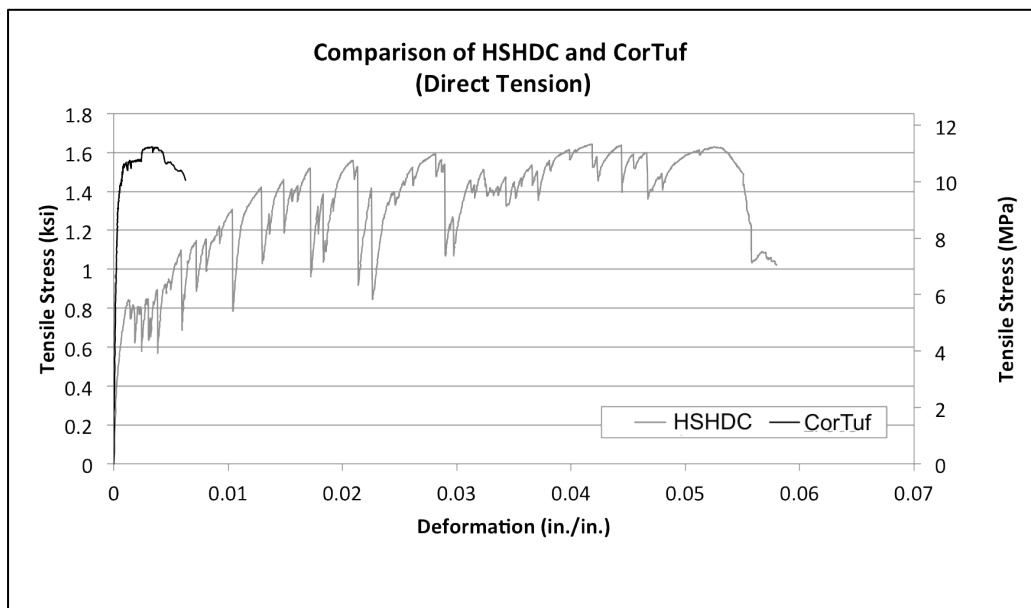


Figure 2.4 Direct Tension of HSHDC and CorTuf



Figure 2.5 HSHDC loaded in flexure

2.7 Summary

Sections 2.2 through 2.4 summarized the principles for enhancing compressive strength of concrete. Incorporating high dosages of third generation HRWR admixtures to lower the water to binder ratio and using supplementary cementitious material to refine the microstructure and maximizing C-S-H significantly improves compressive strength, and as a result, the ballistic performance of the concrete. Sections 2.5 and 2.6 summarized historical and recent achievements of HPCs that utilized this methodology. Though these HPCs have successfully achieved high to ultra-high compressive strengths, they also require excessive mechanical vibration, rigorous curing and strict quality control to achieve the desired mechanical properties. Satisfaction of these conditions is not possible with unskilled labor operating in a less-than-ideal environment. A balance between rheology and strength is required for a HPC that can be cast in the field without the benefit of such laboratory resources. A self-consolidating concrete is a concrete that “can be compacted into every corner of a formwork, purely by means of its own weight and without the need for vibrating compaction” [71]. The principles presented in the

previous sections will be utilized to develop a HPC that flows under its own weight.

This research will focus on developing and characterizing a SCHSC with high compressive strength and improved performance under quasi-static and transient loads.

CHAPTER 3

DEVELOPMENT OF A SELF-CONSOLIDATING HSC

3.1 Introduction

3.1.1 Background of Self-Consolidating Concrete

Self-consolidating concrete (SCC) was first introduced in Japan in 1988. The Japanese construction industry recognized a decline in the number of skilled construction workers in early to mid 1980s. The gradual reduction of skilled workers had resulted in a reduction of quality and durability of concrete structures during that time. In 1986, researchers at the University of Tokyo responded with a prototype of durable concrete that was independent of the quality and skill level of construction labor. The durable concrete was called “High Performance Concrete”. During that same period, the American Concrete Institute had used the same term to refer to a completely different type of concrete; as a result, the name was changed to “self-compacting high performance concrete”. The prototype was characterized as having “self-compacting behavior” in the fresh state, with an “avoidance of initial defects” in the early stage and “protection against external factors” in the hardened state. Essentially, the goal was to develop a material that could be easily cast by unskilled labor, yet remain relatively defect free (due to the self-consolidating behavior) [72,73].

The terms “self-compacting concrete”, “self-leveling concrete” and “self-placing concrete” are used to refer to this material, but “self-consolidating concrete” has become

the more common name for this class of HPC. The American Concrete Institute defines SCC as a “highly flowable, non-segregating concrete that can spread into place, fill the formwork, and encapsulate the reinforcement without any mechanical consolidation”. It is the fresh, plastic properties of SCC that differentiates it from conventional concrete. [74]. Similar to conventional concrete, the hardened properties of SCC will vary depending on the particular proportions of material constituents. Because of this, SCC is considered a class of cementitious material, rather than a specific type of concrete. Because of the unique plastic properties of SCC, this class of material is considered to be a HPC.

The benefits of SCC are well documented [27,75]. Some of the more relevant benefits of SCC to this research are:

- Reduces labor and equipment needs
- No need for vibration to ensure proper consolidation
- Achieves the desired mechanical properties independent of labor skills
- Expeditious filling of highly reinforced sections in formwork
- Superior surface quality that is void of honeycombs

The use of SCC in the United States has grown considerably since early 2000. Precast concrete production plants were early adopters and remains the predominate industry to use SCC. It is estimated that the precast concrete industry produced 135,000 m³ of SCC in 2000 and it increased to 1.8 million m³ in 2003. By 2008, approximately 40% of all precast concrete production was SCC. In contract, SCC only constitutes approximately 2-4% of the cast-in-place concrete in 2008, but it appears to be growing. [27,76,77]. ACI committee 237 was organized in 2003 and issued its first report in April 2007 as part of the ACI “Emerging Technology Series” to report the current state of knowledge with respect to SCC. ASTM subcommittee C09.47 currently maintains 5

active standards within its jurisdiction of standard test methods of SCC [74,78]. SCC has become a topic of interest amongst concrete researchers as well. Daczko [27] reports that the first international symposium on SCC was held in 1999. Sixty-five papers were presented at the symposium covering five topics within SCC research. The sixth international symposium was held in 2010 with 126 papers presented covering 16 various topics of SCC research.

3.1.2 Fresh-state properties of a SCC

Figure 3.1 shows a comparison of the fresh-state behavior of typical concrete versus SCC. Figure 3.2 demonstrates how key concrete admixtures affect the fresh-state properties of SCC. As illustrated in Figure 3.2 and discussed in the following, a material must possess all three of these fresh state properties to be considered a SCC [74]:

- Stability (segregation resistance) – the ability of a material to maintain homogeneous distribution of its various constituents during its flow and setting.
- Passing ability (confined flowability) – the ease with which concrete can pass among various obstacles (reinforcement) and narrow spacing in the formwork without blockage (e.g. aggregates separating from paste)
- Filling ability (unconfined flowability) - the ability of a SCC to flow into and fill completely all spaces within the formwork.

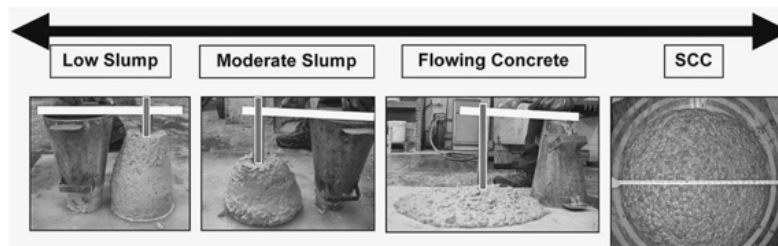


Figure 3.1 Workability Continuum [27]

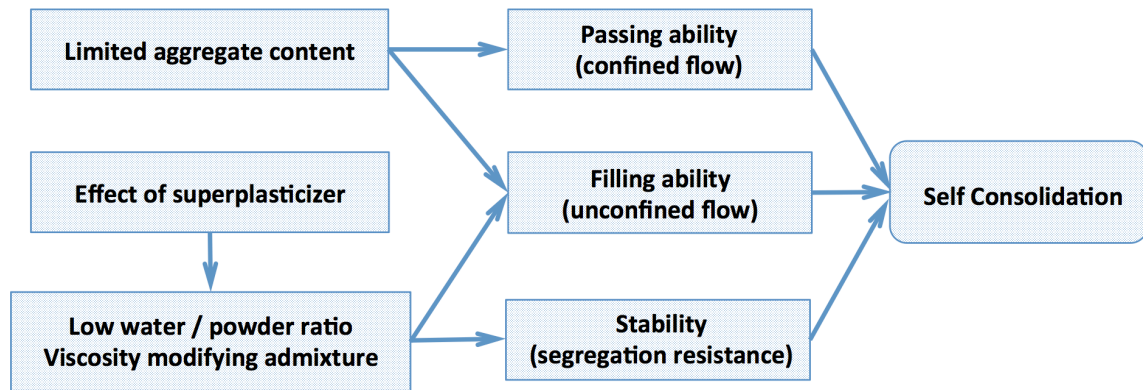


Figure 3.2 Methods of achieving self-consolidation [79]

SCC Passing Ability

Passing ability of a SCC mixture is measured according to the “J-ring test” [80] as demonstrated in Figure 3.3. The test measures how well a SCC mixture passes around obstacles. The J-ring apparatus is used to simulate densely spaced reinforcing bars and measurements are taken to see if the J-ring obstructs flow. Though not adopted by ASTM, the “L-box test” and “U-box test” are alternative test methods to the J-ring test [27]. For this research, the ASTM “J-ring test” was used to evaluate passing ability.

SCC Stability

ACI categorizes stability of SCC as static or dynamic. Static stability is the resistance to bleeding, segregation and surface settlement during the plastic state after material is placed. Stability is achieved through viscosity modifying admixtures (VMAs), powder content (the amount of powder relative to fine and coarse aggregates, and the selection of particles that constitute the powder), and a low water to powder ratio. The “column segregation test” [81], the “penetration test” [80], and the “visual stability index” [80] are ASTM test methods that quantify static stability of a mix. Dynamic

stability is the resistance to segregation during placement of the SCC as the material flows into place. Currently, there is no standard test for measuring dynamic stability. The ASTM “visual stability index” and X-ray computed micro tomography (micro-CT) were used to quantify stability of the mix.

SCC Filling Ability

The most recognizable fresh state property of a SCC mix is filling ability. Filling ability is commonly referred to as “fluidity” or “flow” of a mix and is typically considered to be the primary characteristic of SCC. Filling ability (flow and flow rate) is measured by the ASTM “slump flow test” [80]. The test measures the maximum spread or diameter of flow of the SCC using a standard slump cone. When the slump cone is filled and then removed, the time required for the SCC to flow to a diameter of 500mm is recorded as the T_{500} of the mix and the maximum diameter of the flow is recorded as the slump flow (or, D_{max}). For this research, the ASTM “slump flow test” was used to measure filling ability. The D_{max} and T_{500} values were noted for each mixture.

Filling ability is enhanced with superplasticizer, but a high dosage of superplasticizer results in poor stability. To offset the loss of stability from high dosages of superplasticizers, viscosity modifying admixtures (VMAs) and high powder content (cement, fly ash, GGBFS, and other finely ground SCMs) are used to promote stability. VMAs improve stability by increasing cohesiveness of constituents in the fresh state. Furthermore, it has also been shown that VMAs decrease sensitivity of the mix to variations in material supply. Variations in moisture content of aggregates, gradation of aggregates, or minor changes in mixing techniques have less impact on fluidity when

VMAs are used. This mix characteristic is referred to as “robustness”. Therefore, VMAs make a SCC mix more robust as well as stable [75,82]. Figure 3.4 illustrates how VMAs improve robustness [75]. VMAs offer several unique benefits to SCC during the fresh and hardened state. A thorough investigation is presented in this chapter to illustrate the benefits of a VMA to the SCHSC matrix developed in this research.

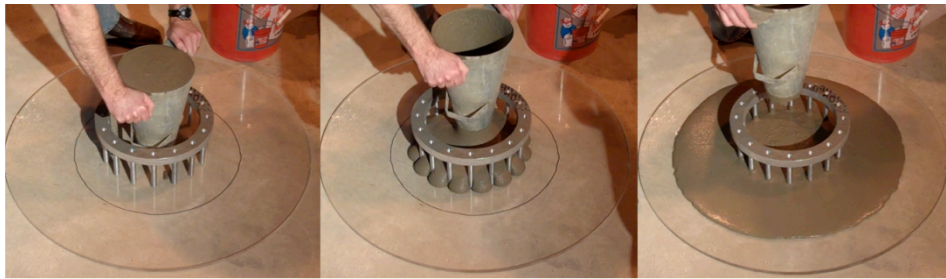


Figure 3.3 J-ring test measuring passing ability of SCC

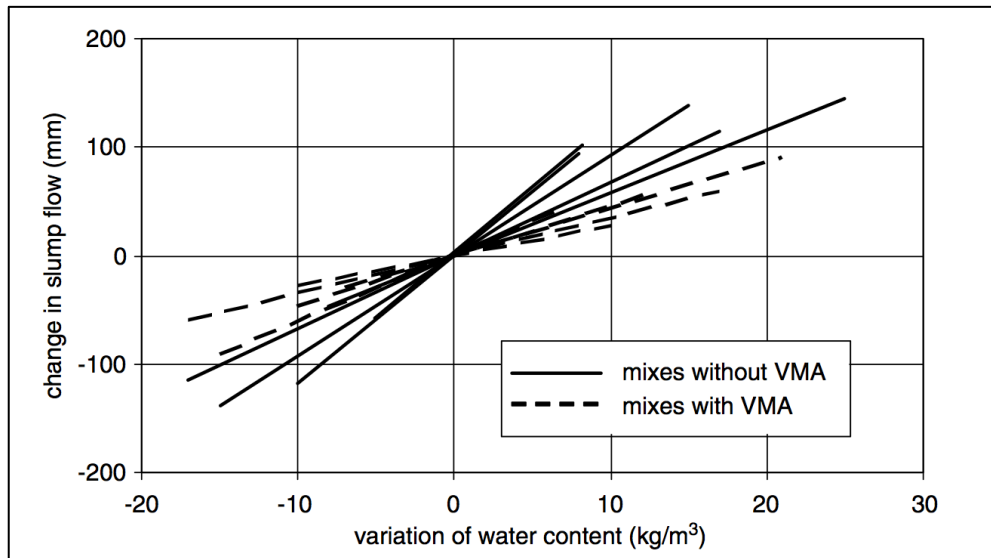


Figure 3.4 Effect of variation of water content of slump flow of SCC mixes with and without VMAs [75]

3.2 Developing a SCC

3.2.1 Overview

The literature suggests three approaches to designing a SCC mix. Mixture proportioning falls into one of the three categories [74,79,83]:

- High powder content and HRWRA: Viscosity is increased with addition of fly ash, silica fume, GGBFS or finely ground fillers. This approach is more common in Europe with readily available blended cements.
- Low powder content, HRWRA and high dosage of VMA: This approach is more common in North America than in Europe where VMAs aren't as readily available.
- Moderate powder content, HRWRA and moderate VMA dose: Stability is controlled through blending of aggregates, lowering water content and the VMA. This approach is a combination of the first two approaches and is the most common approach followed in North America.

A review of SCC mixtures in the literature would provide guidance for the development of a SCHSC mix. Domone [75] presented a thorough review of sixty eight case studies of SCC mixtures found in the literature between 1993 and 2003. All case studies were projects of significant scale, requiring several cubic meters of concrete to qualify for the study. Thus, laboratory sized mixtures and research oriented mixtures weren't included in the case studies. All sixty-eight projects involved practical applications of SCC mixtures. It was reported that a very limited number of case studies were categorized as the second approach of "Low powder content, HRWRA and high dosage of VMA". Domone also reported the following:

- 90% of the SCC mixtures reported a slump flow between 600 mm and 750 mm
- T_{500} values ranged from 1.8 seconds to 12 seconds, with a few exceptions reporting values between 10 seconds and 20 seconds

- There was no pattern of higher slump flows being associated with lower flow rate values, suggesting an independence of the two properties
- Almost all cases reported use of a binary or ternary blend of Portland cement and SCM or finely ground non-reactive powder (e.g. ground limestone)
- Powder content (cement, SCM and ground limestone, or any particles with diameter less than $0.125\mu\text{m}$) ranged from 425 kg/m^3 to 625 kg/m^3
- Water / powder ratios ranged between 0.26 to 0.48, with 80% of the mixtures reporting values in the range of 0.28 to 0.42
- Compressive strengths ranged from 20 MPa to almost 100 MPa. Eighty percent had compressive strengths in excess of 40 MPa
- Thirty-four cases reported the use of a VMA in the SCC mix. VMAs were reported to have improved stability and reduced sensitivity to variations in materials used in the SCC mix, particularly the varying moisture content of coarse and fine aggregate

These findings are in agreement with standard practices found in ACI committee 237 report on SCC[74]. Water to cementitious material ratio between 0.32 and 0.40 is recommended. The ACI publication also reports that an SCC mix with a slump flow less than 560 mm may require mechanical vibration for proper consolidation; therefore, a slump flow greater than 560 mm is preferred for this research.

3.2.2 Fly Ash and GGBFS

Binary and ternary cement blends (replacing a portion of cement with fly ash, GGBFS, or silica fume) have been used to enhance fresh-state and hardened properties of SCC. Due to the spherical shape and smooth surface of fly ash particles, workability is enhanced when 20 to 40 percent of the cement is replaced by fly ash [74]. Similarly, the ACI “Guide for Selecting Proportions for High-Strength Concrete” recommends that 15 to 25 percent of cement be replaced with Class F fly ash to provide strength gain from pozzolanic reaction during secondary hydration (as discussed in Chapter 2). Some

researchers have found that when replacing cement with fly ash, the water to powder ratio must be increased to maintain the same slump flow and V-funnel values achieved without fly ash replacing portions of cement. This indicates that fly ash enhances cohesiveness and viscosity. However, increasing water to powder ratio will typically reduce strength, likely offsetting any potential strength gains from pozzolanic reaction. The research reports that when 20% of the cement is replaced with fly ash, there is no significant effect on hardened properties. If 20% is exceeded, a reduction in compressive strength and split tensile strength is observed. The reduction is less significant at later ages [84].

GGBFS has shown to enhance workability and increase strength. Strength gains can continue to occur up until 91 days after mixing. Similar to fly ash, slag is a by-product and its chemical composition is dependent on the raw materials used to create the by-product. In general, increasing the fineness of GGBFS will increase the strength enhancing potential. ASTM C989 [85] classifies GGBFS (i.e., slag cement) according to performance in the slag activity test into three categories: Grade 80, Grade 100 and Grade 120. A cube that is made with 50% Grade 120 GGBFS and 50% Portland cement must achieve a 28-day compressive strength that is a minimum of 115% of the control cube 28-day compressive strength made from 100% Portland cement. High proportions of Grade 120 GGBFS may improve strength, but it has been reported to affect stability and reduce robustness with problems of consistency control [86]. For this research, Grade 120 GGBFS will be used.

Table 3.1 presents examples of mix proportions and associated 28-day and 91-day compressive strengths and slump flows for two SCC mixtures [74]. These mix

proportions are given in the ACI report as guidelines for how a successful SCC mix can be created. For comparison, two HSC mix designs are shown in Table 3.1. The HSC mix designs are published in the ACI “Guide for Selecting Proportions for High-Strength Concrete Using Portland Cement and Other Cementitious Materials” and “Guide to Quality Control and Assurance of High-Strength Concrete” [87,88]. Table 3.1 also presents the mix design for HSHDC, as discussed in Chapter 2. The HSHDC formula is presented for comparison with the published guidelines by ACI for achieving HSC and SCC. HSHDC would be considered to have highly desirable mechanical properties (like compressive strength, ductility, toughness,) at the sacrifice of rheology, ease of mixing and cost.

Table 3.1 Mix proportions for example SCC and HSC mixtures, HSHDC and baseline control mix

	SCC1	SCC2	HSC1	HSC2	HSHDC	Control 1 & 2
Cement	309 kg/m ³	445 kg/m ³	475 kg/m ³	327 kg/m ³	907 kg/m ³	626 kg/m ³
Slag Cement	120 kg/m ³	0	0	0	0	0
Silica Fume (micro)	0	0	74 kg/m ³ (0.11 of cm)	27 kg/m ³ (0.06 of cm)	353 kg/m ³	0
Fly Ash	0	0	104 kg/m ³ (0.16 of cm)	87 kg/m ³ (0.20 of cm)	0	152 kg/m ³ (0.20 of cm)
Silica Flour (ground)	0	0	0	0	251 kg/m ³	0
Total CM ^(a)	429 kg/m ³	445 kg/m ³	653 kg/m ³	441 kg/m ³	1511 kg/m ³	778 kg/m ³
Coarse Aggregate	1006 kg/m ³	890 kg/m ³	1070 kg/m ³	1120 kg/m ³	0	0
Fine Aggregate	758 kg/m ³	890 kg/m ³	593 kg/m ³	742 kg/m ³	635 kg/m ³	1009 kg/m ³
w/cm	0.43	0.40	0.23	0.32	0.15	0.40 or 0.32
HRWRA	9.8 mL/kg	7.8 mL/kg	25.1 mL/kg	21.5 mL/kg	x mL/kg	0.32% or 0.43% (HRWRA/CM)
VMA	1.95 mL/kg	1.0 mL/kg	0	0	0	Varies
Compressive Strength @ 28-day	51.5 MPa	62.1 MPa	107 MPa	73 MPa	166 MPa	
Compressive Strength @ 91-day	n/a	n/a	119 MPa	89 MPa	166 MPa	
Flow (D _{max}) Slump	710 mm n/a	660 mm n/a	0 235 mm	0 205 mm	0 n/a	

Table Notes:

- (a) CM (Cementitious material) = cement + slag + silica fume + fly ash
- (b) HRWRA and VMA units are mL per kg of cementitious material (powder) of ratio to CM
- (c) SCC1 and SCC2 [74]
- (d) HSC1 and HSC2 [88]
- (e) HSHDC [9]

A major objective of this research is to develop a high strength concrete with self-consolidating properties. A SCHSC could be easily mixed in a non-laboratory environment (battlefield) by semi-skilled labor (soldier). To accomplish this, an initial mix was designed using the principles outlined in chapter 2 and 3 for achieving high-strength and self-consolidating properties, respectively. The remainder of this chapter

will focus on a detailed investigation of the optimum dosage of a naturally occurring pozzolan to be used as a VMA to achieve the ideal rheology (through thixotropic properties) and hardened mechanical properties (through pozzolanic reaction) within the control mix. Table 3.1 presents the baseline formula for the SCHSC matrix developed and characterized throughout this research. Proportions were selected based on the principles for attaining high-strength and self-consolidating properties as presented in Chapter 2 and in this chapter.

3.3 Materials

3.3.1 VMA (Purified Palygorskite Nanoclay)

Purified palygorskite nanoclay (PPNC) is a mineral VMA. It was selected to control stability, flow and robustness during the fresh-state, and enhance mechanical properties during the hardened state. The PPNC used in this study (Actigel 208®) is a self-dispersing highly purified magnesium alumino silicate clay commercially available from Active Minerals International, LLC. It is an anti-settling agent and rheology modifier used in a range of water based industrial applications such as ceramic glazes, paints, joint compounds, specialty pesticides, herbicides and fertilizers. It is purified through a proprietary process using chemical exfoliation. The process removes impurities from palygorskite $(\text{Si}_8)_{20}(\text{Al}_2\text{Mg}_2)(\text{OH})_2(\text{OH}_2)_4\cdot\text{H}_2\text{O})_4$, such as quartz and smectite clay, to reduce water-demand tendencies and preserve a uniform shape and particle size of the mineral. The primary source of palygorskite clay in the United States is in North Florida and South Georgia. American commercial businesses that mine,

process and use the clay commonly use the term “attapulgate” clay, which is derived from the town “Attapulcus” Georgia where the mineral is most abundant. However, the International Nomenclature Committee has stated that the two terms are synonymous and that “palygorskite” is the preferred term [89-92].

PPNC is sold as a thixotropic anti-settling agent and rheology modifier.

Thixotropy is a property of material to thin upon isothermal agitation and thicken upon subsequent rest[10]. It is a time dependent behavior in which viscosity of a material decreases under shearing deformation, but recovers to its original value when the shearing ceases. A cementitious material with high thixotropy would have a quick recovery of viscosity. The material property is also commonly referred to as “shear thinning”. PPNC particles have an average length of 1.5 to 2.0 μm and an average diameter of 3nm. The PPNC “bristle like” particles are negatively charged along the axis and positively charged at ends (depicted in Figure 3.5), which causes particles to agglomerate at rest but disperse and enhance flow on agitation. Figure 3.6 shows (a) non-purified palygorskite nanoclay particles dispersed in suspension and (b) large purified palygorskite agglomerates [93,94].



Figure 3.5 PPNC particles are negatively charged along axis and positively charged on the ends

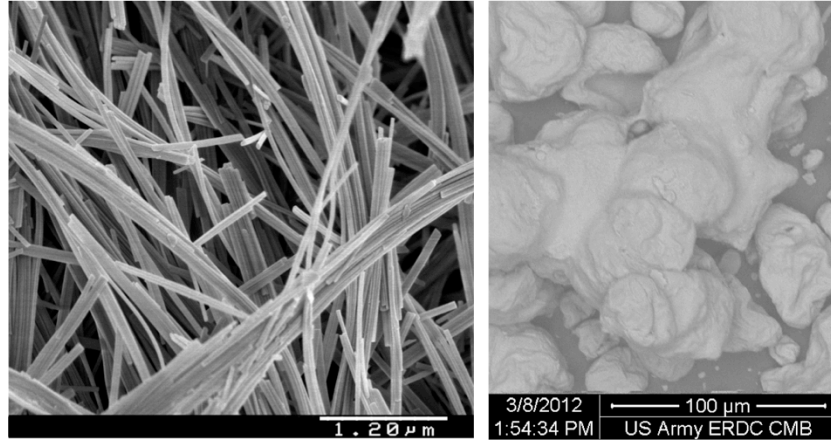


Figure 3.6 (left) Dispersed non-purified palygorskite clay particles [93] and (right) PPNC agglomerates

Some researchers have shown that PPNC enhances the “green strength” or “shape stability” of cementitious material without sacrificing flow. This is material’s ability to hold its shape while still in the “fresh” or “green” state (immediately after the material is mixed and cast into a desired shape). This is particularly important for slip-form paving where an economical SCC mix is shaped into a particular geometry as the formwork is pulled across the newly mixed concrete. An example of slip-form paving would be concrete curbs, sidewalks or roadways. The studies showed that HRWRA and fly ash provide necessary economic benefits to slip-form paving SCC mixes, but are deleterious to shape stability, while PPNC significantly enhances it. The studies showed that PPNC also reduces formwork pressure and considerably increases viscosity and thixotropy. These benefits are all achieved at very small dosages of PPNC, such as 0.33 percent of binder (by mass), and not exceeding one percent of binder by mass [90,95,96]. Another study showed that rheological parameters (plastic viscosity, Bingham yield value and apparent viscosity) will increase as the length to width ratio increases for non-purified

palygorskite nanoclay particles [94]. The purification process is therefore necessary to control variability of the rheology by maintaining uniform particle size and shape.

Some studies have stated that micro- or nano-sized layer silicates do not exhibit pozzolanic reactions in Portland cement, but that they do accelerate cement hydration and improve strength and durability. The studies were conducted with kaolinite clay and belite clay (though palygorskite clay wasn't included in the study, it is also categorized as a nano-sized layer silicate). The enhancement to material properties was attributed to the clay particles acting as microfillers in the cement microstructure and serving as nucleation sites (due to the ratio of very high surface area to volume) for the formation of the C-S-H hydration products [97]. Another study by the same authors claimed the same was true for palygorskite clay (non-purified). This study investigated the microstructure utilizing atomic force microscopy (AFM), helium porosimetry, and nitrogen adsorption and concluded that when 10% of the Portland cement (by mass) was replaced with palygorskite, a more open pore structure with fine pores was observed (assuming this means that the microstructure had smaller pores, but the pores were interconnected). However, the study assumed 373% water absorption for palygorskite clay (by mass) and added additional water to compensate from the control mix. Further, the study acknowledged that clay particles could not be observed in the hydrated materials using AFM, thus leaving the question - whether pozzolanic reaction did or didn't occur [98].

He et al. specifically investigated pozzolanic reaction with six different clays and effect of the clay on pore size distribution. This study concluded that the Si and Al from the various clays do participate in pozzolanic reaction and that even slight pulverization of the raw clay particles resulted in considerable variations in the particle size

distribution, which has been shown to strongly influence material behavior in the matrix[99]. Garg et al. [100] investigated heat of hydration, setting time, air content and compressive strength of PPNC when used at 0.5% to 3.0 % of binder. The study concluded the following:

- 1) The rate of heat evolution increases as the content of PPNC increases
- 2) There is a reduction in initial and final set time with an associated increase in PPNC
- 3) The air content (in the fresh mortar mixture) increased on the average by at least 2.5% when 1.5% of PPNC and 3.0% PPNC were added to the mixture
- 4) PPNC (dosage of 0.5% to 1.0%) had no effect on compressive strength and therefore the results of same weren't presented

The author acknowledged that the compressive strength cubes were not compacted well due to lack of flow from the dry mix and water absorption from PPNC. The cubes had severe honeycombs on the surface and large air pockets appeared to be visible throughout the specimens. The paper also acknowledged that HRWRA was not used and might have resolved the problem.

An oxide analysis by X-ray fluorescence (XRF) spectrometry was conducted on a sample of PPNC as received from Active Minerals. The analysis was conducted per ASTM C114 [101]. The data is presented in Table 3.2. It should be noted that PPNC meets some, but not all of the requirements of ASTM C618 for a natural pozzolan. The intent is to “ensure that sufficient potentially reactive constituents are present” [57,102]. PPNC meets the minimum requirement of 70% for $\text{SiO}_2 + \text{Al}_2\text{O}_3 + \text{Fe}_2\text{O}_3$ and the maximum allowance of 4.0% of SO_3 , but exceeds the maximum limit of 10% for loss on ignition (LOI). This is common for clay minerals that have tendencies for high water absorption. PPNC water absorption is approximately 200% and is stated to be surface

absorption rather than internal. Additional water was added to offset the absorption of PPNC.

3.3.2 Cement

The cement used was ASTM [103] Type I/II Portland cement from TXI in Texas. The Blaine fineness was 367 m²/kg. The physical and chemical properties are shown in Table 3.2.

3.3.3 Fly Ash and GGBFS (Slag Cement)

The Fly ash was ASTM [57] class F with a relatively high content of 13.6% CaO and a Blaine fineness of 441 m²/kg. The GGBFS was ASTM [85] Grade 120 with a Blaine fineness of 478 m²/kg. The chemical composition of the materials used was determined by X-ray fluorescence and the results are shown in Table 3.2.

3.3.4 Fine Aggregate

The fine aggregate was comprised of sand and silts, and had a specific gravity of 2.68. A gradation analysis was conducted on a sample and the results are shown in Table 3.3.

3.3.5 HRWRA

Sika® Viscocrete® 225 powder is a high range water reducing powdered superplasticizer. It is a third generation polycarboxylate superplasticizer. Though liquid

HRWRA are more common for use in HSC, a powder form of HRWRA was selected to simplify the mixing process for a soldier.

Table 3.2 Chemical and physical properties of materials used in the mix

Chemical analysis	Cement (%)	Fly ash (%)	Slag (%)	PPNC (%)
SiO ₂	19.53	52.36	36.19	54.52
Al ₂ O ₃	4.10	20.30	11.89	11.86
Fe ₂ O ₃	3.34	6.47	0.57	3.66
CaO	64.22	13.60	39.60	2.73
MgO	1.35	2.78	8.45	10.29
SO ₃	3.00	0.51	1.53	0.7
Na ₂ O	0.15	0.57	0.26	0.58
K ₂ O	0.62	1.03	0.47	0.67
TiO ₂	0.20	0.92	0.42	0.46
P ₂ O ₅	0.19	0.36	-	0.63
Mn ₂ O ₃	0.65	0.06	0.35	-
SrO	0.17	0.28	0.07	-
Cr ₂ O ₃	0.07	0.02	0.02	0.1
ZnO	0.02	0.01	-	0.1
BaO	-	0.30	0.09	0.01
L.O.I.	2.46	0.05	-	13.43
C3S	72	-	-	-
C2S	2	-	-	-
C3A	5	-	-	-
C4Af	10	-	-	-
Blain (m ² /kg)	357	441	478	-

Table 3.3 Gradation analysis of fine aggregate

Sieve size (mm)	Passing (%)
#10 (2.00)	100.0
#16 (1.18)	98.8
#20 (0.85)	87.2
#30 (0.600)	57.8
#40 (0.425)	45.2
#50 (0.300)	37.7
#70 (0.212)	31.4
#100 (0.150)	26.6
#140 (0.106)	22.9
#200 (0.075)	20.3

3.4 Mixture Proportions

Table 3.4 shows the proportions for all of the SCC mixtures evaluated. PPNC was evaluated for two water-to-cementitious materials (w/cm) ratios. Throughout this research, w/cm was defined as the ratio of weight of water to all cementitious materials (i.e. total weight of cement, slag and fly ash). Unless otherwise noted, all constituent and admixture proportions are referenced to cementitious materials as a whole, rather than just cement alone. For all mixtures shown in Table 3.4, the total amount of cementitious material remains unchanged, only the proportions of cement, slag and fly ash that make up the total amount of cementitious material are varied among the mixtures. The nomenclature used in table 3.5 can be explained as follows: $P_xS_yW_z$

Where: “P” indicates PPNC and “x” = the ratio of PPNC / CM

“S” indicates slag or GGBFS and “y” = the ratio of GGBFS / CM

“W” indicates water and “z” = the ratio of Water / CM

As seen in Table 3.4, PPNC was evaluated at a minimum of three ratios (0.3% and 0.6% of cm) at each w/cm ratio. For the final two mixtures (“P6S15W32” and “P3S15W37”), GGBFS was added to further enhance compressive strength and refine the microstructure. For both of these mixtures, the cementitious material consisted of seventy percent cement, fifteen percent fly ash and fifteen percent GGBFS.

Table 3.4 Proportions of the concrete mixtures

Mix	Total cm	Cement (c/cm)	Slag (s/cm)	Fly ash (f/cm)	Aggregate (a/cm)	Water (w/cm)	HRWR (h/cm)	PPNC (ppnc/cm)
P0S0W40 (Control 1)	1.00	0.80	0	0.20	1.30	0.40	0.0032	0
P3S0W40	1.00	0.80	0	0.20	1.30	0.40	0.0032	0.003
P6S0W40	1.00	0.80	0	0.20	1.30	0.40	0.0032	0.006
P0S0W32 (Control 2)	1.00	0.80	0	0.20	1.30	0.32	0.0043	0
P1S0W32	1.00	0.80	0	0.20	1.30	0.32	0.0043	0.001
P2S0W32	1.00	0.80	0	0.20	1.30	0.32	0.0043	0.002
P3S0W32	1.00	0.80	0	0.20	1.30	0.32	0.0043	0.003
P6S0W32	1.00	0.80	0	0.20	1.30	0.32	0.0043	0.006
P6S0W32_2	1.00	0.80	0	0.20	1.30	0.32	0.0121	0.006
P6S15W32	1.00	0.70	0.15	0.15	1.30	0.32	0.0150	0.006
P3S15W37	1.00	0.70	0.15	0.15	1.30	0.37	0.0085	0.003
P6S15W37	1.00	0.70	0.15	0.15	1.30	0.37	0.0113	0.006

Table Notes:

- (a) CM (Cementitious material) = cement + slag + fly ash
- (b) The total amount of CM does not vary between mixtures; only the proportions of CM vary (i.e. cement, fly ash and slag)

3.5 Mixing and Casting of Specimens

A simple mixing procedure was developed to enable consistent quality control and quality assurance when followed by a semi-skilled laborer(s) in field conditions. The mixing procedure was designed to mimic the ASTM “standard practice for mechanical mixing of hydraulic cement pastes and mortars of plastic consistency” [104] with suitable modifications for field conditions. An Eibenstock 21 S twin paddle concrete mixer, shown in Figure 3.7, was used to mix the material in a five-gallon bucket as seen in Figure 3.7. The Eibenstock 21 S twin paddle mixer generates high shear with two paddles rotating in opposing directions. All powders and fine aggregates were combined and dry mixed in a five-gallon bucket for a minimum of two minutes to ensure no clumps exist in the dry mix. The dry mix was slowly added to the water in the mixing bucket over a three-minute time frame while being mixed at half throttle (approximately 200

rpm). Once all ingredients were thoroughly mixed, further mixing continued at full throttle for five minutes and then stopped. The mixture was allowed to stand for 90 seconds. After 90 seconds, mixing continued at full throttle for three minutes. Slump flow, flow rate (T_{500}) and J-ring tests were conducted immediately after mixing was stopped as shown in Figure 3.3. The cubes (50.8mm x 50.8mm x 50.8mm) were cast in brass molds, single fiber pull-out specimens were cast in brass molds (designed to accommodate fiber embedment lengths up to approximately 25.4mm) with the fiber clamped into position for the appropriate embedment, and flexure beams were cast in high density polyethylene (HDPE) molds. Two different sizes of flexure beam molds were used to cast beams that were 25.4mm x 25.4mm x 140mm and 101.6mm x 101.6mm x 381mm. The casting process is shown in Figure 3.8. All specimens were covered for 24 hours and then de-molded. Specimens were cured for 56 days in a temperature controlled lime-water bath at 23 degrees Celsius (as per ASTM C192 [105]).



Figure 3.7 Mixing with Eibenstock 21 S twin paddle concrete mixer

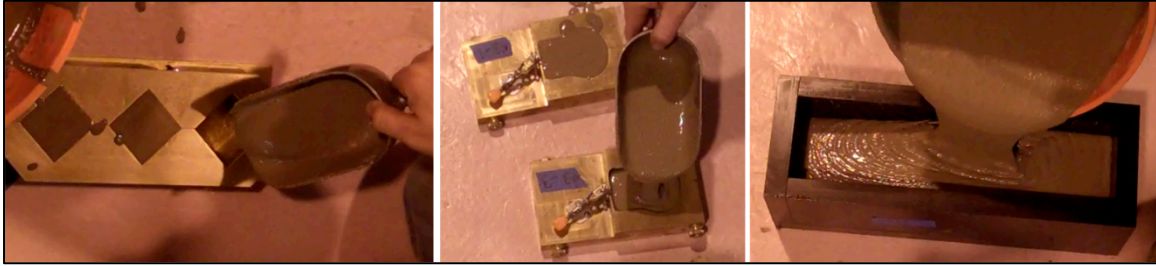


Figure 3.8 Casting cubes, single fiber pull-out specimens and beams

3.6 Specimen Preparations and Experimental Procedure

3.6.1 MicroCT

Cores were taken from all of the 101.6mm x 101.6mm x 381mm beam casts from each mixture to investigate the microstructure. The 19mm diameter cores were examined using a “SkyScan 1173” high-energy X-ray micro-CT system. The SkyScan 1173 has a fixed X-ray source, which was used with a voltage of 130kV and a current of 61 μ A. All 19mm cores were conducted at a resolution of 10.0 μ m (1 voxel = 10.0 μ m in X, Y and Z directions) with a 0.2° rotational step. A 0.25mm brass filter was placed between the source and the sample/detector to reduce beam-hardening effects and low-energy beam artifacts. Random vertical movement, frame averaging and ring artifact corrections were all optimized to provide high image quality. NRecon (SkyScan), three-dimensional (3D) reconstruction software, was used to convert X-ray images into horizontal cross-sectional views. CTVox (SkyScan) was used to generate 3D representations of the two-dimensional reconstructed cross sections. A volume of interest (VOI) was selected and remained constant throughout the analysis for all specimens. Therefore, all data presented was based on the exact same VOI for each specimen.

After all data were collected from the 19mm diameter cores, a 6.35mm diameter core was taken from the center of each 19mm core. The purpose of taking a smaller diameter core from the original core was to increase pixel resolution and identify smaller voids or flaws in the material. A smaller specimen can physically be located closer to the source. Since the X-ray beam geometry is conical, a higher pixel resolution is achieved as a specimen is moved away from the detector and towards the source: the closer to the source, the higher the magnification at the detector, and thus the higher the resolution. The 6.35mm diameter cores were scanned with a voltage of 80KV and a current of 80 μ A. The pixel resolution was 5.36 μ m (1 voxel = 5.36 μ m in X,Y and Z directions). All other settings for the 6.35mm diameter cores analysis were the same as for the 19mm diameter cores. Figure 3.9 shows a specimen mounted in the SkyScan 1173. Figure 3.10 (left) shows a 19mm diameter specimen that was used for the 10.0 μ m pixel resolution analysis. Figure 3.10 (middle) shows how the 19mm diameter specimen was cored to obtain a 6.35mm diameter specimen for the 5.36 μ m pixel resolution analysis and Figure 3.10 (right) shows the 6.35mm diameter specimen.



Figure 3.9 Concrete specimen mounted in the SkyScan 1173 X-ray micro-CT device

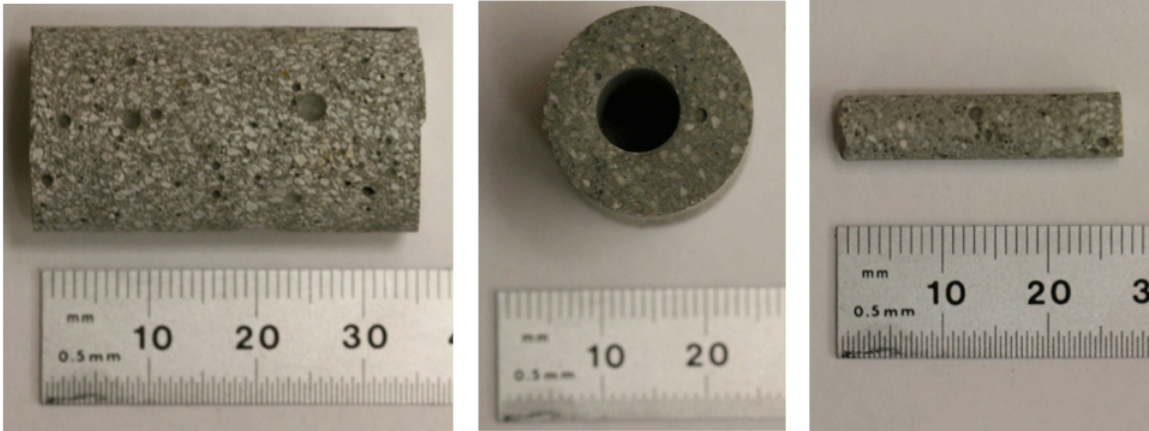


Figure 3.10 (left) 19mm diameter specimen used for the 10.00 μ m pixel resolution analysis (middle) 6.35mm diameter specimen was cored from 19mm diameter specimen after the 10.00 μ m pixel resolution analysis (right) 6.35mm diameter specimen used for the 5.35 μ m pixel resolution analysis

3.6.2 Compressive Strength

A minimum of at least fifteen 50mm cubes were cast and broken for each mix, as listed in Table 3.4. Cubes were broken at 56 days following the procedure outlined in ASTM C109[106].

3.6.3 Flexure

A third-point flexure experiment was designed as a scaled version of the ASTM C78 [107]. Figure 3.11 shows the experimental setup for a 25.4mm x 25.4mm x 140mm beam that spans 120mm and is equally loaded at the third-points. Similar to ASTM C78, the beam was loaded at the third points to isolate flexure (zero shear) in the middle-third of the beam. Specimens were prepared with minimal grinding of the troweled surface on a fully automated Chevalier precision hydraulic surface grinder to ensure uniform geometry of the beam and full contact between applied load and the beam. To prevent damage to the beam during grinding, settings on the Chevalier were used to remove

0.127mm of material per pass of the table surface across the grinding wheel. Precision grinding was necessary to compensate for missing degrees of freedom in the bottom supports (i.e. no steel rod or ball as shown in ASTM C78). After precision grinding, all specimens had full contact at both supports indicating that no torsional deformation would be caused during seating of the specimen under load. The load was applied at the third-points through a spherically seated head allowing rotational adjustment to ensure equal loading at both contact points. Tests were conducted on an Instron Electropulse universal testing machine (UTM) with a 5KN load cell with a stress-controlled rate of 1.05MPa per minute. Mid point displacement of the beam was measured using an external linear variable differential transformer (LVDT) with a sample rate of 10Hz (or one sample every 0.1 seconds). The LVDT was a Solartron AX/0.5/S with a $\pm 0.5\text{mm}$ stroke. The external LVDT was mounted to isolate midpoint displacement of the beam from specimen seating during the loading process and was used to control the stress-control rate of the experiment.

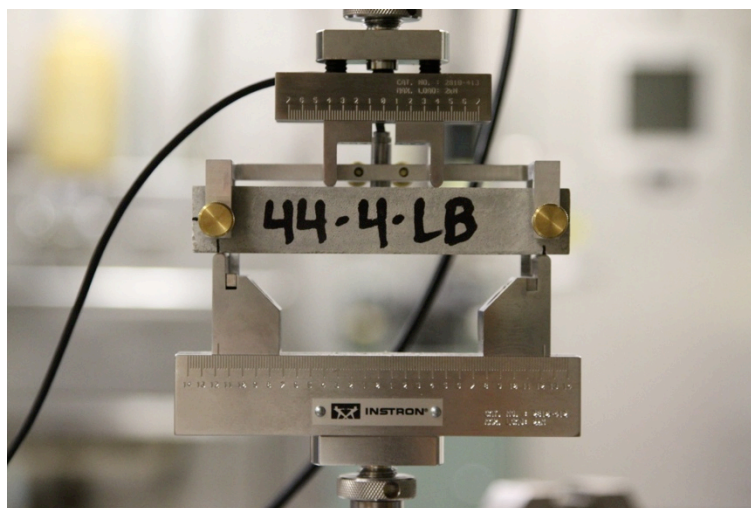


Figure 3.11 Flexure using a simply supported beam spanning 120mm with third point loading

3.6.4 Single Fiber Pull-Out

A single fiber pull-out experiment was conducted to determine the bond capacity between the matrix and steel fiber. The purpose of the experiment was to determine the effect of PPNC on the interfacial transition zone (ITZ). The fiber selected for these experiments was Helix Polytorex 5-25 high carbon steel with a length of 25mm and diameter of 0.50mm and a minimum tensile strength of 1700 N/mm². A detailed investigation of the fiber material is presented in Chapter 5, but is considered here only to examine the effect of PPNC on the interfacial bond between the matrix and fiber (i.e., the ITZ). The Polytorex steel fibers were positioned in molds to maintain various embedment lengths during casting. However, the most meaningful data was observed at an embedment of L/2 (or 12.5mm). The effects of the PPNC/cm ratio for mixes P0S0W32 (0% PPNC), P3S0W32 (0.3% PPNC), and P6S0W32 (0.6% PPNC) with a 12.5mm embedment are presented in the results section. After the specimens were cured for 56 days, they were mounted in the gripping device as shown in Figure 3.12. The fibers were directly clamped and load displacement curves were collected for a minimum of three samples for each embedment length. These experiments were conducted with an Instron Electropuls UTM with a 2-KN load cell and a displacement rate control of 0.254 mm per minute. Figure 3.12 shows the single fiber pull-out test.

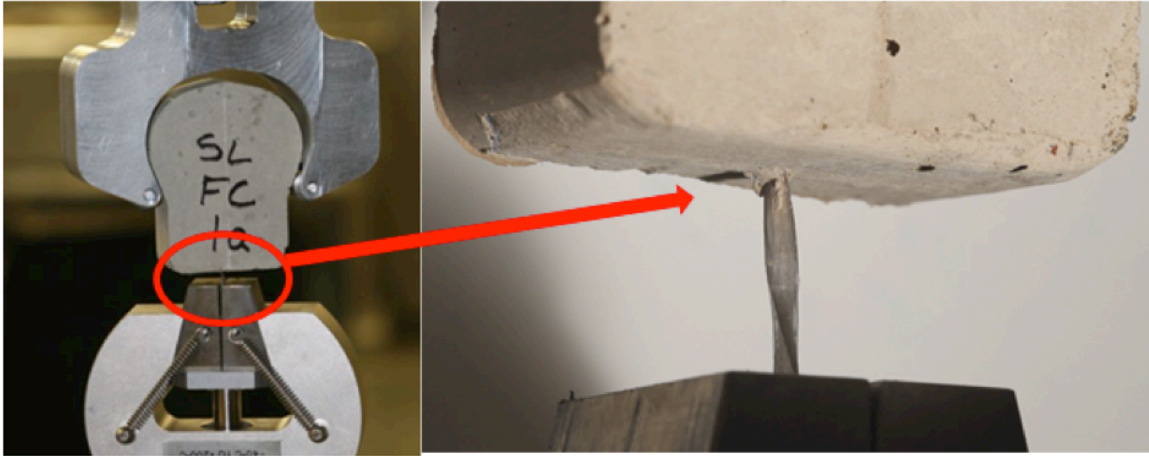


Figure 3.12 Single fiber pull-out to investigate PPNC affect on ITZ

3.7 Results

3.7.1 Flow and Flow Rate Results

Table 3.5 summarizes the results from the flow test and flow rate test for each mix. Figures 3.13 and 3.14 show the plot of these values. PPNC has considerable effect on flow and flow rate. The effect was more pronounced with a w/cm ratio of 0.32 than with a w/cm of 0.40. Mix P6S0W32 (0.6% PPNC) had a flow that was less than 560mm. Recalling the ACI [74] recommendation for use of mechanical vibration of SCC mixtures with a flow less than 560mm, a second mixture was designed with additional HRWRA to improve flow (P6S0W32_2). The additional HRWRA improved flow and flow rate, but adversely affected other properties that are presented later in this chapter. It was observed during the mixing process that a PPNC/CM ratio of 0.6% is the upper bound for the material to be easily mixed. Additional PPNC would require adding more HRWRA.

Table 3.5 Results for flow and flow rate for each mix

	T_{500}	D_{max}
P0S0W40 (Control 1)	3 seconds	914 mm
P3S0W40	3 seconds	864 mm
P6S0W40	3 seconds	813 mm
P0S0W32 (Control 2)	9 seconds	762 mm
P1S0W32	11 seconds	660 mm
P2S0W32	11 seconds	660 mm
P3S0W32	28 seconds	584 mm
P6S0W32	52 seconds	508 mm
P6S0W32_2	25 seconds	635 mm
P6S15W32	18 seconds	749 mm
P3S15W37	11 seconds	889 mm
P6S15W37	10 seconds	813 mm

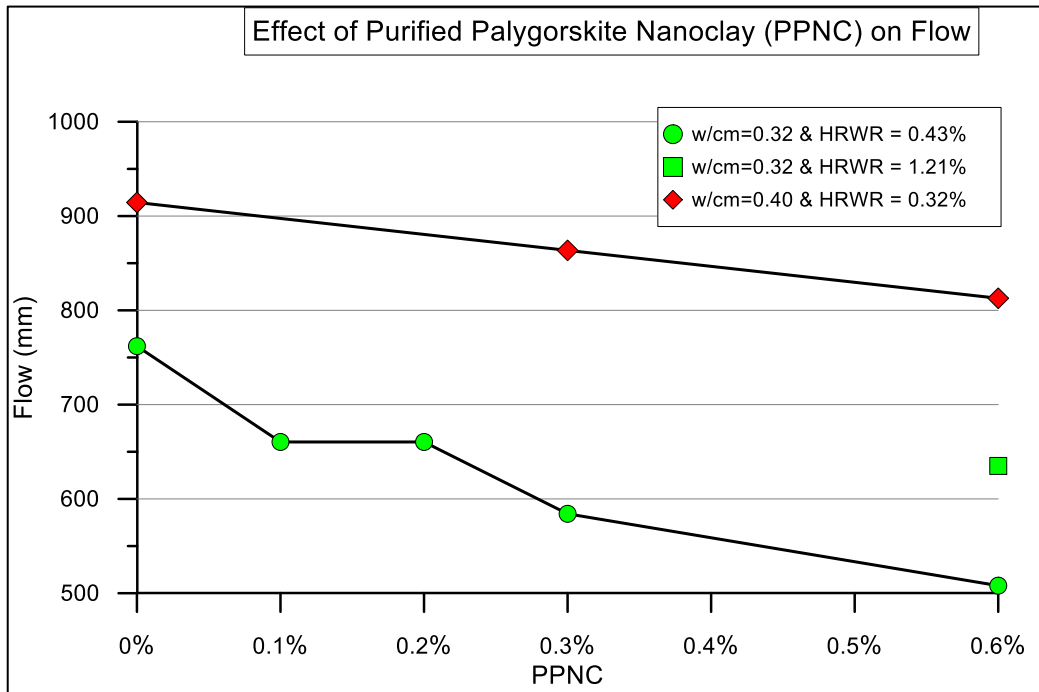


Figure 3.13 Flow for mix PxS0W32, P6S0W32_2 and PxS0W40

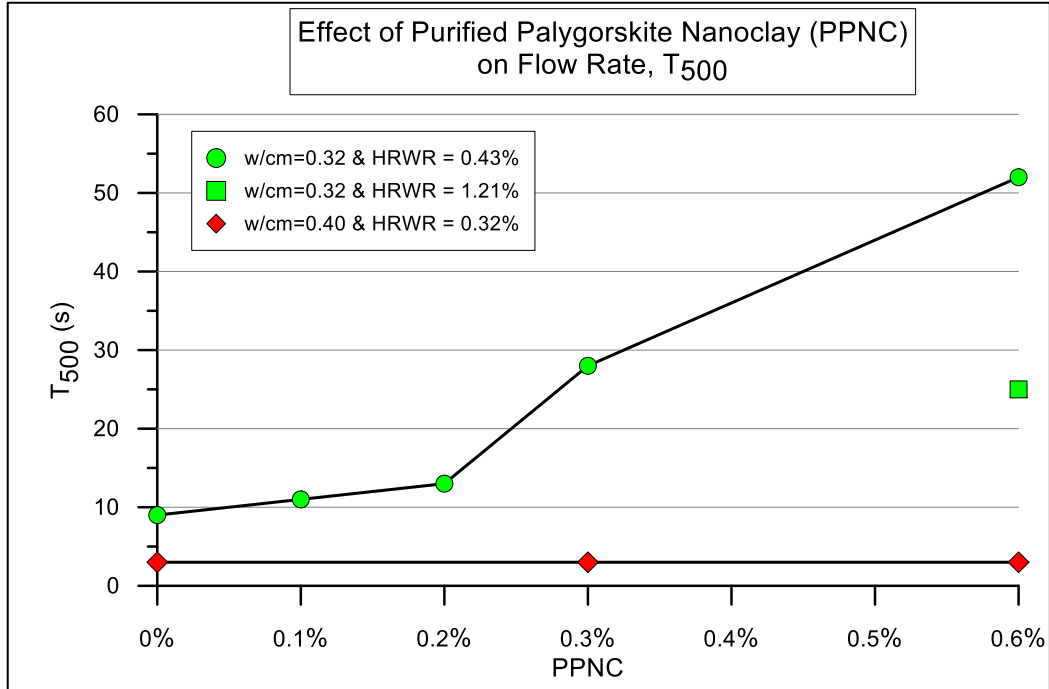


Figure 3.14 Flow rates for mixtures PxS0W32, P6WS0W32_2 and PxS0W40

3.7.2 Micro-CT Results

Figure 3.15 presents the 19mm and 6.35mm diameter specimen microstructure porosity values for each mix. Table 3.6 shows additional information, such as the total number of pores, VOI, maximum and minimum pore volume, and the pixel resolution for each specimen. A minimum pore volume of 64 voxels was selected for the analysis. Any void detected that was less than 64 voxels was not included in the analysis. A volume of 64 voxels would be the equivalent of a cube that is 4 pixels long by 4 pixels wide by 4 pixels high. This minimum voxel limit enabled the analysis to run more efficiently and resulted in higher fidelity data, as pores with very few voxels are subject to error during the thresholding step of the analysis.

Figures 3.16 (left), 3.16 (right), 3.17 (left) and 3.17 (right) are representative 2D images through the cross section of the 19mm specimens with a resolution of one pixel

equal to $10.00\mu\text{m}$. Figures 3.18 (left), 3.18 (right), 3.19 (left) and 3.19 (right) are representative 2D images through the cross section of the 6.35mm specimen with a resolution of one pixel equal to $5.36\mu\text{m}$. These images are presented to visually demonstrate the microstructure and porosity of each mix.

Figure 3.20 shows the pore size distribution for all mixes with a w/cm ratio of 0.32. Both pixel resolutions ($10.0\mu\text{m}$ and $5.36\mu\text{m}$) are plotted for each mix. The pore size distribution is constructed by sorting each individual pore volume in descending order and plotting these values on a log scale versus the cumulative porosity. The cumulative pore volume at the smallest pore size represents the porosity of the specimen. Similar plots are often reported for a porosity analysis using mercury intrusion porosimetry.

Figure 3.21 presents an in-depth summary of the number of pores detected in the 19mm diameter specimen of the control mix (P0S0W32). Figure 3.21 is a histogram showing the number of pores detected in the control mix VOI, and the corresponding range of “equivalent pore diameters”. The “equivalent pore diameter” is the diameter of an idealized sphere that has the same volume as the void. Though the particular void may not resemble the shape of a sphere, a diameter is more easily visualized than a volume expressed in μm^3 . Figure 3.21 indicates that 99.4% of the pores in the VOI have an equivalent pore diameter less than $400\mu\text{m}$. Figure 3.22 is also a histogram showing the percent of the total volume of voids in the VOI, and the corresponding equivalent pore diameter. As seen here, 72% of the total pore volume consists of pores with an equivalent pore diameter that is less than $400\mu\text{m}$. Table 3.6 reports pores ranging in size from an equivalent pore diameter of $26\mu\text{m}$ to $3,000\mu\text{m}$. Since Figures 3.21 and 3.22

indicate that 99.4% of the pores have a diameter less than 400 μm , and these pores comprise 72% of the pore volume in the VOI, the data presented hereafter will focus on this particularly important range of pore sizes.

Figure 3.23 compares the volume of pores for a corresponding range of equivalent pore diameters for four different mixtures all with a w/cm ratio of 0.32. As indicated by the mix number, the only variable between mixes P0S0W32, P3S0W32 and P6S0W32 is the amount of PPNC. Comparing these three curves indicates that PPNC is clearly affecting the pore volume across the range of pore diameters, but it also appears to have a more significant impact on larger pores than smaller pores. The effect of GGBFS on porosity is observed by comparing mix P6S0W32 (black curve) and P6S15W32 (gold curve). Mix P6S15W32 has the same ratio of PPNC/cm as P6S0W32. These two mixtures also have the same w/cm and amount of total powder (i.e. cm). The difference between P6S15W32 and P6S0W32 is the addition of GGBFS and a 5% reduction of fly ash (i.e. GGBFS=15%, Fly ash=15%, Portland cement=70%). Figure 3.23 indicates there is a further refinement of pores and reduction of porosity with the addition of GGBFS. The same trend is observed for GGBFS as with PPNC, the volume of pores is reduced more significantly for larger pores (pores with a diameter greater than 95 μm) than small pores.

Figure 3.24 is a histogram showing the total number of pores that have a diameter between 50 μm and 410 μm . The histogram bin size is 20 μm , which is based on recommendations from Haldar and Mahadevan [108]. Comparing P0S0W32 (0% PPNC), P3S0W32 (0.3% PPNC) and P6S0W32 (0.6% PPNC) shows the reduction in total number of pores in the respective pore diameter ranges as the amount of PPNC is

increased. The same is found for GGBFS when comparing P6S0W32 (0% GGBFS) and P6S15W32 (15% GGBFS). Both Figures 3.23 and 3.24 show that increasing the amount of PPNC and adding GGBFS will decrease the total volume of voids and number of voids. Figures 3.23 and 3.24 suggest that the trend is more prevalent for larger pores than smaller pores, suggesting an effect on the pore size distribution. Figure 3.25 illustrates the trend more clearly. Figure 3.25 shows the relative frequency of the number of pores for a given range of equivalent pore diameters. This graph compliments Figures 3.23 and 3.24 to illustrate that as the amount of PPNC is increased, the pore size distribution is improved. When GGBFS is added, the pore size is refined further. All four curves converge and then diverge at a pore diameter of approximately $90\mu\text{m}$ to $110\mu\text{m}$. This suggests that there are more small pores and less large pores and that the affect is more pronounced as the amount of PPNC is increased. Adding GGBFS continues to show this trend in the cement microstructure. Since large pores are more detrimental to mechanical properties than smaller pores, refining the cement microstructure should enhance mechanical properties. Based on the information presented in Chapter 2, adding PPNC and GGBFS will result in improved material properties.

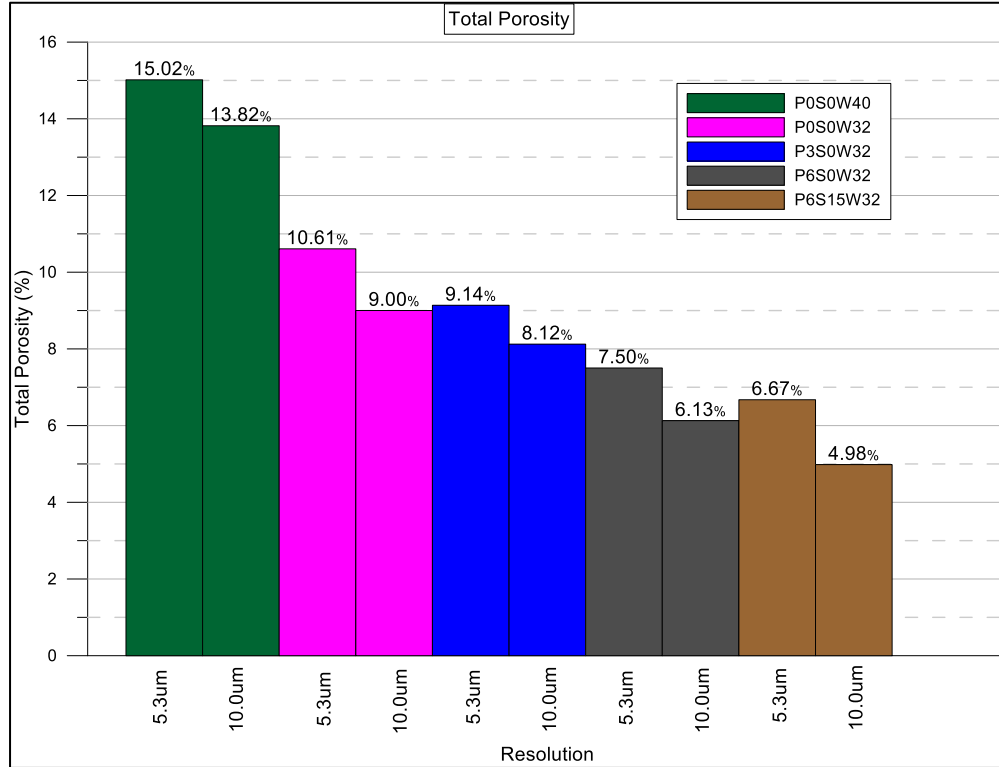


Figure 3.15 Total porosity for mix PxS0W32, P0S0W40 and P6SW32

Table 3.6 Overview of findings from the micro-CT analysis

Mix #	Pixel size	Specimen volume of interest	Number of pores greater than 64 voxels	Maximum pore size	Minimum pore size	Porosity
P0S0W40	5.36 µm	339 mm ³ 2.20E9 voxels	15,463	9.914 mm ³ 6.44E7 voxels	9,854 µm ³ 64 voxels	15.02 %
P0S0W32	5.36 µm	339 mm ³ 2.20E9 voxels	26,188	1.604 mm ³ 1.04E7 voxels	9,854 µm ³ 64 voxels	10.61 %
P3S0W32	5.36 µm	339 mm ³ 2.20E9 voxels	26,796	1.08 mm ³ 7.04E6 voxels	9,854 µm ³ 64 voxels	9.14 %
P6S0W32	5.36 µm	339 mm ³ 2.20E9 voxels	30,635	1.35 mm ³ 8.73E6 voxels	9,854 µm ³ 64 voxels	7.50 %
P6S15W32	5.36 µm	339 mm ³ 2.20E9 voxels	26,584	1.58 mm ³ 1.03E7	9,854 µm ³ 64 voxels	6.67 %
P0S0W40	10.00 µm	3,055 mm ³ 3.06E9 voxels	79,094	14.11 mm ³ 1.41E7 voxels	64,000 µm ³ 64 voxels	13.82 %
P0S0W32	10.00 µm	3,055 mm ³ 3.06E9 voxels	144,573	3.71 mm ³ 3.71E6 voxels	64,000 µm ³ 64 voxels	9.00 %
P3S0W32	10.00 µm	3,055 mm ³ 3.06E9 voxels	110,895	4.27 mm ³ 4.27E6 voxels	64,000 µm ³ 64 voxels	8.12 %
P6S0W32	10.00 µm	3,055 mm ³ 3.06E9 voxels	102,116	3.56 mm ³ 3.56E6 voxels	64,000 µm ³ 64 voxels	6.13 %
P6S15W32	10.00 µm	3,055 mm ³ 3.06E9 voxels	103,560	2.88 mm ³ 2.88E6 voxels	64,000 µm ³ 64 voxels	4.98 %

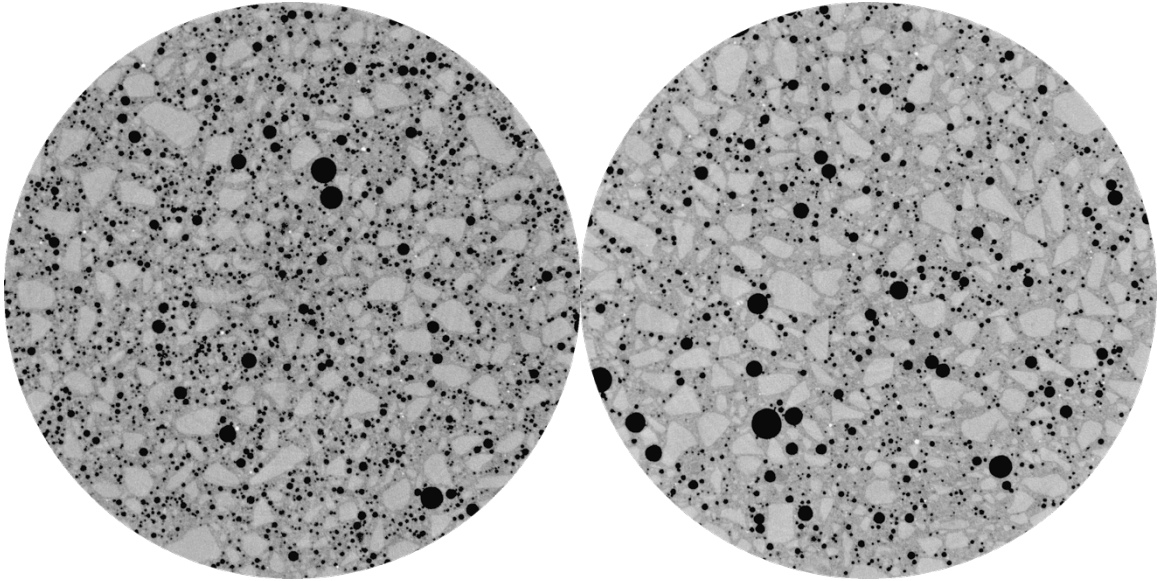


Figure 3.16 Representative image from (left) P0S0W32 (1 pixel = 10.0 μ m): 0% PPNC
(right) P3S0W32 (1 pixel = 10.0 μ m): 0.3% PPNC

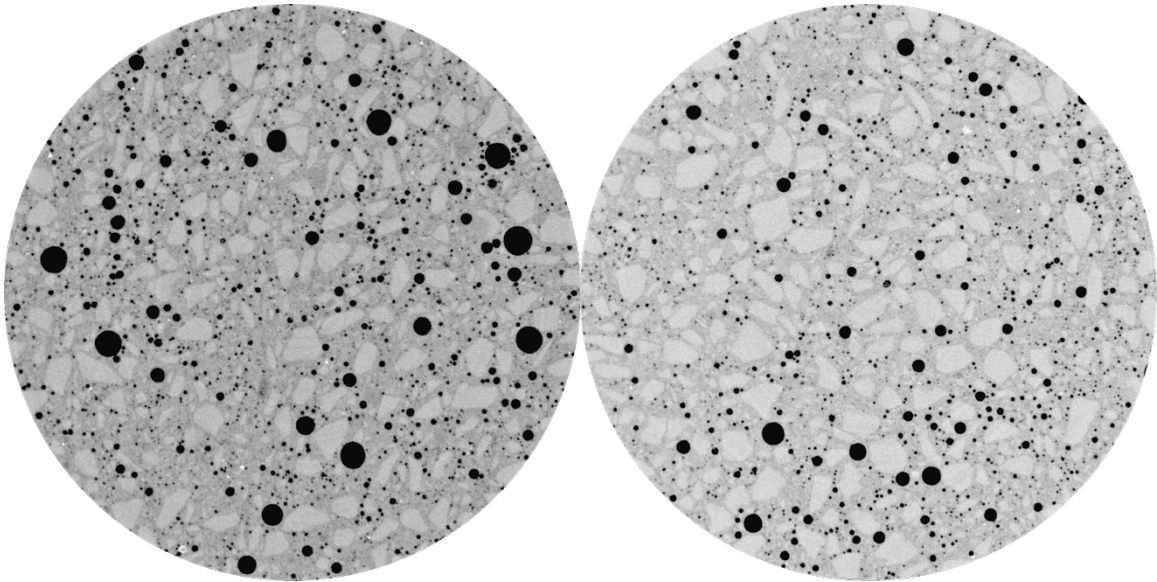


Figure 3.17 Representative image from (left) P6S0W32 (1 pixel = 10.0 μ m): 0.6% PPNC
(right) P6S15W32 (1 pixel = 10.0 μ m): 0.6% PPNC with GGBFS

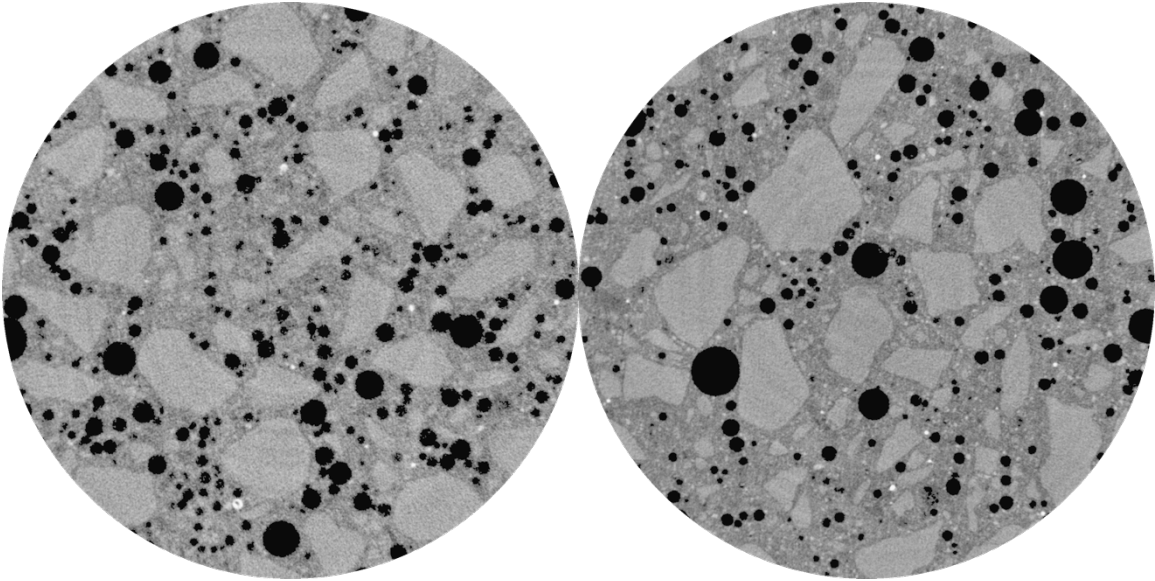


Figure 3.18 Representative image from (left) P0S0W32 (1 pixel = 5.36 μ m): 0% PPNC
(right) P3S0W32 (1 pixel = 5.36 μ m): 0.3% PPNC

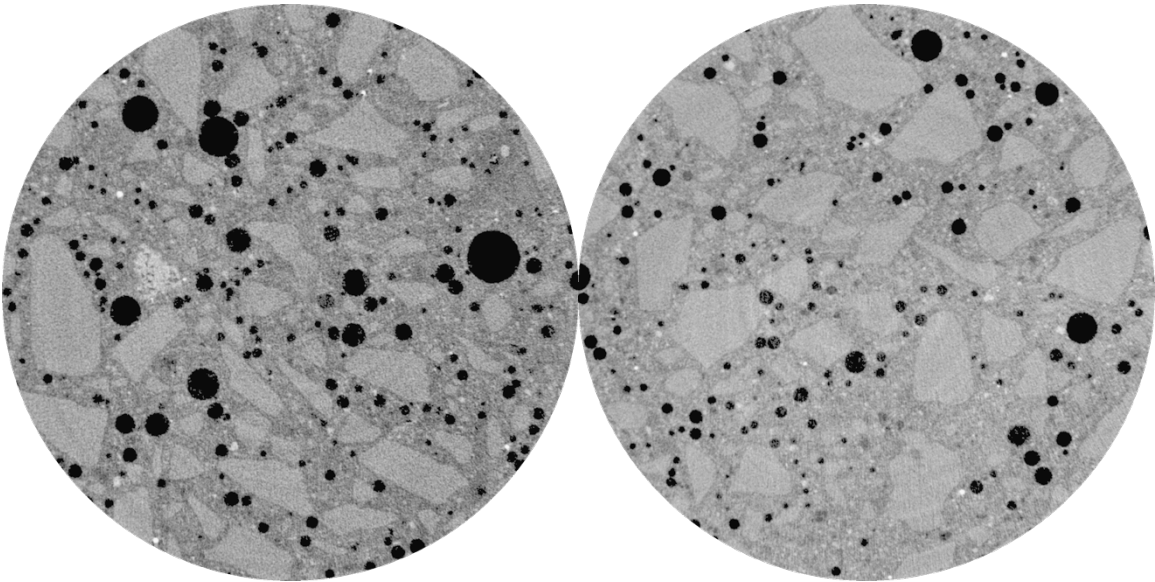


Figure 3.19 Representative image from (left) P6S0W32 (1 pixel = 5.36 μ m): 0.6% PPNC
(right) P6S15W32 (1 pixel = 5.36 μ m): 0.6% PPNC with GGBFS

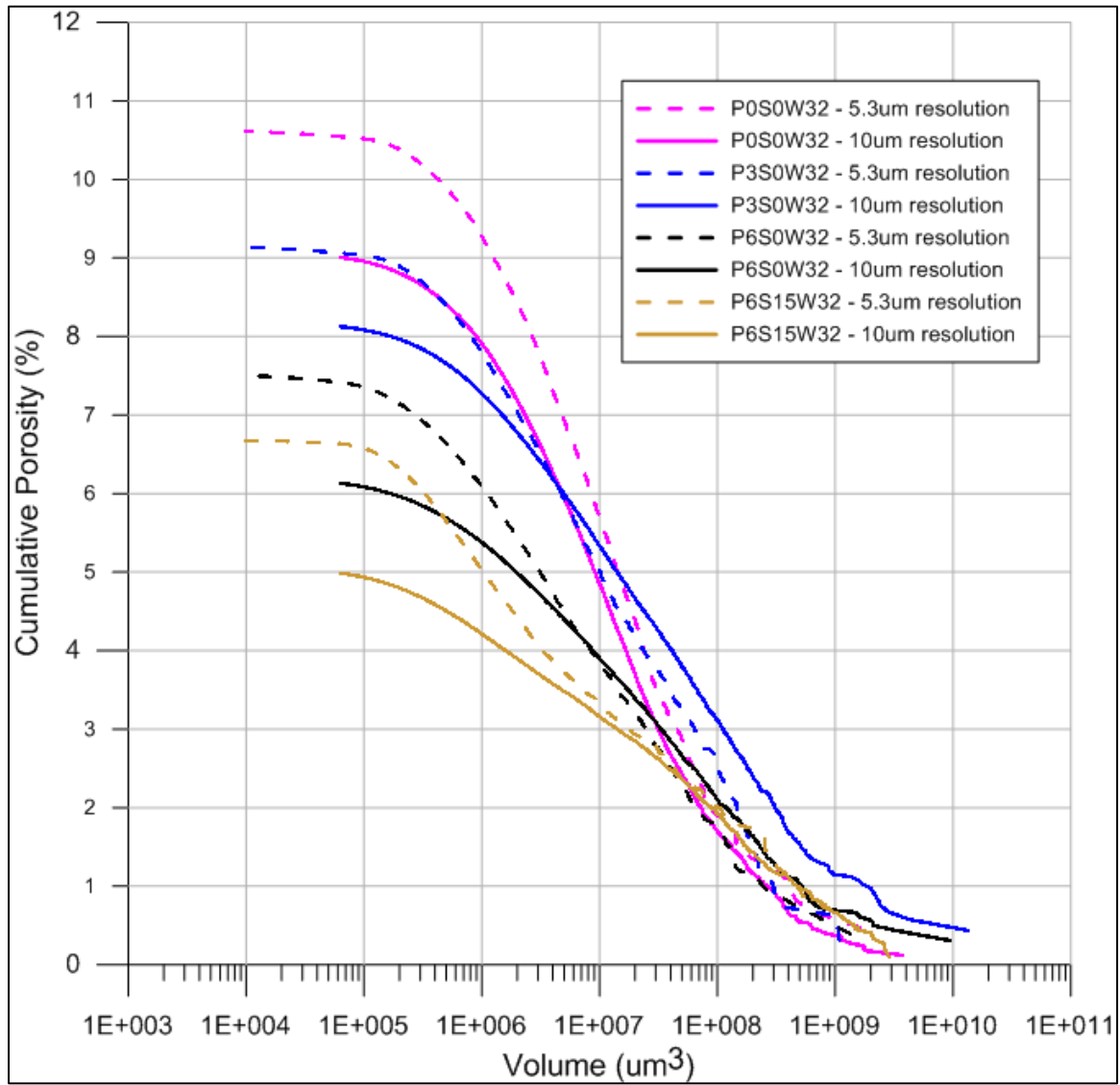


Figure 3.20 Pore size distribution for mix P0S0W32, P3S0W32, P6S0W32 and P6S15W32

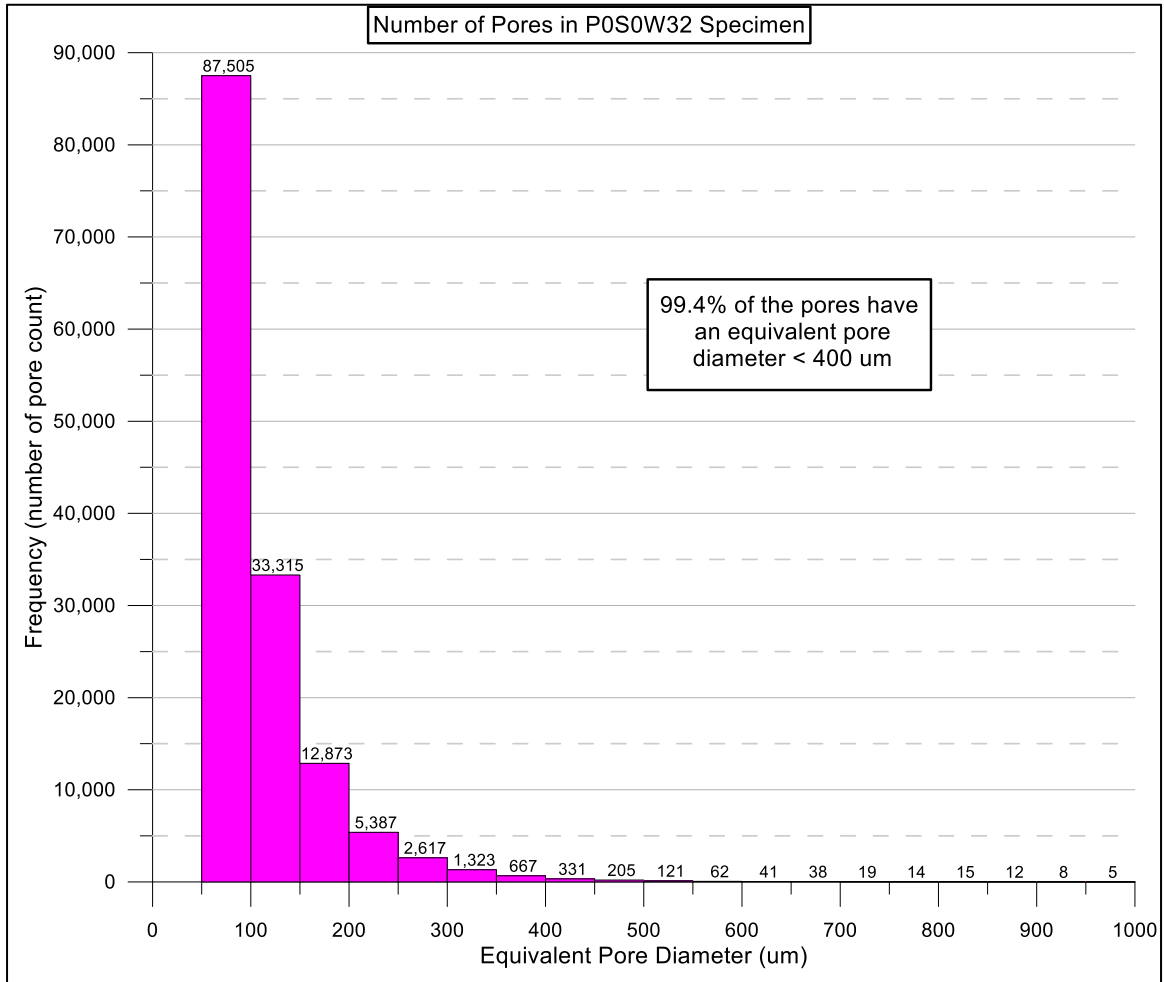


Figure 3.21 Number of pores for a given pore diameter

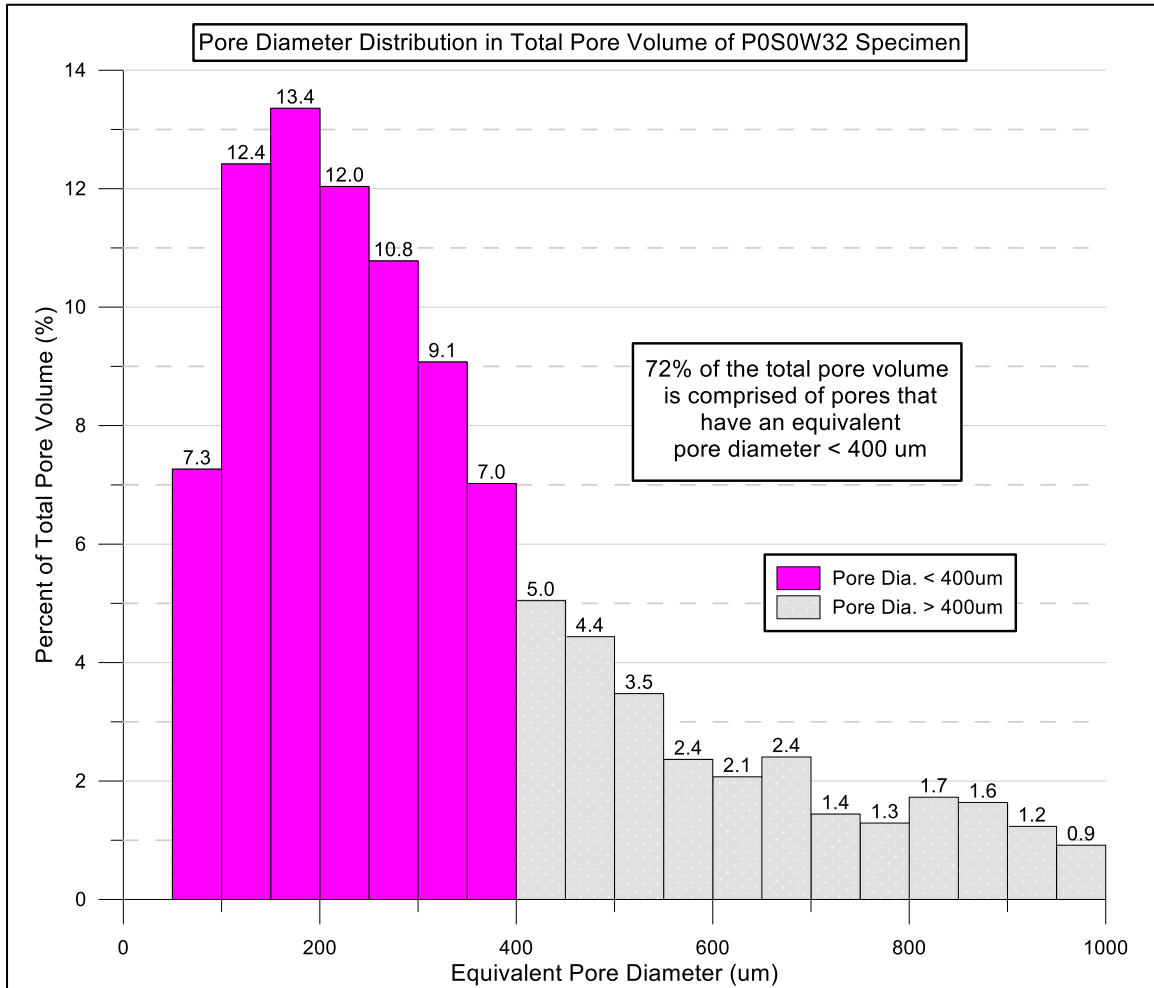


Figure 3.22 Percent of pore volume for a given range of pore diameter

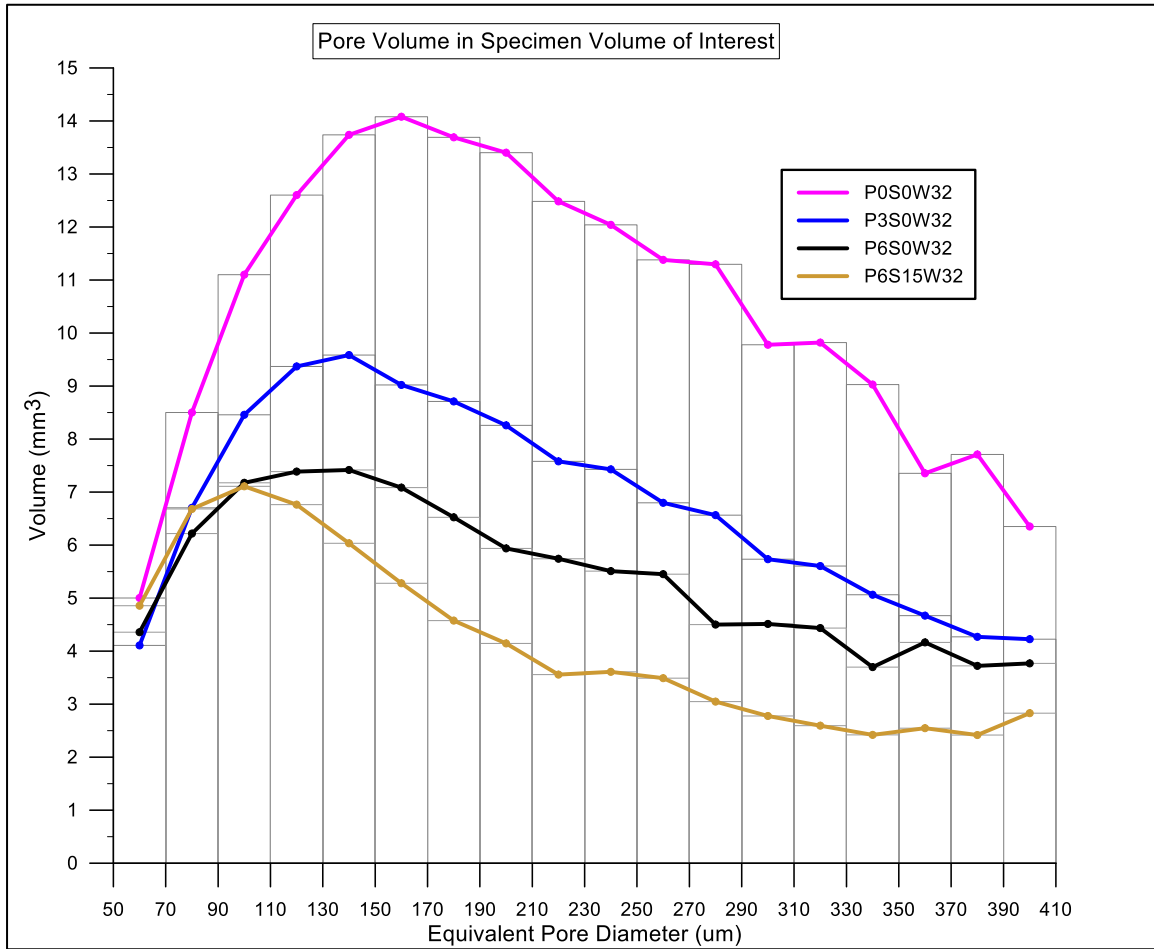


Figure 3.23 Volume of pores for a given pore size diameter

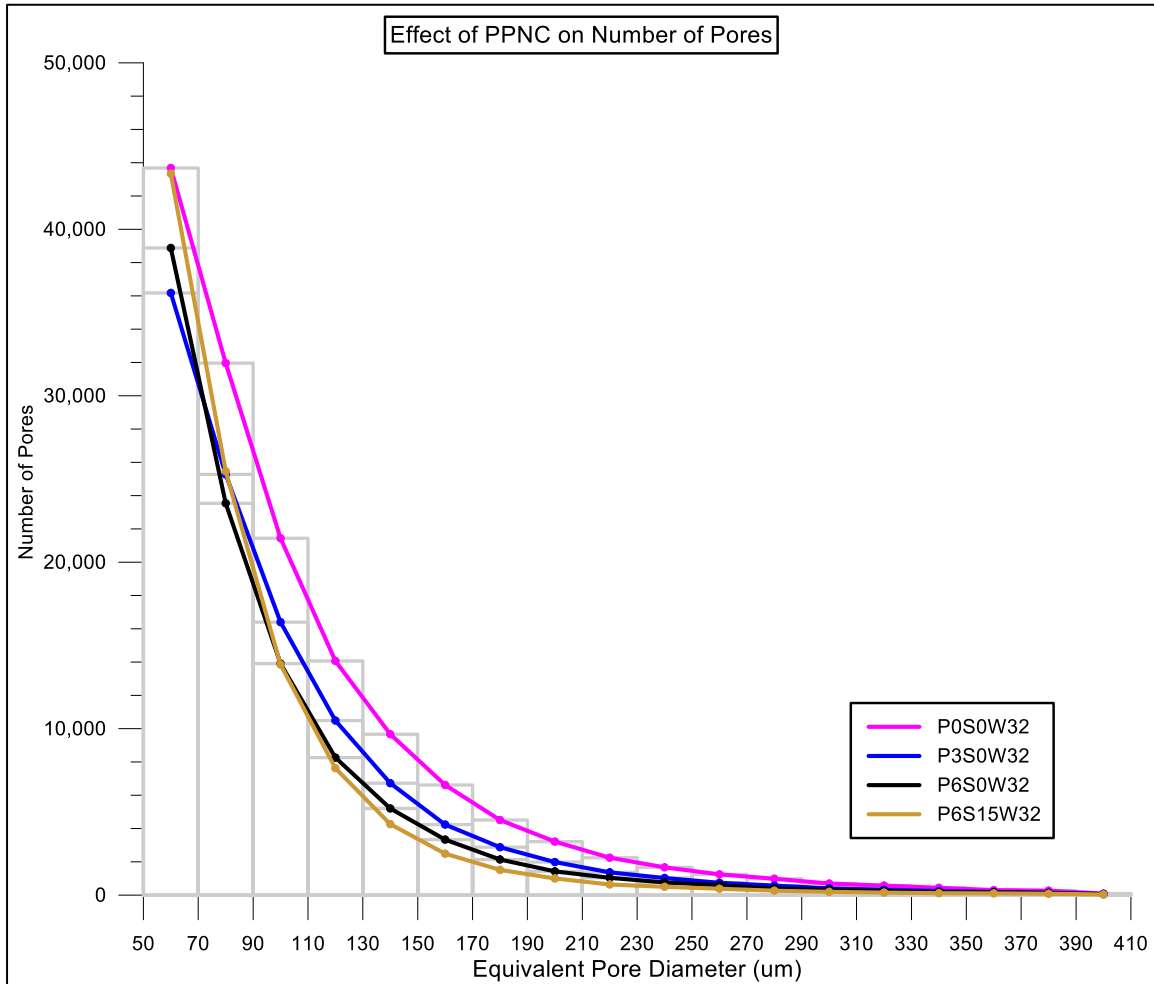


Figure 3.24 Histogram indicating the number of pores in a given range of pore diameter

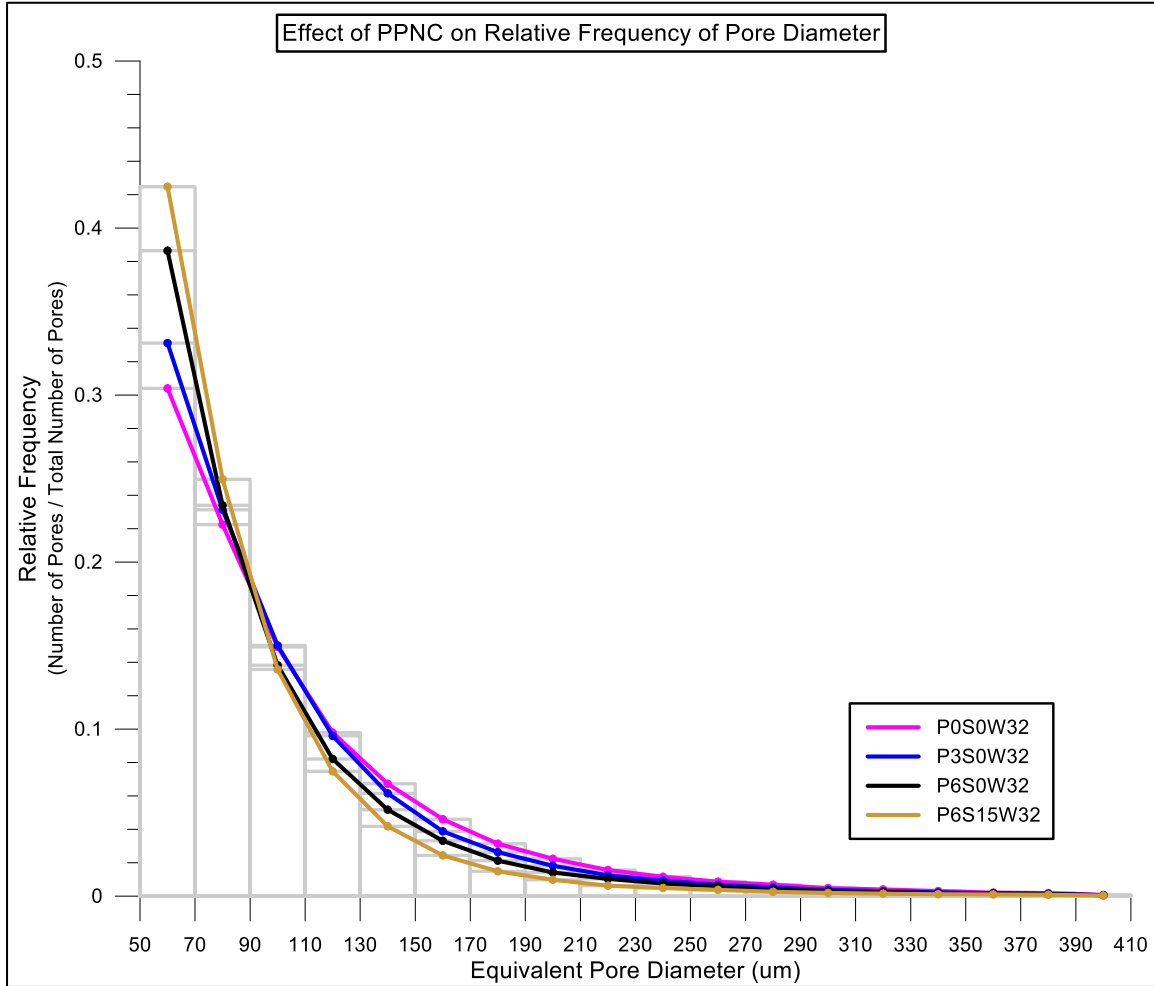


Figure 3.25 Relative frequency of pores in mixes with a w/cm=0.32

3.7.3 Compressive Strength Results

Figure 3.26 shows the results of compressive strengths for all mixtures not containing GGBFS. This is a box and whisker plot that shows how compressive strength was affected as the PPNC/cm ratio was increased. The plot is grouped according to w/cm ratio. The w/cm ratio of 0.40 is shown in red; the w/cm ratio of 0.32 is shown in green; and mix P6S0W32_2 is shown in yellow. The only variable within the grouping of the box and whisker plots was the PPNC/cm ratio. This allows a direct comparison of the PPNC/cm ratio effect on compressive strength at two different w/cm ratios. As

previously discussed, the difference between P6S0W32 and P6S0W32_2 is the amount of HRWRA. The ratio of HRWRA/cm was increased from 0.43% to 1.21% to achieve a workable flow and flow rate. Though flow and flow rate were improved by the additional HRWRA, it clearly reduced the compressive strength for the mix. Figure 3.27 shows the average compressive strength and standard deviation for all mixtures investigated. As seen in Figure 3.27, P6S15W32 mix had the highest compressive strength. The difference between P6S0W32 and P6S15W32 was the addition of GGBFS. P6S0W32 had 20% of the cement replaced with fly ash and P6S15W32 had 15% of the cement replaced with fly ash and 15% replaced with GGBFS. This change increased the average compressive strength from 78.1 MPa to 104.8 MPa.

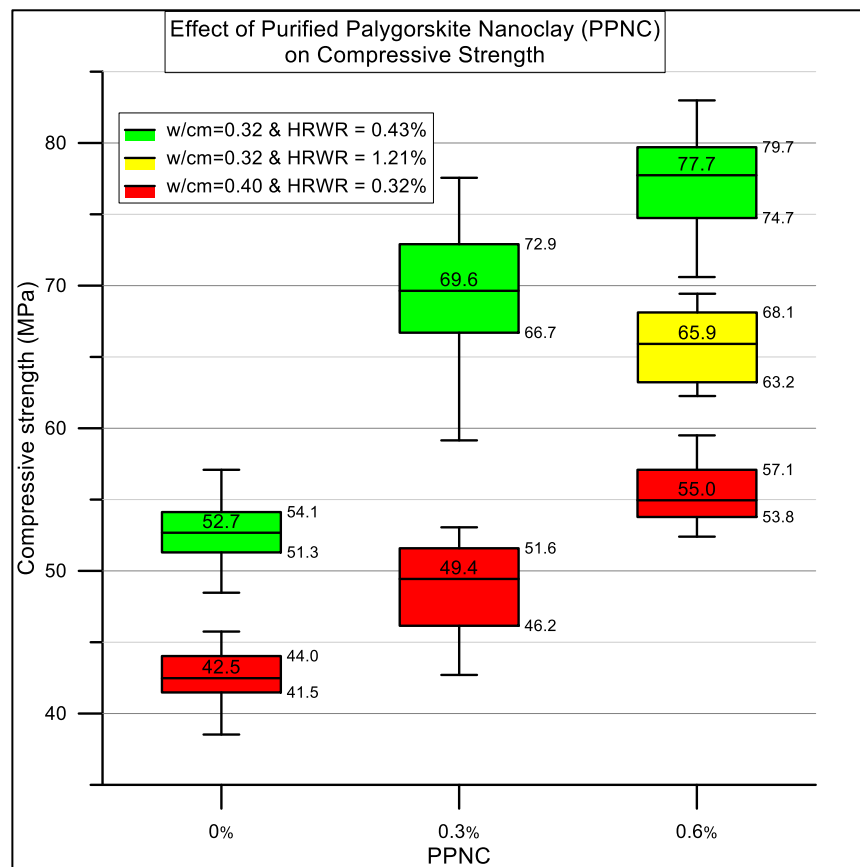


Figure 3.26 Effect of PPNC on compressive strength

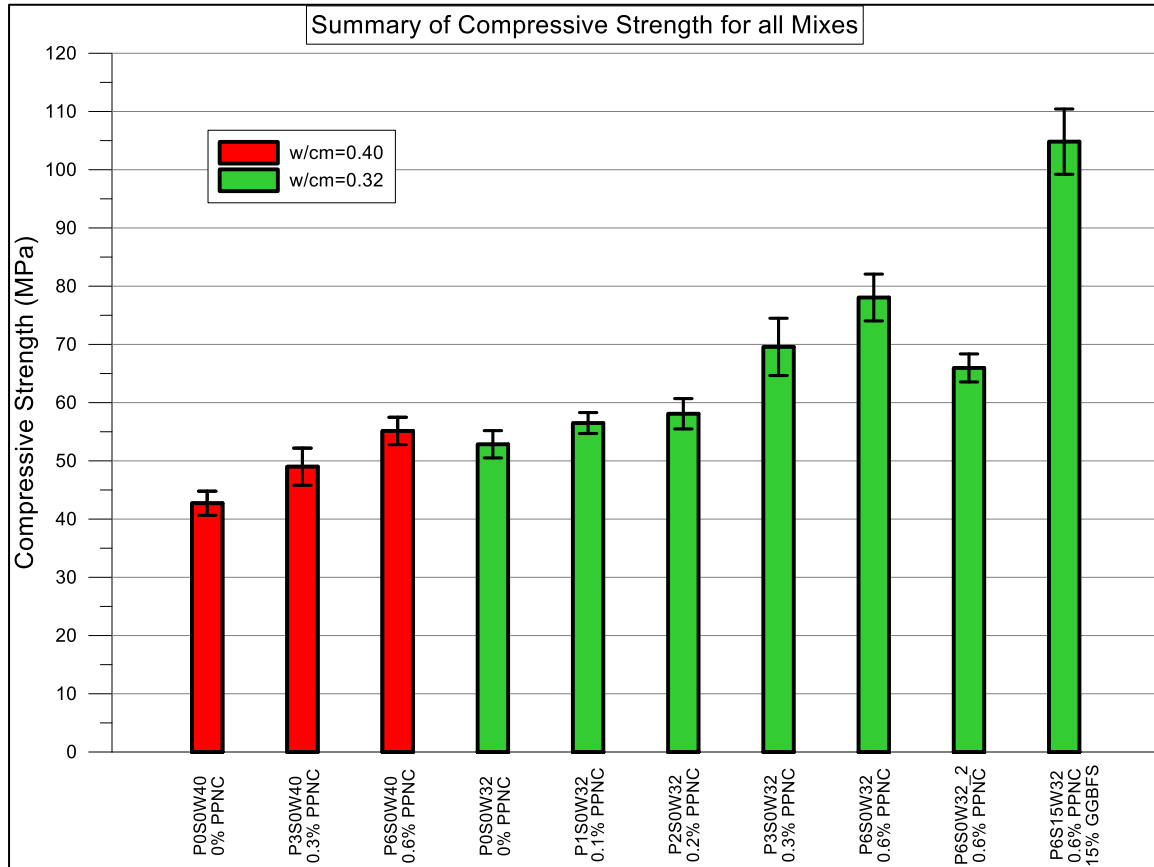


Figure 3.27 Summary of compressive strengths with standard deviation for all mixtures

3.7.4 Flexure Results

Figure 3.28 shows representative data from the flexure experiment using simply supported beams with third point loading. For the data shown in Table 3.7 and Figure 3.28, failure occurred in the middle third of the beam indicating that flexure was the mode of failure. The data presented in Figure 3.28 is the engineering stress versus midpoint displacement from the experiments listed in Table 3.7. The peak engineering stress at failure is reported as the modulus of rupture (MOR). Due to heterogeneity of cementitious mixtures, the MOR can vary significantly between experiments for beams cast from the same batch. This is observed in the values reported for standard deviation of the MOR. There were a total of 42 experiments conducted on the 25.4mm x 25.4mm x

140mm beams. The PPNC did not have a significant affect on the modulus of rupture. However, there was a clear distinction between mixtures with w/cm ratio of 0.32 and 0.40. The most significant difference was the flexure response of mixture P6S15W32. The addition of GGBFS (15% cement replacement) and reduction of fly ash from 20% to 15% appears to have a significant impact on MOR.

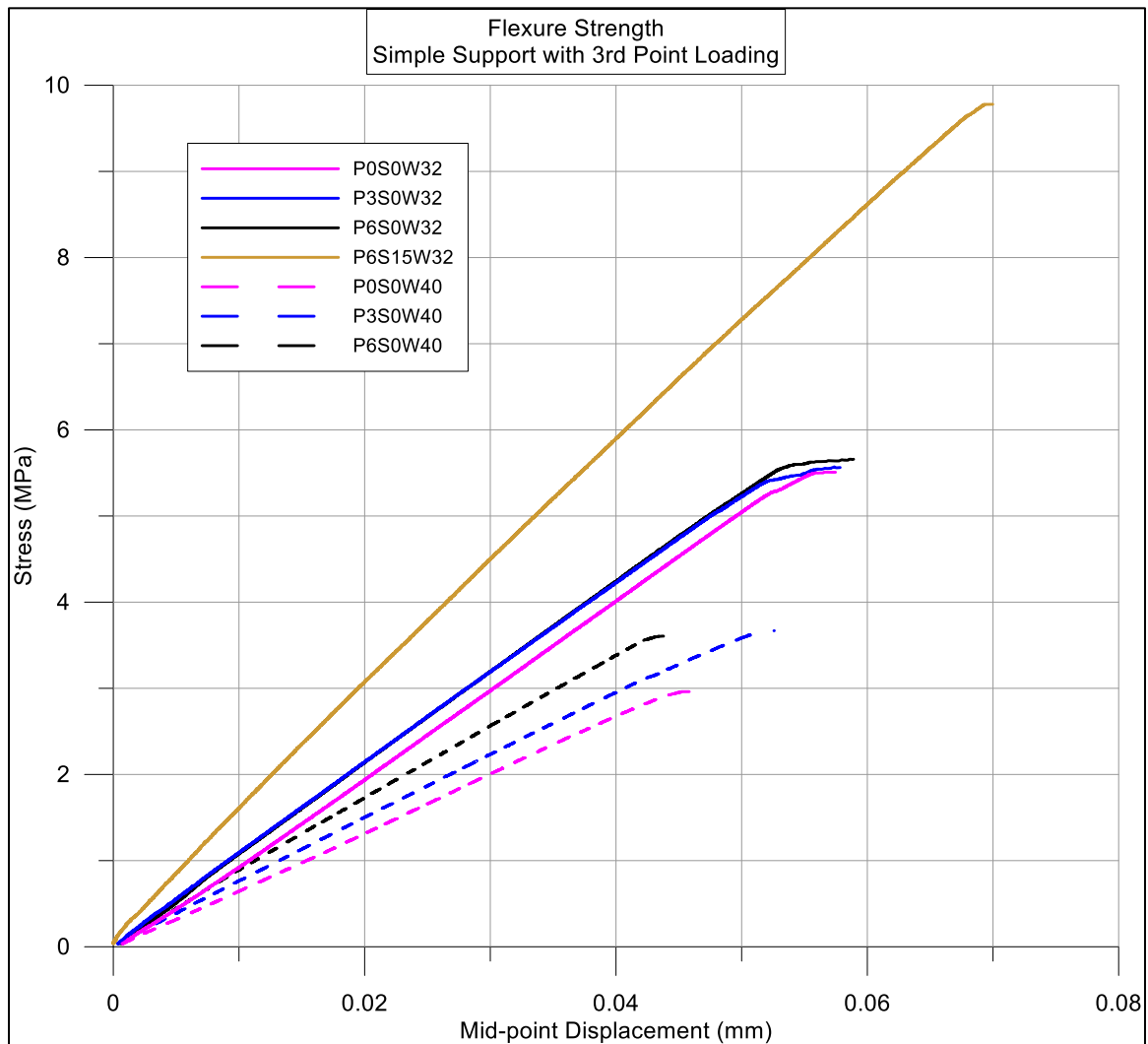


Figure 3.28 Effect of PPNC on flexure strength from third-point loading experiment

Table 3.7 Summary of results from flexure experiment

Mix	Number of Beams tested	Modulus of Rupture (MPa)	Stddev (MPa)	Toughness (N*mm)
P0S0W40 (Control 1)	3	2.96	0.22	45
P3S0W40	4	3.61	0.44	66
P6S0W40	9	3.67	0.22	53
P0S0W32 (Control 2)	6	5.51	0.61	105
P3S0W32	8	5.57	0.35	113
P6S0W32	8	5.66	0.72	118
P6S15W32	6	9.78	0.73	232

3.7.5 Single Fiber Pull-out Results

Results for the single fiber pull-out experiment are shown in Figure 3.29 below. Three experiments were conducted using Helix Polytortex steel fibers with a 12.5mm embedment length for each of the following three mixtures: P0S0W32, P3S0W32 and P6S0W32. The average of these three curves are plotted in Figure 3.29. There is a very distinct trend in the results. After the initial bond was broken for P0S0W32 (i.e. PPNC = 0%), the fiber pulled-out as the load gradually decreased. However after the initial bond was broken for P3S0W32 and P6S0W32 (i.e. PPNC = 0.3% and PPNC = 0.6%), the load increased as the fiber began to pull out. This pseudo hardening effect occurs when the matrix is capable of providing frictional resistance as the fiber pulls through the tunnel. The behavior was more prevalent when the percent of PPNC was increased. This behavior is preferred over rupturing of the matrix as observed in the load-displacement curve for P0S0W32. Table 3.8 reports the key findings from the single fiber pull-out experiments. Values of toughness and peak loads are reported.

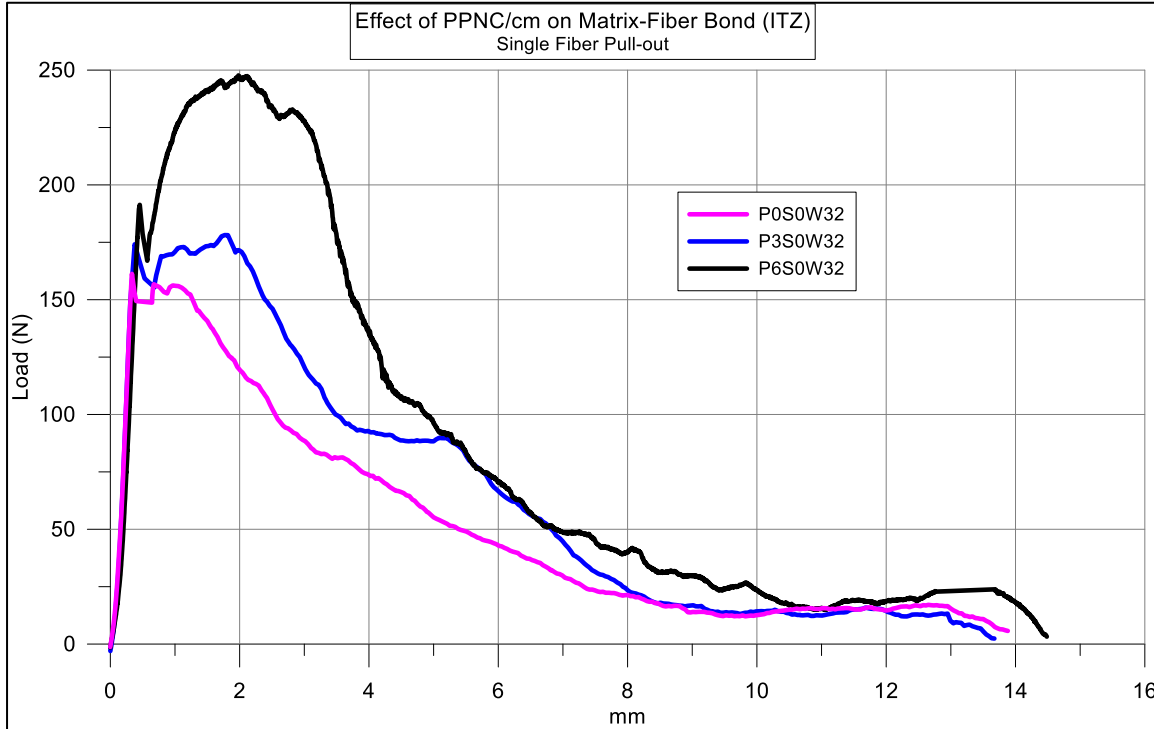


Figure 3.29 Load versus displacement curve for single fiber pull-out experiment

Table 3.8 Summary of results from the single-fiber pull-out experiments

Mix	Peak Load (N)	Toughness (N*mm)
P0S0W32	161	708
P3S0W32	178	891
P6S0W32	248	1239

3.7.6 Stability Results

A 101.6mm x 101.6mm x 381mm beam was cast with Helix Polytorex 5-25 high carbon steel fiber reinforcement (25mm long with a diameter of 0.50mm). The beams were cast with three percent steel fiber reinforcement (by volume) in mixture. After the beams were tested in flexure, a 50.8mm diameter x 101.6mm long specimen was cored from the top of the beam through the depth of the beam. Figure 3.30 shows a beam and the cored specimen. The purpose of coring a specimen from a fiber-reinforced beam was

to determine the actual distribution of fibers through the depth of the beam. As previously presented, a SCC mix must maintain stability while retaining filling ability, or unconfined flow characteristics. The PPNC is a viscosity-modifying admixture that should keep heavy particles (i.e. steel fibers) in suspension and prevent segregation. To verify actual fiber distribution, the 50.8mm x 101.6mm cored specimen was placed in the SkyScan microCT device and scanned to detect location of the Helix steel fibers throughout the depth of the specimen. Figure 3.31 shows the 3D image reconstructed from the 2D X-ray images using the microCT technique. The percent area of steel fibers was calculated through the cross section along the length of the specimen. These values are plotted and shown in the graph next to the 3D image in Figure 3.31. As shown in Figure 3.31, steel fibers did not segregate or settle toward the bottom of the mold in the highly flowable mixture.



Figure 3.30 Specimen cored from beam to evaluate fiber distribution using MicroCT

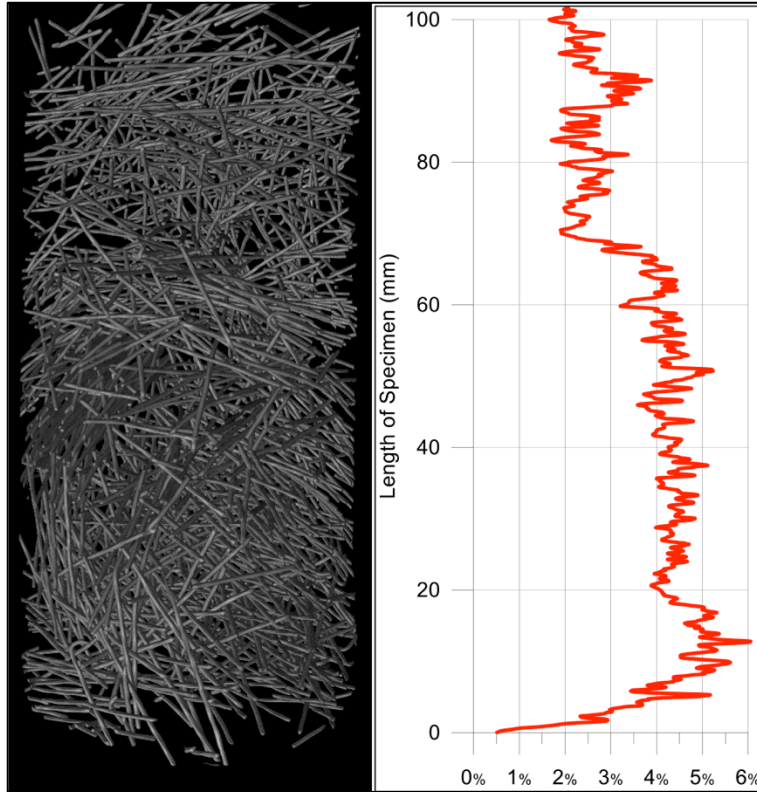


Figure 3.31 3D MicroCT image of fiber reinforcement through depth of beam with the associated percent of fiber cross sectional area along the length of the specimen indicating good distribution of fibers

3.8 Summary & Conclusions

This chapter presented the development of a SCHSC. An effective and simple mixing procedure was established for the SCHSC that could be utilized by semi-skilled labor in an uncontrolled (or, non-laboratory) environment. Section 1 summarized the background and fundamental attributes of a properly designed SCC. Sections 2 and 3 presented details of the raw materials used to design the SCHSC and guidelines for maximizing their effectiveness in the mix. Section 4 detailed the proportions for each mix investigated to determine the effect on multi-scale material properties. Sections 5 and 6 described the mixing and casting processes, and the experimental procedures utilized to evaluate various material properties as affected by the addition of a VMA and

SCM. The results were presented in Section 7. The SCHSC was developed by a multi-scale experimental investigation. The findings include a microCT investigation of the cement microstructure, the unconfined compressive strength, flexure strength, the interfacial bond between the matrix and steel fiber, and the flow characteristics of the mix. Table 3.9 presents a summary of the results from this chapter. From the results, the following conclusions can be drawn:

- The maximum practical limit of PPNC is approximately 0.6% of the total cementitious material. The flow characteristics degrade when this upper limit is exceeded.
- For a w/cm ratio of 0.32, the optimum amount of PPNC to cementitious material is approximately 0.3%. This achieves the ideal filling ability and stability of the mix. If 0.3% is exceeded, the desirable flow characteristics can only be achieved with additional HRWRA.
- Due to the small particle size of the fine aggregate, passing ability was not an issue for any mix evaluated in this investigation.
- Total porosity is reduced as the amount of PPNC is increased in the mix. Increasing the amount of PPNC also refines the cement microstructure by reducing the number of large pores. PPNC improves the pore size distribution, which improves mechanical properties.
- Replacing cement with Grade 120 GGBFS also reduces total porosity. The GGBFS improves the pore size distribution. Pore volume is decreased for pore sizes with a diameter greater than 90 μ m, but slightly increased for pore sizes with a diameter less than 90 μ m.

- Compressive strength increased as the amount of PPNC was increased for both w/cm ratios investigated.
- GGBFS improves the compressive strength considerably.
- PPNC did not appear to affect the MOR.
- GGBFS increased the MOR.
- PPNC significantly increased the toughness of the interfacial bond between the steel fiber and matrix.
- PPNC helps maintain stability of the mix while achieving high flow values and flow rates.

Table 3.9 Summary of findings.

Mix	Flow Properties		Porosity (%)		Compressive Strength			Flexure				Single Fiber Pull-out	
	Max Flow D _{max} (mm)	Flow Rate T ₅₀₀ (sec)	Total Porosity	No. of Pores	No. of cubes	F'c avg. (MPa)	F'c stdev. (MPa)	No. of beams	MOR (MPa)	MOR Stdev. (MPa)	MOR / F'c	Peak Load (N)	Toughness (N*mm)
P0S0W40 (Control 1)	914mm	3s	13.82 %	79,094	18	42.7	2.07	3	2.96	0.22	6.9%	-	-
P3S0W40	864mm	3s	-	-	18	49.0	3.19	4	3.61	0.44	7.3%	-	-
P6S0W40	813mm	3s	-	-	24	55.1	2.34	9	3.67	0.22	6.7%	-	-
P0S0W32 (Control 2)	762mm	9s	9.00 %	144,573	16	52.8	2.34	6	5.51	0.61	10.4%	161	708
P1S0W32	660mm	11s	-	-	9	56.5	1.80	-	-	-	-	-	-
P2S0W32	660mm	11s	-	-	9	58.1	2.61	-	-	-	-	-	-
P3S0W32	584mm	28s	8.12 %	110,895	32	69.6	4.92	8	5.57	0.35	8.0%	178	891
P6S0W32	508mm	52s	6.13 %	102,116	15	78.0	4.02	8	5.66	0.72	7.3%	248	1239
P6S0W32_2	635mm	25s	8.36 %	-	17	66.0	2.41	-	-	-	-	-	-
P6S15W32	749mm	18s	4.98 %	103,560	35	104.8	5.61	6	9.78	0.73	9.3%	-	-
P3S15W37	889mm	11s	4.01 %	-	10	107.1	6.65	6	12.16	0.77	11.3%	-	-
P6S15W37	813mm	10s	-	-	-	-	-	-	-	-	-	-	-

Note: Mix “P6S15W37” is investigated throughout the remaining chapters.

CHAPTER 4

CHARACTERIZATION OF A SCHSC WITH HYDROSTATIC, DEVIATORIC AND TENSILE LOADING

4.1 Introduction

The development of a SCHSC was presented in the preceding chapters. The development of this material involved an extensive experimental investigation. Multi-scale experiments were undertaken to optimize the control mix for quasi-static compression and flexure loading conditions, flow characteristics, interfacial bond between the matrix and high-strength steel fiber, and microstructure pore size distribution and porosity. As stated in Chapter 1, developing a new material implies that there are unknown material properties that must be quantified (or characterized) for the intended application. Therefore, it is important to experimentally characterize the material response under loading conditions that are representative of intended applications. A thorough characterization of material response to such loading conditions will foster higher fidelity models to simulate and predict the endless scenarios that the material may encounter in use. This chapter discusses and quantifies relevant quasi-static material properties necessary for a clearer understanding of the SCHSC constitutive behavior when subjected to projectile impact and penetration. Chapter 5 will investigate the rate sensitivity of SCHSC, and Chapter 6 will evaluate the subsequent material response from a laboratory ballistic experiment.

The stress environment resulting from a projectile penetrating into a brittle geomaterial is highly localized, complex, and multiaxial. For the specific problem at

hand, high-velocity impact of a relatively rigid projectile on a brittle SCHSC panel, the impact event is complicated by material heterogeneity and anisotropy. The previous chapter focused on development of the SCHSC with a particular emphasis on refinement of the microstructure to enhance the unconfined compressive strength. It has been established that enhancing the compressive strength will improve the ballistic performance of concrete, but shear and tensile strengths play a significant role as well. There is a direct correlation between the compressive strength, and the shear and tensile strengths of concrete. This relationship is shown by the fundamental ACI equations that govern shear and tensile capacities of a concrete structural element. This indicates that by enhancing the cement microstructure to improve compressive strength, the shear and tensile capacities will also be increased. However, characterizing only the unconfined compressive strength will not adequately describe the constitutive behavior of the material. As will be presented in Chapter 6, a projectile impact and penetration event is far more complex than quasi-static uniaxial compression (i.e. unconfined compression). For such a dynamic event with a relatively small diameter projectile impacting a thin panel with a significantly larger width, the stress state is multiaxial with tension and shear capacities controlling the material response. Thus, it is crucial to fully characterize the shear and tensile capacities of the SCHSC.

In addition to shear and tension, this chapter addresses the importance of lateral confinement when characterizing compressive strength. It has been shown in the literature that the shear response of concrete (and many other brittle geomaterials) is pressure dependent. This was clearly established in a very thorough investigation sponsored by the Department of Defense on the penetration of “inert bombs” into various

types of “rock” [109] in 1951 that showed depth of penetration was strongly influenced by lateral confinement, shear strength and tensile strength. The technical report, titled “Bomb Penetration Project”, was originally classified as “Confidential” and “Restricted”, but was re-graded in 1963 as “unclassified” and was approved for public release. The report stated:

“Field observations, laboratory work, and theoretical considerations all point to an increased resistance to penetration with increased depth of rock. This is tantamount to saying that the rock is ‘stronger’ at depth. The increased strength of rock at depth as a result of the impact and penetration of a bomb is analogous to the increased strength of a rock specimen subjected to a triaxial compression test, if the lateral confinement is increased.” [109]

The report indicated that confining pressures significantly changed the understanding of the penetration response of brittle geomaterials. Essentially, the strength of the material changes as the lateral pressure on the geomaterial is increased. It has also been shown that the shear response is pressure dependent and that as lateral pressure is increased, the geomaterial responds with increased ductility[110]. Given this, to properly characterize a geomaterial, the material should be evaluated under states of multiaxial stress observing the shear and compressive strengths with varying levels of lateral confinement. The following section presents an experimental series conducted on the SCHSC mixture “P6S15W37” to determine the material response under increasing levels of hydrostatic compression (HC), triaxial compression (TXC) and direct tension (DT).

4.2 Preparation of Specimens

The SCHSC was mixed according to the procedure established in Chapter 3. The material was cast and cured in 5 gallon buckets for a minimum of 56 days. After the curing period, specimens were cored directly from the 5 gallon buckets. All hydrostatic and triaxial experiments were conducted on cylindrical specimens with a nominal 50-mm diameter and 100-mm length. To ensure uniformly distributed loading on all three principle axes under axisymmetric conditions, the specimens were cored from the 5-gallon buckets with a diamond core drill bit and sectioned to approximate lengths as shown in Figure 4.1. Specimens were ground to the final precise lengths having parallel and flat ends within 0.05 mm tolerance using a Chevalier precision hydraulic surface grinder, Model FSG-3A818. The grinding process and an example of a finished specimen are also shown in Figure 4.1. For the DT experiment, specimens were cast in brass molds, demolded after 24 hours, and cured for a minimum of 56 days in a temperature controlled lime-water bath at 23 degrees Celsius (as per ASTM C192 [105]). Dimensions of the specimen are shown in Figure 4.2. Specimens were painted white with a random black speckle pattern to enable the use of digital image correlation (DIC). DIC is an experimental technique using calibrated stereo digital cameras to capture specimen surface displacement / deformation and an algorithm to calculate the associated surface strain. The technique is described in more detail in the section that follows.



Figure 4.1 Coring (top left), sectioning (top right), precision grinding (bottom left), and a final specimen used for the hydrostatic, triaxial or uniaxial strain experiment

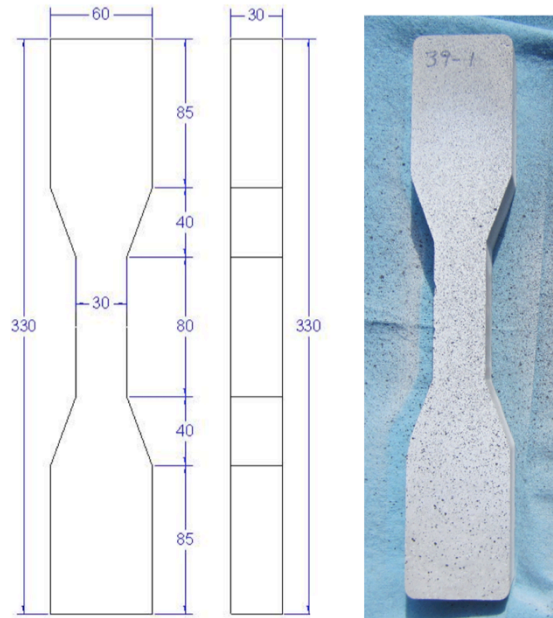


Figure 4.2 Dimensions for the direct uniaxial tension specimen (left) and a specimen prepared for testing with DIC (right)

4.3 Experimental Approach (Methodology)

4.3.1 Constitutive Models

The U.S. Army ERDC has developed a material model to describe the behavior of concrete and other brittle geomaterials under high-strain rate and high-pressure impact loading conditions. The new constitutive model, the Advanced Fundamental Concrete (AFC), was thoroughly described by Adley et al. [111], and was further reviewed by Nordendale et al. [112]. The material model was modified and implemented into a commercial finite element code (Abaqus) by Sherburn [113] and further modified by researchers at Vanderbilt University [112,114]. The specific details of the AFC material model are already adequately covered in the literature. Therefore, the research presented in this section does not reiterate the information, but rather cites the model as an example of a typical material model used to accurately simulate impact-loading conditions of a geomaterial, thus, further establishing the need for the extensive supporting experimental data.

Similar to most constitutive models for brittle geomaterials, the AFC model has four basic elements: 1) an equation of state (EOS) for the pressure-volume relation that includes the nonlinear effects of compaction, 2) a representation of the deviatoric strength of the intact and fractured material in the form of a pressure-dependent yield surface, 3) a damage model that transitions the material from the intact state to the fractured state, and 4) a strain-rate law that is coupled with the failure surface. Each of these four elements are outlined and discussed in detail by Nordendale et al. [115]. As with most constitutive models for geomaterials, the AFC model separates the hydrostatic and deviatoric

responses. Since they are decoupled and independent of each other, the hydrostatic part of the model is a function of the first invariant of the stress tensor and the deviatoric part of the model is a function of the second invariant of the stress tensor. The model addresses the extension failure surface through a factor that is a function of the third invariant of the deviatoric stress tensor. The following section presents the experimental approach to determine the pressure-volume response, deviatoric response and direct tension response, all of which would be used to determine the material constants required for the AFC, or similar, material model.

4.3.2 Pressure-Volume Response

Hydrostatic Compression

Specimens are tested under hydrostatic compression when the axial and lateral stresses are equal as indicated in Equation (1). The specimens are placed in a high-capacity pressure vessel using a mixture of kerosene and hydraulic oil to apply the hydrostatic pressure. Figure 4.3 illustrates the axisymmetric loading conditions and sign convention, noting that compression is taken to be “positive”. The hydrostatic compression experiments determine the material pressure-volume response used to describe the compaction behavior of the SCHSC. The final data are typically reported as “mean normal stress” versus “volumetric strain”, where the mean normal stress is calculated as shown in Equation (2) and the volumetric strain is calculated as shown in Equation (3), which assumes small strains. Volumetric strain is determined by combining the specimen deformations measured along the three principal axes of the

specimen; therefore, it is based on an assumed deformed shape. It should be noted that equation (3) is used to calculate “engineering strain”, whereas the mean normal stress (calculated by equation(2)) is the “true stress”, rather than “engineering stress”.

$$\sigma_1 = \sigma_2 = \sigma_3 = \sigma \quad (1)$$

$$p = \frac{\sigma_{kk}}{3} = \frac{(\sigma_1 + 2\sigma_3)}{3} = \sigma \quad (2)$$

$$\varepsilon_v = \varepsilon_{kk} = \varepsilon_1 + 2 * \varepsilon_3 \quad (3)$$

Figure 4.4 shows a specimen mounted in the instrumentation fixture just before placing in the pressure vessel. This figure also illustrates a diagram of the extensive preparation required to instrument and seal the specimen to prevent leakage of fluid into the specimen during the experiment. As shown here, specimens were wrapped in two layers of latex membranes with an additional exterior coating of a liquid synthetic rubber to protect the membrane from deteriorating under load. The “aqua-seal membrane” is also occasionally required for specimens with significant surface voids that, under high pressure, may rupture the latex membranes and allow fluid to leak into the specimen. For the SCHSC specimens used in this experimental series, the aqua-seal membrane was not required. Two vertically mounted LVDTs were positioned 180 degrees apart to capture axial deformation, and a linear string potentiometer was mounted outside of the chamber to record axial deformation if displacement exceeded the vertical LVDTs calibrated stroke. Radial deformation was measured with the lateral LVDT and the strain-gage spring arm device is also shown in Figure 4.4. Figure 4.5 shows a schematic diagram of

the testing vessel. During testing, the vessel pressure and axial displacements were regulated by a servo-controlled data acquisition system. Confining pressure was monitored with a pressure transducer mounted in the pressurized line connected to the vessel.

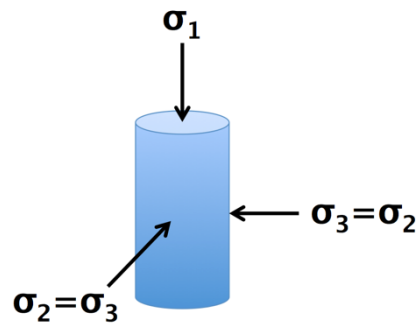


Figure 4.3 Axes and sign convention for cylindrical specimen under hydrostatic or triaxial loading noting that compression is taken to be “positive”

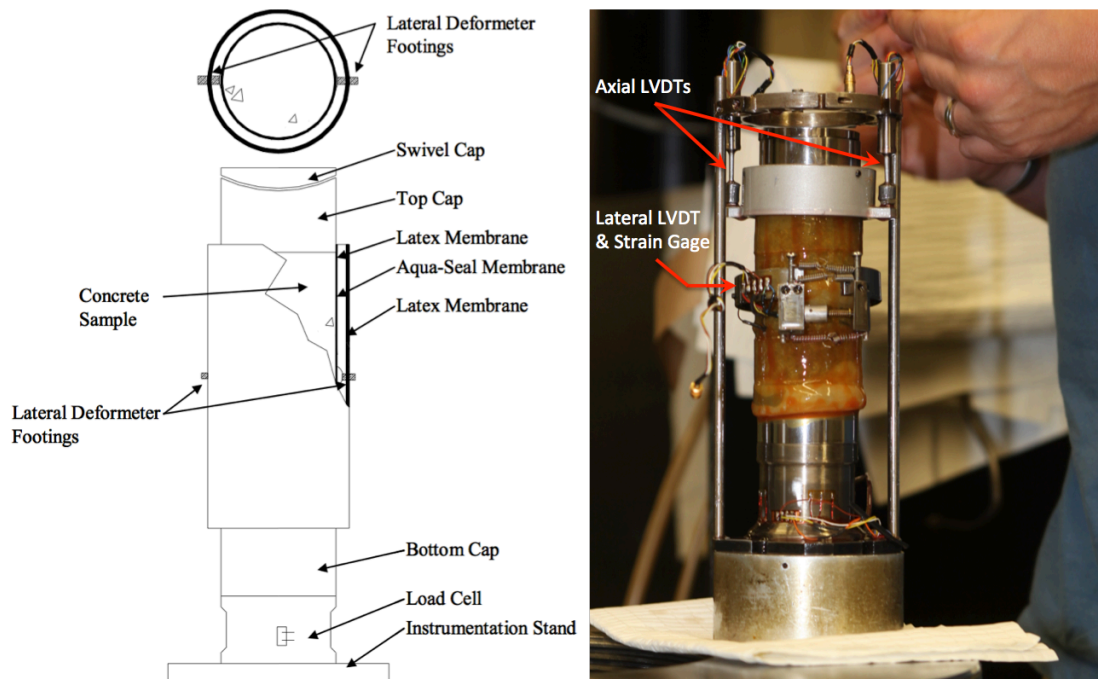


Figure 4.4 Schematic diagram of specimen for hydrostatic and triaxial experiments (left); Specimen mounted with instrumentation ready for testing (right)

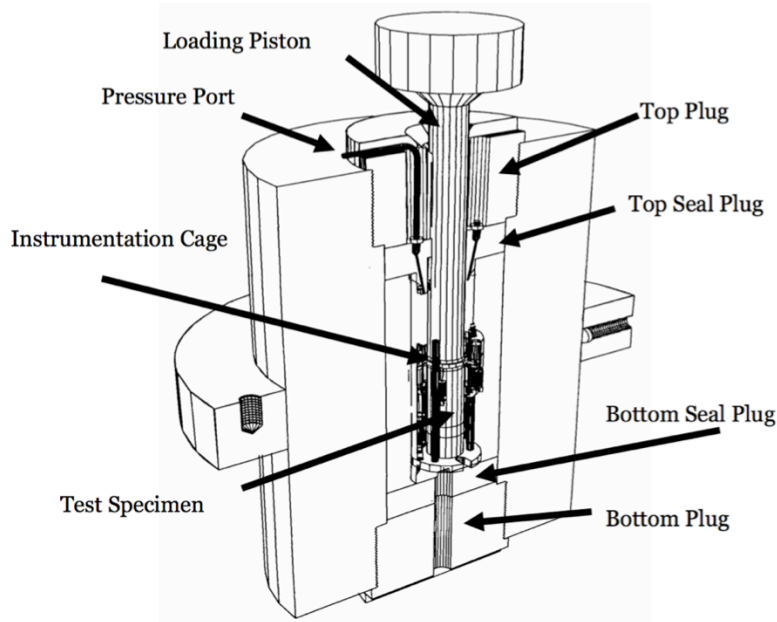


Figure 4.5 Schematic diagram of the 600 MPa capacity pressure vessel used for the hydrostatic and triaxial compression experiments

Cement Microstructure with Hydrostatic Compression

To correlate the localized microstructural changes with the macroscale response of a typical concrete under hydrostatic compression, an example pressure-volume response is shown in Figure 4.6 [110]. This figure clearly demonstrates that the typical concrete response to hydrostatic compression is nonlinear. The response stages are broken into four phases, as shown on Figure 4.6. In the first phase of hydrostatic compression, the concrete constituents can adequately carry the load without any significant changes in the microstructure. Therefore, the first phase is primarily linear elastic. The slope of the linear elastic phase is the elastic bulk modulus, typically denoted by “K”. As the hydrostatic pressure is increased, compression cracking begins to occur within the mortar and the mortar begins to breakdown. During this second phase, the

shape of the pressure-volume curve is concave towards the strain axis. As the slope of the pressure-volume curve begins to change and the shape changes from concave towards the strain axis to concave towards the stress axis, the material enters into the third phase. During this phase, sliding takes place along internal microstructure cracks along with the closure of some internal voids and cracks. This change in concavity indicates changes are occurring in the microstructure. However, if the pressure is removed at this stage, the unloading curve slope is primarily linear and very minimal damage is visible on the exterior of the specimen. The slope of the unloading curve is called the bulk unloading modulus, and is typically denoted as “ K_{un} ”. If the hydrostatic pressure is increased further, the material transitions into the fourth phase. During this phase, there is significant closure of internal voids and coalescence of cracks.

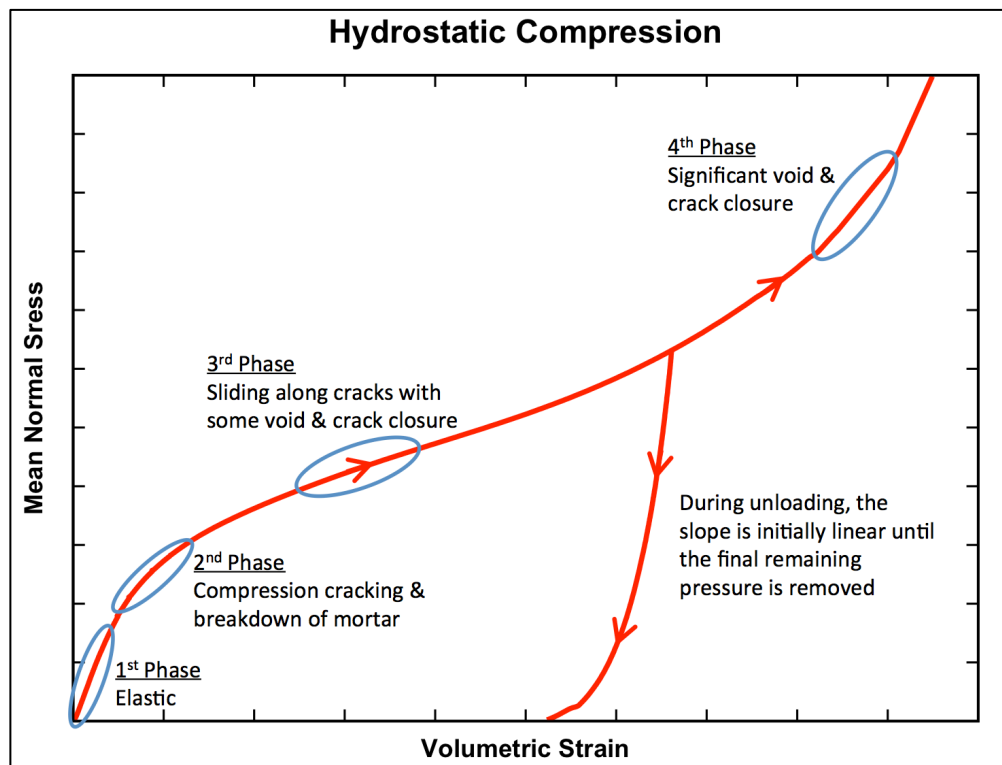


Figure 4.6 Pressure-volume relationship during hydrostatic compression experiment.

Uniaxial Compressive Strain

As presented in this section, the hydrostatic compression test is often used to determine the pressure-volume relationship of geomaterials. By definition, hydrostatic compression requires lateral pressure to be increased at the same rate as the axial pressure, while allowing the radial and axial deformation to determine the total volumetric strain of the specimen. Alternatively, the pressure-volume relationship can be determined from a uniaxial compressive strain experiment (UXC). In a UXC experiment, the lateral stress is adjusted throughout the test to maintain zero radial deformation. Similar to the hydrostatic compression test, the data are presented as the mean normal stress versus volumetric strain. It can be argued that this quasi-static experiment more closely represents the mechanics of projectile impact than the hydrostatic compression tests, simply due to the lack of radial expansion during a high rate event. Because of this, the data from a UXC experiment was also included in the characterization of P6S15W37.

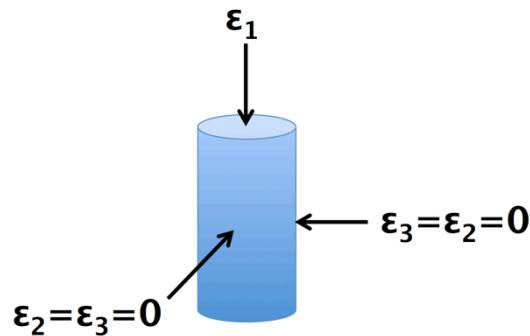


Figure 4.7 Boundary conditions for UXC experiment

4.3.3 Deviatoric Response

The triaxial compression test evaluates the deviatoric response of the geomaterial. During the triaxial compression test, the axial and lateral stresses are not equal. Because

of this, the specimen is subjected to a shear stress characterized by the “principal stress difference” (PSD), or the difference between the axial stress (applied through the loading piston depicted in Figure 4.5 and the vessel fluid) and lateral stress (applied by the vessel fluid). Recalling that “stresses” throughout this chapter are “true stresses” the PSD is calculated by Equation (4). For the triaxial experiment, the PSD is related to the second invariant of the deviator stress tensor as shown in Equation (5). The triaxial experiment is typically conducted at various levels of confining pressures. The specimen is first loaded under hydrostatic compression until the desired confining pressure is achieved. After the pressure vessel reaches the desired hydrostatic pressure, the axial load is applied through the loading piston while axial and radial deformations are measured using the same experimental setup described in the preceding section and shown in Figure 4.4. Once a series of curves are generated for increasing levels of confining pressure, the failure surface can be established from the stress difference and mean stress at each failure point of the specimens.

$$PSD = (\sigma_1 - \sigma_3) = \frac{\text{Axial Load}}{A_o(1 - \epsilon_3)^2} \quad (4)$$

$$\sigma_{eff} = \sqrt{3J_2} = \sigma_1 - \sigma_3 \quad (5)$$

Cement Microstructure in Triaxial Compression

As presented in Chapter 3, many initial flaws exist in the concrete microstructure. These flaws may be present as microcracks at the ITZ between the matrix and aggregate, and are randomly distributed transversely and laterally throughout the microstructure. When the axial load is continuously increased for a certain level of unconfined

compression, the cracks start to coalesce into continuous cracks that roughly align parallel to the direction of the load. Propagation of these cracks ultimately results in the failure of the concrete. Shah et. al. [116] presented a summary of studies of the fracture mechanics of concrete cylinders and compressive failure. The study reported that lateral displacement was uniform across the height of the cylinder until approximately 80% of the peak load was achieved. At this point, strain localization occurs at mid-height as microcracks coalesce and propagate resulting in a significant increase in specimen volume due to lateral displacement at mid-height. Cargile [110] reported similar findings for unconfined compression tests with low confining pressures, but as the confining pressure was increased, concrete transitioned from a brittle to a ductile regime. Microcracks still coalesce at high confining pressures, but deformation occurs at the intercrystalline level resulting in a ductile response.

Test Matrix for Quasi-static compression

The test matrix for the compression and shear experimental series is shown in Table 4.1. The table summarizes the number of tests for unconfined compression (UC), uniaxial strain in compression (UXC) and triaxial compression with confining pressures of 10 MPa (TXC/10), 20 MPa (TXC/20), 50 MPa (TXC/50), 100 MPa (TXC/100), 200 MPa (TXC/200), 300 MPa (TXC/300) and 400 MPa (TXC/400). Specimen dimension and weights are also reported in Table 4.1.

Table 4.1 Test matrix for hydrostatic and triaxial compression experiments

Test Number	Type of Test	Specimen Dimensions		Specimen Wt. (g)	Density	
		Ht. (cm)	Dia. (cm)		(Mg/mm ³)	(lb/ft ³)
1	UC	10.937	5.060	468.20	2.129	132.9
2	UC	10.960	5.075	453.67	2.046	127.7
3	UC	10.544	5.070	439.93	2.067	129.0
4	UC	10.602	5.070	427.62	1.998	124.7
5	UXC	10.937	5.062	459.95	2.089	130.4
6	UXC	10.922	5.065	462.50	2.102	131.2
8	HC	11.029	5.072	472.26	2.119	132.3
9	TXC/10	10.724	5.072	435.79	2.011	125.5
10	TXC/10	10.612	5.075	441.57	2.057	128.4
11	TXC/20	10.970	5.075	454.94	2.050	128.0
12	TXC/20	10.544	5.075	439.74	2.062	128.7
13	TXC/50	10.813	5.075	438.09	2.003	125.0
14	TXC/50	11.034	5.067	471.70	2.120	132.3
15	TXC/100	10.965	5.077	455.86	2.053	128.2
16	TXC/100	10.691	5.070	456.42	2.115	132.0
17	TXC/200	11.029	5.070	473.09	2.125	132.7
18	TXC/200	10.881	5.075	453.60	2.061	128.7
19	TXC/300	10.724	5.075	433.21	1.997	124.7
20	TXC/300	10.775	5.075	446.98	2.051	128.0
21	TXC/400	10.917	5.070	465.11	2.110	131.8
23	TXC/400	10.975	5.072	453.63	2.045	127.7

4.3.4 Direct Tension Response

To determine the tensile response of the SCHSC, a direct uniaxial experiment was developed. In the literature, there appears to be no consensus on the recommended procedure for testing concrete in direct uniaxial tension. Some researchers have attempted using prismatic specimens with various epoxy bonded end designs to transfer the load to the sample through the grips of the UTM. However, this approach involved tedious sample preparation and has the potential for slippage due to inadequate strength of epoxy. More importantly, this method tends to induce significant clamping forces on the sample area held within the grips of the testing equipment and the possibility of non-uniform load transfer through shear in the epoxy and an uneven concrete surface. An alternative approach is to vary the sample geometry near the ends to enable load transfer from the grips through friction. With this approach, stress concentrations are developed at any

abrupt change in sample geometry. However, the sample geometry can be chosen to minimize this effect. The Japan Society of Civil Engineers has adopted a recommended procedure for testing HPC under direct uniaxial tension based on this approach [117]. This approach formed the basis for conducting the DT experiments on the SCHSC specimens. Figure 4.8 shows a tension specimen mounted in the loading fixture. The loading fixture incorporated the appropriate degrees of freedom to minimize eccentric loads or flexure in the test specimen. Tests were conducted on an MTS 810 testing machine with a 98-KN load cell. The loading machine head was monitored with a closed-loop feed-back control monitoring system to maintain a displacement rate of 0.5 mm per minute throughout testing. Head displacement was recorded in addition to measurements obtained using two external LVDTs. The external LVDTs were Honeywell Model S5 with a ± 5 -mm stroke and were mounted on both sides of the sample slightly above the tapered region. The external LVDTs were mounted slightly in front of and behind the specimen front and back surfaces, respectively. This positioning ensured sample flexure would be easily detected from the data. The sample rate for the exterior LVDTs was 20 Hz, or one sample every 0.05 second. DIC was used to capture specimen surface displacements during testing. DIC is a 3D full-field optical technique to measure surface deformation and strain. Figure 4.8 shows the test setup using stereo digital cameras calibrated to capture movement of the specimen surface in 3D space. As shown in the picture, intense lighting was used to enhance the depth of field for the cameras. VIC-3D [118] was the DIC system used for the DT experiment. A thorough presentation of the theory and description of the experimental technique is provided by Sutton et al.[119]. A one-second DIC step size was selected and used throughout testing. This step size

provided adequate resolution for data acquisition of the 0.5mm per minute displacement control experiment.

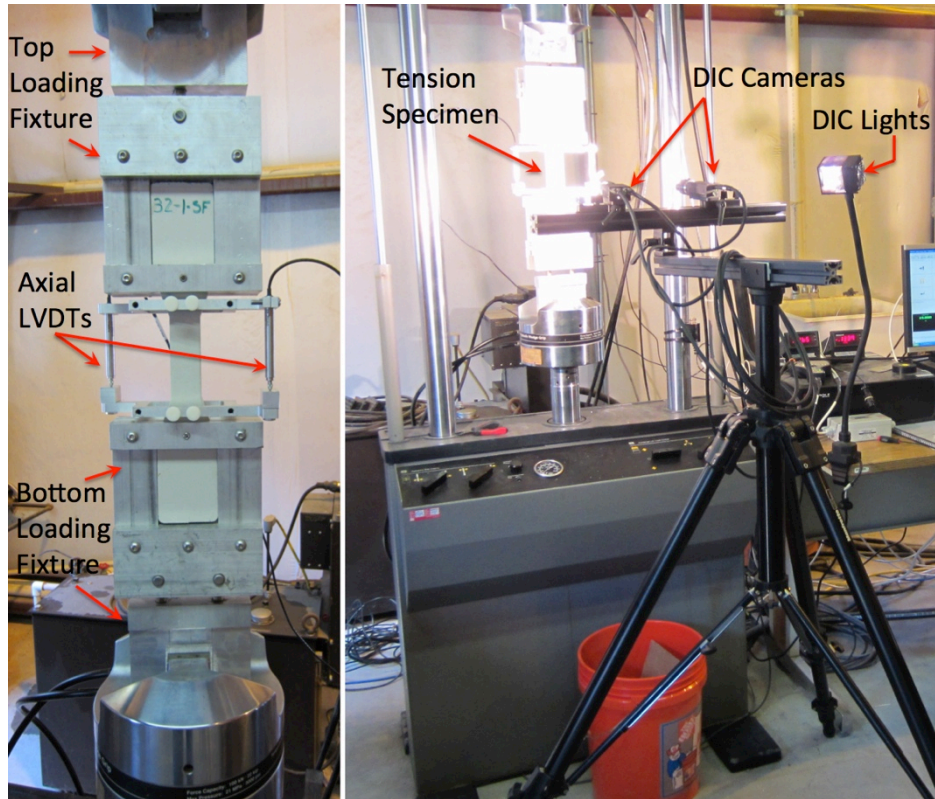


Figure 4.8 DT specimen mounted in loading fixture (left) DIC setup during the DT experiment (right)

4.4 Results

4.4.1 Pressure-Volume Results

Figure 4.9 shows the pressure vs. time history for the HC experiment. As shown here, the hydrostatic pressure was increased to a maximum of 400 MPa, and then held constant for approximately ten minutes before the pressure was decreased. The subsequent axial and radial strains are shown in Figure 4.10. The maximum radial strain

is approximately 4.6%, while the maximum axial strain is approximately 4.3%. The material continues to undergo radial and axial strain while the confining pressure is held constant. This is an indicator that the material (mixture P6S15W37) might be susceptible to creep. Figure 4.11 shows the overall pressure-volume response of the SCHSC. The initial elastic bulk modulus “K” was calculated from Figure 4.11 to be 11.6 GPa. Figure 4.11 also indicates that the specimen undergoes microstructural changes in three of the four phases, as discussed in the preceding sections. Figure 4.12 shows the condition of the specimen after the test was concluded. The deformed shape of the HC specimen in Figure 4.12 validates the assumption for Equation (3).

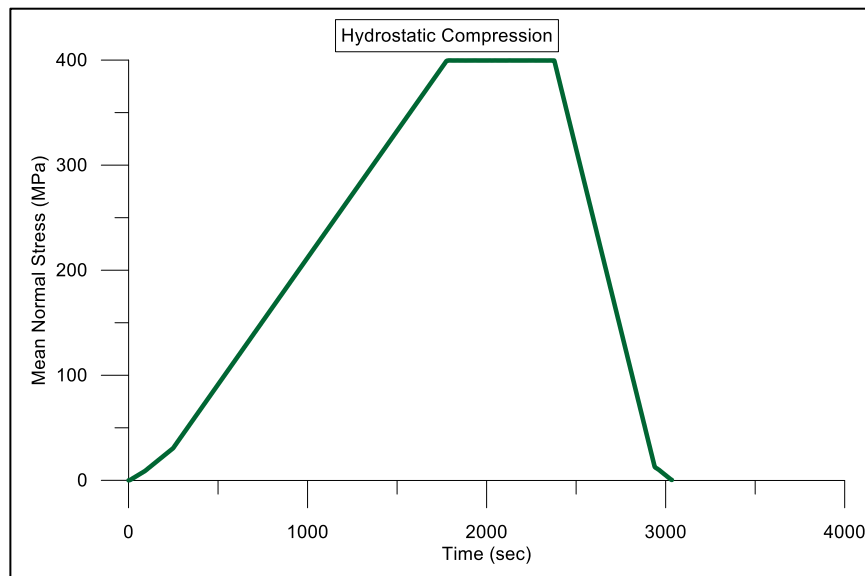


Figure 4.9 Pressure time history for the HC experiment

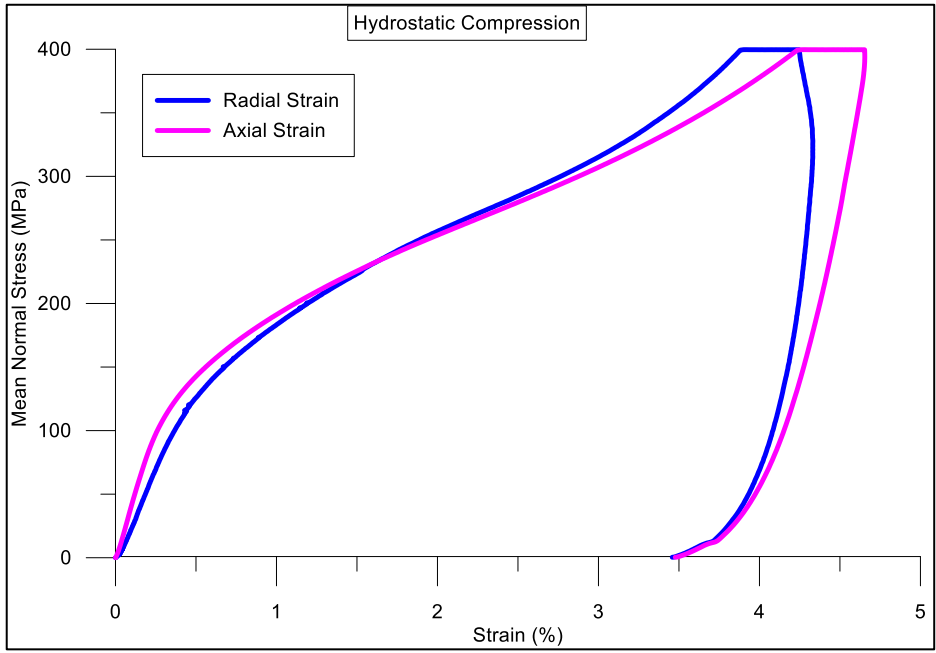


Figure 4.10 Comparison of radial and axial strain with HC

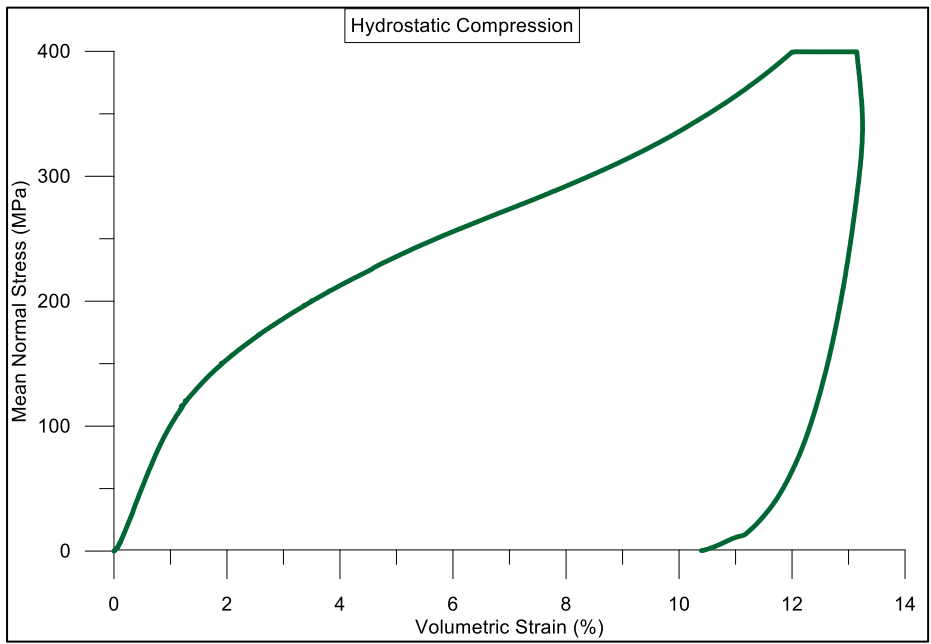


Figure 4.11 Pressure volume response



Figure 4.12 Specimen after the HC experiment was completed (no visible damage)

Results from two UXC experiments are presented in Figures 4.13 and 4.14.

Figure 4.13 shows the axial stress versus axial strain for tests 5 and 6. Throughout the loading of tests 5 and 6, the radial confinement was continuously adjusted to prevent any radial deformation, as the cylinder was compressed axially. The constrained modulus “M” can be determined from a plot of axial stress versus axial strain for a specimen in an undrained state of uniaxial strain [120]. The constrained modulus “M” was determined to be 24.2 GPa. It is related to Poisson’s ratio “ ν ” and bulk modulus “K” by Equation (6). Equation (6) and the previously determined value of “K” indicate a Poisson’s ratio of 0.18. Given these values, Young’s modulus “E” is calculated to be 22.3 GPa and the shear modulus “G” is 13.6 GPa from Equations (7) and (8), respectively. The pressure-volume responses for two UXC tests are shown in Figure 4.14. To compare the pressure-volume responses of UXC and HC, the results from the HC experiment are included in Figure 4.14 as well. Figure 4.15 shows the deformed specimens after completing the UXC experiment.

$$M = \left(\frac{\sigma_1}{\epsilon_1} \right)_{\text{Uniaxial Strain}} = \frac{3K(1-\nu)}{(1+\nu)} \quad (6)$$

$$G = \frac{3K(1-2\nu)}{2(1+\nu)} \quad (7)$$

$$E = 3K(1-2\nu) \quad (8)$$

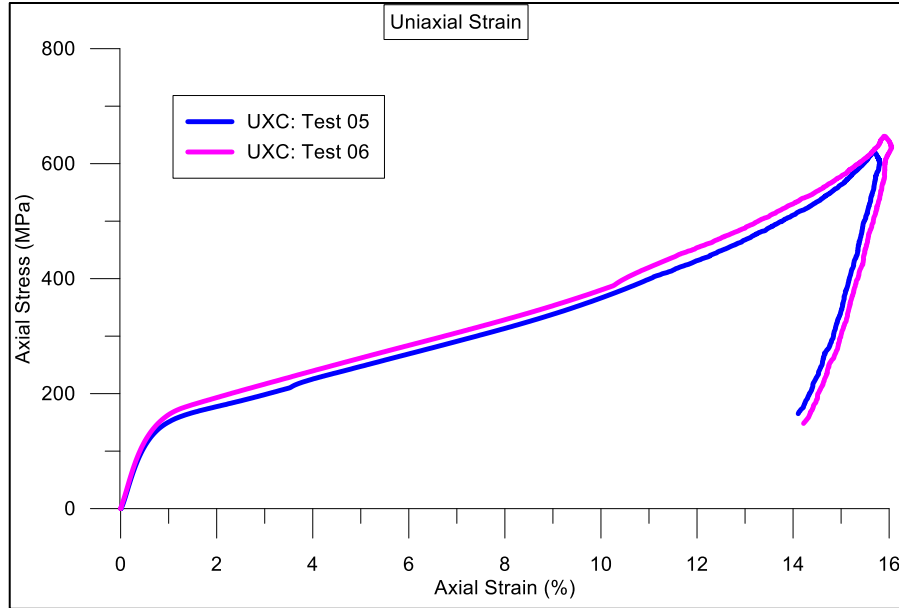


Figure 4.13 Stress versus strain response for two UXC experiments

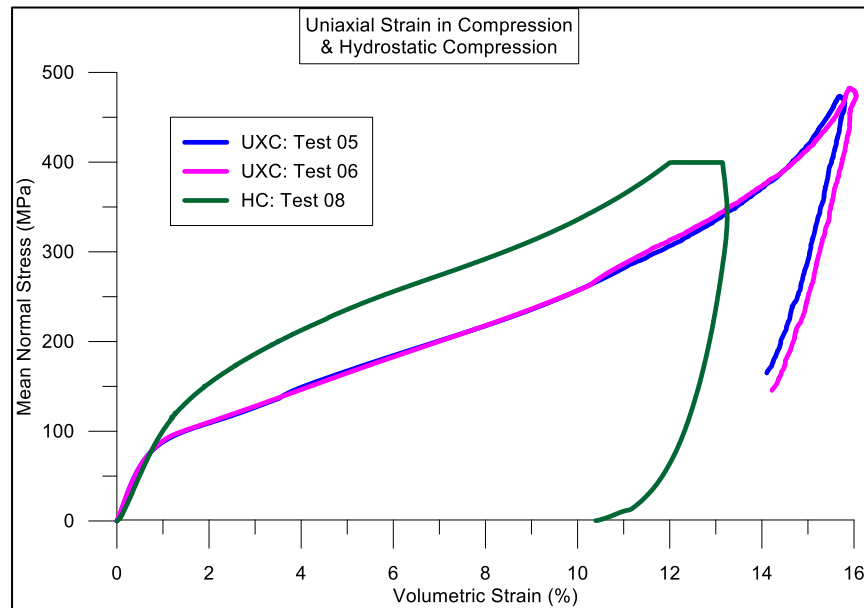


Figure 4.14 Pressure-volume responses for two UXC experiments and HC experiments



Figure 4.15 UXC specimens: before test (left); after test 5 (middle); after test 6 (right)

4.4.2 Deviatoric Results

Figure 4.16 presents the axial stress versus axial strain results for four UC specimens. The maximum axial stresses for the four specimens (tests 1 through 4) vary from 62 MPa to 82 MPa. Table 4.1 indicates densities for these four specimens range from 1.988 Mg/mm³ to 2.129 Mg/mm³. Given this range of densities, variation in peak axial stress is to be expected. However, the average value of Young's Modulus from the four curves is 22.6 GPa, which agrees closely with the previously calculated value of 22.3 GPa. Figure 4.17 shows the axial stress versus volumetric strain response for the four UC specimens. Recalling that compression is considered positive, and that Figure 4.16 established the axial strain as "compressive", the reversal in volumetric strain is due to the rapidly increasing radial deformation under "negative" or tensile strain. Figure 4.18 shows the radial deformation for the four UC tests. It should be reiterated that volumetric strain is based on an assumed deformed shape, as noted in Equation (3). This

assumed shape proved to be valid for the HC and UXC experiments; however, the assumed shape might not be valid for UC and TXC deformation. As the material responds to higher levels of lateral confinement, the deformed shape changes significantly. Radial deformation is primarily uniform along the height of the specimen at low confining pressures, but at high levels of lateral confinement, the specimen assumes a “barreling” shape with significant bulging at specimen mid-height. This effect can lead to misleading volumetric strain values when calculated by Equation (3). The actual deformed and fractured shapes for the four UC tests are shown in Figure 4.19.

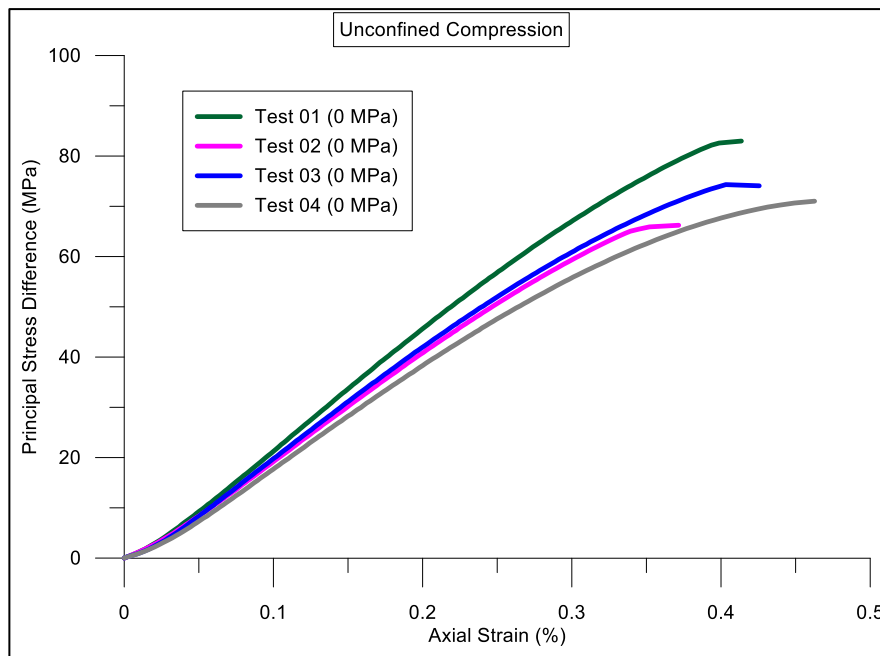


Figure 4.16 UC: PSD vs axial strain

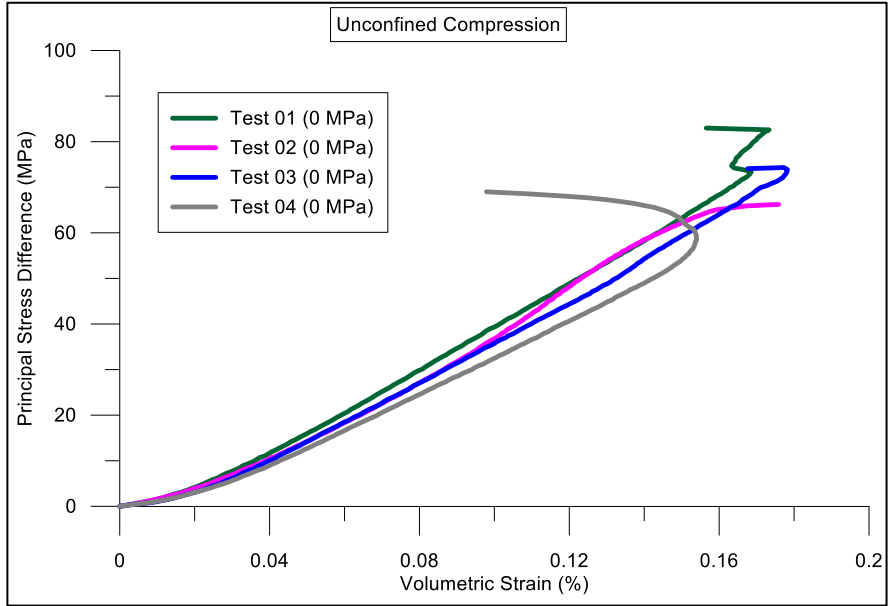


Figure 4.17 UC: PSD vs volumetric strain

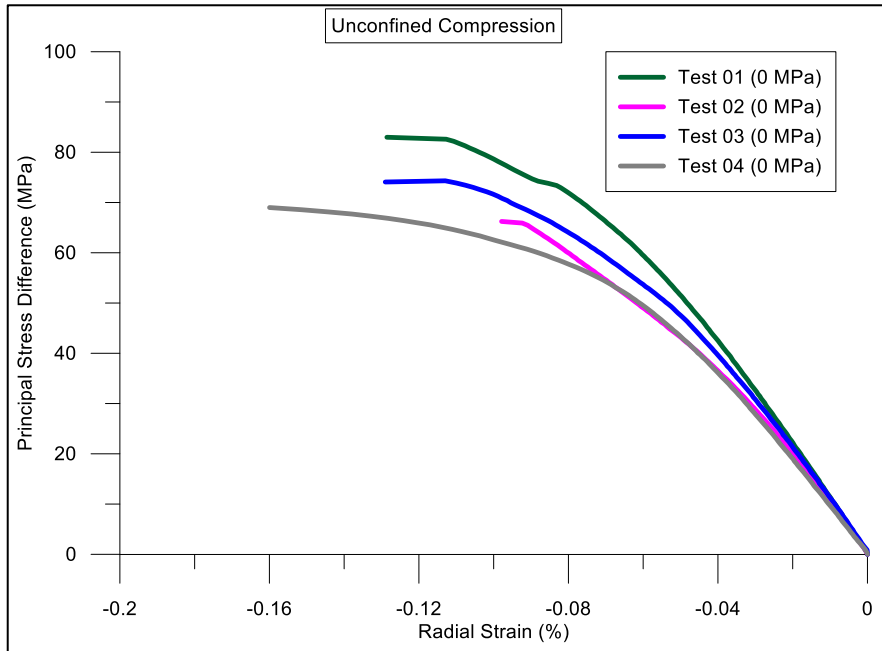


Figure 4.18 UC: PSD vs radial strain



Figure 4.19 Specimens at failure for UC test 1 (left); UC test 2 (left-middle); UC test 3 (right-middle); and UC test 4 (right)

PSD versus axial strain results are shown in Figures 4.20 and 4.21 for the different confinement levels of the TXC experiment. All of the strain values reported in the TXC tests are due to shear loading only. As previously discussed, the specimen was first loaded in HC prior to shear loading. To isolate shear deformation, the TXC strain values presented in the following graphs were collected after the HC confining pressure was fully achieved. Two specimens were tested at each of the following confining pressures: 10 MPa, 20 MPa, 50 MPa, 100 MPa, 200 MPa, 300 MPa and 400 MPa. All specimens were loaded until failure occurred. Figure 4.22 combines the PSD versus axial strain data for all tests at the full range of confining pressures. This plot illustrates the transition from brittle behavior to ductile behavior at the higher confining pressures. In addition to the axial strain, PSD versus radial strain is shown in Figure 4.23 for the TXC tests with confinement levels ranging from 0 MPa to 50 MPa. Figure 4.24 combines all PSD versus radial strain plots for the TXC tests (0 MPa to 400 MPa). Figure 4.24 indicates dilation of the radius at high-confining levels. Trends in Figures 4.22 and 4.24

suggest that the specimens could have experienced a “barreling” effect with the compressive axial strain decreasing the cylinder height and the tensile radial strain increasing the cylinder radius near mid-height. This effect becomes more pronounced at higher levels of confinement. This effect is noticeable in the deformed specimen pictures shown in Figure 4.25. Combining the axial and radial strain responses, Figures 4.26 through 4.28 present the overall PSD versus volumetric strain response for the UC and all TXC tests. In these Figures, the change from positive volumetric strain to negative volumetric strain is an artifact of Equation (3) and the sign convention. Recalling compression (axial strain) was positive and tension (radial strain) was negative, the specimens with 300 MPa and 400 MPa confining pressures showed more pronounced radial deformation than the specimens tested at lower confining pressures. This phenomenon was beginning to occur in the specimens with 50 MPa, 100 MPa and 200 MPa confining pressures, but the load was removed before significant dilation of the radius occurred, thus the observed “loop” for some of data in Figures 4.26, 4.27 and 4.28.

Plotting the PSD versus MNS for each experiment defines points on the failure surface of the material. This is shown in Figure 4.29. It is evident from the shape of the failure surface that the shear strength for P6S15W37 increases with confinement; however, the shear strength does not exceed 300 MPa. This upper limit of 300 MPa does not appear to increase when the confining pressure is increased beyond 200 MPa. Figure 4.30 shows the relationship between the UXC experiment and the failure surface. This figure illustrates the UXC material response and adherence to the established failure surface for the material.

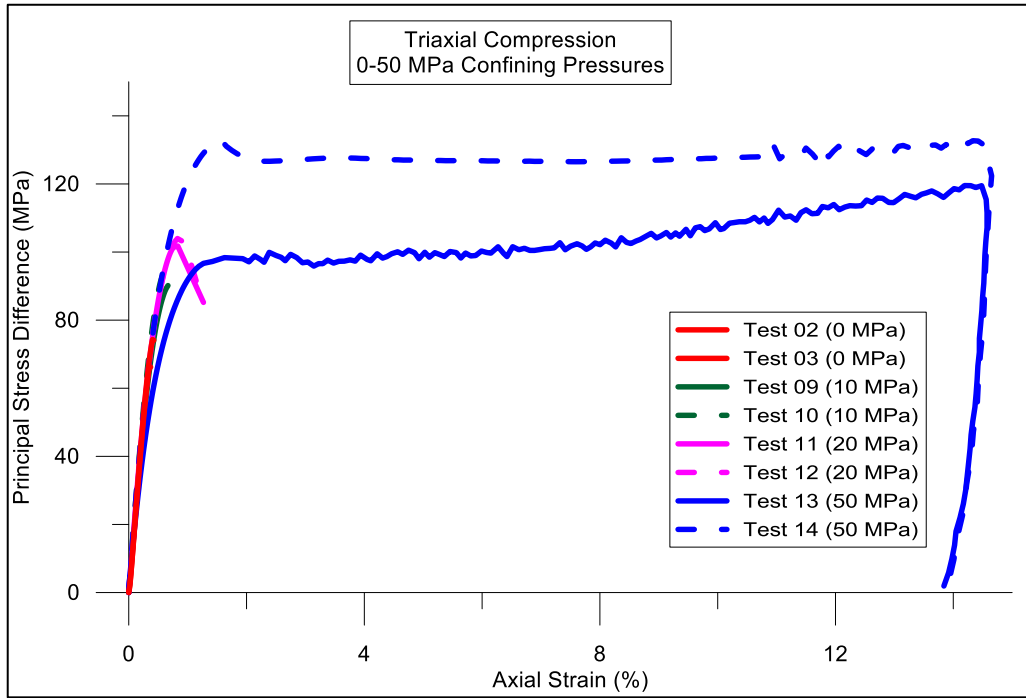


Figure 4.20 TXC: PSD vs axial strain for confining pressures 0 MPa to 50 MPa

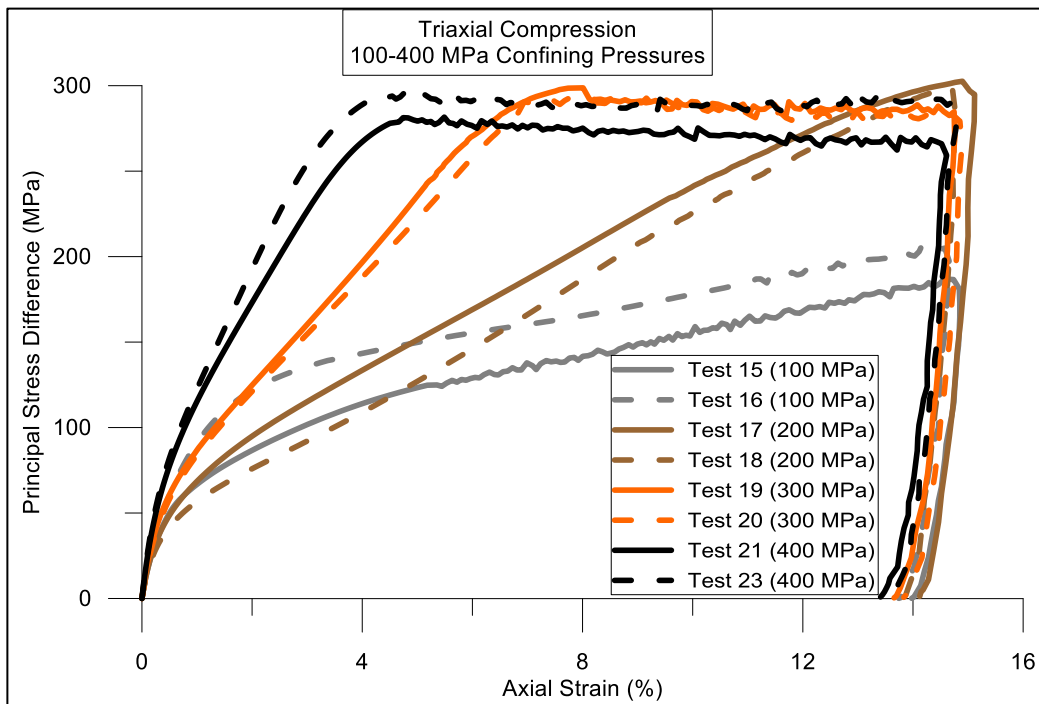


Figure 4.21 TXC: PSD vs axial strain for confining pressures 100 MPa to 400 MPa

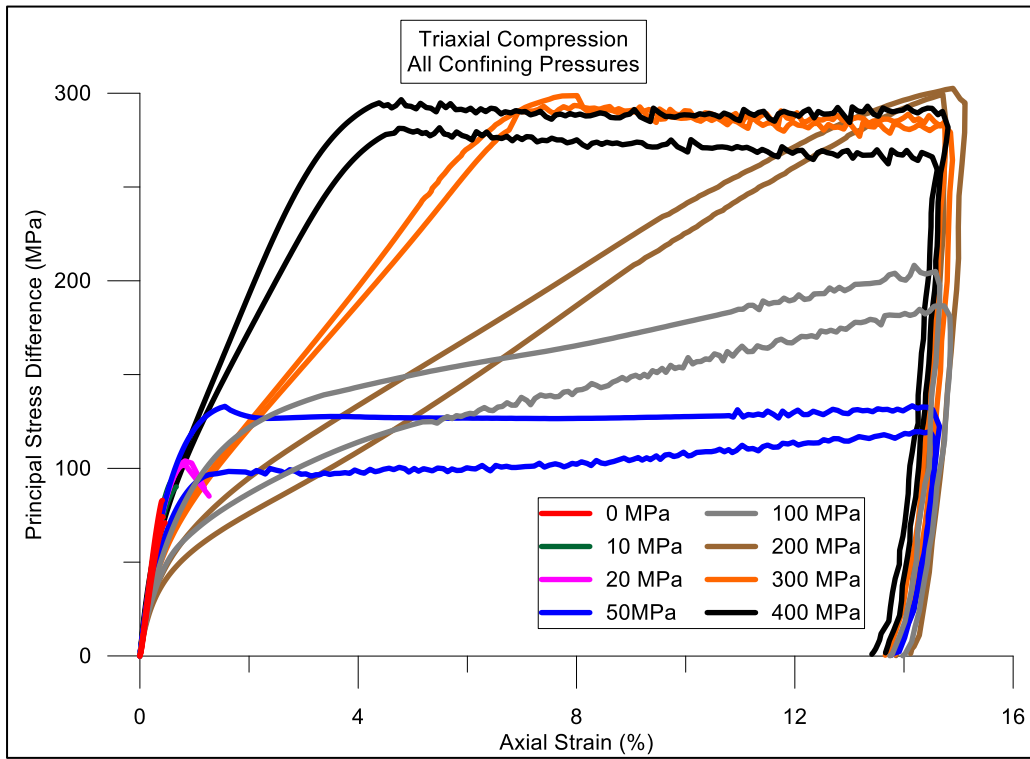


Figure 4.22 TXC: PSD vs axial strain for all confining pressures 0 MPa to 400 MPa

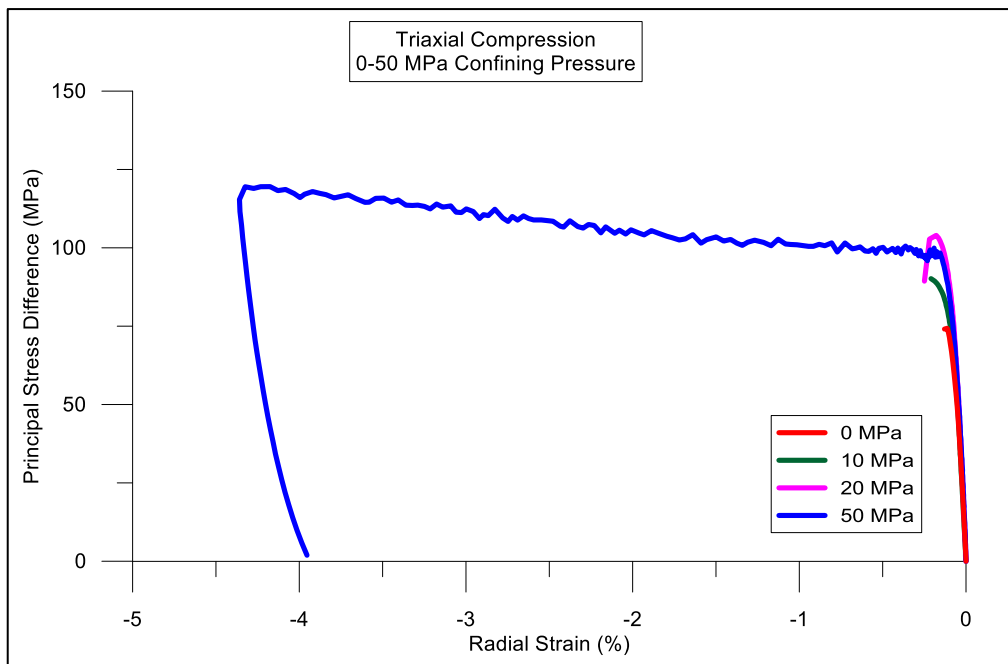


Figure 4.23 TXC: PSD vs radial strain for confining pressures 0 MPa to 50 MPa

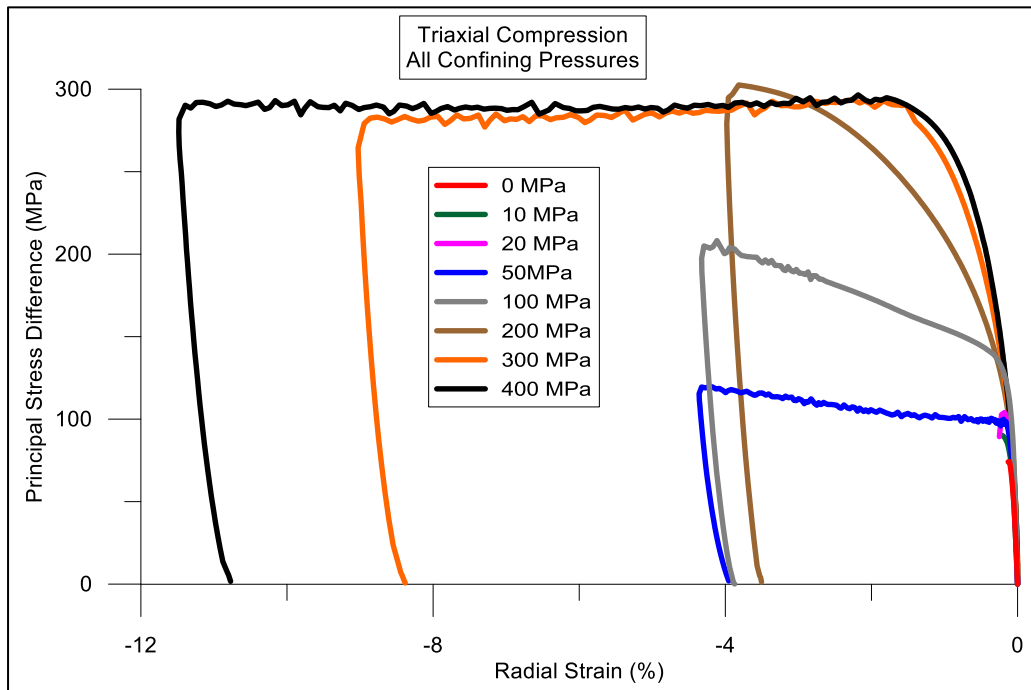


Figure 4.24 TXC: PSD vs radial strain for all confining pressures 0 MPa to 400 MPa

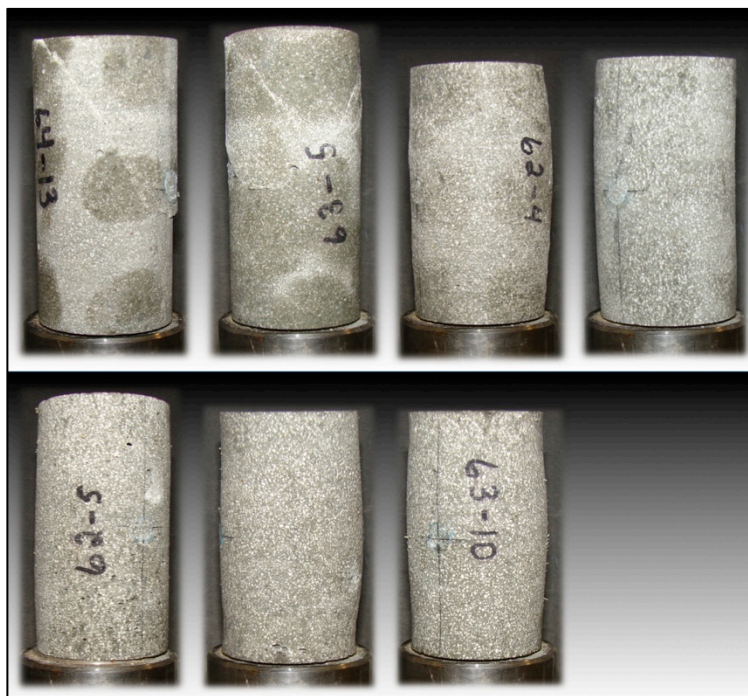


Figure 4.25 TXC specimens after testing - top row: 10 MPa (left); 20 MPa (left middle); 50 MPa (right middle); 100 MPa (right) - bottom row: 200 MPa (left); 300 MPa (middle); 400 MPa (right)

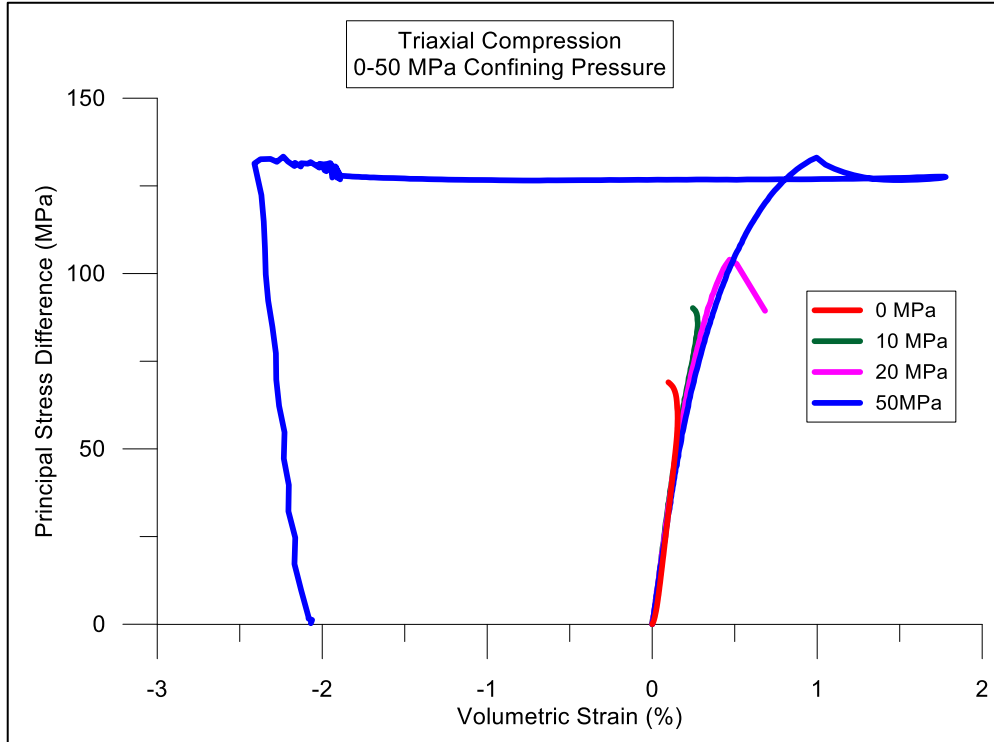


Figure 4.26 TXC: PSD vs volumetric strain for confining pressures 0 MPa to 50 MPa

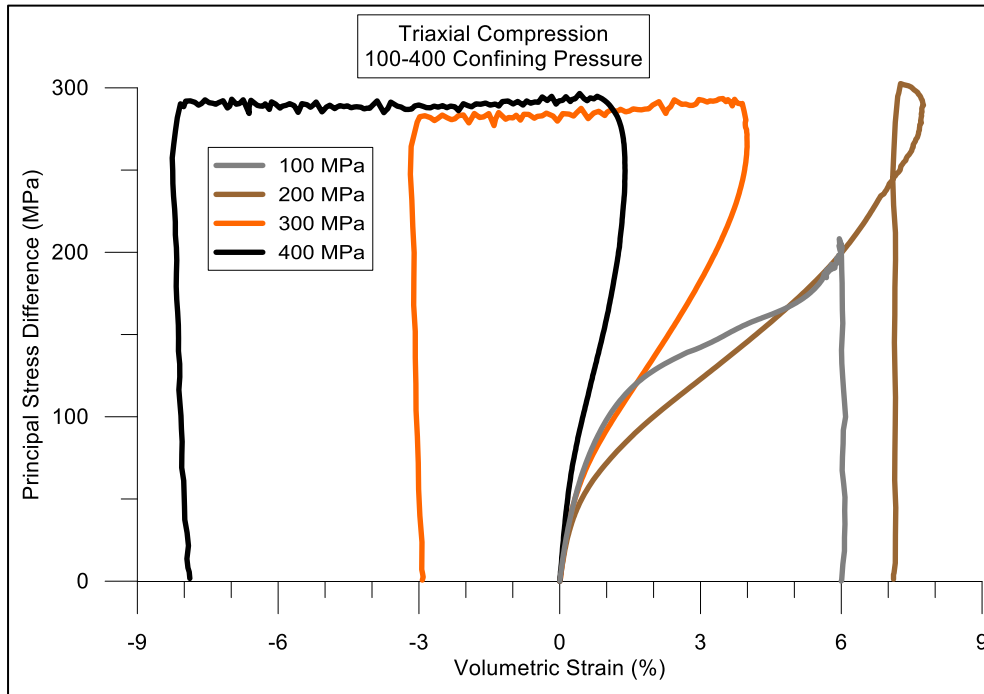


Figure 4.27 TXC: PSD vs volumetric strain for confining pressures 100 MPa to 400 MPa

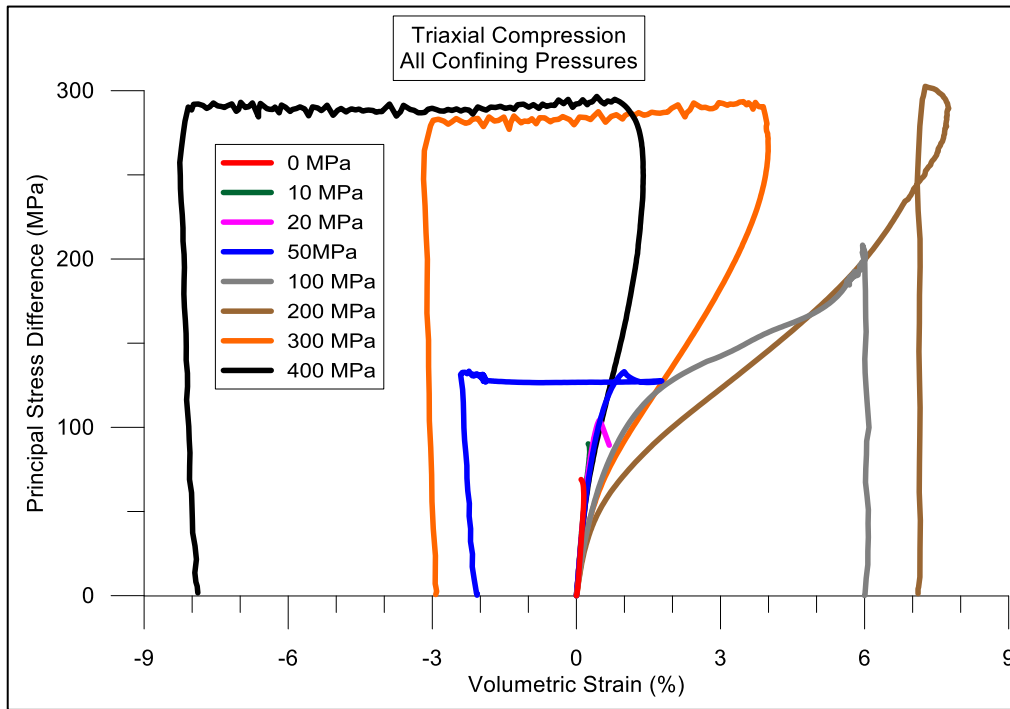


Figure 4.28 TxC: PSD vs volumetric strain for all confining pressures 100 MPa to 400 MPa

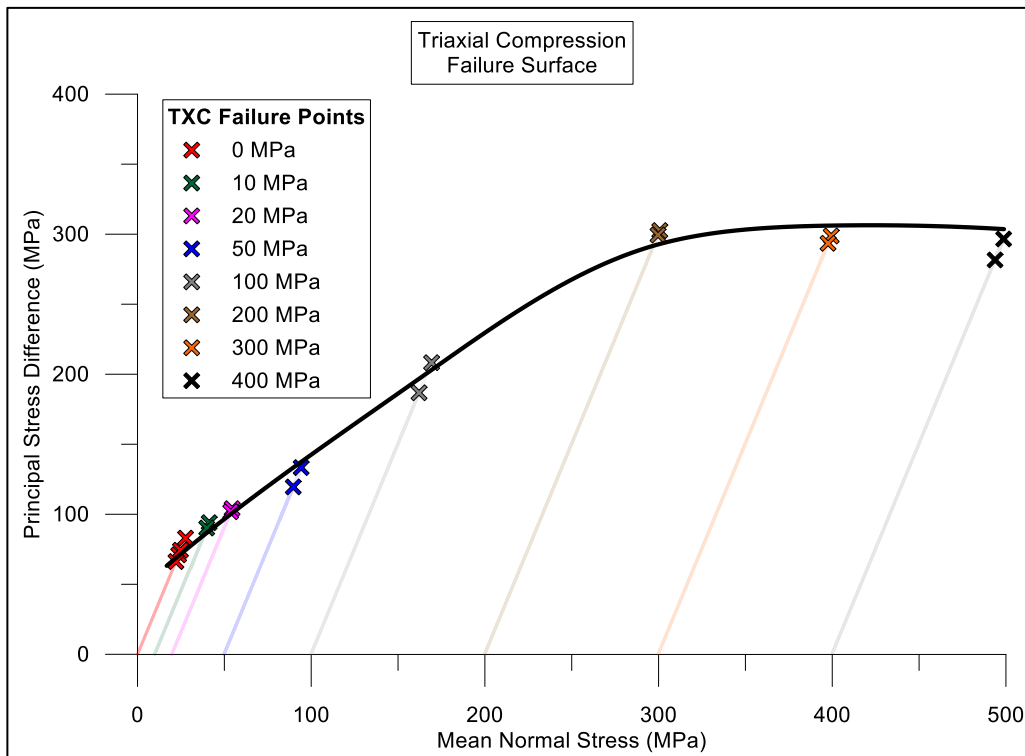


Figure 4.29 TxC and UC failure points and surface for SCHSC material

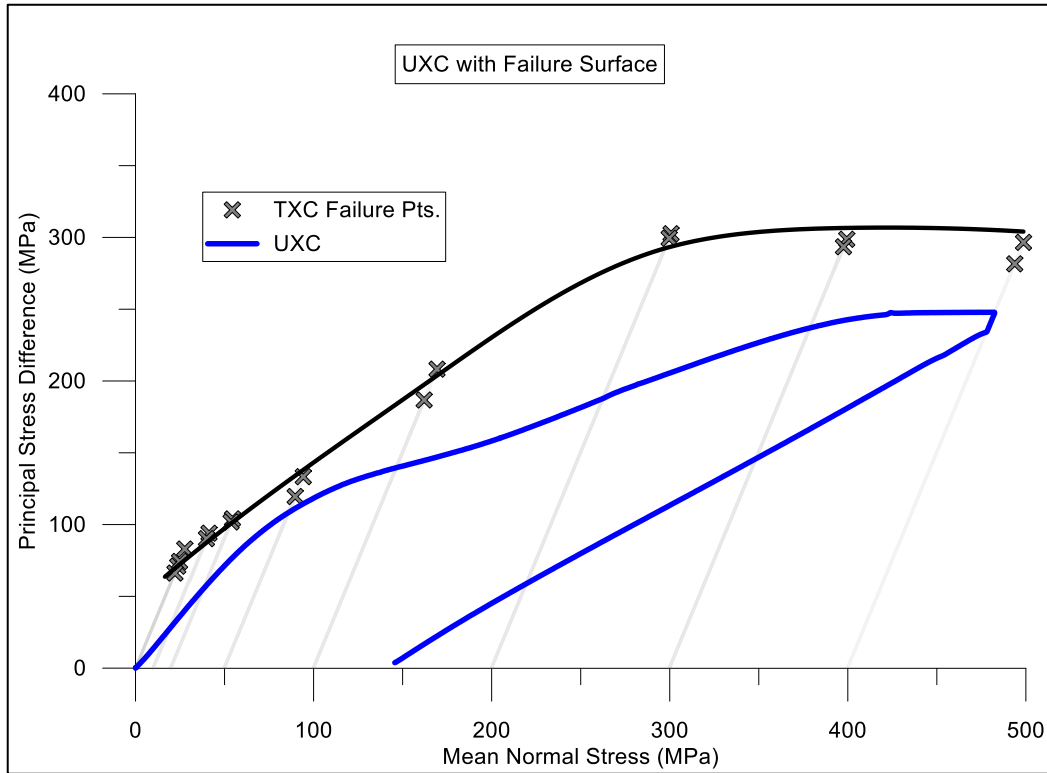


Figure 4.30 UXC: PSD vs MNS with TXC failure points and surface

4.4.3 Direct Tension Results

Load versus displacement data from DT tests 1, 2 and 3 are plotted in Figure 4.31. The data plotted in Figure 4.31 represents the average value of displacement for each of the three tests as determined from the two external LVDTs, and an overall “average” response determined from the three tests together. Upon close inspection of the data, the load versus displacement response of the individual LVDTs for Test 1 indicate the presence of an eccentric load with one LVDT indicating compression and the second LVDT indicating tension at loads as small as 360 N. This issue was detected during testing and the appropriate adjustments were made to prevent similar results for Tests 2 and 3. Results from Tests 2 and 3 reported very clean and DT data with no eccentric loads. For Tests 2 and 3, the first crack occurred at 3,550 N and 4,105 N respectively.

The location of both initial cracks were at the inside corner of specimen taper, where the change in geometry caused a stress concentration. Both Tests 2 and 3, fibers bridged the initial crack and ultimately achieved a peak load of 6,280 N and 6,530 N, respectively. To further investigate the presence of any eccentric load and the effectiveness of fibers bridging microcracks, DIC virtual extensometers were used in post processing as shown in Figure 4.32. Figure 4.33 compares the Test 3 LVDT load versus displacement response with the virtual DIC extensometer located near the centerline of specimen 3. Figure 4.33 indicates very good agreement between the two independent experimental measurement techniques, thus validating both methods for measuring deformation of the specimen. However, DIC offers many unique post-processing measurement capabilities that are not possible or practical with physical external LVDTs. For example, the axial extension data collected from the left and right extensometer (shown in Figure 4.32) are compared in Figure 4.34. This data shows that extension of the specimen on the left side and right side track closely together until the initial crack occurs at a load value of 4,105 N. After this initial crack, there is a slightly larger increase in deformation along the left side as compared to the right side, suggesting a very small amount of flexure about the Z-axis. After reaching a peak load of 6,371 N, the difference is increased which indicates a crack opening from the left side and progressing toward the right. This trend continues as the load increases. It becomes evident when evaluating the displacement contours along the Y-axis (axis of the specimen) as shown in Figure 4.35. The precise geometric locations and shapes of the microcracks are detected within the step size time interval (1 second) in the axial displacement contours. Figure 4.36 identifies six of the major cracks

on a zoomed-in view of the load displacement plot and identifies when they occurred during the test.

Displacement contours in the Z-direction are shown in Figure 4.37. The scale of the contour for this figure is plus or minus $5\mu\text{m}$. The contours show that there is only a very small amount of displacement along the Z-axis when the specimen reaches the peak load, indicating that flexure about the X-axis is negligible. After the peak load, a second crack appears and the load drops and redistributes within the specimen, resulting in Z-axis displacement. With all of the preceding information, virtual extensometers were placed at the precise location of the microcracks as shown in Figure 4.38. Data from these DIC extensometers were compiled and the results are shown in Figure 4.39. The data is presented as load versus time and crack opening displacement versus time. This graph gives the sequence of events to determine when a crack occurs, under what value of load, the crack width, and how subsequent microcracks affect each other. All such information allows evaluation of the fiber crack bridging effectiveness.

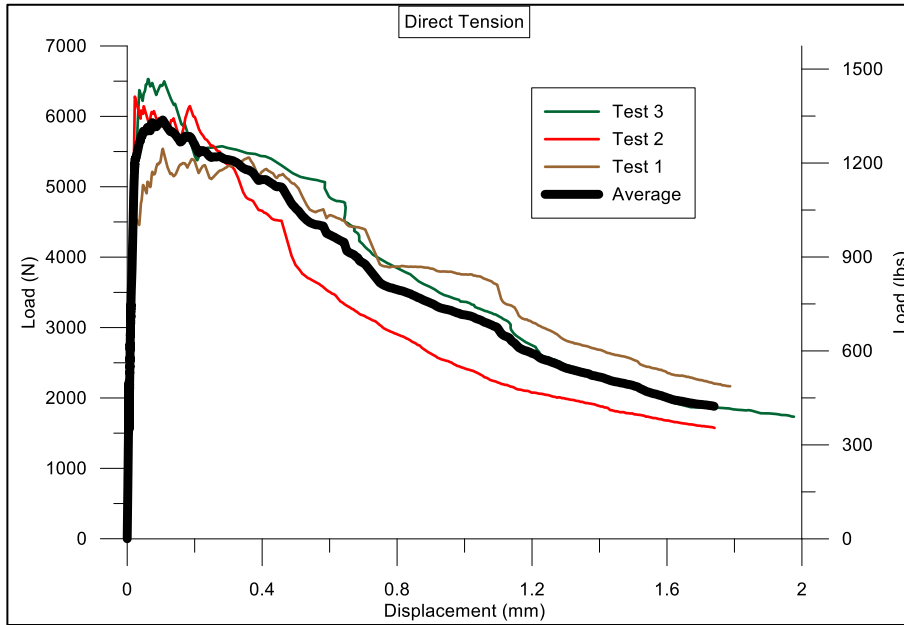


Figure 4.31 Load vs displacement results from the DT external LVDTs for three tests

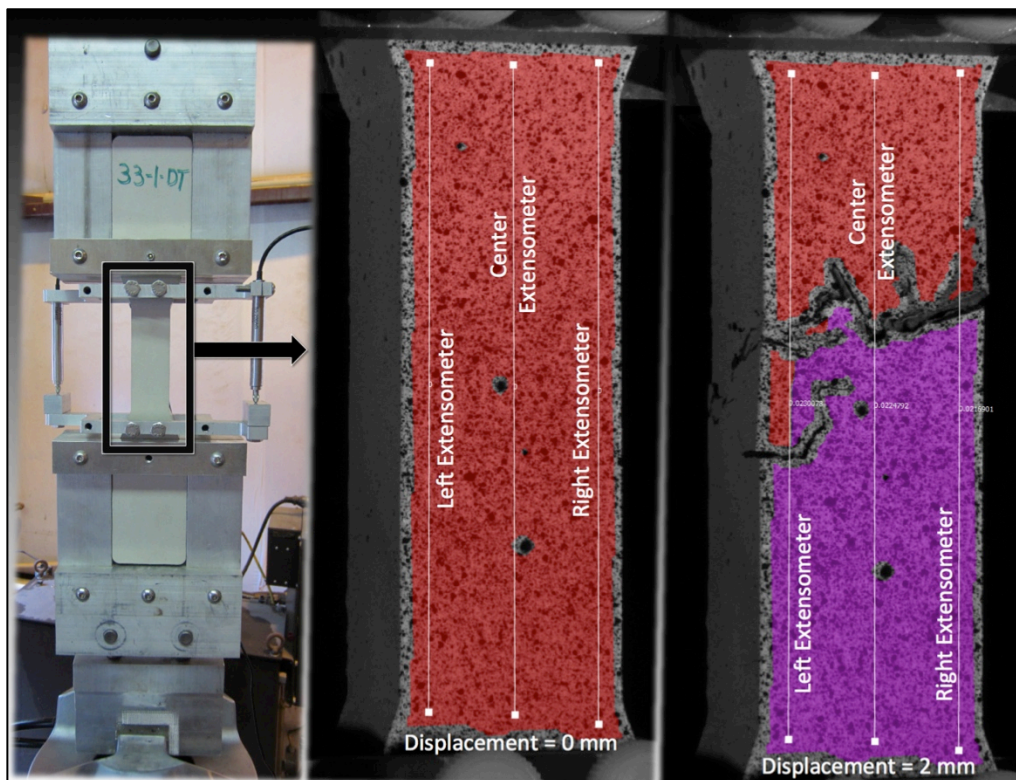


Figure 4.32 Location of three virtual DIC extensometers to capture displacement on the left side, center and right side of the specimen during test 3.

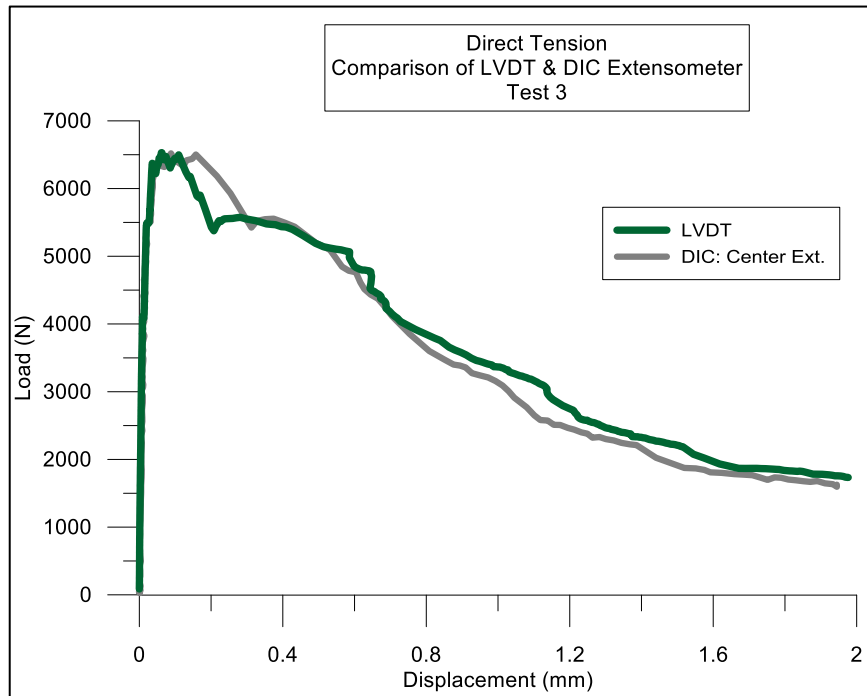


Figure 4.33 Comparison of the load vs displacement responses from the DT external LVDT and DIC center extensometer during test 3.

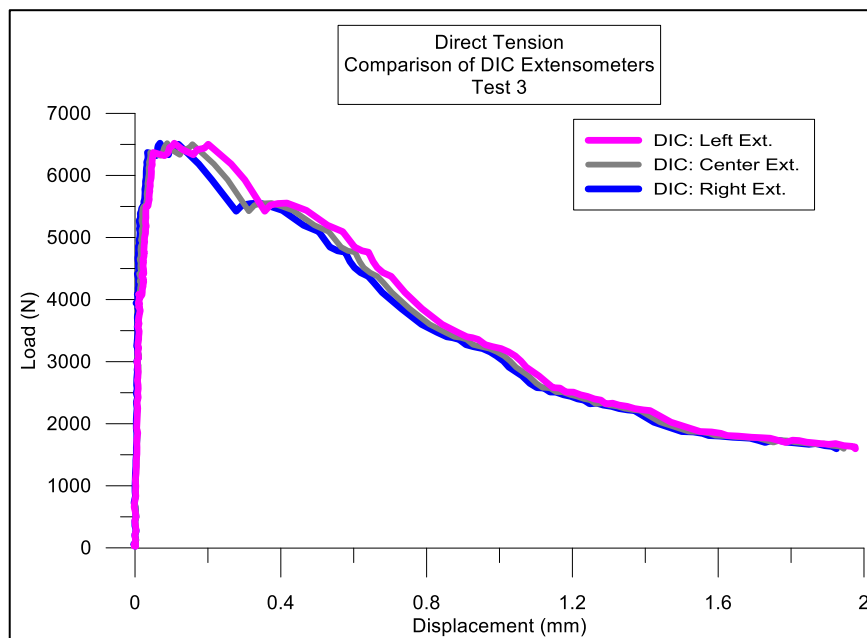


Figure 4.34 Comparison of the load vs displacement responses of the left, center and right DIC extensometers

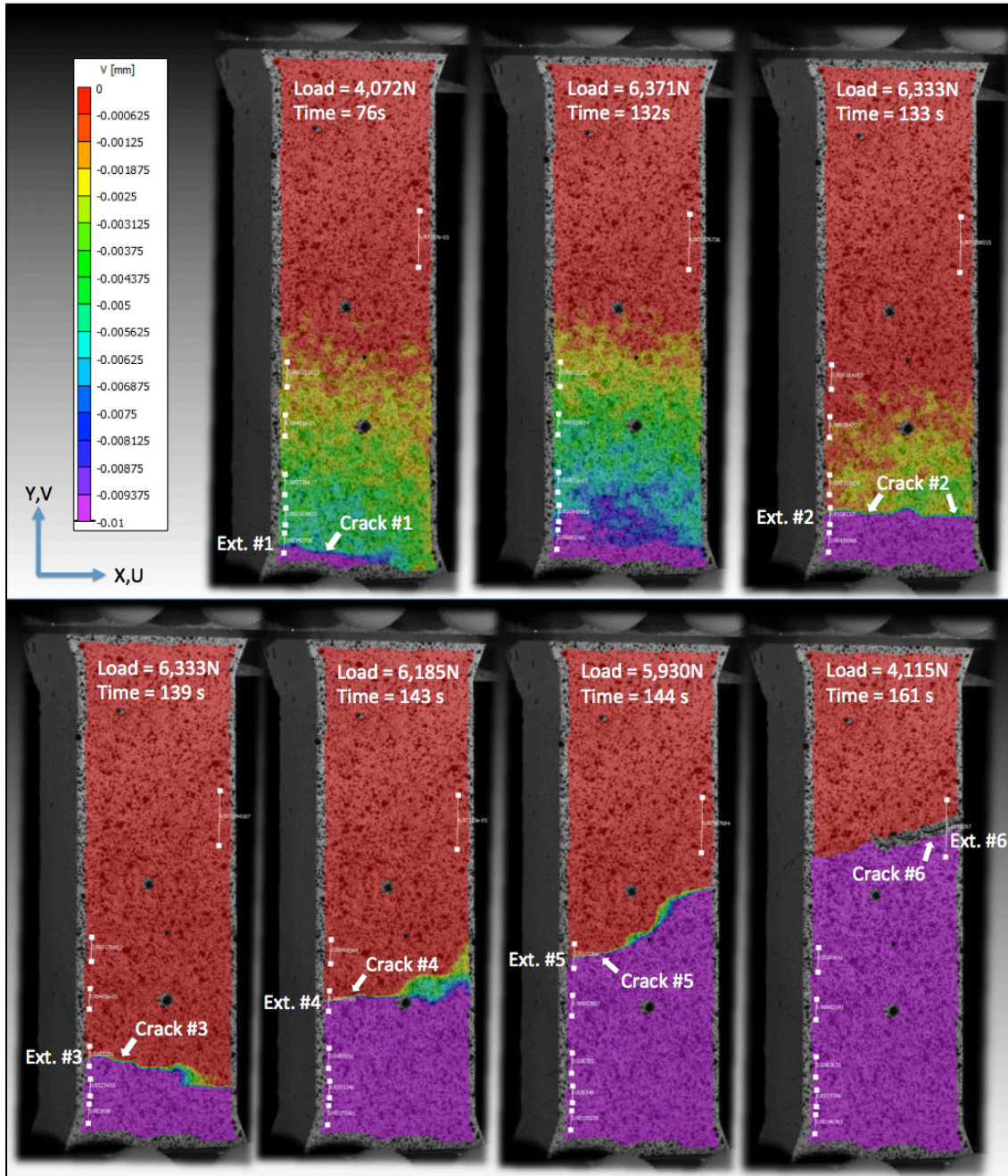


Figure 4.35 DIC displacement contours along the Y-axis identifying microcracks in test 3

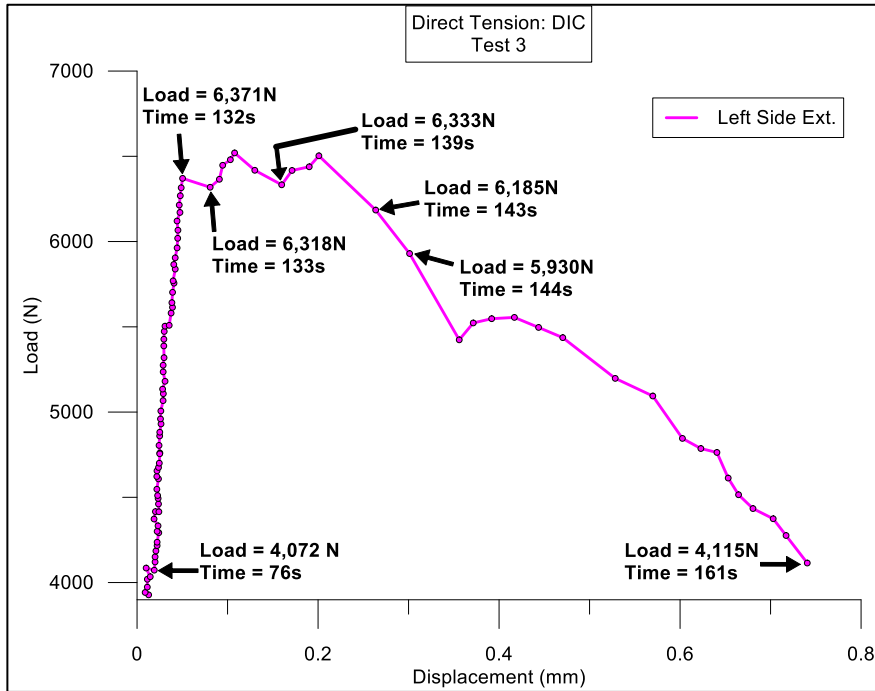


Figure 4.36 Load vs displacement plot showing the location of microcracks identified by the DIC extensometer displacement gradients shown as in Figure 4.35

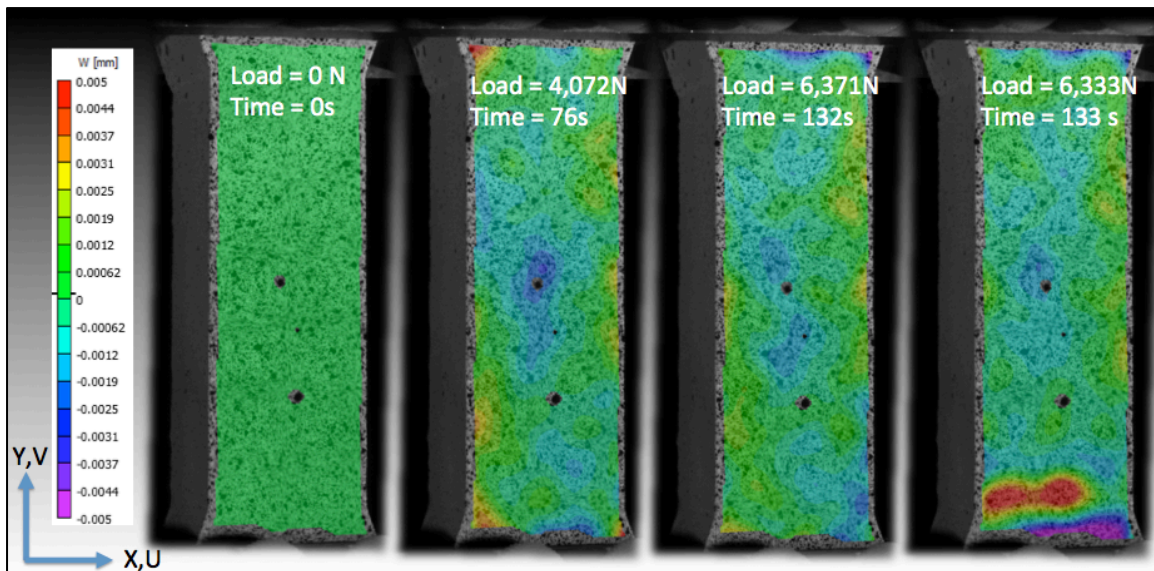


Figure 4.37 DIC displacement contours along the Z-axis to determine if flexure occurred about the X-axis in test 3

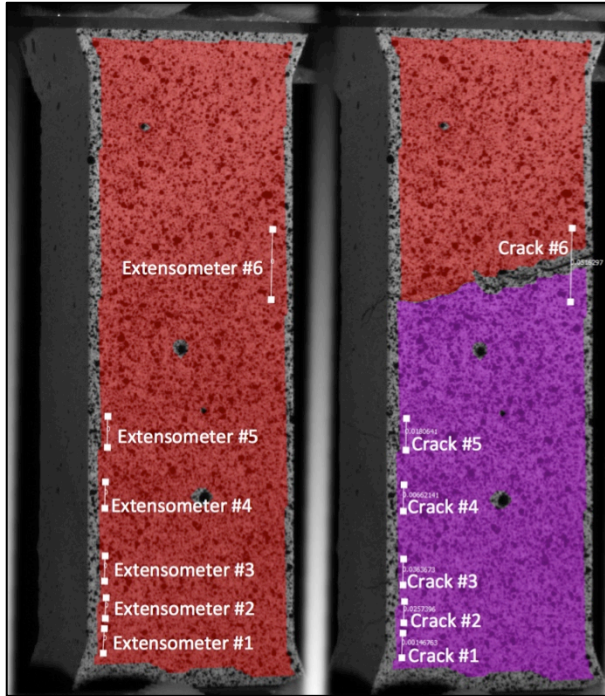


Figure 4.38 Location of DIC extensometers to evaluate crack opening displacements

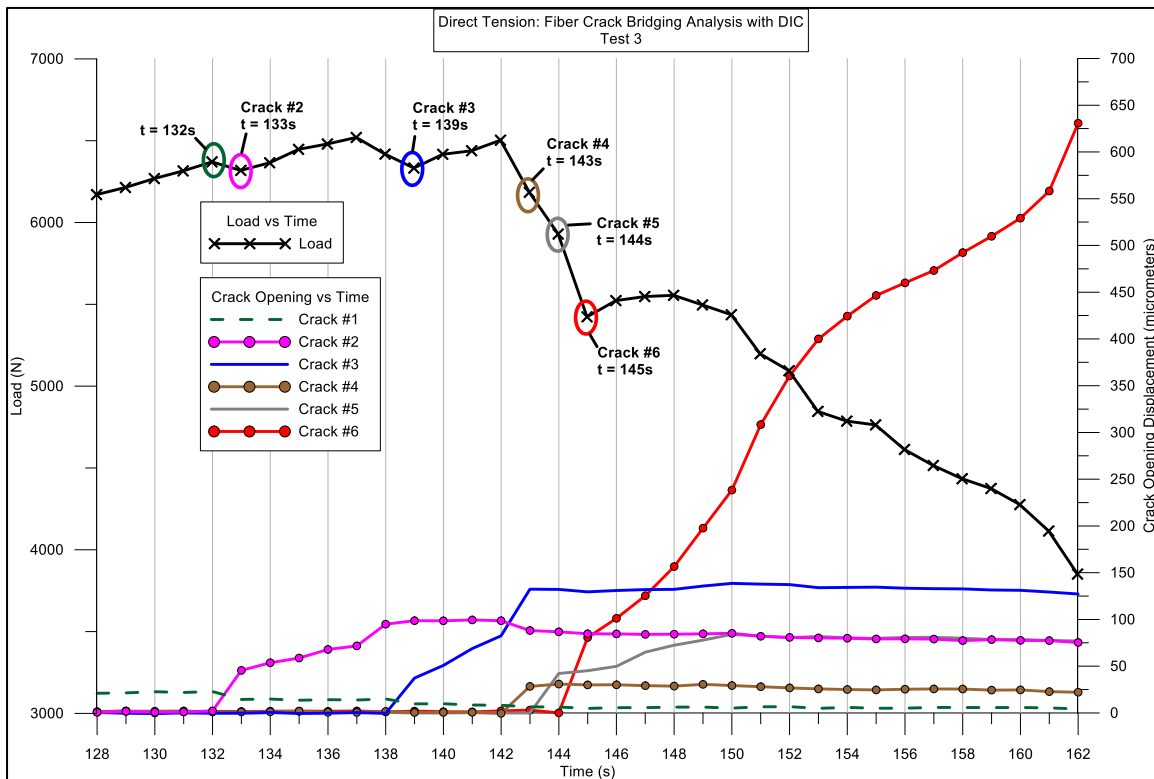


Figure 4.39 Load vs time and crack opening displacement vs time to evaluate fiber crack bridging in test 3

4.5 Summary and Conclusions

A series of experiments were conducted on the “P6S15W37” SCHSC mixture. The pressure-volume response of the material was determined from hydrostatic compression tests with confining pressures reaching 400 MPa. The material reached approximately 13% volumetric strain before unloading the specimen. No visible exterior damage was observed. The pressure volume response was also determined from a UXC experiment. The material achieved a volumetric strain in excess of 15% under a mean normal stress of nearly 500 MPa with no visible exterior damage.

Multiple triaxial experiments were conducted on the SCHSC at the following levels of lateral confinement: 0 MPa, 10 MPa, 20 MPa, 50 MPa, 100 MPa, 200 MPa, 300 MPa and 400 MPa. The material response was reported as PSD versus axial, radial and volumetric strain. The triaxial data were also used to construct the failure points and surface for the material.

A DT experiment was designed and conducted on the SCHSC. Two independent experimental techniques were used to evaluate load versus displacement response of the material. DIC was used to identify any eccentric loads that may result in flexure. DIC was also used to identify multiple microcracks in the specimen and to evaluate the crack bridging capability of the fiber. Data was presented that showed: 1) when a microcrack was initiated during the test, 2) value of load that caused the microcrack, 3) location and shape of the microcrack, 4) the variation of crack opening displacement throughout the test.

The conclusions about the characteristics of the new SCHSC material “P6S15W37” can be summarized as below:

- The elastic bulk modulus “K” was calculated to be 11.6 GPa.
- Young’s modulus “E” was calculated to be 22.6 GPa.
- The shear modulus “G” was calculated to be 13.6 GPa.
- The constrained modulus “M” was calculated to be 24.2 GPa.
- Poisson’s ratio “ν” was determined to be approximately 0.18.
- After the initial elastic phase of hydrostatic compression, the specimen entered the second phase indicating the presence of compression cracking and initial breakdown within the microstructure. As the curvature of the pressure-volume curve shifts from being concave towards the strain axis to being concave towards the stress axis, the material is entering the third phase. As presented in preceding sections, this change in curvature indicates sliding along internal cracks in the microstructure. The vessel capacity for this experiment was 400 MPa, therefore, the pressure was maintained at this level during this third phase, and then slowly decreased to unload the specimen. As a result, it is believed that the specimen did not undergo the fourth phase of microstructural changes. No visible evidence of damage on the exterior, and the lack of increase in slope of the pressure-volume curve also support this belief.
- The average unconfined compressive strength was 73.7 MPa with a standard deviation of 7.0. Densities for the specimens used for the unconfined compression experiment also varied significantly more than any other specimens used in the experimental series. Densities for these specimens varied from 1.998 Mg/mm³ (124.7 lb/ft³) to 2.129 Mg/mm³ (132.9 lb/ft³). The

high level of powder HRWRA is believed to be a major contributor to this variation. At the time of testing for the experiments in this chapter and subsequent chapters, the mix design for this material was not fully optimized; therefore, P6S15W37 is not the fully optimized mix. Refinement of the mixture to decrease the amount of HRWRA would likely improve the material and reduce variation.

- For tensile strength, the first crack occurred at 6.4 MPa. The fiber bridged the initial two cracks achieving an ultimate (nominal) tensile strength of 10.1 MPa.
- In all three DT experiments, the fibers were able to successfully bridge multiple cracks before ultimately pulling out with subsequent softening in the load versus displacement response.
- The material shear response was significantly different when the confining pressure was 50 MPa or above. The material had a clear transition from a brittle failure to a ductile failure with 50 MPa or more lateral confinement. This is clearly seen when looking at the PSD versus radial strain plots and the final shape of the deformed specimens.
- The shear strength did not exceed 300 MPa. This upper limit of 300 MPa does not appear to increase when the confining pressure is increased beyond 200 MPa.

CHAPTER 5

HIGH-STRAIN RATE RESPONSE OF A SCHSC

5.1 Background and Introduction

The development of a SCHSC was presented in Chapter 3. The material formula was optimized for quasi-static loads. Chapter 4 characterized the quasi-static pressure-volume response and deviatoric response at increasing levels of lateral confinement. The tensile properties were also investigated in Chapter 4. Given the intended use of the new SCHSC, it is important to understand the material response to dynamic loads and rate sensitivity. This chapter presents an investigation of a new pulse shaping experimental technique to determine the response of this material to dynamic compression. The high-strain rate response of SCHSC material “P6S15W37” covered in Chapter 3 is being considered in this Chapter.

Kolsky Compression Bar

A Kolsky bar (also known as split Hopkinson pressure bar) is an instrumented device used to characterize the dynamic response of materials under uniaxial stress loading conditions. John Hopkinson first introduced a crude version of the technique in 1872. Bertram Hopkinson (son of John Hopkinson) improved the method in the early 1900's, and Harry Kolsky significantly enhanced the compression version of the experiment in 1949. The technique is based on one-dimensional stress wave theory in elastic solids. A schematic of a typical Kolsky compression bar is shown in Figure 5.1.

The device is comprised of a gas gun, striker bar, incident bar, transmission bar and an instrumentation system to collect the data. The bars are typically machined from very high strength materials (e.g., maraging steel: yield strength = 1900MPa) to extremely high tolerances. In general, the gas gun-driven striker bar impacts one end of the incident bar (through proper pulse shaping) to generate an incident pulse that travels to the opposite end of the incident bar and loads the specimen bearing against it at a high strain rate. As the specimen undergoes loading, part of the input energy is reflected back while the rest is transmitted through the specimen into the transmission bar. Strain gages mounted on the incident and transmission bars record the strain wave histories, which can be used to calculate specimen stress and strain. Adjustments can be made to the loading conditions (i.e., pulse shaper geometry, the striker bar length and striker bar velocity) to capture the material stress-strain response at multiple high-strain rates.

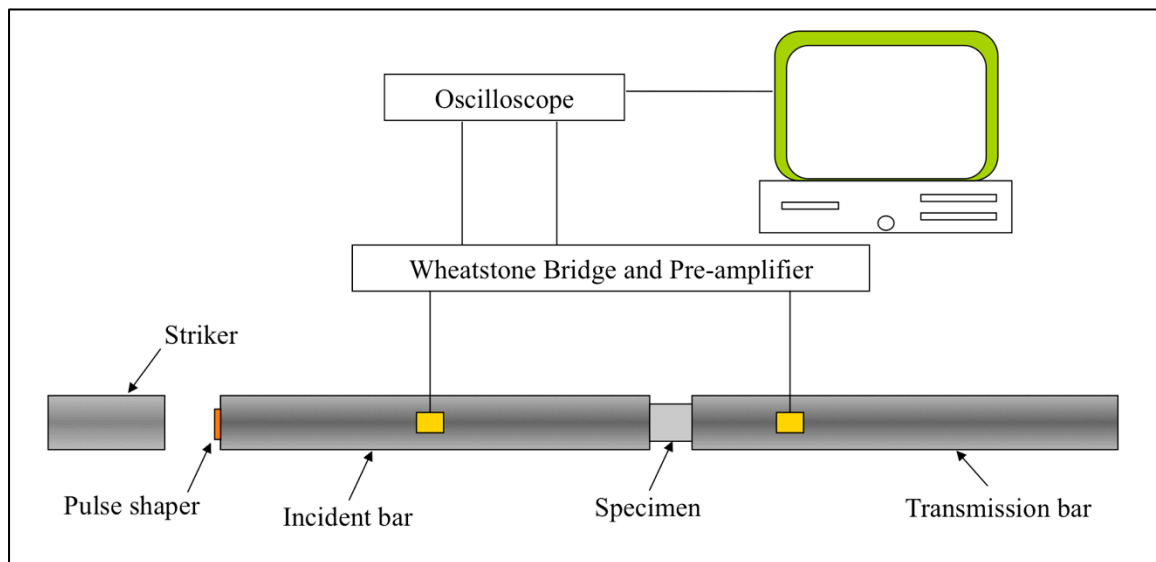


Figure 5.1 Schematic of a Kolsky compression bar to characterize high-strain response of a specimen

The stress-strain behavior of a material at high-strain rates can be determined by using one-dimensional stress wave propagation theory in a long rod. The fundamental assumption is that the bars are homogeneous, isotropic, remain linearly elastic and is dispersion free. The assumptions imply that the axial stress distribution is uniform over the entire cross section, and that the pulse measured at the strain gage locations of the incident and transmission bars are representative of the pulse at the specimen and bar interfaces. The equations for analyzing Kolsky bar data can be established by examining a differential element of the bar with an applied dynamic stress, σ , as shown in Figure 5.2

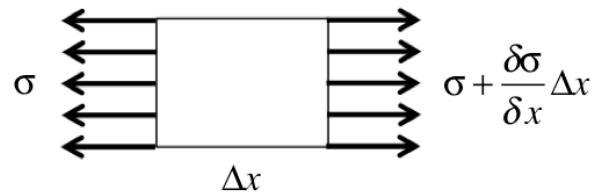


Figure 5.2 Differential element with an applied dynamic stress

The equation of motion in the x-direction is given by equation (9):

$$-\sigma A + \left(\sigma + \frac{\partial \sigma}{\partial x} \Delta x \right) A = \rho A \Delta x \frac{\partial^2 u}{\partial t^2} \quad (9)$$

Where:

A = cross-sectional area of the bar

P = density of the bar

u = displacement of the bar

Equation (9) reduces to:

$$\frac{\partial \sigma}{\partial x} = \rho \frac{\partial^2 u}{\partial t^2} \quad (10)$$

Since the bar is not stressed beyond elastic limit, Hooke's law is used.

$$\sigma = E\varepsilon \quad (11)$$

Where:

E = Young's Modulus

ε = axial strain, as shown in equation (12)

$$\varepsilon = \frac{\partial u}{\partial x} \quad (12)$$

Substituting equation (12) into equation (10) yields equation (13)

$$\frac{\partial}{\partial x} \left(E \frac{\partial u}{\partial x} \right) = \rho \frac{\partial^2 u}{\partial t^2} \quad (13)$$

Where:

ρ = density of the bar material

Since the bar is homogeneous and “ E ” and “ ρ ” do not vary along the length, equation

(13) can be written as:

$$\frac{\partial^2 u}{\partial x^2} = \frac{1}{c_o^2} \frac{\partial^2 u}{\partial t^2} \quad (14)$$

Where:

c_o = wave speed of the bar

Wave speed is given by equation (15)

$$c_o = \sqrt{\frac{E}{\rho}} \quad (15)$$

The 2nd order partial differential equation given in equation (14) can be used to analyze one-dimensional motions in an elastic bar. Using D'Alembert's method, the solution of equation (14) is given by equations (16) and (17).

$$u_1(x,t) = f(x - c_o t) + g(x + c_o t) \quad (16)$$

$$u_2(x,t) = h(x - c_o t) \quad (17)$$

Where:

u_1 = displacements in the incident bar

u_2 = displacements in the transmission bar

In equations (16) and (17), “ f ” and “ h ” are arbitrary functions for a wave traveling in the positive “ x ” direction and “ g ” is an arbitrary function for a wave traveling in the opposite direction. Therefore, the equations can be viewed as follows, where the subscripts “ i ”, “ r ”, and “ t ” represent “*incident*”, “*reflected*” and “*transmission*”, respectively.

$$u_1(x,t) = f(x - c_o t) + g(x + c_o t) = u_i + u_r \quad (18)$$

$$u_2(x,t) = h(x - c_o t) = u_t \quad (19)$$

Differentiating equations (18) and (19) with respect to “ x ” gives strain in the incident bar and transmission bar and is shown as equations (20) and (21).

$$\frac{\partial u_1}{\partial x} = f'(x + c_o t) + g'(x - c_o t) = \epsilon_r + \epsilon_i \quad (20)$$

$$\frac{\partial u_2}{\partial x} = h'(x + c_o t) = \epsilon_t \quad (21)$$

Similarly, differentiating equations (18) and (19) with respect to time gives bar particle velocities.

$$v_1 = \frac{\partial u_1}{\partial t} = -c_o f'(x - c_o t) + c_o g'(x + c_o t) = c_o (\epsilon_r - \epsilon_i) \quad (22)$$

$$v_2 = \frac{\partial u_2}{\partial t} = -c_o h'(x - c_o t) = -c_o (\epsilon_t) \quad (23)$$

Given the assumption that the bars are dispersion free, equations (22) and (23) would give velocities at any location of the bar. Therefore, velocities at the interfaces of the incident bar and specimen, and the specimen and transmission bar can as well be calculated from equations (22) and (23). For a specimen undergoing homogeneous deformation, the average engineering strain rate in the specimen can be given by:

$$\dot{\varepsilon}_s = \frac{v_1 - v_2}{l_s} \quad (24)$$

Where:

$$l_s = \text{initial length of the specimen}$$

Substituting equations (22) and (23) into equation (24) gives:

$$\dot{\varepsilon}_s = \frac{c_o}{l_s} (-\varepsilon_i + \varepsilon_r + \varepsilon_t) \quad (25)$$

By definition, the stresses at each end of the bar segments are given as:

$$\sigma_1 = \frac{A}{A_s} E (\varepsilon_i + \varepsilon_r) \quad (26)$$

$$\sigma_2 = \frac{A}{A_s} E \varepsilon_t \quad (27)$$

Where:

$$A_s = \text{area of the specimen}$$

$$\sigma_1 = \text{stress in the specimen (incident bar side)}$$

$$\sigma_2 = \text{stress in the specimen (transmission bar side)}$$

A fundamental assumption for Kolsky bar experiments is that the specimen is in a state of stress equilibrium. In reality, stress equilibrium is achieved after an initial “ringing up” of the specimen. The “ringing up” period occurs as the stress wave

propagates through the specimen until the specimen is deforming uniformly. The duration is dependent upon the wave speed and length of the specimen. For brittle materials that fracture after undergoing only small amounts of strain (i.e., less than 1%), the “ringing up” period and shortened duration of strain prior to fracture, complicate achieving a reasonable duration of constant strain-rate while in a state of stress equilibrium. Because of this, a technique to manipulate the shape of the incident pulse aids to achieve a constant strain rate in the specimen. This technique is called “pulse shaping” and is treated thoroughly in this chapter. If stress equilibrium is assumed, then equations (26) and (27) give:

$$\varepsilon_t = \varepsilon_i + \varepsilon_r \quad (28)$$

Substituting equation (28) into equation (25):

$$\dot{\varepsilon}_s = 2 \frac{C_0}{l_s} \varepsilon_r \quad (29)$$

Integrating equation (29) gives strain in the specimen as a function of the reflected wave in the incident bar, thus equation (30) is given as:

$$\varepsilon_s = 2 \frac{C_0}{l_s} \int_0^t \varepsilon_r \quad (30)$$

Again, if the bars are assumed to be non-dispersive, then equation (27) gives the stress in the specimen as a function of the transmitted strain pulse:

$$\sigma_s = E \frac{A}{A_s} \varepsilon_t \quad (31)$$

Thus, equations (29), (30) and (31) are the primary equations used to determine the strain rate and stress-strain response of a specimen using the Kolsky bar experimental technique. It is important to make a few observations from these equations that are

helpful while observing raw data collected from the experiments, prior to reducing the data:

- The shape of the reflected strain wave in the incident bar is an indicator of the strain rate history of the specimen. A constant value observed in the reflected strain wave will suggest that a constant strain rate was successfully achieved in the specimen.
- The profile of the strain wave in the transmission bar is an indicator of the stress history of the specimen.

The purpose of a Kolsky bar experiment is to establish the stress-strain response of a material at various constant strain rates. Since the experimental technique does not involve a closed-loop feed-back control monitoring system for real-time adjustments of loading conditions like quasi-static experiments that are either “load control” or “displacement control”, the Kolsky bar technique is a trial and error process. In other words, the loading conditions to achieve the desired strain rate are dependent up the specimen response, which is initially unknown. This is true for a quasi-static experiment; however, the quasi-static load conditions are adjusted as the material responds via the closed-loop feed-back control monitoring system. This isn’t possible for a dynamic open-loop experiment. Further, if the unknown specimen response is also varying between specimens due to material heterogeneity, the iterative process and selection of the loading conditions becomes quite tedious. The process is further obfuscated by the brittle nature of concrete, which complicates achieving a constant strain rate during the shortened duration of stress equilibrium. The striker velocity (determined by the tank

pressure used to launch the striker), duration of the incident pulse (determined by the length of the striker bar) and the infinite options of pulse shaper material properties and geometry, are variables that establish the loading conditions for each experiment. The following sections present the investigation to establish the proper loading conditions and to identify the correct material stress-strain response at multiple strain rates with repeatability.

5.2 Experimental Procedure

High-strength steel bars (stainless steel PH-13-8 Mo, H1000 condition: $E = 203.62 \text{ GPa}$, $\rho = 7817 \text{ kg/m}^3$) with a 50mm diameter were used to characterize the SCHSC specimens. The incident and transmission bars were 3.657m and 3.352m long, respectively. High-pressure MoS_2 paste lubricant was applied at the specimen-bar interfaces to reduce the friction induced at the specimen ends. Air bushings were used in lieu of conventional brass bearings to reduce the friction experienced by the bars while in motion. The experimental setup is shown in Figure 5.3

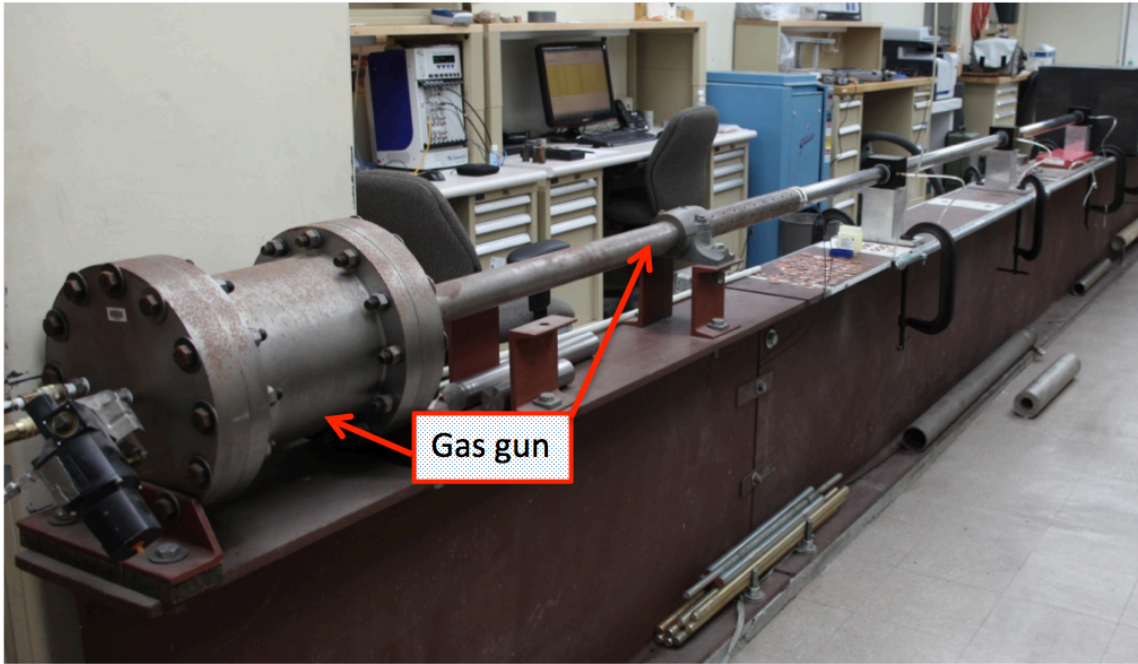
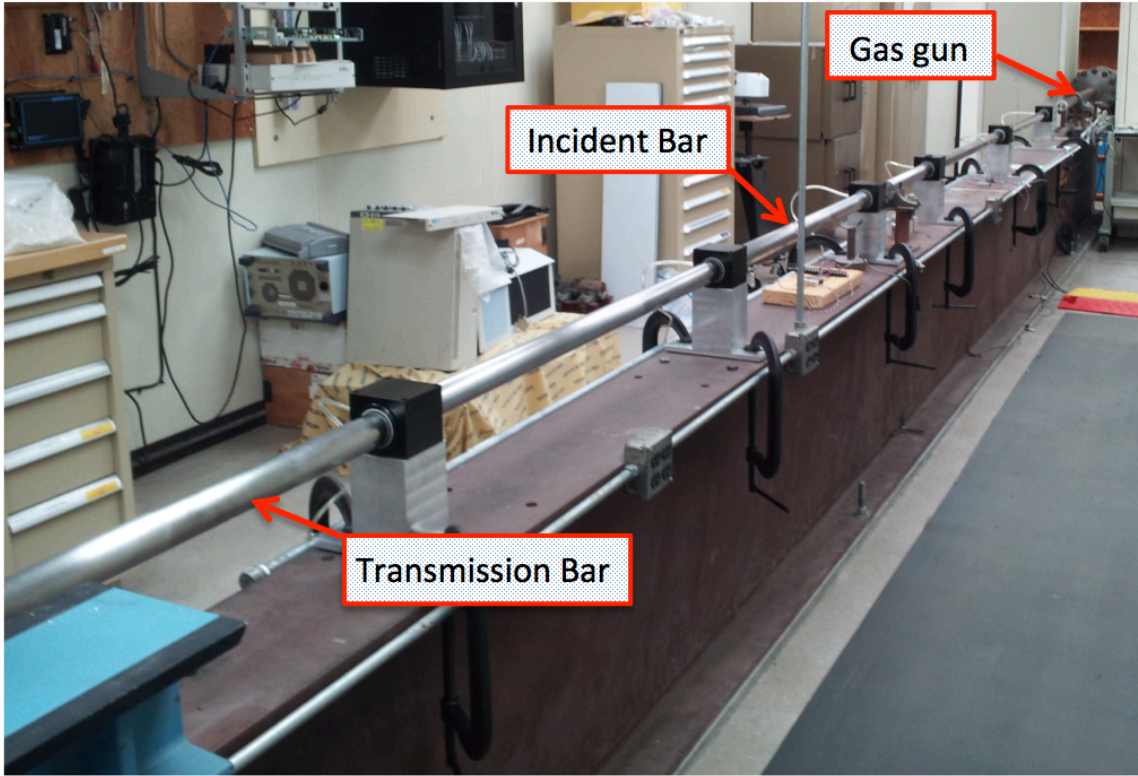


Figure 5.3 Gas gun and 50mm diameter Kolsky incident and transmission bars

5.3 Pulse Shaping Technique

5.3.1 Radial Inertia in Pulse Shapers

The Kolsky bar pulse shaping technique for brittle materials has been developed and extensively practiced over the past two decades [121-129]. The effectiveness of applying this technique to different materials is mainly evaluated by two criteria: (i) dynamic stress equilibrium and (ii) constant strain rate deformation of the specimen. To satisfy these two criteria in Kolsky bar experiments on brittle materials, a linear loading pulse is needed given the linear elastic nature of these materials [123]. Such a pulse can be realized with reasonable repeatability by using a solid copper disk pulse shaper placed at the striking end of the bar. Examples of successful application of this technique have been reported in the literature [125-129], but are limited to relatively small diameter Kolsky bars.

However, most concretes exhibit substantial heterogeneity due to the various particle sizes of the raw materials, and the hydration process that introduces uncertainty due to the underlying chemical reaction that yields the final hardened material. To obtain a representative volume, and thus minimize fluctuations of experimental data, large size specimens are usually desired for mechanical characterization. For this reason, the diameter of the Kolsky bars also need to be increased to accommodate the large size concrete specimens. For pulse shaping, an intuitive approach is to apply the current proven method for a small diameter Kolsky bar, but to linearly scale up the diameter of the small pulse shapers (which have proved to produce nice linear incident waves) with

the same proportion of the bar diameters. However, the increase of bar diameter also results in decrease of cutoff frequency, f_c , of a long bar as evident from Equation (32).

$$f_c = 0.3 \frac{\sqrt{2}C}{2\pi R_o \nu} \quad (32)$$

Where:

f_c = cutoff frequency for the bar

C = wave speed for the bar

R_o = radius of the bar

ν = Poisson's ratio

A large diameter bar, due to the 3D inertia effects, may not properly respond to incident waves with components over this cutoff frequency. The calculated cutoff frequency for a 50mm diameter steel bar is approximately 25kHz, which is higher than the frequency (5kHz) of a typical linear incident wave required for high-rate brittle materials characterization on Kolsky bars [129]. Therefore, through proper pulse shaping it may be possible to achieve the desired loading profile for concrete on a 50mm diameter Kolsky bar.

Figure 5.4 shows a typical incident waveform obtained on the 50mm Kolsky compression bar with a solid copper disk pulse shaper of 25mm diameter and 1.5mm thickness. The pulse shaper dimensions as well as the striker impact velocity were carefully designed according to the previous brittle material test results from smaller Kolsky bars. It is evident that the incident pulse does not exhibit a triangular waveform as expected. Instead, there are low frequency oscillations in the wave throughout the entire duration. To investigate whether the oscillations were introduced by the experimental setup itself, the pulse shaper was reduced to a 9mm diameter, which is

identical to what has been used by others for brittle material [129]. The corresponding incident waveform is shown in Figure 5.5. From this figure, it is clear that a linear incident wave was not achieved, which was expected because the pulse shaper dimension was excessively small compared to the 50mm diameter Kolsky bar. However, no low frequency oscillations were observed on the waveform compared to Figure 5.4. This suggests that the undesirable oscillations on the incident pulse may have been introduced by increasing the pulse shaper diameter. To obtain quantitative pulse shaper deformation information for further analysis, the 25mm diameter by 1.5mm thick pulse shaper was placed in the specimen gage segment between the incident and transmission bars. The purpose of treating the pulse shaper for a test specimen was to record the stress (transmitted wave) and strain rate (reflected wave) histories for further calculations. An incident pulse, directly generated by striker impact without using any pulse shaper at the impact interface, loaded the pulse shaper specimen. The associated specimen stress and strain rate histories are shown in Figure 5.6. It can be observed from this figure that the oscillations on the stress history are similar to those of Figure 5.4. Also, the specimen strain rate is not constant, but rather shows a triangular shape with distinctive acceleration and deceleration slopes. The peak of the strain rate profile roughly corresponds to the peak-to-valley stress decrease on the specimen stress history curve. All of these findings point to one possibility- the oscillations in the incident wave are due to the effect of inertia in the pulse shaper. This has not been reported in any previous work related to pulse shaper design for Kolsky bar experiments.

The specimen inertia effect in Kolsky compression bar experiments has been studied by several authors including Kolsky himself [130-137]. There are two main

sources for generating inertia; the first is due to acceleration of specimen strain rate during the initial ramp-up process causing the specimen strain rate to increase from zero to a certain constant level. As the axial strain rate increases, the specimen radial expansion rate also accelerates which mobilizes extra force to overcome the inertia. This extra force appears in the form of radial confinement, which reflects in the axial direction as extra stress component in addition to the inherent material constitutive response. The other source is induced by large deformation. When the specimen deformation is sufficiently large, the radial expansion rate will keep increasing even when the axial strain rate remains constant to satisfy the volume conservation. Song et al. observed the explicit impact of inertia effects on experimental results on soft materials [138,139]. Most recently, Warren and Forrestal [136] proposed a continuum mechanics model with rigorous formulations to provide analytical estimation of this inertia-induced pressure in incompressible solid disk specimens. The inertia-induced stress is given by Equation (33).

$$\bar{p} = \frac{\rho a_0^2}{8(1-\varepsilon_x)^2} \ddot{\varepsilon}_x + \frac{3\rho a_0^2}{16(1-\varepsilon_x)^3} (\dot{\varepsilon}_x)^2 \quad (33)$$

Where:

\bar{p} = inertia induced pressure in axial and radial directions

ρ = density of the solid disk specimen

a_0 = initial radius of the solid disk specimen

ε_x = axial engineering strain of the specimen

$\dot{\varepsilon}_x$ = axial strain rate

$\ddot{\varepsilon}_x$ = axial strain rate acceleration

The first term in the equation describes the inertia induced by strain rate acceleration ($\ddot{\epsilon}_x$) in the specimen. This term usually reduces to zero while the specimen deformation reaches constant strain rate ($\ddot{\epsilon}_x = 0$). The second term in this equation is a function of strain rate ($\dot{\epsilon}_x$) and strain (ϵ_x), and increases quickly with accumulation of specimen strain even at constant strain rate. It is evident from this equation that the inertia stress is a function of specimen strain, strain rate, and strain rate acceleration. To assess if \bar{p} may have possibly caused the stress variation on the transmitted pulse, the inertia stress at the peak (point *a*) and valley (point *b*) of the oscillation are calculated and compared. Given $\rho = 9 \times 10^3 \text{ kg / m}^3$ and $a_o = 12.5 \text{ mm}$ for the solid disk copper pulse shaper and other parameters indicated on Figure 5.6, the calculated difference in \bar{p} is approximately -444 MPa between *a* and *b*. The negative sign indicates that the inertia induced axial stress has decreased between these two states, which qualitatively agrees with the drop in the stress history curve from points *a* to *b*. However the actual stress drop directly measured from the curve shows a value of only 270 MPa, which is smaller than the analytical results. One explanation for this difference is that while the pulse shaper specimen deforms from state *a* to *b*, the plastic strain increases from approximately 0.28 to 0.51. Therefore, it is possible that the specimen stress accumulated from strain hardening has compensated part of the pressure drop, which resulted in a reduced net axial stress decrease, as measured by the strain gages.

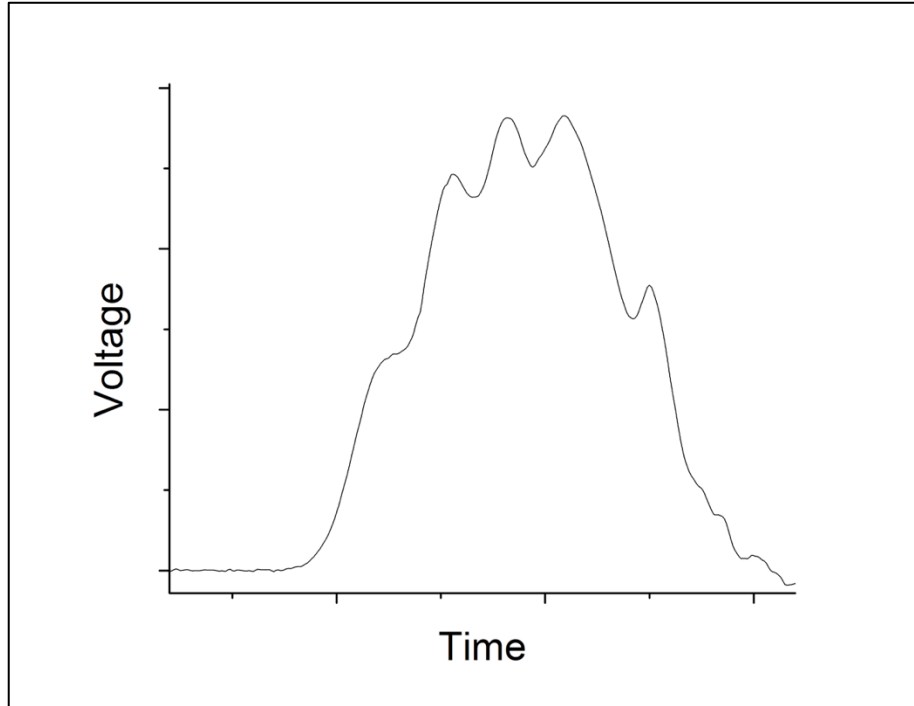


Figure 5.4 Typical incident pulse waveforms on a 50mm diameter Kolsky compression bar setup using a 25mm diameter solid copper pulse shaper

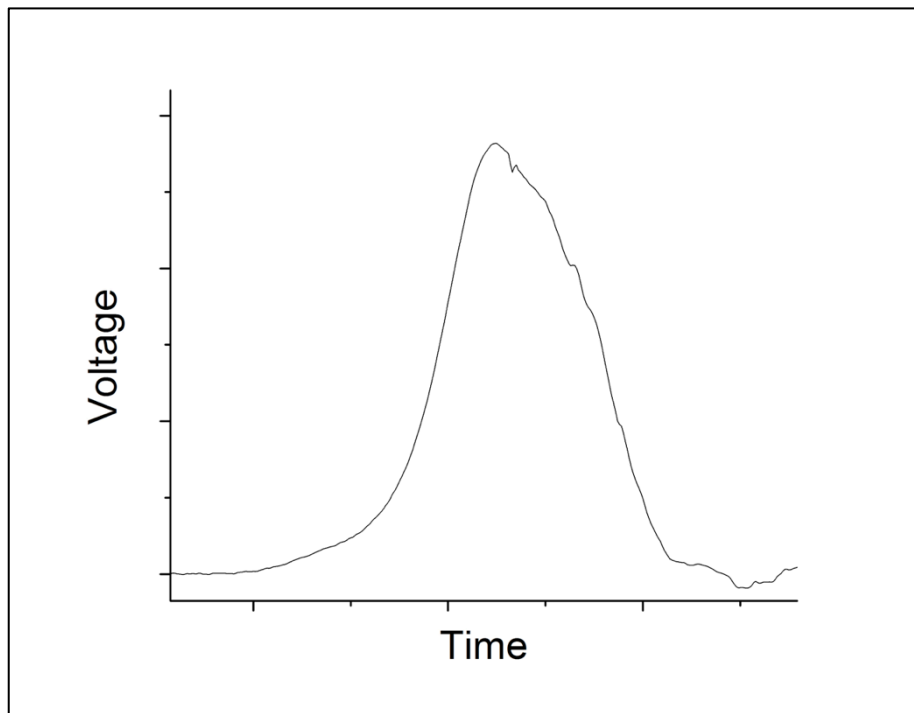


Figure 5.5 Typical incident pulse waveforms on a 50mm diameter Kolsky compression bar setup using a 9mm solid copper pulse shaper

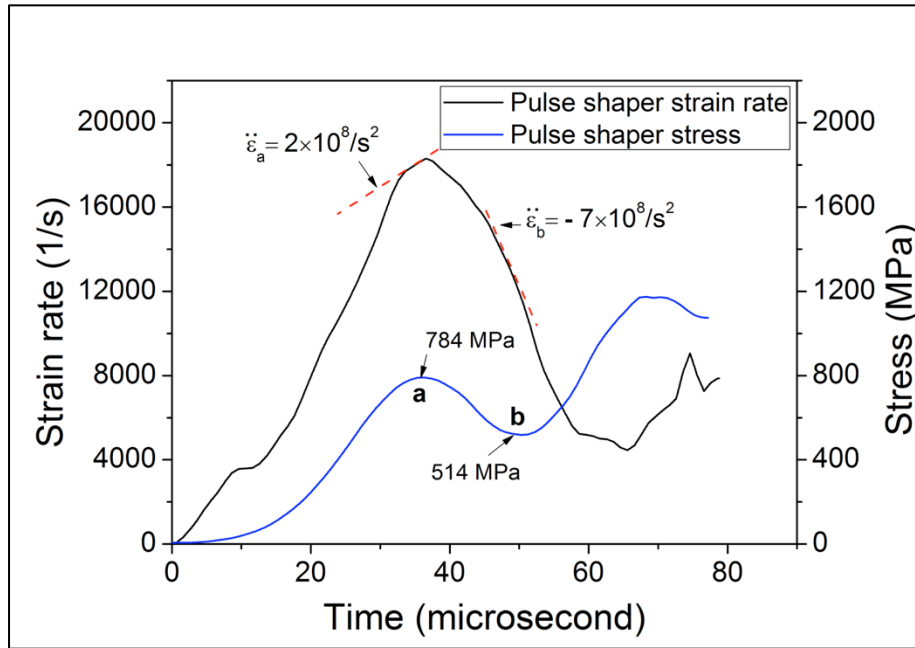


Figure 5.6 Stress and strain rate histories of the solid copper pulse shaper specimen

5.3.2 Annulus Pulse Shapers

Previous studies on high-rate compression testing of soft materials revealed similar radial inertia effects in soft disk specimens [138,139]. With the specimen, the distribution of this inertia pressure follows a parabolic function along the diameter. At the specimen center the pressure is highest, while at the circumference the pressure becomes zero due to a stress-free boundary conditions. Researchers extended this stress-free boundary condition to the specimen center by making washer type specimens, which substantially reduced the amplitude of the inertia pressure [138]. This same concept might be applied to design the pulse shaper for the 50mm Kolsky bar, reducing the pressure to a level that is negligible compared to the intrinsic response of the pulse shaper material. Equation (33) substantiates this argument, since inertial pressure also exists in small-diameter copper pulse shapers; however, the magnitude of this pressure is not high

enough to induce oscillations within the incident pulse. Based on this concept, an 1 mm diameter central hole was introduced to the 25 mm diameter solid copper pulse shaper. After adjusting for the proper striker velocity, a nearly linear incident pulse (free of oscillations) was produced as shown in Figure 5.7. To build on this approach, similar pressure reduction may also be achieved by using multiple small diameter copper shapers that have equivalent cross section area as the annulus pulse shaper. From a practical standpoint, evenly spacing multiple small shapers on the incident bar and ensuring even contact between the striker and each individual small pulse shaper during impact is a tedious and challenging task. Furthermore, the pulse from each small pulse shaper shall not overlap with its neighbors and thus interfere with the deformation; otherwise the quality of incident pulse may be affected adversely. Annulus pulse shaper offers a solution to reduce the inertia effect while avoiding any of these uncertainties. This technique has great potential and worth further exploring for large diameter Kolsky bar experiments for a variety of materials.

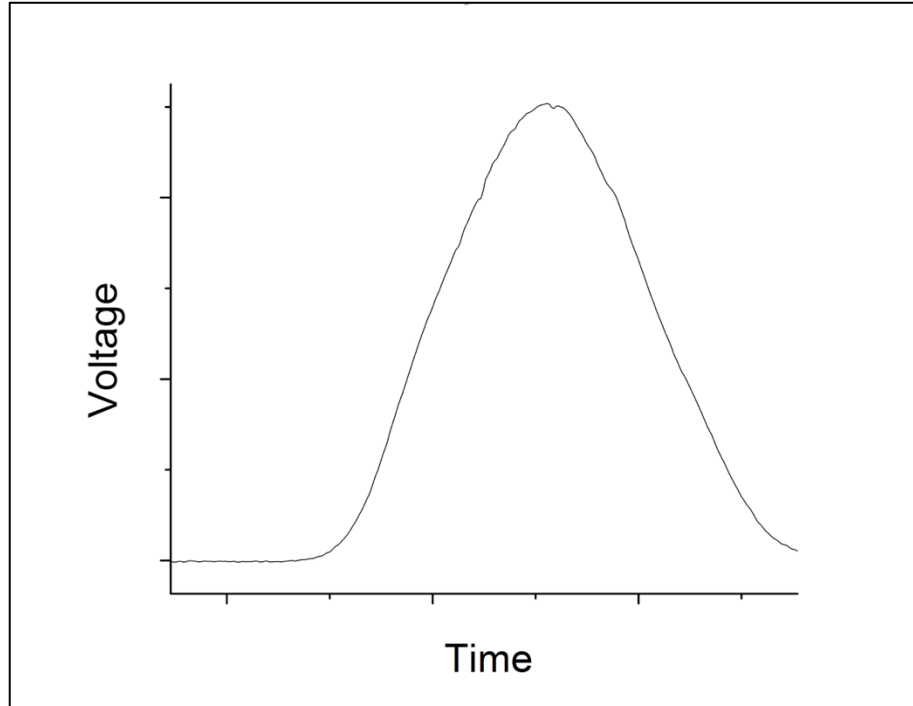


Figure 5.7 Linear incident pulse generated by annulus copper pulse shaper (O.D.=25mm, I.D.=11mm). Note that compared to Figure 5.4, the inertia induced oscillations are eliminated

5.4 Results

5.4.1 Mechanical Properties of SCHSC at High Rates

The effectiveness of the annulus pulse shapers were examined through Kolsky bar compression experiments on the SCHSC at two different rates. As described in previous sections, maintaining dynamic stress equilibrium and constant strain rate deformation in the specimens are two key factors for evaluating the validity of Kolsky bar experiments. For the characterization of brittle materials, these two factors become particularly important because the total specimen deformation before failure is typically very small ($\leq 1.0\%$), therefore such testing conditions need to be established within a relatively short period of time (typically less than $50\mu\text{s}$). For this reason, two sets of pulse shapers were

specifically designed to achieve 240s^{-1} and 100s^{-1} strain rates. Pulse shapers for the 240s^{-1} strain rate were annulus copper washers with a 25.4mm O.D., 14.4mm I.D. and thickness of 0.8mm. Shapers for 100s^{-1} strain rate had similar dimensions with a 25.4mm O.D., 15.9mm I.D. and thickness of 1mm. One slight modification introduced for the 100s^{-1} shapers was the addition of six small solid disk shapers with a 3.2mm diameter and 0.51mm thickness on top of the annulus shaper to further decrease the strain rate acceleration and avoid large fluctuations in strain rate prior to plateauing at the desired rate of 100s^{-1} . Figure 5.8 shows both the 240s^{-1} pulse shaper (top photo) and a 100s^{-1} pulse shaper (bottom photo) mounted on the incident bar prior to testing. Figures 5.9 and 5.10 show an example set of original experimental data for 100s^{-1} and 240s^{-1} . In these figures, plateaus are evident in the reflected waves indicating the specimens achieved constant strain-rate deformation prior to specimen failure that is indicated by the sharp increase in the strain-rate profile. In general, the total specimen deformation time before failure (up to the end of the constant strain rate region) increases from $60\mu\text{s}$ to $140\mu\text{s}$ as the strain rate decreases from 240s^{-1} to 100s^{-1} . It should be noted that the duration of constant strain-rate prior to failure is longer for the strain rate of 100s^{-1} .

As presented in the previous section, Equations (26) and (27) are used to calculate specimen stress on the specimen interfaces of the incident and transmission bars, respectively. With Equations (26) and (27) and the experimentally collected incident, reflected and transmitted wave signals, the dynamic stress histories of the SCHSC specimen on both ends can be calculated and compared. An example of such comparison at 240s^{-1} strain rate is shown in Figure 5.11. The two stress history curves agree with

each other reasonably well, indicating that the concrete specimen was under stress equilibrium during dynamic deformation.

Six concrete specimens were loaded by nearly identical incident pulses at each strain-rate under well-controlled experimental conditions. The stress-strain curves are summarized in Figure 5.12 with the results obtained under a quasi-static rate of 10^{-4}s^{-1} . Figure 5.13 shows the resulting strength increase factor versus strain rate. These results indicate a strong rate dependency in failure strength. At a strain-rate of 240s^{-1} , the maximum compressive strength is 220 MPa, approximately 3 times the quasi-static strength. Over the Kolsky bar strain rate regime (100s^{-1} to 240s^{-1}), the compressive strength also increased by 20%. The elastic modulus, however, does not exhibit noticeable strain rate sensitivity other than minor variations between specimens. These results are in agreement with previous studies on dynamic compressive response of a pure mortar [140]. The cited study revealed that the pure mortar did exhibit apparent strain rate sensitivity, but not until after 290s^{-1} , while in this case, the strength of the SCHSC has increased by a factor of three, from 10^{-4}s^{-1} to 240s^{-1} . In principle, the experimental data on SCHSC showed similar trends in strain-rate dependency as reported by other authors on concrete materials both in compression [140-143] and tension [144-147].

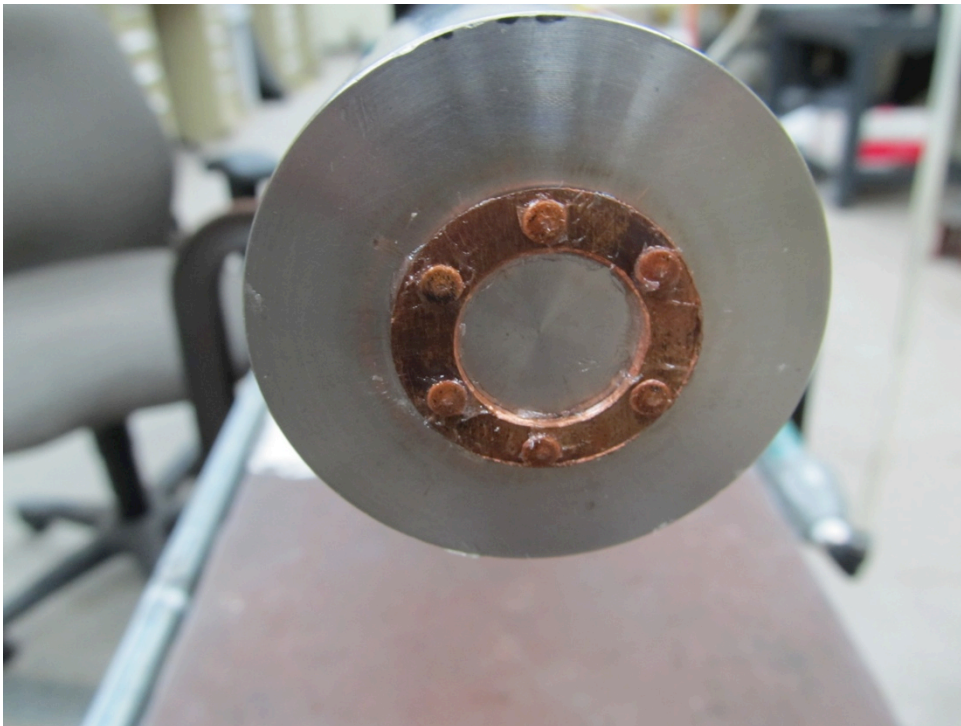
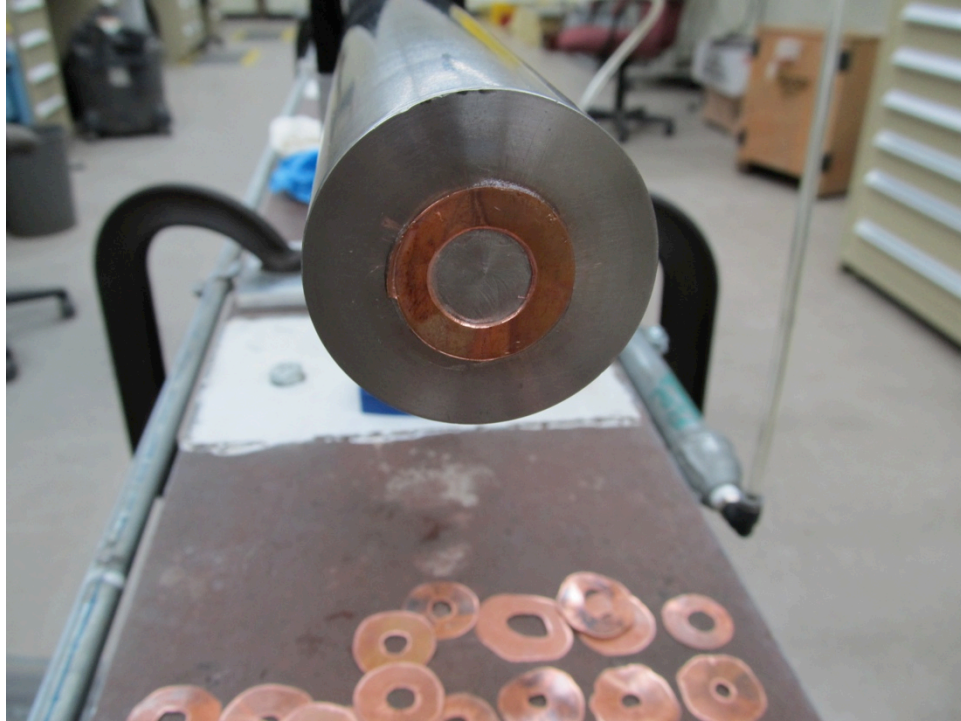


Figure 5.8 Pulse shaper mounted on impact face of incident bar (top) 240s^{-1} pulse shaper (bottom) 100s^{-1} pulse shaper

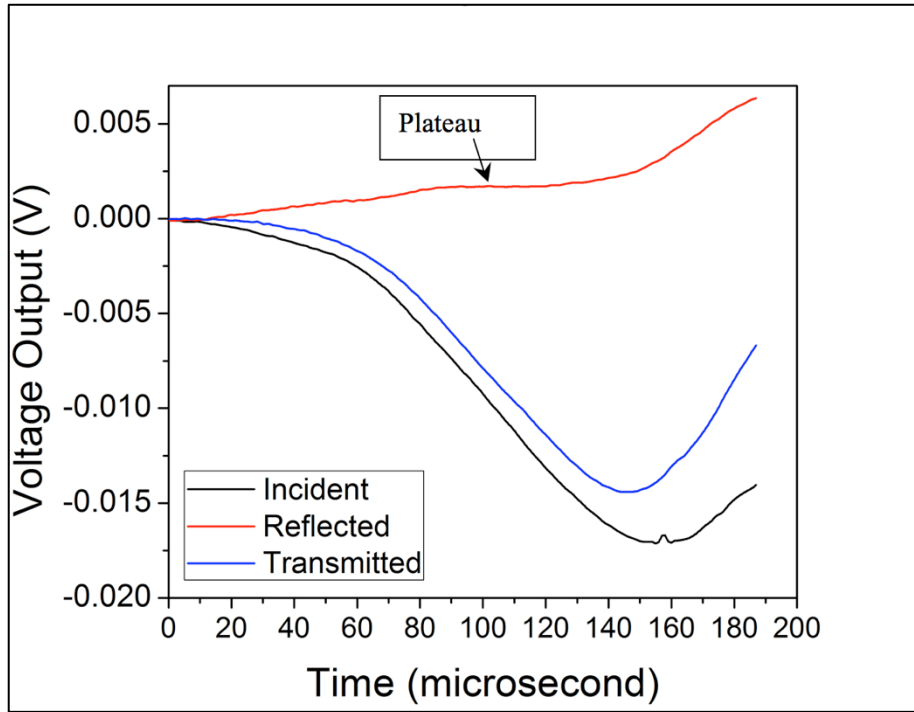


Figure 5.9 The original Kolsky bar stress waveforms collected from 100s^{-1} experiment

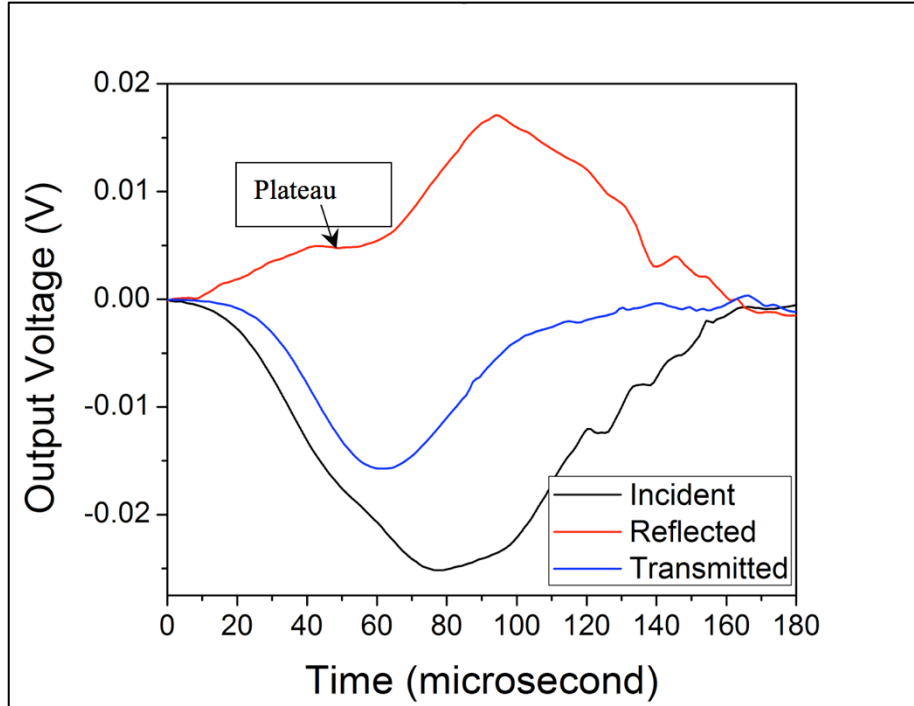


Figure 5.10 The original Kolsky bar stress waveforms collected from 240s^{-1} experiment

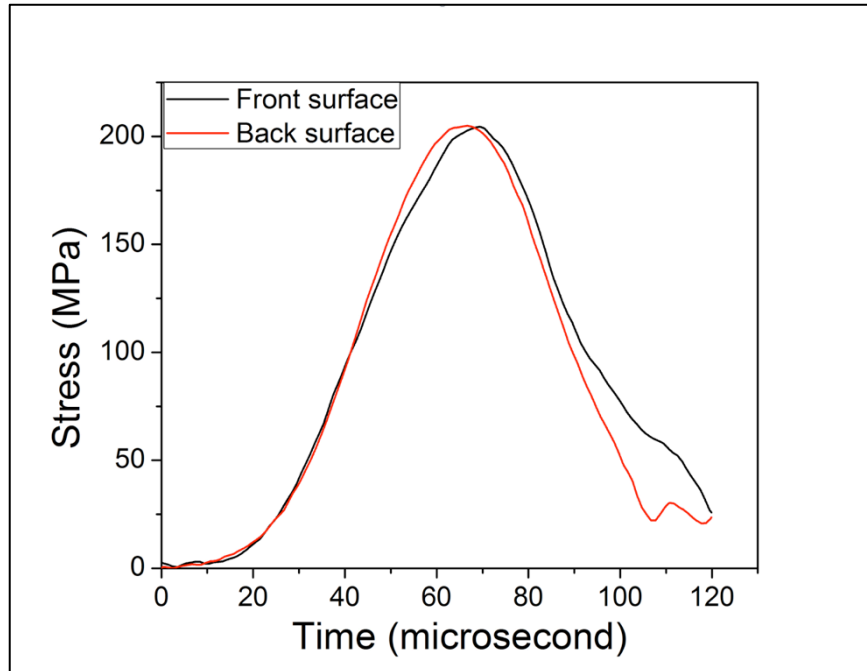


Figure 5.11 Dynamic stress equilibrium check at $240s^{-1}$

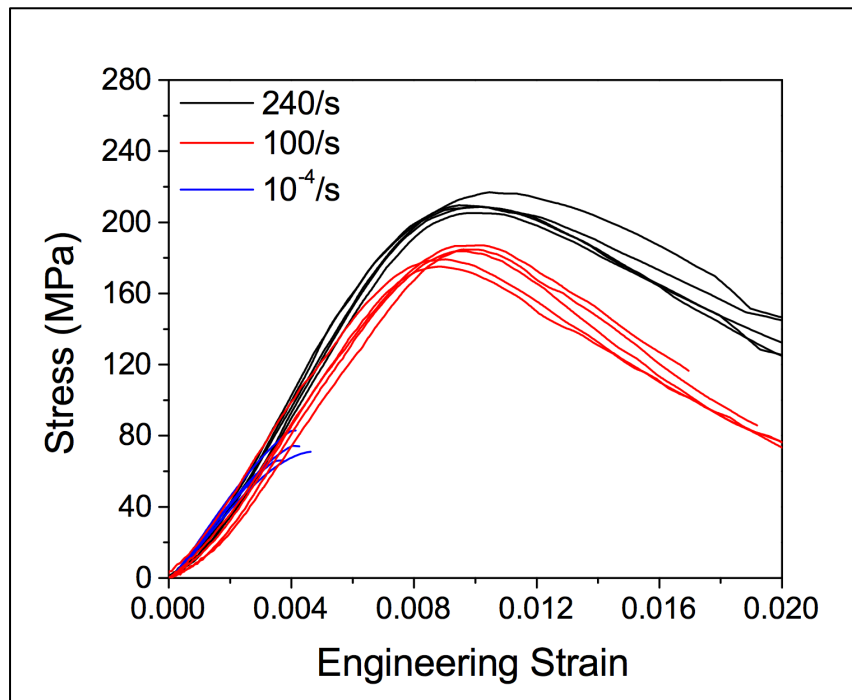


Figure 5.12 Engineering stress-strain curves for SCH516 under different strain rates

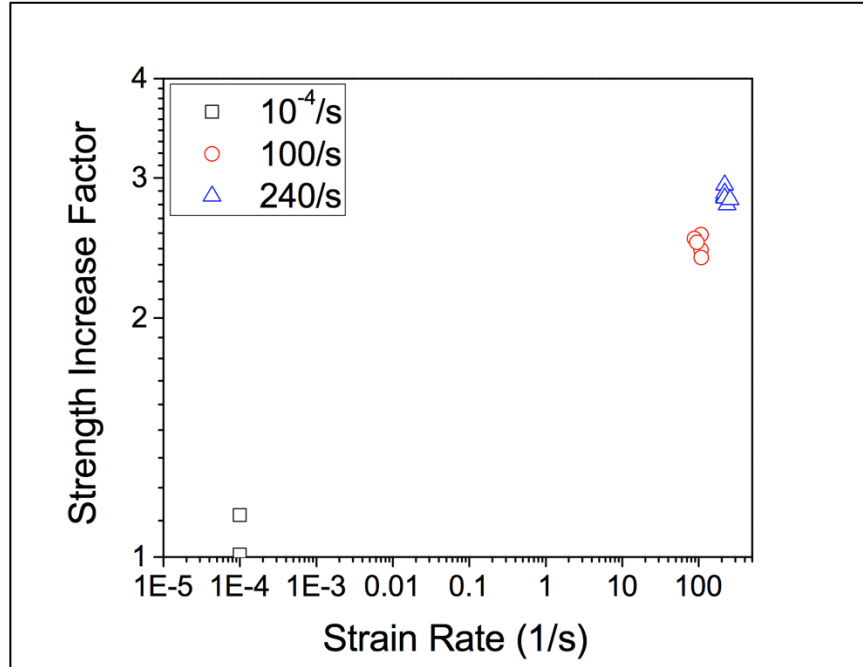


Figure 5.13 Strength increase factor for a given strain rate for the SCHSC

5.4.2 Effect of Specimen Inertia

According to equation (33), the inertia induced pressure in any deformable solid is a strong function of specimen radius a_0 . As the diameter of the concrete specimen increases, the specimen inertia may impose significant constraint in the radial direction (in addition to the extra axial stress component). Since concrete is a pressure sensitive material, the inertia in the specimen may play an important role in the failure strength enhancement and therefore needs to be carefully investigated. This possible effect on brittle material was studied by Li et al. [148] through numerical simulations. Forrestal et al. later presented a set of analytical solutions summarized in the following equations [135].

$$\sigma_r = \frac{\nu(3-2\nu)}{8(1-\nu)}(a^2 - r^2)\rho\ddot{\epsilon}_x \quad (34)$$

$$\sigma_x = \frac{\nu^2(3-2\nu)}{4(1-\nu)} \left[a^2 - \frac{2r^2}{3-2\nu} \right] \rho \ddot{\epsilon}_x \quad (35)$$

Where:

σ_r = inertia induced stress in the radial direction at location “ r ”

σ_x = inertia induced stress in the axial direction at location “ r ”

r = distance from specimen center to location of calculated stress

a_o = specimen radius

ν = Poisson’s ratio

Since brittle material fail at relatively small strains ($\leq 1\%$), equations (34) and (35) do not account for the inertia stress caused by large deformation as seen in the second term of equation (33). Equations (34) and (35) determine the strain rate acceleration induced inertia (the first term of equation (33)). From a physical point of view, σ_r is the radial confinement pressure acting on the specimen that varies with location along the radius. It is at a maximum at the center and zero at the surface. The axial confinement pressure “ σ_x ” also varies with location. To get the total stress in the axial direction, σ_x would be added to the axial stress calculated by Equation (31), which is measured experimentally.

Poisson’s ratio ($\nu = 0.18$) was determined in Chapter 4. The average density of the SCHSC Kolsky bar specimens is 2150 kg/m^3 ; the specimen radius is 25mm. The estimation of strain rate acceleration ($\ddot{\epsilon}_x$) can be made from a typical specimen strain rate history profile as shown in Figure 5.14. As seen in Figure 5.14, as specimen deformation reaches constant strain rate, the strain rate acceleration quickly reduces to zero. This indicates that the inertia induced confinement pressures are minimal before

the specimen starts to fracture. During the early stage of deformation, Figure 5.14 indicates that the strain rate acceleration is approximately $7.35 \times 10^6 \text{ s}^{-2}$. Substituting these numbers into equations (34) and (35) and then integrating equation (35) over the cross section area of the specimen yields:

$$\sigma_{r=0} = 0.7 \text{ MPa} \quad (36)$$

$$\int \sigma_x dA = 0.3 \text{ MPa} \quad (37)$$

The results indicate that even at the center of the specimen where σ_r is the maximum value, the magnitude of the confinement pressure is only 0.7 MPa. This is small enough not to induce any noticeable enhancement to the compressive strength. Compared to the average dynamic compressive strength of approximately 200MPa, the additional axial stress by inertia (0.3MPa) is also small enough to be neglected from the specimen stress.

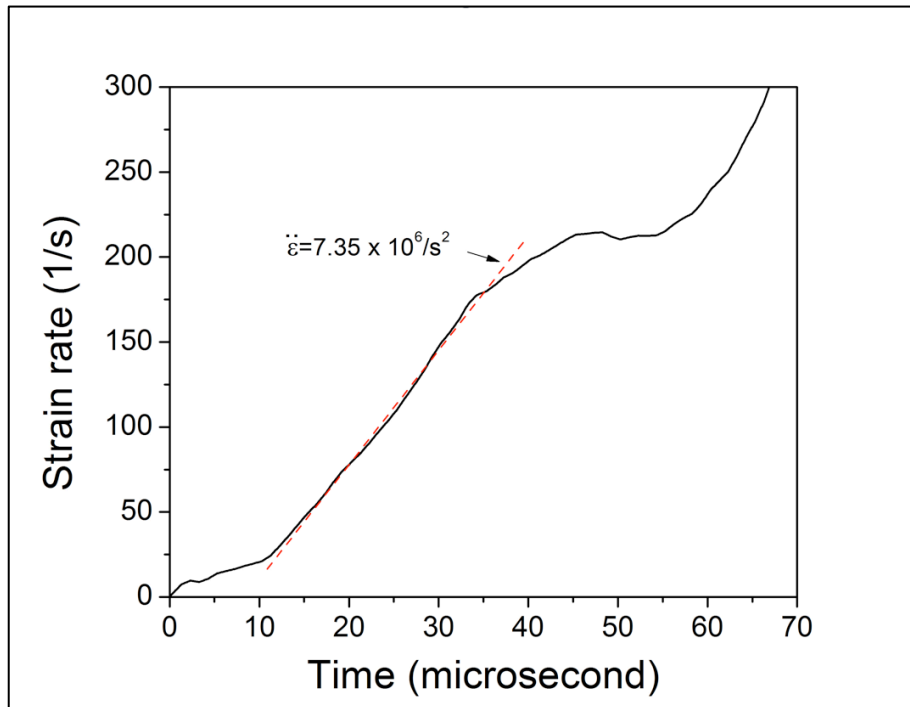


Figure 5.14 Strain rate acceleration for a typical SCHSC specimen

5.5 Summary and Conclusions

The main purpose of this study was to develop a viable pulse shaping technique for large-diameter Kolsky bar experiments on concrete materials, and to utilize the technique to determine the dynamic stress-strain response of the SCHSC at multiple strain rates. The previous pulse shaping technique for brittle materials were established with smaller diameter Kolsky bars and consequently, smaller pulse shapers. As the size of both Kolsky bars and pulse shapers are increased to accommodate the typically large size concrete specimens, radial inertia in pulse shapers become non-negligible which interferes with the intrinsic shaper material response during deformation. The inertia induced stress significantly distorted the incident pulse which would otherwise exhibit a linear ramp. The study suggested that by implementing annulus geometry to the large

size pulse shapers, the radial inertia effects could be reduced to a level that does not noticeably influence the incident wave. In other words, a linear pulse, which is desired for Kolsky bar brittle materials testing, was realized through this new pulse shaping technique.

The validity of this concept was examined through testing the SCHSC material on a 50mm diameter Kolsky compression bar at the Air Force Research Lab. The experimental results show that with proper design of the annulus shapers, the concrete specimens deformed under dynamic stress equilibrium at constant strain rate until failure occurred. Since the testing conditions were well controlled at both strain rates (100s^{-1} and 240s^{-1}), minimal scatter in strain rate and failure strengths were observed for different specimens. The specimen inertia effects were investigated to determine if material failure strength under uniaxial stress loading conditions is artificially enhanced for the SCHSC material on a 50mm Kolsky bar. Using continuum mechanics models in the literature and the experimental data, the results show that the inertia induced stress is almost negligible compared to the intrinsic strength of the material. The techniques developed in this study may be applied to characterize the dynamic response of other geomaterials on large Kolsky bars.

The stress-strain curves for the SCHSC showed a strong rate dependency in failure strength. The failure strength at 240s^{-1} was 220 MPa, which is nearly three times stronger than the quasi-static failure strength (74MPa). There was also an additional increase of failure strength of 20% when strain rates were increased from 100s^{-1} to 240s^{-1} .

CHAPTER 6

BALLISTIC EVALUATION OF THE SCHSC

6.1 Introduction

The preceding chapters presented the development of a SCHSC material. The material formula was optimized and characterized at the macro, meso and micro length scales. The quasi-static pressure-volume response and the deviatoric response were characterized at increasing levels of confinement. The material response to direct tension and a micro-scale investigation of the fiber crack-bridging capability were presented. The material dynamic increase factor was determined using dynamic compression with a new pulse shaping technique. To investigate the overall performance of the SCHSC, this chapter presents a ballistic evaluation of the SCHSC. The material is evaluated at two different panel thicknesses, both with and without fiber reinforcement.

The projectile mass, velocity, geometry, mechanical properties and angle of impact are all factors that affect the target response in a ballistic event. Since velocity is a second-order term for initial impact kinetic energy, the target response can vary significantly, depending on the impact velocity. Consequently, an impact event is often categorized under different velocity regimes. Zukas [149] classifies impact dynamics into four striking velocity regimes: low (< 2.0 m/s), intermediate (0.5 – 1.5 km/s), high (2 – 3 km/s) and ultra-high (> 12 km/s). The low velocity regime involves local indentations or penetrations that are strongly coupled with the overall deformation and global response of the target or structure. Typical loading and response times occur within a range of

milliseconds. As the impact velocity increases into the intermediate velocity regime, the target response becomes far more localized and dominated by material behavior within a small impact zone typically two to three times the projectile diameter. The loading and reaction times are in the order of microseconds. When velocities are elevated into the high velocity regime, colliding solids can be treated as fluids in the early stage of impact. Finally, the ultra-high velocity regime occurs at such a high-rate that explosive vaporization of colliding materials may occur. For the ballistic evaluation of the SCHSC, the striking velocity regime falls into the intermediate-to-low category, with impact velocities ranging just below or above 0.5 km/s. This indicates that the ballistic event will primarily be highly localized, while some indication of a global response may also appear.

Zukas [149] describes six failure modes for thin and intermediate targets as shown in Figure 6.1. Thin targets are defined as “if stress and deformation gradients throughout its thickness do not exist”, and intermediate targets as “if the rear surface exerts considerable influence on the deformation process during nearly all of the penetrator motion” [149]. For the present ballistic evaluation, a projectile was selected to impact the SCHSC panel rather than a penetrator; however, the failure modes stated by Zukas are still applicable. In addition to the failure modes described by Zukas and shown in Figure 6.1, Figure 6.2 presents additional impact failure modes [150] typical for concrete targets. As illustrated in Figure 6.2, spalling is a “tensile failure due to the reflection of the initial compressive wave from the rear surface of a finite thickness plate” [149]. As presented in Chapter 5, an initial compression wave will reflect off of a surface abutting a lower impedance material. This phenomenon is fundamental to the Kolsky compression bar

test technique, and also applies to the impact scenario of a finite thickness SCHSC panel with a free surface behind it. Crater formation occurs in the impact face due to the ejection of target material resulting from spalling [149,150]. Spalling is of common occurrence in concrete due to the relatively lower tensile strength in comparison with the compressive strength. Scabbing is another common failure mechanism for concrete. The appearance of spalling is similar to scabbing, but scabbing is formed from the fracture and break-up of target material due to large deformation on the exit face of the target [150]. The degree of scabbing, and the resulting surface, is determined by the amount of local inhomogeneities and anisotropies of the target material [149]. The punch type shear failure shown in Figure 6.2 occurs when a projectile pushes out a cone of target material from the exit face. The cone is commonly called as the “shear cone”. This occurs when the concentrated force at the tip of the projectile is greater than the shear capacity of the target material, where the surface area of the cone and the material shear strength determine the punching shear capacity of the target material. If the projectile continues to have enough residual velocity after forming the shear cone, it can push out the shear cone breaking it up into fragments. Any of these types of failure mechanisms can be a predominant failure mode, but more often, the fracture and penetration of a thin or intermediate concrete target from projectile impact is due to the interaction of a variety of such mechanisms [110,151].

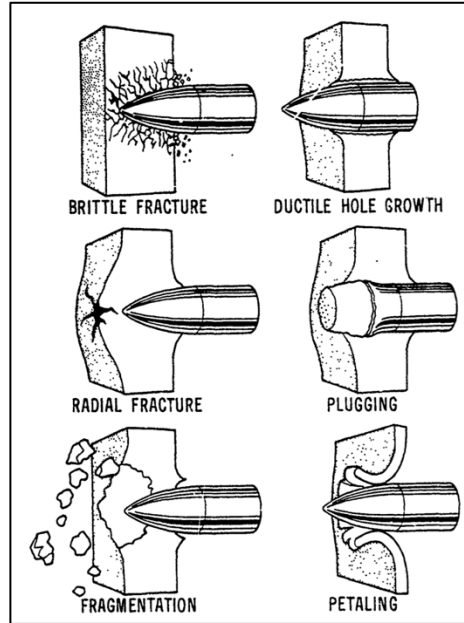


Figure 6.1 Failure modes in impacted plates [149]

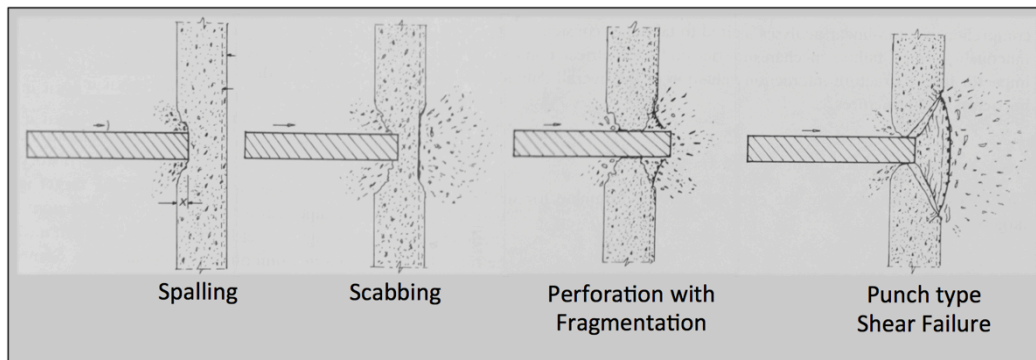


Figure 6.2 Failure modes for concrete targets [150]

The impact of a projectile or penetrator on a concrete target with a finite thickness has been described to have three possible phases [110]. The first one is the impact phase. This involves the initial high-pressure impact of the projectile onto the target creating an ejecta cloud of pulverized target material and formation of an impact crater due to spall and fragmentation. The pulverized and fragmented target material is ejected from the face of the target in the direction opposite to that of projectile travel. The impact phase

response is a function of tensile and shear strengths of the target material, but occurs under such high pressures that the concrete behaves more like a granular material rather than a hardened concrete mass. The second possible phase is the tunneling phase. It is characterized by the creation of a cylindrical opening through the interior of the target material as the projectile continues to penetrate. The third phase is the complete penetration of the projectile through the exit face of the target. This phase involves one or more of the mechanisms shown in Figures 6.1 and 6.2. It should be noted that if the target material is relatively thin for the given projectile velocity, mass, geometry and material properties, the tunnel phase may not occur and the impact crater and exit crater may intersect. As the target material thickness is increased, the tunneling phase becomes more prominent.

6.2 Experimental Approach

The ballistic evaluation was conducted at the Survivability Engineering Branch fragment simulating facility (FSF) at the ERDC. The facility consists of an underground ballistic range with a smooth bore powder gun with a 50-caliber barrel. Figure 6.3 is a photo of the FSF showing the experimental setup. As shown in Figure 6.3, the gun is mounted and secured opposite a blast panel to prevent unwanted debris from triggering the strike velocity screens. Four infrared photoelectric strike velocity screens were connected to two chronographs to capture two different velocity measurements as the projectile traveled downrange. The screens were positioned as shown in Figure 6.3 to determine the impact velocity using Equation (38).

$$V_{\text{Impact}} = V_2 + \left(\frac{L_2}{L_1} \right) (V_2 - V_1) \quad (38)$$

where:

V_1 = velocity as determined by screens one and three

V_2 = velocity as determined by screens two and four

L_1 = distance between V_1 and V_2

L_2 = distance between V_2 and the impact side of the test panel

The SCHSC test panel was supported as shown in Figure 6.4 with a flange and four hand-tightened bolts. A 0.5mm thick 2024-T₃ aluminum witness panel was placed behind the target to assess whether the ballistic event resulted in a complete penetration (CP) or a partial penetration (PP). A CP is defined as any breach in the witness panel that allows light to be visible when emanating from a 60-watt bulb behind the witness panel. A PP is defined as any other impact on the witness panel, whether by the projectile or by the secondary debris from the test panel [152]. Two Phantom V710 high-speed cameras were positioned as shown in Figure 6.3 to capture the ballistic event from two different perspectives. Camera one was positioned to capture events in the impact face of the test panel, whereas camera two captured the sequence of events occurring in the exit face of the test panel. The two cameras were synchronized with an acoustic trigger recording the events at 15,001 frames per second with a 0.5 μ s exposure and a 544 pixel x 608 pixel resolution. These camera settings resulted in a full frame view of the test panel front and back faces synced with time to capture the entire ballistic event with a 66.67 μ s interval between frames. The resulting video showed the panel response just prior to projectile impact until the projectile exited the back face of the test panel. A third set of velocity screens was positioned behind the witness panel to capture the exit velocity of the projectile in the event of a CP.

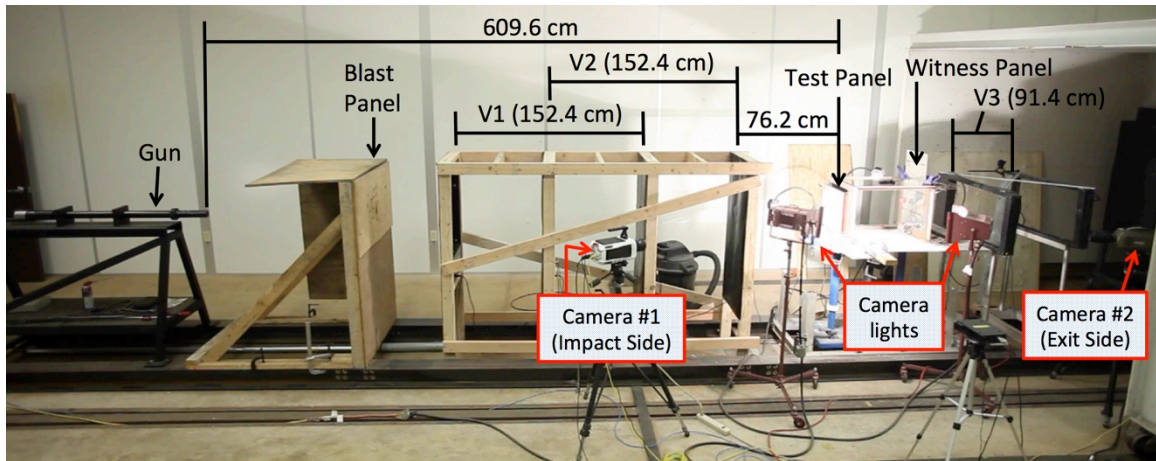


Figure 6.3 Experimental setup for ballistic evaluation of SCHSC



Figure 6.4 SCHSC panel mounted with witness panel for ballistic evaluation

The purpose of the ballistic experiment was to evaluate the SCHSC material response at two different panel thicknesses, both with and without the steel fiber reinforcement presented in Chapter 3. All panels were 305mm by 305mm by either 25mm thick or 50mm thick. A minimum of eight panels were cast for each of the four test conditions:

- 1) 25mm thick panels without steel fiber reinforcement: (Test series #1).
- 2) 25mm thick panels with steel fiber reinforcement: (Test series #2).
- 3) 50mm thick panels without steel fiber reinforcement: (Test series #3).
- 4) 50mm thick panels with steel fiber reinforcement: (Test series #4).

The SCHSC material was mixed, cast and cured according to the procedures established in Chapter 3. As in Chapters 4 and 5, the new armor material characterized as “P6S15W37” was used in all the ballistic evaluation tests. The only difference in mix formula across the four tests series was the addition of steel fiber reinforcement. The fibers were 2% by volume of the mix. In addition to material response, the V_{50} ballistic limit of the SCHSC was determined. The V_{50} ballistic limit, or just “ V_{50} ”, is an important ballistic experiment that enables comparison of various candidate armor materials for a specific projectile. V_{50} is a cost-effective method to determine the impact velocity of a specific projectile where a CP or an incomplete penetration are equally likely to occur [152]. V_{50} is taken as the average of at least two CPs and two PPs with a maximum velocity span. The velocity span is determined as difference between the highest velocity resulting in a CP and the lowest velocity resulting in a PP. Maximum velocity spans of 18 m/s, 27 m/s, 30 m/s and 38 m/s are typically used. For a non-homogeneous material such as concrete, V_{50} will often result in a phenomenon known as a “zone of mixed results”. This occurs when the velocity of PP is greater than the velocity of CP. The projectile for this V_{50} test was a 12.7mm rigid sphere constructed of S-2 tool steel. This projectile was selected to benchmark the SCHSC material, because of the availability of a vast database previously gathered at the ERDC for various candidate armor materials. The projectiles were hand-mounted in the cartridge with a sabot shown in Figure 6.5.



Figure 6.5 Cartridge with plastic sabot and 12.7mm spherical projectile

6.3 Results

The ballistic test results are presented in Table 6.1. This table reports the impact and residual velocity from each test, and whether the test resulted in a complete penetration (CP) or partial penetration (PP). The panel dimensions and weights are reported as well. In the sections that follow, the failure mechanisms are investigated for a representative panel from each test series and the final V50 values are compiled. .

Table 6.1 Individual results for each panel tested in the ballistic evaluation

SCHSC Panel Description	Test #	Avg. Thickness (mm)	Weight (N)	Impact Velocity (m/s)	Residual Velocity (m/s)	Results	Notes
25mm: No fibers	1-1	25.4	54.7	427	68	CP	E
25mm: No fibers	1-2	26.2	56.6	405	~	CP	A
25mm: No fibers	1-3	24.6	53.3	383	36	CP	-
25mm: No fibers	1-4	26.2	57.3	426	43	CP	-
25mm: No fibers	1-5	26.2	56.3	382	0	PP	-
25mm: No fibers	1-6	25.4	54.8	373	27	CP	-
25mm: No fibers	1-7	25.4	55.3	363	~	N/A	B
25mm: No fibers	1-8	27.0	59.2	370	0	PP	-
25mm: Fibers	2-1	28.6	63.6	451	~	CP	-
25mm: Fibers	2-2	30.2	65.4	449	~	CP	-
25mm: Fibers	2-3	25.4	53.1	441	99	CP	-
25mm: Fibers	2-4	25.4	52.3	391	27	CP	-
25mm: Fibers	2-5	24.6	50.4	353	~	CP	-
25mm: Fibers	2-6	25.4	51.8	362	~	CP	-
25mm: Fibers	2-7	24.6	50.9	331	0	PP	-
25mm: Fibers	2-8	25.4	54.3	347	0	PP	-
25mm: Fibers	2-9	25.4	55.2	357	51	N/A	C
25mm: Fibers	2-10	25.4	57.3	332	0	PP	-
25mm: Fibers	2-11	25.4	53.1	368	~	CP	D
25mm: Fibers	2-12	25.4	52.3	336	0	PP	D
25mm: Fibers	2-13	25.4	51.8	349	0	PP	D
50mm: No fibers	3-1	51.6	110.8	760	~	CP	E
50mm: No fibers	3-2	51.6	109.3	773	~	CP	-
50mm: No fibers	3-3	50.8	109.8	767	31	CP	-
50mm: No fibers	3-4	49.2	102.4	722	~	CP	-
50mm: No fibers	3-5	49.2	103.8	712	0	PP	-
50mm: No fibers	3-6	49.2	105.2	706	~	CP	-
50mm: No fibers	3-7	50.0	106.0	712	~	CP	-
50mm: No fibers	3-8	50.0	106.3	708	~	CP	-
50mm: No fibers	3-9	50.8	107.2	685	~	CP	-
50mm: No fibers	3-10	50.0	108.4	680	0	PP	-
50mm: No fibers	3-11	50.8	107.7	689	0	PP	-
50mm: Fibers	4-1	50.0	106.0	896	195	CP	-
50mm: Fibers	4-2	50.8	108.4	748	0	PP	-
50mm: Fibers	4-3	50.8	110.5	794	0	PP	-
50mm: Fibers	4-4	50.8	110.5	818	~	CP	-
50mm: Fibers	4-5	51.6	111.7	802	0	PP	-
50mm: Fibers	4-6	51.6	111.7	815	0	PP	-
50mm: Fibers	4-7	50.8	108.4	816	69	CP	E

Notes:

A: Projectile cracked witness panel but did not trigger chronograph

B: Not included in V-50 calculation due to impact on witness panel in a damaged area

C: Not included in V-50 calculation due to omitted witness panel prior to shot

D: Second shot on a previously tested panel

E: Panel was cracked prior to the shot. This test was used as an initial “scoping shot” only

6.3.2 SCHSC 25mm panel: No fibers (Test# 1-8)

Using the two synchronized high-speed cameras, the ballistic event and failure sequence were observed from both impact and exit sides of the SCHSC target panel. For the camera settings used in the experiment, a photograph of each side of the panel was taken every $67\mu\text{s}$. Time “zero” was established as the moment when the projectile made initial contact with the impact side of the panel, but before any penetration occurred. Figure 6.6 shows the annotated photographs of both the views at $0\mu\text{s}$, $67\mu\text{s}$, $133\mu\text{s}$, $200\mu\text{s}$, $267\mu\text{s}$, $333\mu\text{s}$, $1,400\mu\text{s}$ and $5,400\mu\text{s}$ for Test 1-8.

As shown in Figure 6.6 at time $0\mu\text{s}$, the spherical projectile has made initial contact with the impact face of panel 1-8. For this test, the impact velocity of the projectile was 370 m/s. At time instant of “ $67\mu\text{s}$ ”, the formation of the ejecta cloud is seen on the impact side. As previously discussed, the ejecta cloud is comprised of pulverized target material generated from the intense high pressures induced by projectile impact. The pulverized material is ejected in the opposite direction of projectile travel. At this point in time, five to six very small (approximately 15mm long) cracks radiated from a single point on the exit side at the panel center. This corresponds to the failure mechanism described in Figure 6.1 as “radial fracture” or “fragmentation”; however, the next time frame at $133\mu\text{s}$ clearly showed the formation of a shear cone on the exit side of the panel. The shear cone has additional cracks radiating out from the circular base of the shear cone. Only one crack appeared to extend out approximately halfway to the outer corner of the panel at $133\mu\text{s}$. This crack is labeled as “crack #1” in Figure 6.6. The cracks that extended from the shear cone did not appear to align or propagate from the initial radial cracks observed in the previous time instant at “ $67\mu\text{s}$ ”. Rather, these cracks

appear to initiate at the circular base of the shear cone. This would possibly indicate that the SCHSC panel was initially failing due to radial fracture and fragmentation until a shear cone formed which became the more predominant failure mechanism.

At time instant of $200\mu\text{s}$, cratering on the impact side due to spalling and fragmentation occurred and the shear cone continued to displace outward from the exit side of the target panel. At this stage, “Crack #1” widened and propagated to the edge of the panel. Also, a second crack (Crack#2) was initialized which reached to the panel edge. Neither “Crack #1” nor “Crack #2” was visible in the image of the impact face at $200\mu\text{s}$.

At $267\mu\text{s}$, fragmentation and spalling continued to expand the impact crater as “Crack #2” appeared on the impact face and extended to the panel edge. This indicated that at this time instant, the panel developed a through-crack that extended from the center to the edge of the panel. Scabbing and fragmentation continued to expand the exit crater. At time instant $333\mu\text{s}$, “Crack #1” had propagated through to the impact side and a third crack was visible on the exit side. With two cracks extending from the impact side to the exit side and from opposite panel edges, the target panel had clearly undergone a global response in addition to the initial localized damage that was anticipated. It appears that the panel was broken into two pieces before the projectile had completely penetrated through the target.

Data was collected at $67\mu\text{s}$ time intervals after $333\mu\text{s}$, but the panel showed a progression of the same damage pattern already established. The sequence of events for time instants $1,400\mu\text{s}$ and $5,400\mu\text{s}$ are shown in Figure 6.6 as evidence of this. At the time instant of $1,400\mu\text{s}$, the projectile had continued to penetrate the target. The exit side

showed a breakup of the shear cone from the penetrating projectile. At time instant 5,400 μ s, the projectile was visible within additional target fragments behind the exit face of the panel.

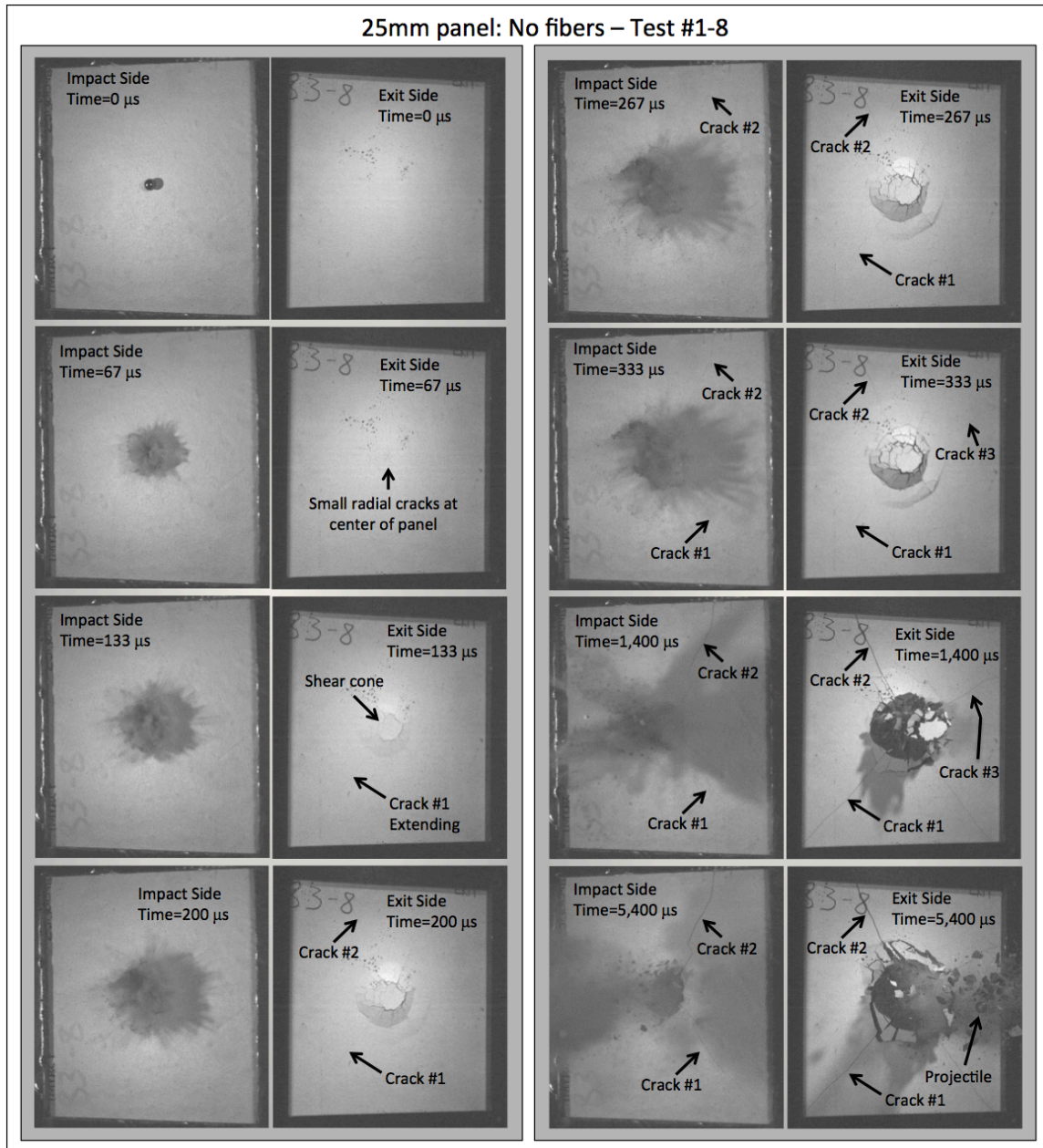


Figure 6.6 Impact and exit side of test #1-8 at the various time intervals indicated

Figure 6.7 shows the final damage to the SCHSC panel in Test 1-8 and Figure 6.8 shows the witness panel from the same test. Though the projectile completely penetrated and exited the target, there was no breach in the witness panel. This is by definition considered to be a PP. Figure 6.8 shows the indentation of the projectile along with a close-up view. Data similar to that presented for Test 1-8 was collected and analyzed for all eight tests in the first test series (i.e. 25mm panels with no fibers), but the damage and failure sequence were very similar for all eight tests. Figure 6.9 shows a cross section of a typical test panel from the first test series. As shown, the impact and exit craters intersect indicating that no tunneling phase occurred. Two CP and two PP results were obtained and the V_{50} was determined to be 378 m/s with a maximum velocity span of 13 m/s. Since a PP impact velocity exceeded the value of a CP, the V_{50} value would be considered a “zone of mixed results”. As discussed previously, this is to be expected for a non-homogeneous brittle geomaterial. The ballistic reports generated during the V_{50} evaluation of all four test series at the FSF are presented in Appendix A.

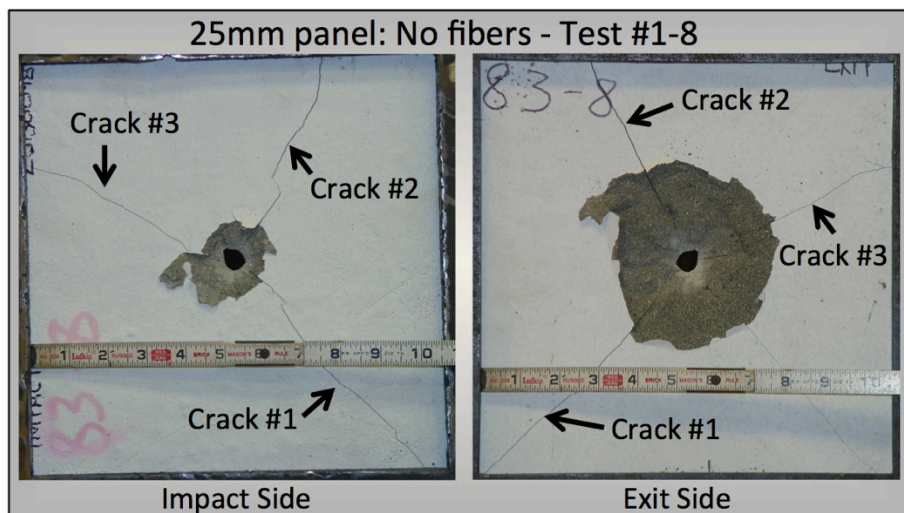


Figure 6.7 Impact side and exit side showing damage from Test #1-8

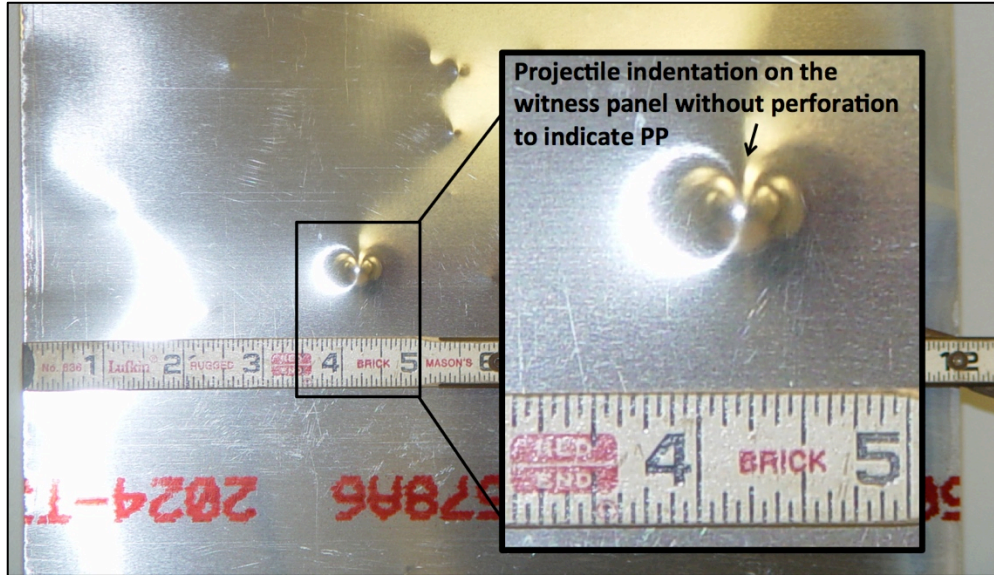


Figure 6.8 Witness panel for Test #1-8 to indicate a PP



Figure 6.9 Typical cross section showing overlap of impact and exit craters for all panels in Test series #1 (25mm: No fibers)

6.3.3 SCHSC 25mm panel: Fibers (Test #2-6)

The SCHSC panels used in test series two were 25mm thick with steel fiber reinforcement. Figure 6.10 shows the high-speed images with annotations from the ballistic event for Test 2-6. As with the previous test series, selected images are shown with the noted time instants to identify the failure sequence and progression of damage on each side of the panel. The damage and failure processes were very similar for all of the SCHSC panels in this test series. As shown in Figure 6.10, the projectile is making initial contact with the target impact side at time $0\mu\text{s}$. At time instant $67\mu\text{s}$, pulverized material has formed the ejecta cloud on the impact side. Identical to the first test series, several very small cracks originate from the center point on the exit side. This is most likely due to radial fracture and fragmentation. As time increased to $133\mu\text{s}$, the radial cracks grew and propagated, but the damage remains contained in a much more localized region. This is different from the previous test series that showed the formation of a shear cone and propagation of cracks towards the panel edge. At time instant $333\mu\text{s}$, fragmentation and scabbing appeared to be the failure mechanisms on the exit side, while cratering was observed on the impact side. This process continued as shown at time instants $1,400\mu\text{s}$ and $5,400\mu\text{s}$. The projectile was not identified in the image, but was evidently concealed in the rubble fragments. Figure 6.11 shows the damage from the projectile impact on both sides of the panel. Compared to Figure 6.7, the damage is much more localized. The limitation of damage to a small region was evident after tests 2-11, 2-12 and 2-13. These tests were conducted on undamaged areas of previously tested panels after all available panels had been used. These additional tests were required to meet the 18 m/s maximum velocity span criteria. Previously tested panels were inspected closely, and

because the damage was limited to such a localized area of the impact location, there was no difference in performance when previously tested panels were tested a second time with a different impact location. Though new panels are preferable, this procedure is common practice in the FSF when needing to narrow the velocity span of the V_{50} .

Upon investigation of the impact and exit craters, the craters intersected with no indication of a tunneling phase. Figure 6.12 shows the witness panel from test 2-6 with a small tear at the point of projectile impact. This indicates that a CP had occurred. The V_{50} for the second test series (25mm thick panels with fiber reinforcement) was 353 m/s with a maximum velocity spread of 15 m/s. Because both PP impact velocities were lower than the CP impact velocities, this V_{50} was not considered a “zone of mixed results” as before. It must be noted that the V_{50} for test series one was 6.8% higher than the V_{50} for test series two. This was not expected and is counter-intuitive. Fiber reinforcement should not decrease the ballistic performance of similar mixtures. Upon further investigation, it was determined that the compressive strength for the batch of concrete mixed for test series two had a compressive strength that was 13.8% lower than the compressive strength of the material used in all other three test series and reported in Chapter 4. The compressive strength should have been nearly the same as that reported in Chapter 4 for all four batches of this mix. This was unfortunate, but time and costs did not allow for the material to be recast, cured and retested. Therefore, the lower V_{50} value is attributed to lower strength concrete. Previous V_{50} test results of other 25mm thick concrete panels have historically been roughly the same for those with or without fiber reinforcement [15].

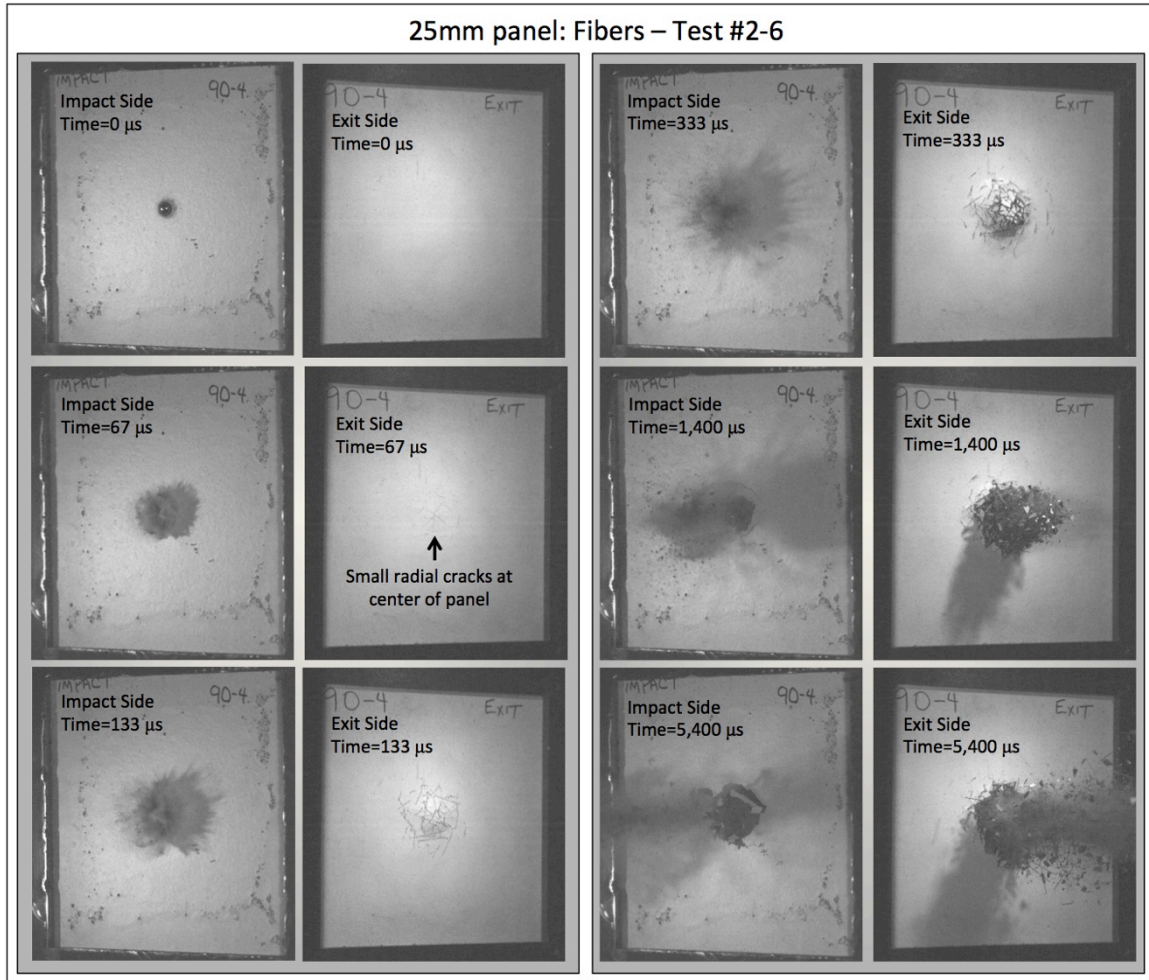


Figure 6.10 Impact and exit side of test #2-6 at the various time intervals indicated

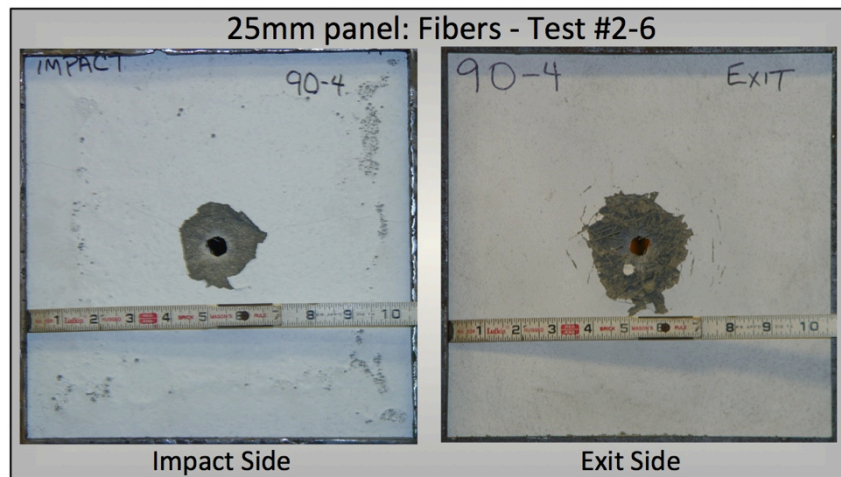


Figure 6.11 Impact side and exit side showing damage from Test #2-6

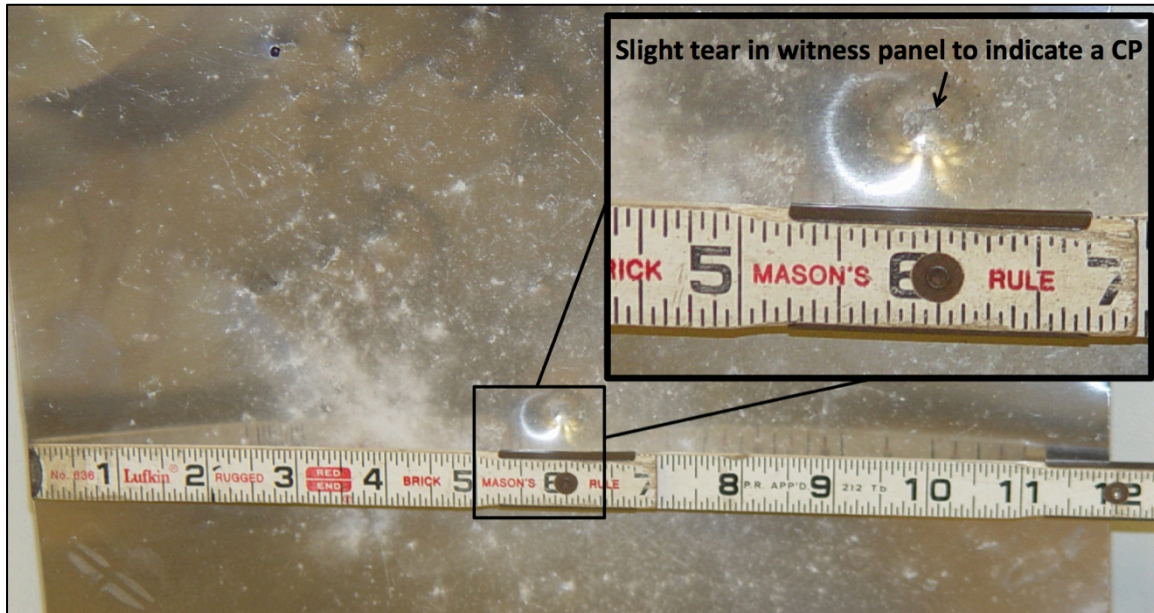


Figure 6.12 Witness panel for Test #2-6 showing a small breach to indicate a CP

6.3.4 SCHSC 50mm panel: No fibers (Test #3-4)

The time sequence images from test series three are shown in Figure 6.13. The projectile is shown making initial contact with the impact side of the target panel at time $0\mu\text{s}$. The initial formation of the ejecta cloud is shown on the impact side at time $67\mu\text{s}$. There was no evidence of projectile impact visible on the exit side until $133\mu\text{s}$. As observed in the previous two test series, several very small cracks extended radially from a single point on the exit face directly behind the projectile impact location. The cracks extended approximately 15mm toward the panel edge. Upon close inspection of the impact face at $133\mu\text{s}$, four thin cracks are visible. The cracks labeled as “Crack #1” and “Crack #2” extended to the edge of the panel. It is not certain if “Crack #3” and “Crack #4” extended completely to the panel edge yet, but they were visible on the impact side image at $133\mu\text{s}$. At $200\mu\text{s}$, all four cracks were clearly visible across the length of the panel and a shear cone had formed on the exit side with several cracks extending out

from the circular base of the shear cone. As noted in the first test series with 25mm panels without fiber reinforcement, the damage pattern for this test series seemed to also initially indicate radial fracture and fragmentation that was quickly superseded by the formation of the shear cone. The remaining images at 267 μ s, 333 μ s, 400 μ s, 600 μ s, 1,400 μ s and 5,400 μ s all showed the continuation of damage process with spalling and fragmentation on the impact face creating the impact crater, while scabbing and fragmentation on the exit face creating the exit crater. In the image recorded at 1,400 μ s, the projectile had sufficient velocity to break up the shear cone. The projectile is visible in the last image of Figure 6.13.

Figure 6.14 shows the damage incurred from Test 3-4. This result was very similar for all panels tested in this test series. The final V_{50} was determined to be 698 m/s with a maximum velocity span of 17 m/s. Figure 6.15 shows portions of two pieces recovered from two different target panels from this test series (50mm thick with no fibers). The impact crater and exit craters are seen to be intersected, indicating that the tunneling phase did not occur in panels that were 50mm thick and contained no fiber reinforcement.

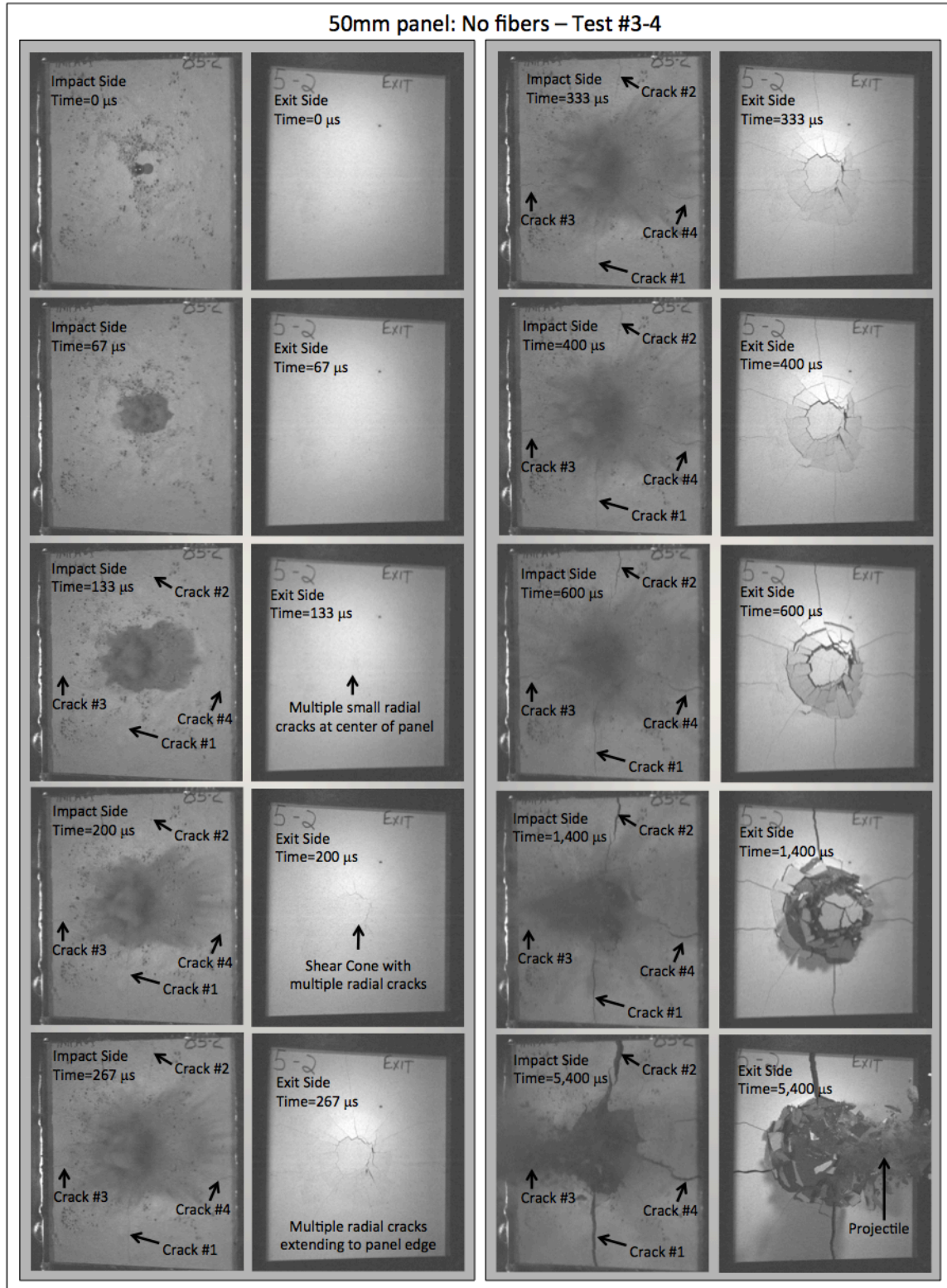


Figure 6.13 Impact and exit side of test #3-4 at the various time intervals indicated

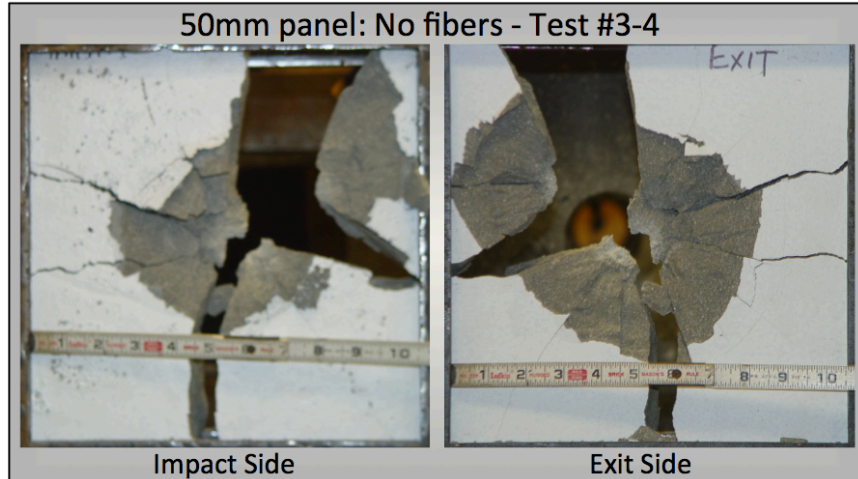


Figure 6.14 Impact side and exit side showing damage from Test #3-4



Figure 6.15 Portions of two different target panels from Test series three showing intersection of impact and exit craters indicating no projectile tunneling occurred

6.3.5 SCHSC 50mm panel: Fibers (Test #4-2)

The high-speed images in Figure 6.16 indicate that the failure mechanisms for Test 4-2 (50mm panel with fibers) were similar to the failure mechanisms of Test series #2 (25mm panels with fibers). Fragmentation and spalling created the impact crater while scabbing and fragmentation produced an exit crater. The failure process and damage incurred in test #2-4 were very similar to all other panels in this test series. Though there were similarities between the failure mechanisms of test series four and test series two, the degree of damage was different. The size of the impact crater for the thicker panels was considerably larger, while the exit craters were similar. Figure 6.17 shows the impact and exit faces of test 4-2. Comparing the impact crater of Figure 6.17 with the impact crater of Figure 6.11, the diameter of the impact crater for test 4-2 was approximately 150mm while the diameter of the impact crater for test 2-6 was approximately 50mm. Most of this was due to the increased depth of penetration from an impact velocity of 748 m/s for the 50mm thick panel and an impact velocity of 362 m/s for the 25mm thick panel.

The V_{50} for the 50mm panel with fiber reinforcement of test series four was 813 m/s. The maximum velocity span was 16 m/s, which met the first level criteria of 18 m/s with a “zone of mixed results”. Figure 6.18 shows a panel from test series four. For this particular test, the projectile remained lodged in the panel at the end of the ballistic test. Upon further investigation of the damage panels from Test Series Four, it was clear that a tunneling phase occurred after the impact crater was formed but prior to the exit condition. The cylindrical cavity of the tunneling phase is visible in Figure 6.18. The

average length of the cylindrical cavity for the seven panels tested in Test Series #4 was approximately 10mm.

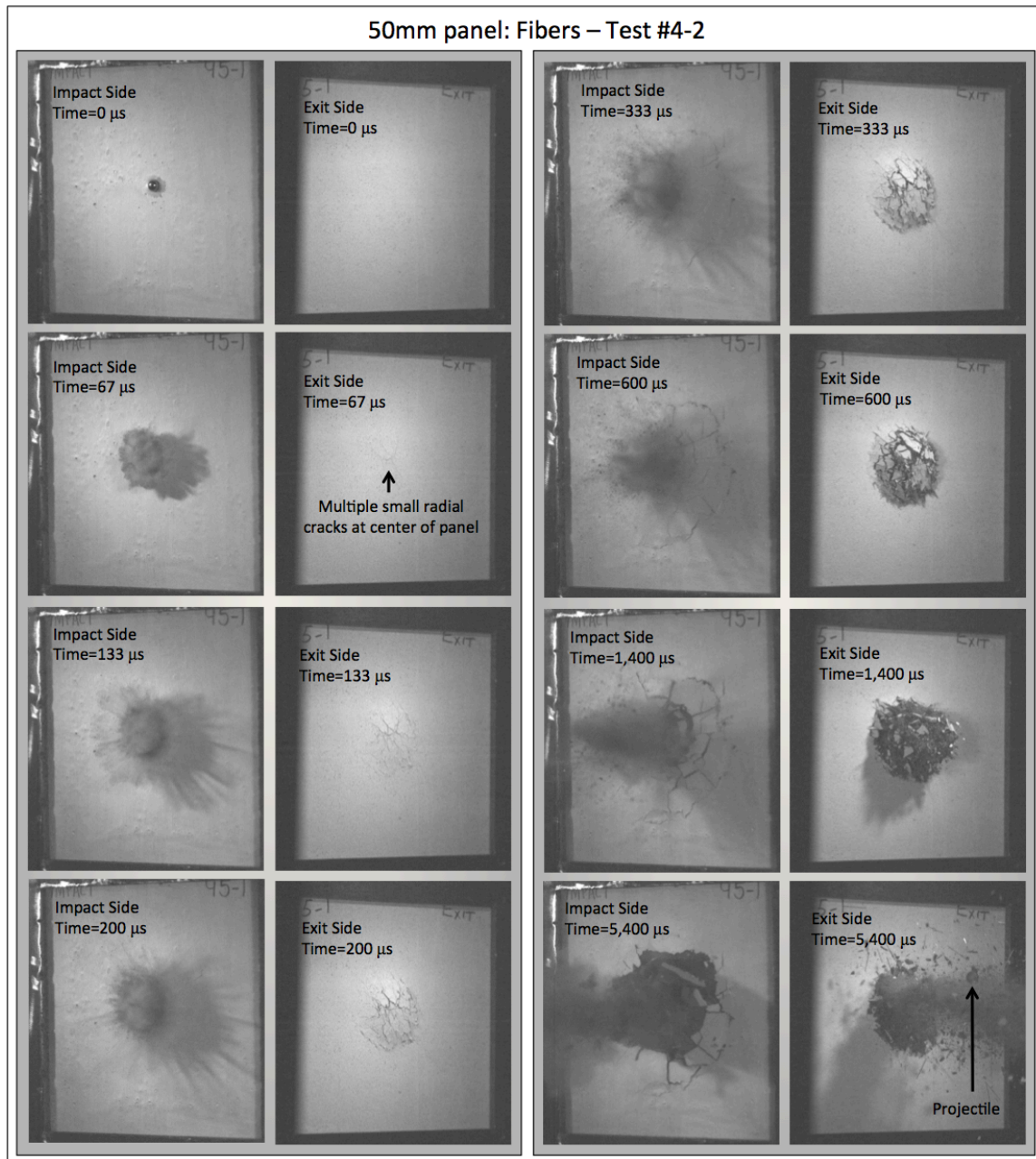


Figure 6.16 Impact and exit side of test #4-2 at the various time intervals indicated

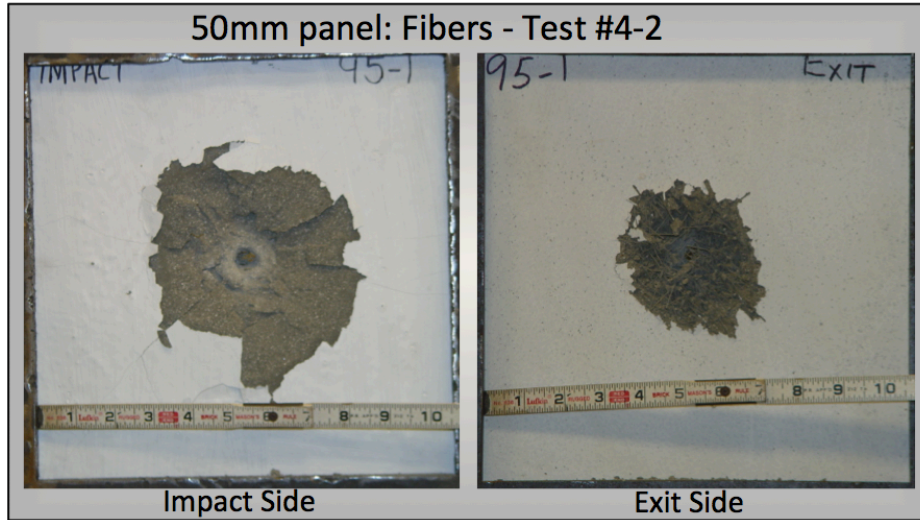


Figure 6.17 Impact side and exit side showing damage from Test #4-2

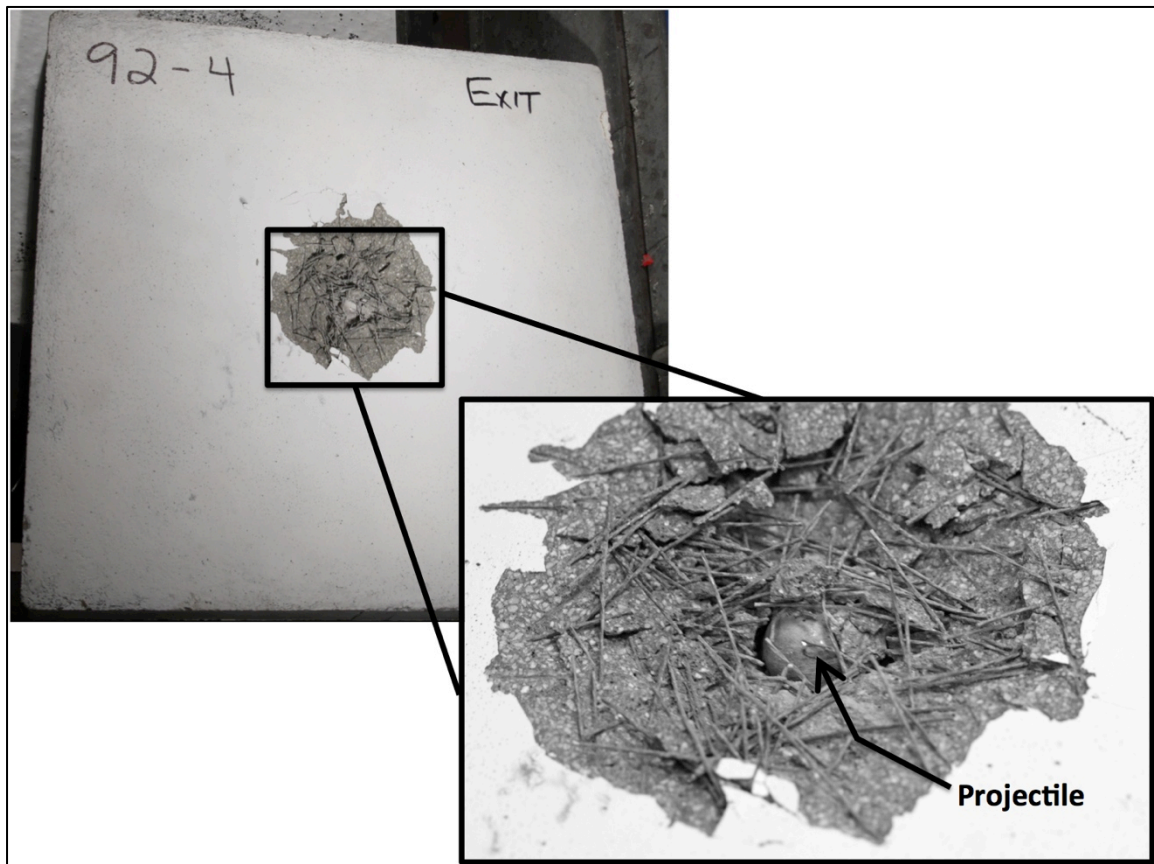


Figure 6.18 Projectile lodged in the tunnel of a Test series #4 panel (50mm: Fibers)

6.4 Summary and Conclusions

A ballistic evaluation was conducted on the mixture described in Table 3.4 of Chapter 3 as “P6S15W37”. The SCHSC was mixed and cast into panels that were 305mm by 305mm by either 25mm or 50mm thick. At least eight panels were cast at each of the two thicknesses both with and without steel fiber reinforcement. The objective was to determine the ballistic limit or V_{50} of the SCHSC material at each thickness, and to observe the influence of fiber reinforcement on performance and damage incurred. Four series of ballistic tests were conducted to isolate the experimental variables considered. Table 6.2 summarizes the results of the ballistic evaluation of the SCHSC.

Table 6.2 Overall results of the ballistic evaluation of the SCHSC

Panel Description	Test Series	V_{50} (m/s)	Max. Span (m/s)	Failure Mechanism	Remarks
25mm thick: No fibers	1	378	13	Shear cone, scabbing, spalling & fragmentation	Multiple cracks extending to edge of panel
25mm thick: Fibers	2	353	15	Spalling, scabbing & fragmentation	Damage was very localized, Low V_{50} was due to low $F'c$
50mm thick: No fibers	3	698	17	Shear cone, scabbing, spalling & fragmentation	Multiple cracks extending to edge of panel
50mm thick: Fibers	4	813	16	Spalling, scabbing & fragmentation	Damage was very localized

The following observations were made throughout the testing of the SCHSC material:

- In Test series 1 and 2: Multiples crack extending from panel center to the outer edge prior to substantial projectile penetration could suggest that edge support conditions may have influenced target response. This has never been a concern

for previous testing of similar thin concrete panels at the FSF. Given this discovery, edge effects of thin brittle geomaterial panels should be investigated further.

- A 25mm thick panel is very thin for a spherical projectile with a 12.7mm diameter. At this thickness, it is difficult to evaluate material behavior. Any improvements, developments or adjustments that would enhance a particular material property, may not be realized when testing at such a relatively thin material thickness compared to the projectile diameter.
- Fiber reinforcement had an effect on the degree of damage and the V_{50} . For the 25mm panels, it limited the damage to a local region and prevented apparent global damage. For the 50mm panels, the fiber reinforcement had the same effect of isolating damage, but also improved the V_{50} by 16.5%. The increase in V_{50} was likely due to the thicker panels remaining intact and allowing a tunneling phase to occur. Projectile tunneling dissipates energy that would otherwise be available for inflicting additional damage or residual velocity during the exit conditions.
- The analysis of damage was assessed by visual inspection of the moderately high-resolution images from high-speed photography. Both the 25mm and 50mm panel with fiber reinforcement appeared to have highly localized damage with no apparent global cracking as was observed in the unreinforced panels. It is possible that microcracking occurred in the reinforced panels, but was not visible to the unaided human eye. The DIC experimental investigative technique presented in Chapter 4 may offer more conclusive data. Using the

synchronized high-speed cameras in stereo to capture surface strains and displacements would identify damage at the micro-scale, along with the sequence of events on either the impact or exit face of the target. This technique should be considered for future ballistic experiments.

CHAPTER 7

SUMMARY AND FUTURE WORK

7.1 Summary

An extensive review of the state-of-the-art on the enhancement of compressive strength and the improvement of the ballistic performance of HPCs was presented. It was observed that by using SCMs, a low water-to-cementitious material ratio and 3rd generation HRWR admixtures, the cement microstructure can be refined, subsequently improving the compressive strength and ballistic limit of the cementitious material. Current techniques to achieve a highly flowable, nonsegregating concrete were reviewed. Based on these observations, a unique mineral viscosity-modifying admixture (PPNC) was introduced in Chapter 3. The PPNC also served as a SCM to enhance the compressive strength of a new SCHSC. The SCHSC was developed through an extensive multi-scale experimental investigation. MicroCT scanning revealed that PPNC refined the microstructure and reduced overall porosity, which resulted in a higher compressive strength and improved interfacial bond between the matrix and fiber reinforcement. PPNC also enhanced stability in the SCHSC while achieving high flow values and flow rates. It was also determined that GGBFS improved the modulus of rupture, the compressive strength and further refined the cement microstructure. A SCHSC formula (P6S15W37) was achieved which adequately satisfied the research objective of developing a material requiring simple manufacturing procedure involving semi-skilled labor and at the same time achieve desired enhancements in mechanical

properties and rheology. A suite of experiments was designed to fully characterize and evaluate performance of P6S15W37 under quasi-static and dynamic loads.

The pressure-volume response of the SCHSC was determined from hydrostatic compression experiments with confining pressures of up to 400 MPa. The SCHSC reached approximately 13% volumetric strain before the unloading phase was initiated. The SCHSC specimen showed no exterior signs of damage. The pressure-volume response was also determined from uniaxial strain in compression. The deviatoric response with increasing levels of lateral confinement of up to 400 MPa was investigated and presented. The shear response showed a clear transition from brittle to ductile behavior when the lateral confining pressures were 50 MPa or greater. With a 20 MPa lateral confining pressure, the SCHSC underwent 0.18% of radial strain; however, when the lateral pressure was increased to 50 MPa, radial strain values in excess of 4% were achieved. Triaxial data were used to construct the failure points and yield surface for the SCHSC. Table 7.1 summarizes material elastic constants determined for the SCHSC developed in this study.

Table 7.1 SCHSC elastic properties

Elastic Constants	Value
Elastic bulk modulus “K”	11.6 GPa
Young’s modulus “E”	22.6 GPa
Shear modulus “G”	13.6 GPa
Constrained modulus “M”	24.2 GPa
Poisson’s ratio “ν”	0.18

A direct tension experiment was designed and conducted on the SCHSC. The load versus displacement response under direct tension was presented. DIC was used to

identify eccentric loads that would have resulted in flexure. The DIC and LVDT data showed only negligible eccentricity in loading resulting from the loading fixture developed for the purpose. The DIC data was analyzed and successfully used to identify microcracks and evaluate fiber crack-bridging capability of the SCHSC. The SCHSC had an ultimate (nominal) tensile strength of 10.1 MPa when fiber reinforcement was used in the mix.

A detailed review of the Kolsky bar technique was presented with derivation of the fundamental equations used with the experimental technique. The need for proper pulse shaping for achieving an ideal incident waveform was established. A new annulus pulse shaping technique was presented to obtain constant strain rate deformation in large diameter high-strength brittle materials. The new technique was utilized to determine the dynamic stress-strain response of the SCHSC material for two strain rates: 100s^{-1} and 240s^{-1} . Data was presented to verify if dynamic equilibrium was achieved under constant strain rate deformation in the SCHSC test specimens. Table 7.2 shows the failure strengths for the three strain rates investigated and the strength increase factor, indicating the degree of sensitivity to strain rate.

Table 7.2 Rate sensitivity of the SCHSC

Strain Rate	Failure Strength	Strength Increase Factor
$1\text{E-}4\text{s}^{-1}$	74 MPa	1.00
100s^{-1}	183 MPa	2.47
240s^{-1}	220 MPa	2.97

The ballistic limit and associated damage mechanisms were investigated for the SCHSC. Panels were cast at two different thicknesses with and without fiber

reinforcement. Using high-speed photography to capture the ballistic event, images of the impact and exit panel faces were analyzed at a frame rate of 15,001 frames per second, or a time interval of 67 μ s. The investigation revealed that fiber reinforcement isolated damage to a local region, prevented a shear cone failure, and improved the ballistic limit by 16.5% at the 50mm panel thickness. However, fiber reinforcement did not noticeably improve the ballistic limit of the 25mm thick panel. This is likely due to the relative size of projectile diameter (12.7mm), length of fiber reinforcement (25mm) and panel thickness (25mm). For all of the panels without fiber reinforcement, multiple cracks extending to the outer edge of the panel were observed within 133 μ s after the initial projectile contact on the impact face. This global cracking occurred prior to significant damage appearing on the exit face of the panel. The ballistic limits (V_{50}) and failure modes are reported in Table 7.3.

Table 7.3 Ballistic limit and corresponding failure mode for each panel test series

Panel Description	V_{50} (m/s)	Failure Mechanism
25mm thick: No fibers	378	Shear cone, scabbing, spalling & fragmentation
25mm thick: Fibers	353	Spalling, scabbing & fragmentation
50mm thick: No fibers	698	Shear cone, scabbing, spalling & fragmentation
50mm thick: Fibers	813	Spalling, scabbing & fragmentation

7.2 Future Work

The development of SCHSC was presented in Chapter 3 and then characterized and evaluated in Chapters 4, 5 and 6. Due to the exceptionally large amount of time expended curing specimens and the following rigorous specimen fabrication procedure

meeting strict dimensional tolerances, the experiments presented in Chapters 4, 5 and 6 were initiated prior to completion of the material development work presented in Chapter 3. In other words, time did not allow for the material development phase to be finalized before samples were cast, cured and machined to tolerance for the characterization phase. As a result, initial findings suggested that P6S15W37 was the optimal mix to use for the characterization phase, but ultimately it did not turn out to be the final optimal mix design. Due to the amount of powder HRWRA used in P6S15W37, a larger variance was observed in some material properties. The formulation P3S15W37 actually achieved higher compressive strengths and more consistent results. Future work might pursue to characterize the properties of this formula following the procedures used to characterize P6S15W37. In this context, some initial data for P3S15W37 is presented in Appendix C.

In addition to characterizing the optimized formula “P3S15W37”, the DIC experimental technique presented in Chapter 4 should be considered for implementation into the ballistic experiments presented in Chapter 6. Using this technique to capture displacement and surface strains during the high-rate event would be highly beneficial and lend to a better understanding of the role played by the fiber reinforcement in the SCHSC. The technique would also provide useful data to investigate panel edge effects and its influence on target response. Furthermore, DIC with high-speed cameras would be a tremendous diagnostic tool for high-rate experiments with the Kolsky bar as well. Some have attempted this, but combining it with the new annulus pulse shaping technique presented in Chapter 4 would potentially provide a wealth of information to researchers working in the field of material development and experimental mechanics for

dynamic loads. It could also aid the study of size effects of other UHPCs using multiple size Kolsky bars.

Appendix A

BALLISTIC REPORTS

Table A.1 Ballistic report from Test series 1 (25mm thick: No fibers)

Description		1" HSC Panel w/o Fibers					
Manufacturer	ERDC - Bill Heard	Plies/Laminates	N/A				
Width (in.)	12	Weight (lbs/sq.ft.)	12.59				
Height (in.)	11.98	Thickness (in.)	1.012				
SET-UP							
Relative Humidity (%)	53	Witness Panel	0.020 in. 2024 T3 AL				
Temperature (°F)	71	Target_to_Witness_Dist:	24				
Barrel/Weapon	.50 Caliber Rifled	Primary Velocity Screen	Ohler Model 57				
Range to Target (ft.)	20	Primary Velocity Screen Distance (ft.)	5				
Obliquity (Deg.)	0	Residual Velocity Screen	Ohler Model 57				
		Residual Velocity Screen Distance (ft.)	3				
Ammunition		Applicable Standards/Procedures					
Projectile	.50 Cal. Steel Sphere	(1)	Mil-Std-662F				
Projectile Wt (gr)	129	(2)					
Powder	Standard	(3)					
Velocities							
<u>Date</u>	<u>Shot</u>	<u>Grains</u>	<u>One</u>	<u>Two</u>	<u>Avg</u>	<u>Residual</u>	<u>Witness Pane</u>
11/8/2013	1	43.5	1402	0	1402	224	CP
11/8/2013	2	40.5	1329	0	1329	N/A	CP
11/8/2013	3	39.0	1272	0	1272	118	CP
11/8/2013	4	37.5	1398	0	1398	140	CP
11/8/2013	5	36.5	1252	0	1252	0	PP
11/8/2013	6	36.5	1224	0	1224	88	CP
11/8/2013	7	36.0	1191	0	1191	N/A	N/A
11/12/2013	8	34.5	1215	0	1215	0	PP
V50 Summary				Remarks			
Nbr of Points	4	Zone of Mixed Results.					
Velocity Span Criteria	60	Shot #2: Cracked witness panel but did not trigger chronograph <input type="checkbox"/>					
High Partial	1252, 1215	Shot #7: Not included in V-50 calculation due to impact on witness panel in a damaged or questionable area.					
Low Complete	1224, 1272						
Criteria Met?	Yes						
V50:	1241						

Table A.2 Ballistic report from Test series 2 (25mm thick: Fibers)

Description	1" UHPC Panel w/ Fibers						
Manufacturer	ERDC - Bill Heard	Plies/Laminates	N/A				
Width (in.)	12	Weight (lbs/sq.ft.)	11.82				
Height (in.)	12	Thickness (in.)	0.991				
SET-UP							
Relative Humidity (%)	34	Witness Panel	0.020 in. 2024 T3 AL				
Temperature (°F)	71	Target_to_Witness_Dist:	24				
Barrel/Weapon	.50 Caliber Rifled	Primary Velocity Screen	Ohler Model 57				
Range to Target (ft.)	20	Primary Velocity Screen Distance (ft.)	5				
Obliquity (Deg.)	0	Residual Velocity Screen	Ohler Model 57				
		Residual Velocity Screen Distance (ft.)	3				
Ammunition		Applicable Standards/Procedures					
Projectile	.50 Cal. Steel Sphere	(1)	Mil-Std-662F				
Projectile Wt (gr)	129	(2)					
Powder	Standard	(3)					
Velocities							
<u>Date</u>	<u>Shot</u>	<u>Grains</u>	<u>One</u>	<u>Two</u>	<u>Avg</u>	<u>Residual</u>	<u>Witness Pane</u>
11/13/2013	1	44.5	1481	0	1481	N/A	CP
11/13/2013	2	43.5	1473	0	1473	N/A	CP
11/13/2013	3	42.0	1446	0	1446	324	CP
11/13/2013	4	36.5	1282	0	1282	89	CP
11/14/2013	5	33.0	1160	0	1160	N/A	CP
11/14/2013	6	33.5	1187	0	1187	N/A	CP
11/14/2013	7	32.0	1087	0	1087	0	PP
11/14/2013	8	32.5	1139	0	1139	0	PP
11/14/2013	9	33.0	1170	0	1170	168	N/A
11/14/2013	10	32.5	1090	0	1090	0	PP
11/26/2013	11	33.1	1206	0	1206	N/A	CP
11/26/2013	12	31.5	1103	0	1103	0	PP
11/26/2013	13	32.8	1145	0	1145	0	PP
V50 Summary				Remarks			
Nbr of Points	4	Shot #5: Hairline crack across the impact face <input type="checkbox"/>					
Velocity Span Criteria	60	Shot #9: Not included in V-50 calculation due to omitted witness panel.					
High Partial	1145, 1139	Shot 11: Panel# 90-1; <input type="checkbox"/> nd Shot					
Low Complete	1160, 1187	Shot 12: Panel# 90-2; <input type="checkbox"/> nd Shot					
Criteria Met?	Yes	Shot 13: Panel# 90-4; <input type="checkbox"/> nd Shot					
V50:	1158						

Table A.3 Ballistic report from Test series 3 (50mm thick: No fibers)

Description	2" UHPC Panel w/o Fibers						
Manufacturer	ERDC - Bill Heard	Plies/Laminates	N/A				
Width (in.)	12	Weight (lbs/sq.ft.)	24.05				
Height (in.)	12	Thickness (in.)	1.980				
SET-UP							
Relative Humidity (%)	70	Witness Panel	0.020 in. 2024 T3 AL				
Temperature (°F)	71	Target_to_Witness_Dist:	24				
Barrel/Weapon	.50 Caliber Rifled	Primary Velocity Screen	Ohler Model 57				
Range to Target (ft.)	20	Primary Velocity Screen Distance (ft.)	5				
Obliquity (Deg.)	0	Residual Velocity Screen	Ohler Model 57				
		Residual Velocity Screen Distance (ft.)	3				
Ammunition		Applicable Standards/Procedures					
Projectile	.50 Cal. Steel Sphere	(1)	Mil-Std-662F				
Projectile Wt (gr)	129	(2)					
Powder	Standard	(3)					
Velocities							
Date	Shot	Grains	One	Two	Avg	Residual	Witness Pane
11/18/2013	1	90.5	2493	0	2493	N/A	CP
11/18/2013	2	92.5	2535	0	2535	N/A	CP
11/18/2013	3	90.5	2517	0	2517	102	CP
11/18/2013	4	85.0	2367	0	2367	N/A	CP
11/18/2013	5	82.0	2335	0	2335	0	PP
11/22/2013	6	82.0	2318	0	2318	N/A	CP
11/22/2013	7	81.7	2335	0	2335	N/A	CP
11/22/2013	8	80.9	2324	0	2324	N/A	CP
11/22/2013	9	79.0	2248	0	2248	N/A	CP
11/22/2013	10	78.5	2232	0	2232	0	PP
11/22/2013	11	79.0	2260	0	2260	0	PP
V50 Summary				Remarks			
Nbr of Points	4	Shot #01: Severely Damaged Panel - Initial Scoping Shot <input type="checkbox"/>					
Velocity Span Criteria	60	Zone of Mixed Results.					
High Partial	2335, 2260						
Low Complete	2248, 2318						
Criteria Met?	Yes						
V50:	2290						

Table A.4 Ballistic report from Test series 4 (50mm thick: Fibers)

Description	2" UHPC Panel w/ Fibers						
Manufacturer	ERDC - Bill Heard	Plies/Laminates	N/A				
Width (in.)	12	Weight (lbs/sq.ft.)	24.63				
Height (in.)	12.03	Thickness (in.)	2.005				
SET-UP							
Relative Humidity (%)	38	Witness Panel	0.020 in. 2024 T3 AL				
Temperature (°F)	71	Target_to_Witness_Dist:	24				
Barrel/Weapon	.50 Caliber Rifled	Primary Velocity Screen	Ohler Model 57				
Range to Target (ft.)	20	Primary Velocity Screen Distance (ft.)	5				
Obliquity (Deg.)	0	Residual Velocity Screen	Ohler Model 57				
		Residual Velocity Screen Distance (ft.)	3				
Ammunition		Applicable Standards/Procedures					
Projectile	.50 Cal. Steel Sphere	(1)	Mil-Std-662F				
Projectile Wt (gr)	129	(2)					
Powder	Standard	(3)					
Velocities							
Date	Shot	Grains	One	Two	Avg	Residual	Witness Pane
11/25/2013	1	114.0	2939	0	2939	640	CP
11/25/2013	2	87.0	2453	0	2453	0	PP
11/25/2013	3	95.5	2603	0	2603	0	PP
11/25/2013	4	99.0	2684	0	2684	N/A	CP
11/25/2013	5	97.5	2630	0	2630	0	PP
11/25/2013	6	99.0	2673	0	2673	0	PP
11/26/2013	7	99.2	2678	0	2678	228	CP
V50 Summary				Remarks			
Nbr of Points	4	Shot #7: Panel# 95-1; 2nd Shot					
Velocity Span Criteria	60						
High Partial	2673, 2630						
Low Complete	2678, 2684						
Criteria Met?	Yes						
V50:	2666						

Appendix B

This appendix presents the impact and exit faces of all SCHSC panels tested in the ballistic evaluation and listed in Table 6.1.

B.1 Photos from Test Series 1 - SCHSC 25mm: No fibers



Figure B.1 Test 1-1 impact side (left) exit side (right)

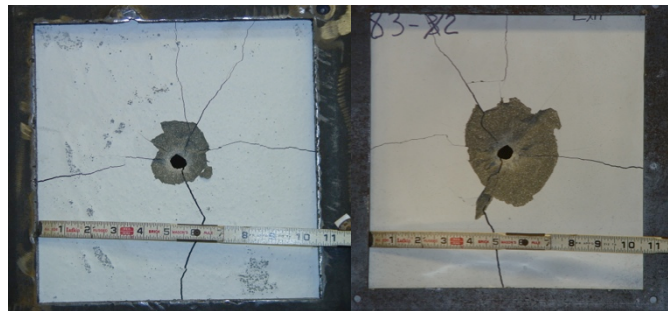


Figure B.2 Test 1-2 impact side (left) exit side (right)

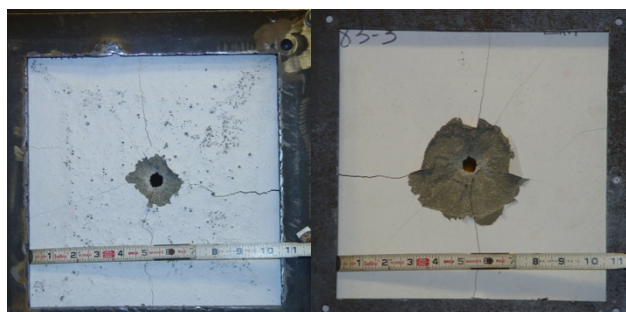


Figure B.3 Test 1-3 impact side (left) exit side (right)

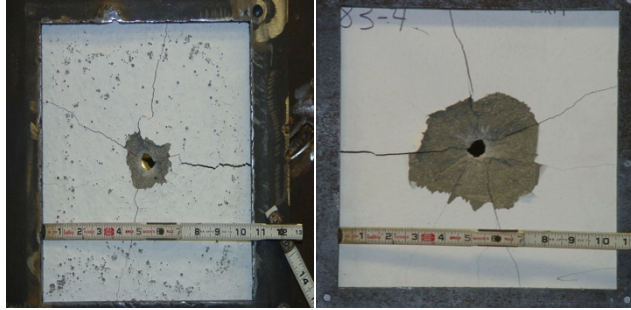


Figure B.4 Test 1-4 impact side (left) exit side (right)

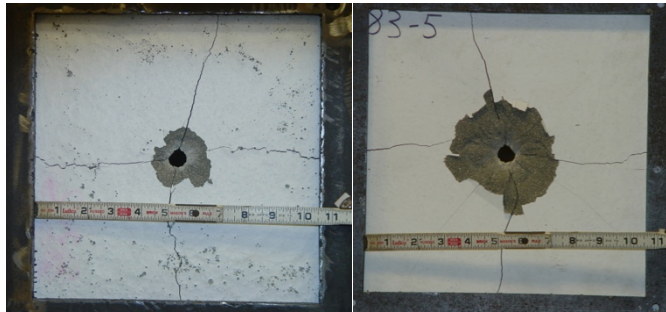


Figure B.5 Test 1-5 impact side (left) exit side (right)

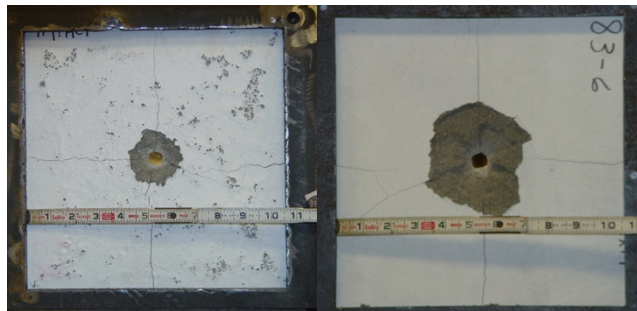


Figure B.6 Test 1-6 impact side (left) exit side (right)

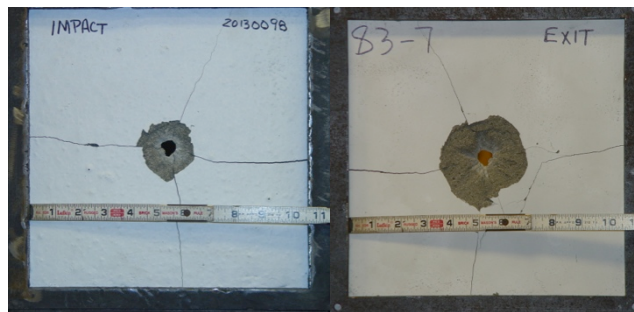


Figure B.7 Test 1-7 impact side (left) exit side (right)

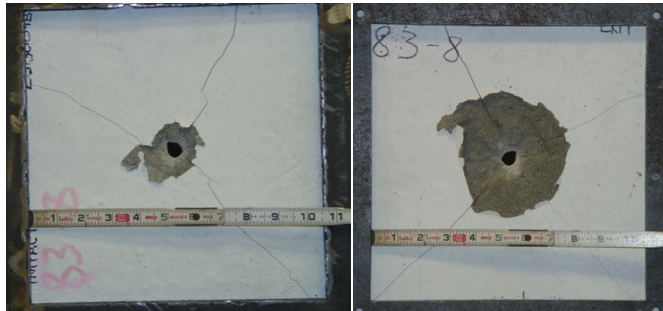


Figure B.8 Test 1-8 impact side (left) exit side (right)

B.2 Photos from Test Series 2 - SCHSC 25mm: Fibers

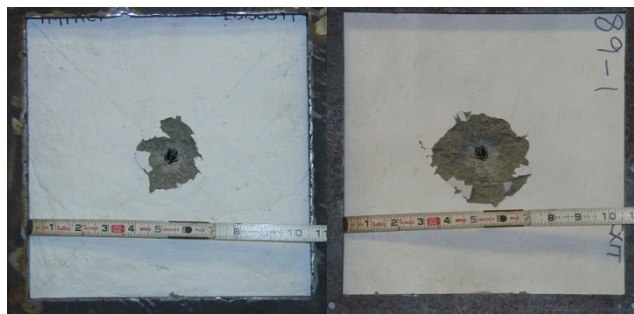


Figure B.9 Test 2-1 impact side (left) exit side (right)

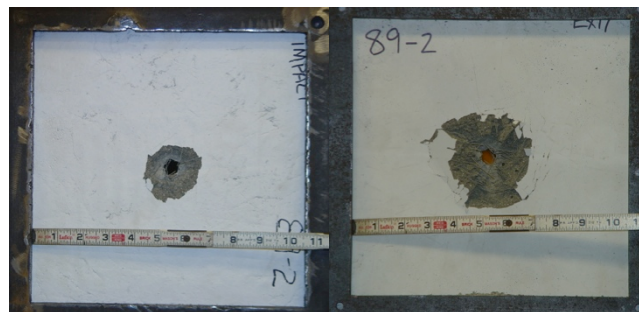


Figure B.10 Test 2-2 impact side (left) exit side (right)

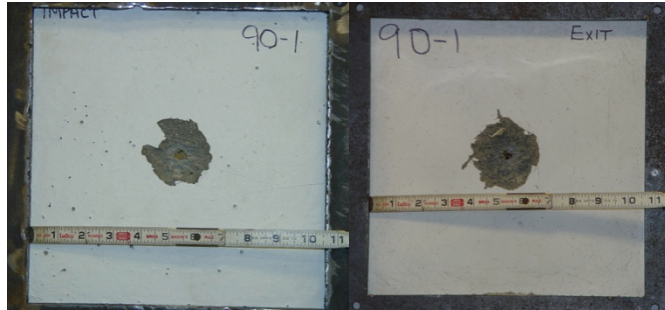


Figure B.11 Test 2-3 impact side (left) exit side (right)

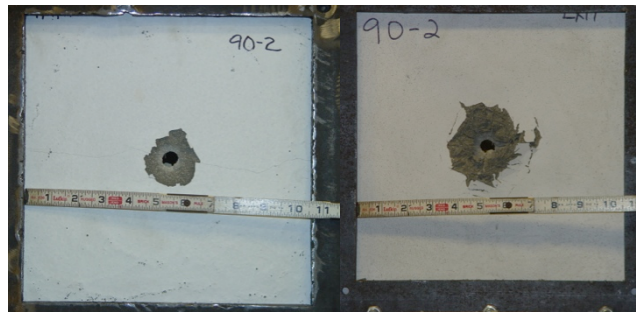


Figure B.12 Test 2-4 impact side (left) exit side (right)

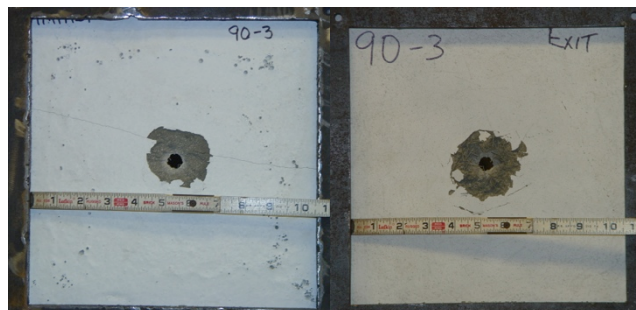


Figure B.13 Test 2-5 impact side (left) exit side (right)

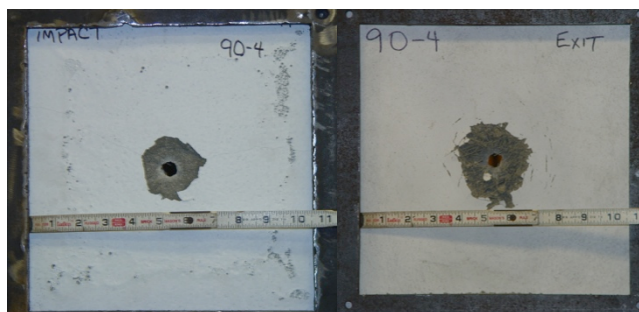


Figure B.14 Test 2-6 impact side (left) exit side (right)

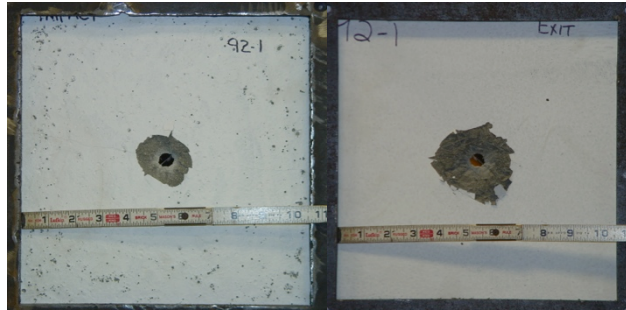


Figure B.15 Test 2-7 impact side (left) exit side (right)

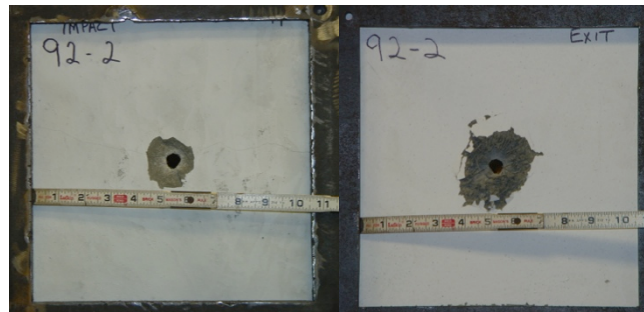


Figure B.16 Test 2-8 impact side (left) exit side (right)

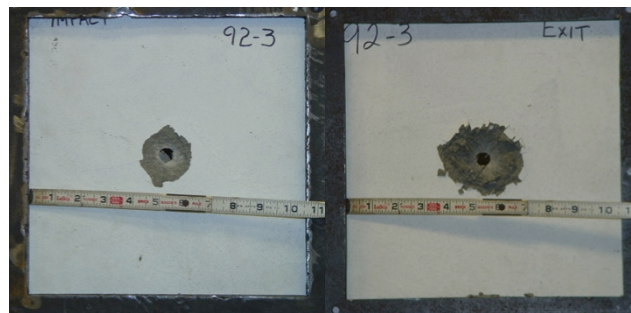


Figure B.17 Test 2-9 impact side (left) exit side (right)

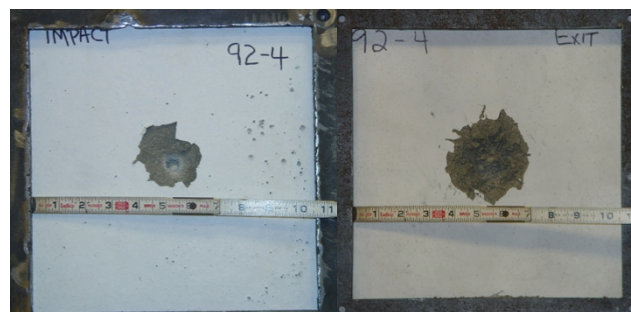


Figure B.18 Test 2-10 impact side (left) exit side (right)

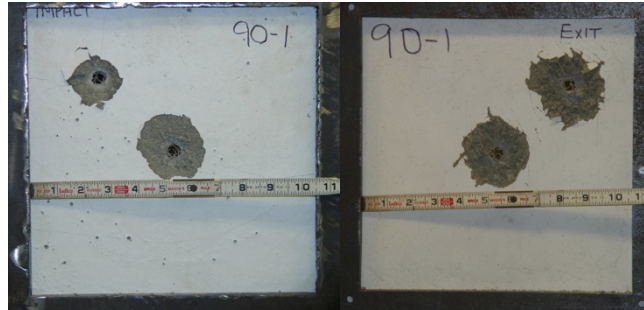


Figure B.19 Test 2-11 impact side (left) exit side (right)

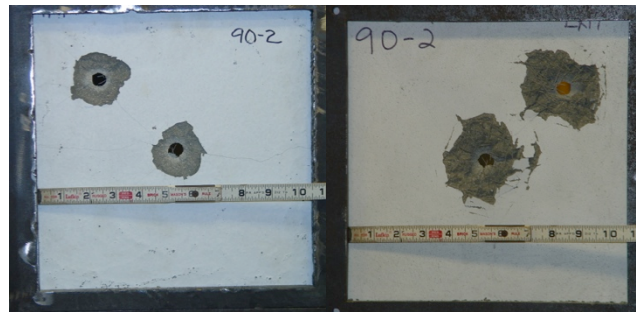


Figure B.20 Test 2-12 impact side (left) exit side (right)

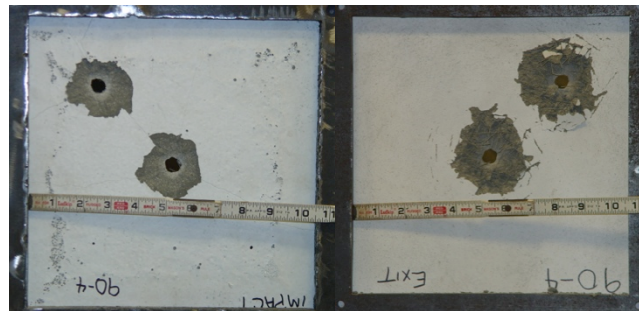


Figure B.21 Test 2-13 impact side (left) exit side (right)

B.3 Photos from Test Series 3 - SCHSC 50mm: No fibers

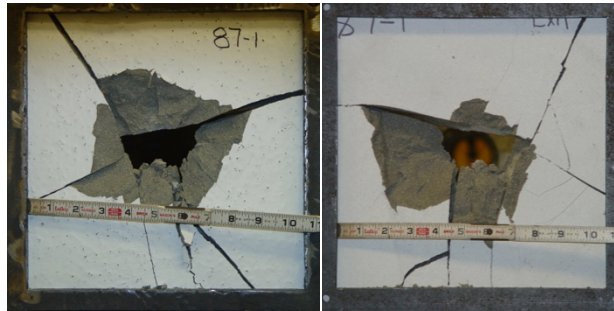


Figure B.22 Test 3-1 impact side (left) exit side (right)

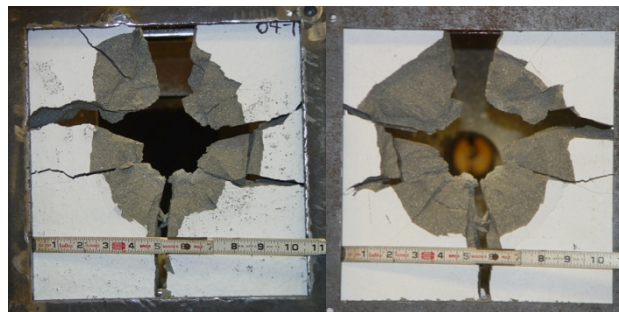


Figure B.23 Test 3-2 impact side (left) exit side (right)

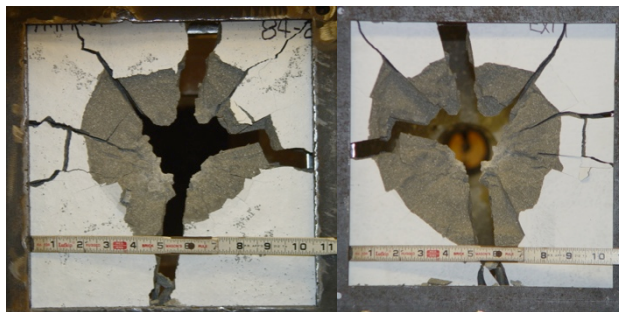


Figure B.24 Test 3-3 impact side (left) exit side (right)

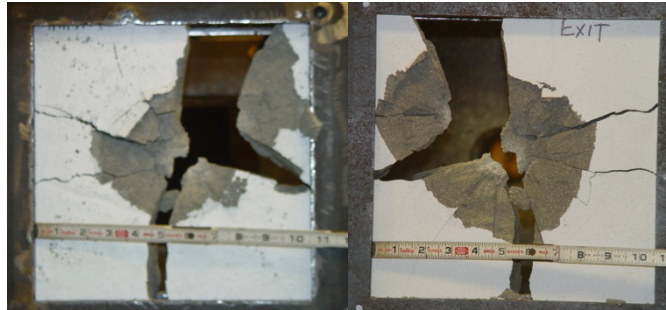


Figure B.25 Test 3-4 impact side (left) exit side (right)

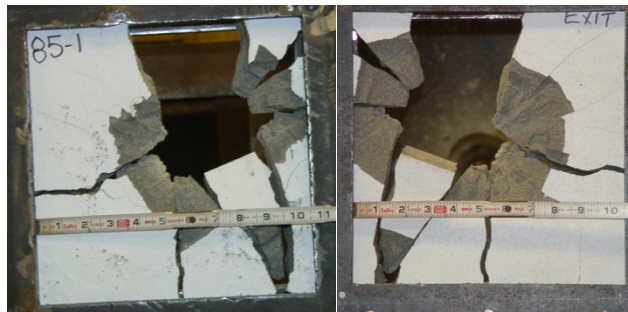


Figure B.26 Test 3-5 impact side (left) exit side (right)

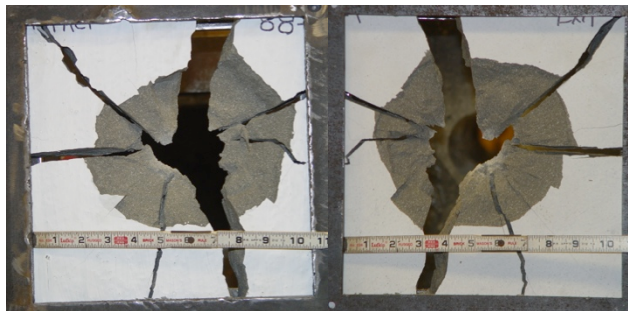


Figure B.27 Test 3-6 impact side (left) exit side (right)

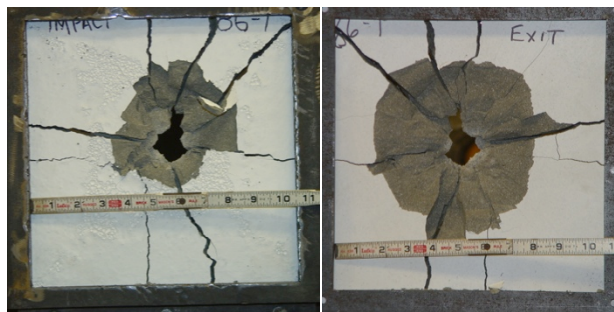


Figure B.28 Test 3-7 impact side (left) exit side (right)

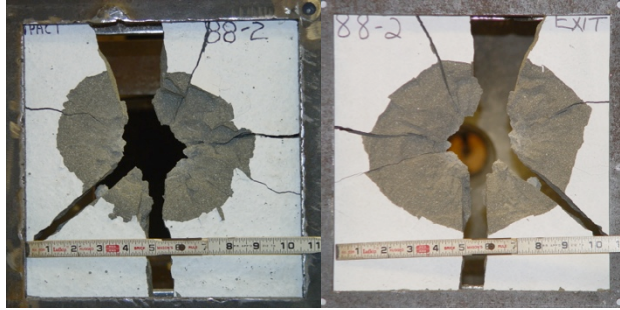


Figure B.29 Test 3-8 impact side (left) exit side (right)

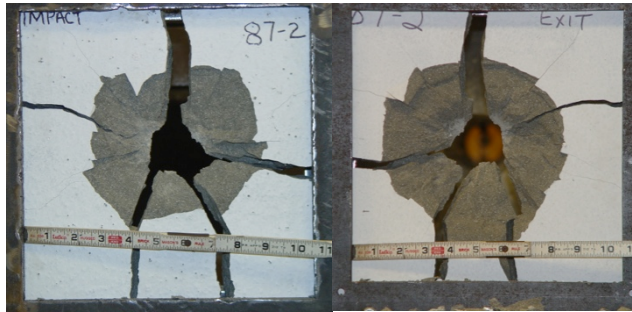


Figure B.30 Test 3-9 impact side (left) exit side (right).

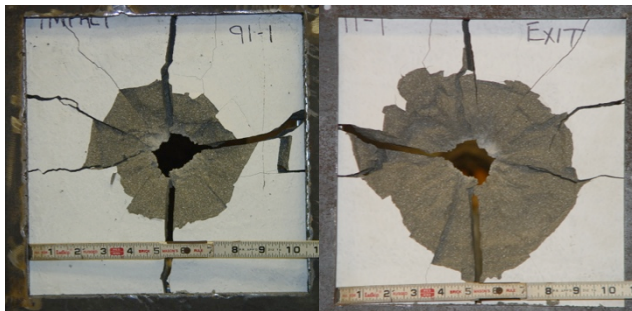


Figure B.31 Test 3-10 impact side (left) exit side (right)

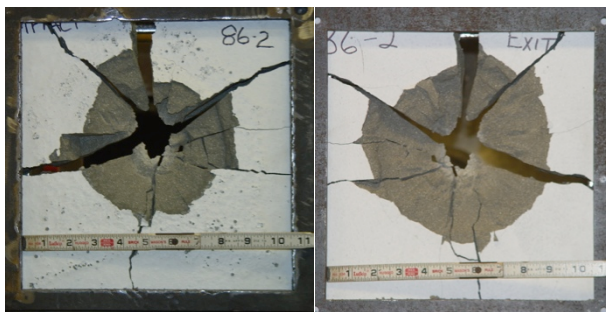


Figure B.32 Test 3-11 impact side (left) exit side (right)

B.4 Photos from Test Series 4 - SCHSC 50mm: Fibers

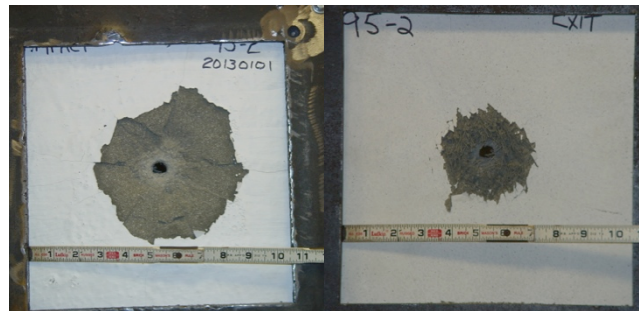


Figure B.33 Test 4-1 impact side (left) exit side (right)

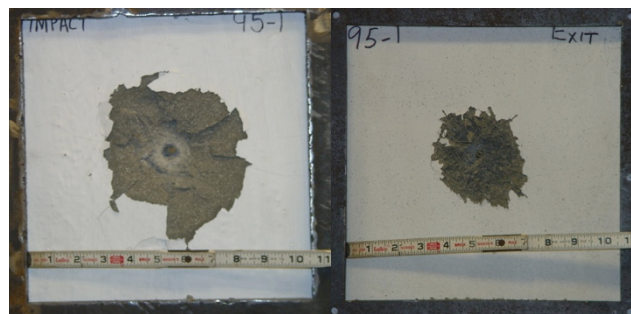


Figure B.34 Test 4-2 impact side (left) exit side (right)

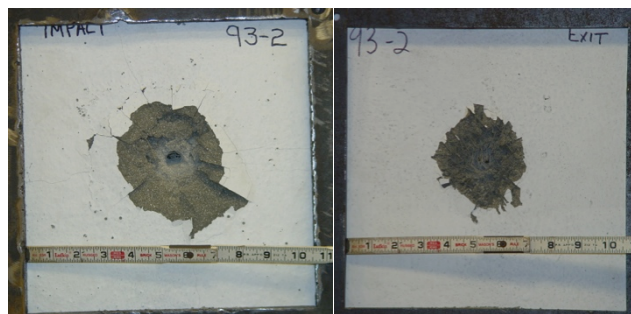


Figure B.35 Test 4-3 impact side (left) exit side (right)

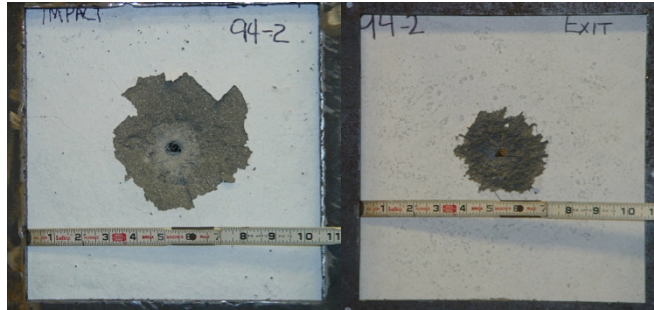


Figure B.36 Test 4-4 impact side (left) exit side (right)

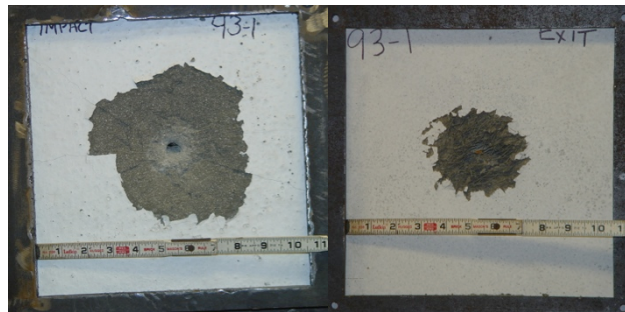


Figure B.37 Test 4-5 impact side (left) exit side (right)

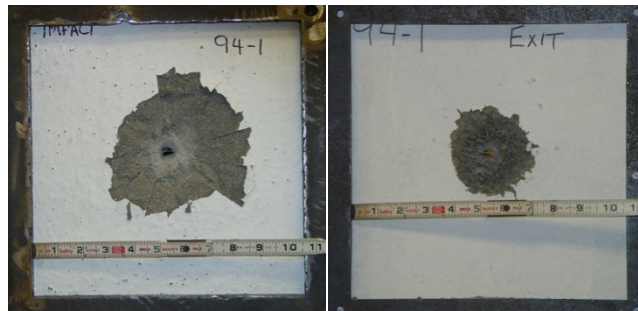


Figure B.38 Test 4-6 impact side (left) exit side (right)

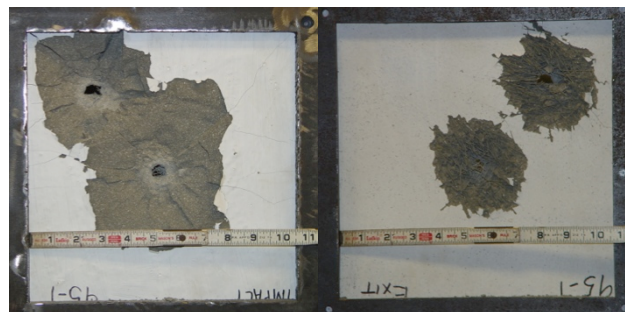


Figure B.39 Test 4-7 impact side (left) exit side (right)

Appendix C

UC RESULTS OF P3S15W37

This appendix presents the UC results for the mix identified in Tables 3.4, 3.5 and 3.9 as “P3S15W37”. During the development phase of this research, initial findings suggested that in certain respects P6S15W37 would be a better-optimized mix. However, P3S15W37 achieved higher compressive strength with less variance and more consistent rheological properties. The difference between P6S15W37 and P3S15W37 is the amount of PPNC and HRWR admixture. Reducing the amount of PPNC from 0.6% to 0.3% reduced the amount of HRWR admixture required to achieve optimum flow and flow rate. As a result, this also improved the hardened mechanical properties. Figure C.1 shows the UC results for UC tests conducted on eight cylindrical specimens with a nominal 50-mm diameter and 100-mm length. The specimens were tested as described in Section 4.3.3.

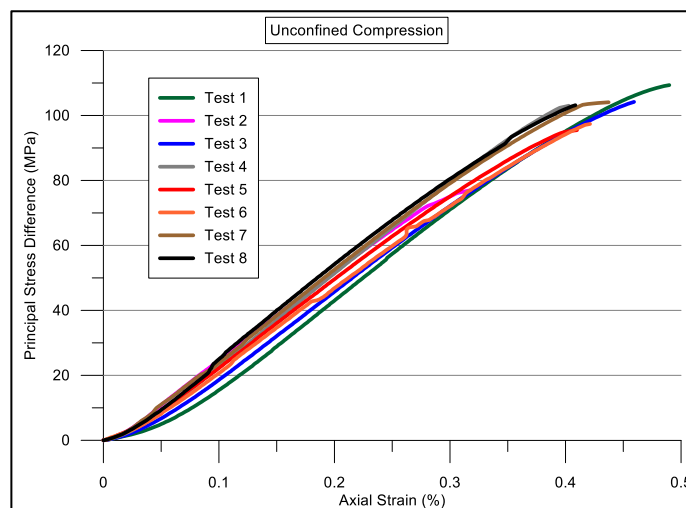


Figure C.1 Principal stress difference vs. Axial strain for P3S15W37

References

- [1] ERDC, 2013, "US Army Corps of Engineers: ERDC," erdc.usace.army.mil [Online]. Available: <http://www.erdcl.usace.army.mil/Media/FactSheets/FactSheetArticleView/tabid/9254/Article/9641/erdcl.aspx>. [Accessed: 05-Jun-2013].
- [2] Nelson D. H., Heard W. F., Roth M. J., and Slawson T. R., 2008, "Development of a Novel, Lightweight, Protective Structure to Resist Impulsive, Dynamic Loads," Orlando, FL.
- [3] O'Neil E. F., Cummins T. K., Durst B. P., and Kinnebrew P. G., 2004, "Development of Very-High-Strength and High-Performance Concrete Materials for Improvement of Barriers Against Blast and Projectile Penetration," Orlando, FL.
- [4] Pittman D., 2008, "ERDC: Force Protection Research," dtic.mil [Online]. Available: <http://www.dtic.mil/ndia/2008maneuver/Pittman.pdf>. [Accessed: Jun-2013].
- [5] Roth M. J., Boone N. R., Kinnebrew P. G., Davis J. L., and Rushing T. S., 2008, "Development of New Protective Solutions to Counter Emerging and Adaptive Threats," Orlando, FL.
- [6] Heard W. F., Boone N. R., Roth M. J., Kinnebrew P. G., and Durst B. P., 2010, "Development of the Modular Protective System: Validation of Protection from Direct Fire, Indirect Fire, and Bare Charge Threats", U.S. Army Corps of Engineers, Vicksburg, Ms.
- [7] Heard W. F., Basu P. K., and Nordendale N. A., 2011, "Material Characterization of Fiber Reinforced Concrete for Improved Blast Performance," Las Vegas, NV.
- [8] Ranade R., Li V. C., Stults M. D., Rushing T. S., Roth M. J., and Heard W. F., 2013, "Micromechanics of High Strength-High Ductility Concrete," ACI Materials Journal, **110**(4), pp. 375–384.
- [9] Ranade R., Li V. C., Stults M. D., Heard W. F., and Rushing T. S., 2013, "Composite Properties of High Strength High Ductility Concrete (HSHDC)," ACI Materials Journal, **110**(4), pp. 413–422.
- [10] ACI, 2013, "ACI CT-13: Concrete Terminology", American Concrete Institute, Farmington Hills, MI.
- [11] Zia P., Ahmad S., and Leming M., 1997, "High-Performance Concretes, a State-of-Art Report", U.S. Dept of Transportation Federal Highway Administration.
- [12] PCA, 1994, "Concrete Technology Today," **15**(1) [Online]. Available: <http://www.cement.org/tech/pdfs/PL941Hirise.pdf>. [Accessed: 05-Jun-2013].

- [13] Zhang M. H., Shim V. P. W., Lu G., and Chew C. W., 2005, "Resistance of High-Strength Concrete to Projectile Impact," *International Journal of Impact Engineering*, **31**(7), pp. 825–841.
- [14] Borvik T., Gjørsvik O. E., and Langseth M., 2007, "Ballistic Perforation Resistance of High-Strength Concrete Slabs," *Concrete International*.
- [15] Rushing T. S., Boone N. R., Irizzary A., and Magee R. E., 2011, "Independent Effects of Matrix Strength and Fiber Reinforcement on Concrete's Ballistic Resistance," *Journal of Critical Technology - SAVIAC*, pp. 1–12.
- [16] Hanchak S. J., Forrestal M. J., Young E. R., and Ehrgott J. Q., 1992, "Perforation of Concrete Slabs with 48 MPa (7 ksi) and 140 MPa (20 ksi) Unconfined Compressive Strengths," *International Journal of Impact Engineering*, **12**(1), pp. 1–7.
- [17] Aitcin P.C., 2004, *High Performance Concrete*, Taylor & Francis.
- [18] Albinger J., and Moreno J., 1981, "High-strength concrete, Chicago style," *Concrete Construction*, pp. 1–3.
- [19] Mehta P. K., 1999, "Advancements in Concrete Technology," *Concrete International*, **21**(6), pp. 69–75.
- [20] Ronneberg H., and Sandvik M., 1990, "High Strength Concrete for North Sea Platforms," *ACI: Concrete International*, **12**(4), pp. 29–34.
- [21] Malhotra V. M., 1981, "Superplasticizers: Their Effect on Fresh and Hardened Concrete," *ACI: Concrete International*, **3**(5), pp. 66–81.
- [22] Tanaka Y. O., Matsuo S., Ohta A., and Ueda M., 1996, "Concrete in the Service of Mankind: Radical Concrete Technology", *Proceedings of the International Conference held at the University of Dundee, Dundee, Scotland*.
- [23] Kotz J. C., Treichel P. M., and Townsend J. R., 2009, *Chemistry and Chemical Reactivity*, Brooks/Cole Publishing Company.
- [24] Sika, "Characteristics and Advantages of Polycarboxylate Ether Technology (PCE)," sika.com [Online]. Available: <http://www.sika.com/shotcrete/en/shotcrete/sika-sprayed-concrete-topics/admixtures/high-range-water-reducers--hrwr-/characteristics-and-advantages-of-polycarboxylate-ether-technology.html>. [Accessed: 05-Jun-2013].
- [25] Collepardi M., and Valente M., 2006, "Recent Developments in Superplasticizers," *ACI Special Publication*, **239**, pp. 1–14.
- [26] Hamada D., Sato T., Yamato F., and Mizunuma T., 2000, "Development of New superplasticizer and Its Application to Self-compacting Concrete," *ACI Special Publication*, **195**, pp. 291–304.
- [27] Daczko J. A., 2012, *Self-Consolidating Concrete*, CRC Press llc.
- [28] Lee N. P., and Chisholm D. H., 2005, "Study Report: Reactive Powder Concrete", Branz Ltd., Judgeford, New Zealand.

- [29] Wu H., Guo H., Lei J., Zhang R., and Liu Y., 2007, “Research on Synthesis and Action Mechanism of Polycarboxylate Superplasticizer,” *Frontiers of Chemistry in China*, **2**(3), pp. 322–325.
- [30] Felekoğlu B., and Sarıkahya H., 2008, “Effect of Chemical Structure of Polycarboxylate-Based Superplasticizers on workability Retention of Self-Compacting Concrete,” *Construction and Building Materials*, **22**(9), pp. 1972–1980.
- [31] Puertas F., Santos H., Palacios M., and Martínez-Ramírez S., 2005, “Polycarboxylate Superplasticiser Admixtures: Effect on Hydration, Microstructure and Rheological Behaviour in Cement Pastes,” *Advances in Cement Research*, **17**, pp. 77–89.
- [32] Yamada K., Takahashi T., Hanehara S., and Matsuhisa M., 2000, “Effects of the Chemical Structure on the Properties of Polycarboxylate-Type Superplasticizer,” *Cement and Concrete Research*, **30**(2), pp. 197–207.
- [33] Sika, “High-range Water Reducers (HRWR),” sika.com [Online]. Available: <http://www.sika.com/shotcrete/en/shotcrete/sika-sprayed-concrete-topics/admixtures/high-range-water-reducers--hrwr-.html>. [Accessed: Jun-2013].
- [34] Abrams D. A., 1918, “Design of Concrete Mixtures,” Structures Materials Research Laboratory.
- [35] Mehta P. K., and Monteiro J., 2006, *Concrete Microstructure, Properties and Materials*, McGraw-Hill Companies, New York, NY.
- [36] Hewlett P., 2003, *Lea's Chemistry of Cement and Concrete*, Butterworth-Heinemann, Burlington, MA.
- [37] Powers T. C., and Brownyard T. L., 1946, “Studies of the Physical Properties of Hardened Portland Cement Paste,” *Journal of the American Concrete Institute*, **43**, pp. 101–132.
- [38] Powers T. C., 1958, “Structure and Physical Properties of Hardened Portland Cement Paste,” *Journal of the American Ceramic Society*, **41**, p. 6.
- [39] Feldman R. F., and Sereda P. J., 1970, “A New Model for Hydrated Portland Cement and its Practical Implications,” *National Research Council of Canada*, **53**, pp. 53–59.
- [40] Jennings H. M., 2000, “A Model for the Microstructure of Calcium Silicate Hydrate in Cement Paste,” *Cement and Concrete Research*, **30**(1), pp. 101–116.
- [41] Tennis P. D., and Jennings H. M., 2000, “A Model for Two Types of Calcium Silicate Hydrate in the Microstructure of Portland Cement Pastes,” *Cement and Concrete Research*, **30**(6), pp. 855–863.
- [42] O'Neil E. F., 2008, “On Engineering the Microstructure of High-Performance Concretes to Improve Strength, Rheology, Toughness, and Frangibility,” Doctoral Dissertation, Northwestern University, pp. 1–228.

- [43] Röbller M., and Odler I., 1985, "Investigations on the Relationship Between Porosity, Structure and Strength of Hydrated Portland Cement Pastes I. Effect of Porosity," *Cement and Concrete Research*, **15**(2), pp. 320–330.
- [44] Odler I., and Röbller M., 1985, "Investigations on the Relationship Between Porosity, Structure and Strength of Hydrated Portland Cement Pastes. II. Effect of Pore Structure and of Degree of Hydration," *Cement and Concrete Research*, **15**(3), pp. 401–410.
- [45] Bapat J. D., 2013, *Mineral Admixtures in Cement and Concrete*, CRC Press, Boca Raton, FL.
- [46] Peng Y. Z., Chen K., and Hu S. G., 2011, "Study on Interfacial Properties of Ultra-High Performance Concrete Containing Steel Slag Powder and Fly Ash," *Advanced Materials Research*, **194-196**, pp. 956–960.
- [47] Mehta P. K., and Gjørv O. E., 1982, "Properties of Portland Cement Concrete Containing Fly Ash and Condensed Silica-Fume," *Cement and Concrete Research*, **12**(5), pp. 587–595.
- [48] Malhotra V. M., and Carrette G. G., 1982, "Silica Fume," *Concrete Construction*, pp. 443-446.
- [49] Yajun J., and Cahyadi J. H., 2004, "Simulation of Silica Fume Blended Cement Hydration," *Mat. Struct.*, **37**(6), pp. 397–404.
- [50] Zhang M.-H., and Gjørv O. E., 1991, "Effect of Silica Fume on Cement Hydration in Low Porosity Cement Pastes," *Cement and Concrete Research*, **21**(5), pp. 800–808.
- [51] ASTM, 2012, "Terminology Relating to Concrete and Concrete Aggregates", ASTM International, West Conshohocken, PA.
- [52] Adesanya D. A., and Raheem A. A., 2009, "Development of Corn Cob Ash Blended Cement," *Construction and Building Materials*, **23**(1), pp. 347–352.
- [53] Biricik H., Aköz F., Berktaş I. L., and Tulgar A. N., 1999, "Study of Pozzolanic Properties of Wheat Straw Ash," *Cement and Concrete Research*, **29**(5), pp. 637–643.
- [54] Ganesan K., Rajagopal K., and Thangavel K., 2007, "Evaluation of Bagasse Ash as Supplementary Cementitious Material," *Cement and Concrete Composites*, **29**(6), pp. 515–524.
- [55] Zhang M. H., and Malhotra V. M., 1996, "High-Performance Concrete Incorporating Rice Husk Ash as a Supplementary Cementing Material," *ACI Materials Journal*.
- [56] Papadakis V. G., and Tsimas S., 2002, "Supplementary Cementing Materials in Concrete", *Cement and Concrete Research*, **32**(10), pp. 1525–1532.
- [57] ASTM, 2012, "Standard Specification for Coal Fly Ash and Raw or Calcined Natural Pozzolan for Use in Concrete", ASTM International, West Conshohocken, PA.

- [58] Bache H. H., 1981, "Densified Cement Ultrafine Particle Based Material," Ottawa, Ontario, pp. 1–36.
- [59] Bache H. H., 1986, "Shaped Article and Composite Material and Method for Producing Same", US Patent 4,588,443.
- [60] Richard P., and Cheyrezy M., 1995, "Composition of Reactive Powder Concretes," *Cement and Concrete Research*, **25**(7), pp. 1501–1511.
- [61] Neeley B. D., Hammons M. L., and Smith D. M., 1991, "The Development and Characterization of Conventional-Strength and High-Strength Portland Cement Concrete Mixtures for Projectile Penetration Studies", U.S. Army Corps, Waterways Experiment Station, Vicksburg, Ms.
- [62] ASTM, 2009, "Standard Specification for Mixing Rooms, Moist Cabinets, Moist Rooms, and Water Storage Tanks Used in the Testing of Hydraulic Cements and Concretes", ASTM International, West Conshohocken, PA.
- [63] ASTM, 2012, "Standard Test Method for Slump of Hydraulic-Cement Concrete", ASTM International, West Conshohocken, PA.
- [64] Neeley B. D., and Walley D. M., 1995, "Very High-Strength Concrete," *The Military Engineer*, Vol. **87**.
- [65] Durst B. P., Neeley B. D., O'Neil E. F., Boone N. R., and Cummins T. K., 2010, "Blast-Resistant Concrete also Suitable for Limiting Penetration of Ballistic Fragments," US Patent 7,744,690.
- [66] ASTM, 2007, "Standard Test Method for Flow of Hydraulic Cement Mortar", ASTM International, West Conshohocken, PA.
- [67] Gettu R., Bazant Z. P., and Karr M. E., 1990, "Fracture Properties and Brittleness of High-Strength Concrete.," *ACI Materials Journal*.
- [68] Williams E. M., Graham S. S., Reed P. A., and Rushing T. S., 2009, "Laboratory Characterization of Cor-Tuf Concrete with and Without Steel Fibers", U.S. Army Corps of Engineers, Vicksburg, Ms.
- [69] Heard W. F., Williams B. A., Roth M. J., Rushing T. S., Ranade R., Stults M. D., and Li V. C., 2014, "Development of High Strength High Ductility Concrete", U.S. Army Corps of Engineers, Vicksburg, Ms.
- [70] Li V. C., "Performance Driven Design of Fiber Reinforced Cementitious Composites," ace-mrl.engin.umich.edu [Online]. Available: http://ace-mrl.engin.umich.edu/NewFiles/publications/performance_driven_design_92.pdf. [Accessed: 08-Dec-2009].
- [71] Mizobuchi T., Yanai S., Takada K., Sakata N., and Nobuta Y., 1999, "Field Applications of Self-Compacting Concrete with Advantageous Performances," Stockholm, Sweden, pp. 605–616.
- [72] Ouchi M., 1998, "History of Development and Applications of Self-Compacting Concrete," Japan, pp. 1–9.
- [73] Gagne R., Pigeon M., Aitcin, P.C., 1990, "Deicer Salt Scaling Resistance of

- High Performance Concrete", ACI: Concrete International.
- [74] ACI, 2007, "Self-Consolidating Concrete", ACI: Concrete International.
- [75] Domone P. L., 2006, "Self-Compacting Concrete: An Analysis of 11 Years of Case Studies," *Cement and Concrete Composites*, **28**(2), pp. 197–208.
- [76] Frank D., 2008, "Acceptance of SCC: Precast Concrete Industry Perspective", ACI Convention, St. Louis.
- [77] Lobo C., 2008, "Acceptance of SCC: Ready-Mixed Perspective", ACI Convention, St. Louis.
- [78] ASTM, "ASTM Subcommittee C09.47: Published Standards Under C09.47 Jurisdiction on Self-Consolidating Concrete," *astm.org* [Online]. Available: <http://www.astm.org/COMMIT/SUBCOMMIT/C0947.htm>. [Accessed: 14-Jun-2013].
- [79] Jin J., 2002, "Properties of Mortar for Self-Compacting Concrete," University of London.
- [80] ASTM, 2009, "Standard Test Method for Slump Flow of Self-Consolidating Concrete", ASTM International, West Conshohocken, PA.
- [81] ASTM, 2010, "Standard Test Method for Static Segregation of Self-Consolidating Concrete using Column Technique", ASTM International, West Conshohocken, PA.
- [82] ACBM, 2007, "Self-Consolidating Concrete," The center for advanced cement based materials [Online]. Available: <http://www.selfconsolidatingconcrete.org/downloads/ACBMWhitePaper.pdf>. [Accessed: Jun-2013].
- [83] Gurjar A. H., 2004, "Mix Design and Testing of Self-Consolidating Concrete using Florida Materials", Florida Department of Transportation.
- [84] Liu M., 2010, "Self-Compacting Concrete with Different Levels of Pulverized Fuel Ash," *Construction and Building Materials*, **24**(7), pp. 1245–1252.
- [85] ASTM, 2012, "Standard Specification for Slag Cement for use in Concrete and Mortars", ASTM International, West Conshohocken, PA.
- [86] EFNARC, 2005, *The European Guidelines for Self-Compacting Concrete*.
- [87] ACI, 2008, "Guide for Selecting Proportions for High-Strength Concrete Using Portland Cement and Other Cementitious Materials", ACI: Concrete International.
- [88] ACI, 2011, "Guide to Quality Control and Assurance of High-Strength Concrete", ACI: Concrete International, Farmington Hills, MI.
- [89] ActiveMinerals, "Acti-Gel® 208: Active Minerals International," *activeminerals.com* [Online]. Available: <http://activeminerals.com/products/high-purity-magnesium-alumino-silicate/>. [Accessed: 19-Jul-2013].

- [90] Tregger N. A., Pakula M. E., and Shah S. P., 2010, "Influence of Clays on the Rheology of Cement Pastes," *Cement and Concrete Research*, **40**(3), pp. 384–391.
- [91] Murray H. H., 2007, *Applied Clay Mineralogy*, Elsevier.
- [92] Galan E., and Singer A., 2011, *Developments in Palygorskite-Sepiolite Research*, Elsevier.
- [93] "The Mineralogical Society of Great Britain and Ireland - Palygorskite," minersoc.org [Online]. Available: <http://www.minersoc.org/photo.php?id=113>. [Accessed: Jul-2013].
- [94] Neaman A., and Singer A., 2000, "Rheological Properties of Aqueous Suspensions of Palygorskite," *Soil Science Society of America Journal*, **64**(1), pp. 427–436.
- [95] Kawashima S., Hou P., Corr D. J., and Shah S. P., 2013, "Modification of Cement-Based Materials with Nanoparticles," *Cement and Concrete Composites*, V. 36, pp. 8-15.
- [96] Wang K., 2011, "Self-Consolidating Concrete - Applications for Slip-Form Paving", National Concrete Pavement Technology Center, Iowa State University, Ames, IA.
- [97] Kroyer H., Lindgreen H., Jakobsea H. J., and Skibsted J., 2003, "Hydration of Portland Cement in the Presence of Clay Minerals Studied by ^{29}Si and ^{27}Al MAS NMR Spectroscopy," *Advances in Cement Research*, **15**, pp. 103–112.
- [98] Lindgreen H., Geiker M., Kroyer H., Springer N., and Skibsted J., 2008, "Microstructure Engineering of Portland Cement Pastes and Mortars through Addition of Ultrafine Layer Silicates," *Cement and Concrete Composites*, **30**(8), pp. 686–699.
- [99] He C., Osbaeck B., and Makovicky E., 1995, "Pozzolanic Reactions of Six Principal Clay Minerals: Activation, Reactivity Assessments and Technological Effects," *Cement and Concrete Research*, **25**(8), pp. 1691–1702.
- [100] Garg N., and Wang K., 2012, "Comparing the Performance of Different Commercial Clays in Fly Ash-Modified Mortars," *Journal of Sustainable Cement-Based Materials*, **1**(3), pp. 111–125.
- [101] ASTM, 2011, "Standard Test Methods for Chemical Analysis of Hydraulic Cement", ASTM International, West Conshohocken, PA.
- [102] ACI, 2001, "Use of Raw or Processed Natural Pozzolans in Concrete", Farmington Hills, MI.
- [103] ASTM, 2011, "Standard Specification for Portland Cement", ASTM International, West Conshohocken, PA.
- [104] ASTM, 2013, "Standard Practice for Mechanical Mixing of Hydraulic Cement Pastes and Mortars of Plastic Consistency", ASTM International, West Conshohocken, PA.

- [105] ASTM, 2007, "Standard Practice for Making and Curing Concrete Test Specimens in the Laboratory", ASTM International, West Conshohocken, PA.
- [106] ASTM, 2011, "Standard Test Method for Compressive Strength of Hydraulic Cement Mortars (using 2-in Cube Specimens)", ASTM International, West Conshohocken, PA.
- [107] ASTM, 2010, "Flexural Strength of Concrete (Using Simple Beam With Center-Point Loading)", West Conshohocken, PA.
- [108] Haldar A., and Mahadevan S., 2000, *Probability, Reliability, and Statistical Methods in Engineering Design*, Wiley.
- [109] Livingston C. W., and Smith F. L., 1951, "Bomb Penetration Project", DTIC, Golden Colorado.
- [110] Cargile J. D., 1999, "Development of a Constitutive Model for Numerical Simulation of Projectile Penetration into Brittle Geomaterials", US Army ERDC.
- [111] Adley M., Frank A., Danielson K., Akers S., and O'Daniel J., 2010, "The Advanced Fundamental Concrete (AFC) Model", U.S. Army ERDC, Vicksburg, Ms.
- [112] Nordendale N. A., Heard W. F., Hickman M. A., Zhang B., and Basu P. K., 2013, "Cementitious Material Models for Simulating Projectile Impact Effects," *Computational Materials Science*, **79(C)**, pp. 745–758.
- [113] Sherburn J., Heard W. F., Park H., and Chen W., 2011, "Modeling of the Split Hopkinson Pressure Bar: Application to Cortuf," Baltimore, MD.
- [114] Nordendale N. A., Heard W. F., and Basu P. K., "Modeling of High-Rate Ballistic Impact of Brittle Armors with Abaqus/Explicit", Simulia Community Conference, Vienna, Austria.
- [115] Nordendale N. A., 2013, "Modeling and Simulation of Brittle Armors Under Impact and Blast Effects," Vanderbilt University.
- [116] Shah S. P., Swartz S. E., and Ouyang C., 1995, *Fracture Mechanics of Concrete*, John Wiley & Sons.
- [117] Yokota H., Rokugo K., and Sakata N., 2007, "JSCE Recommendations for Design and Construction of High Performance Reinforced Composite with Multiple Fine Cracks," Japan Society of Civil Engineers.
- [118] Correlatedsolutions.com [Online]. Available: <http://www.correlatedsolutions.com>. [Accessed: 21-Jan-2014].
- [119] Sutton M. A., Orteu J. J., and Schreier H., 2009, *Image Correlation for Shape, Motion and Deformation Measurements*, Springer.
- [120] Jackson J. G. Jr, 1969, "Analysis of Laboratory Test Data to Derive Soil Constitutive Properties", US Army ERDC.

- [121] Nemat-Nasser S., Isaacs J. B., and Starrett J. E., 1991, "Hopkinson Techniques for Dynamic Recovery Experiments," *Proceedings of the Royal Society: Mathematical, Physical and Engineering Sciences*, **435**(1894), pp. 371–391.
- [122] Frew D. J., Forrestal M. J., and Chen W., 2001, "A Split Hopkinson Pressure Bar Technique to Determine Compressive Stress-Strain Data for Rock Materials," *Experimental Mechanics*, **41**(1), pp. 40–46.
- [123] Frew D. J., Forrestal M. J., and Chen W., 2002, "Pulse Shaping Techniques for Testing Brittle Materials with a Split Hopkinson Pressure Bar," *Experimental Mechanics*, **42**(1), pp. 93–106.
- [124] Chen W., and Luo H., 2003, "Dynamic Compressive Testing of Intact and Damaged Ceramics," onlinelibrary.wiley.com, John Wiley & Sons, Inc., Hoboken, NJ, USA, pp. 411–416.
- [125] Chen W., and Luo H., 2004, "Dynamic Compressive Responses of Intact and Damaged Ceramics from a Single Split Hopkinson Pressure Bar Experiment," *Experimental Mechanics*, **44**(3), pp. 295–299.
- [126] Song B., Chen W., and Weerasooriya T., 2003, "Quasi-Static and Dynamic Compressive Behaviors of a S-2 Glass/SC15 Composite," *Journal of Composite Materials*, **37**(19), pp. 1723–1743.
- [127] Jiao T., Li Y., Ramesh K. T., and Wereszczat A. A., 2005, "High Rate Response and Dynamic Failure of Structural Ceramics," *International Journal of Applied Ceramic Technology*, **1**(3), pp. 243–253.
- [128] Paliwal B., Ramesh K. T., and McCauley J. W., 2006, "Direct Observation of the Dynamic Compressive Failure of a Transparent Polycrystalline Ceramic (AlON)," *Journal of the American Ceramic Society*, **89**(7), pp. 2128–2133.
- [129] Nie X., Chen W. W., Sun X., and Templeton D. W., 2007, "Dynamic Failure of Borosilicate Glass Under Compression/Shear Loading Experiments," *Journal of the American Ceramic Society*, **90**(8), pp. 2556–2562.
- [130] Kolsky H., 1949, "An Investigation of the Mechanical Properties of Materials at Very High Rates of Loading," pp. 676–700.
- [131] Davies E., and Hunter S., 1963, "The Dynamic Compression Testing of Solids by the Method of the Split Hopkinson Pressure Bar," *Journal of mechanics and physics of solids*, **11**.
- [132] Dharan C. K. H., and Hauser F. E., 1970, "Determination of Stress-Strain Characteristics at Very High Strain Rates," *Experimental Mechanics*, **10**(9), pp. 370–376.
- [133] Samanta S. K., 1971, "Dynamic Deformation of Aluminium and Copper at Elevated Temperatures," *Journal of the Mechanics and Physics of Solids*, **19**(3), pp. 117–135.
- [134] Gorham D. A., 2000, "Specimen Inertia in High Strain-Rate Compression," *J. Phys. D: Appl. Phys.*, **22**(12), pp. 1888–1893.

- [135] Forrestal M. J., Wright T. W., and Chen W., 2007, “The Effect of Radial Inertia on Brittle Samples during the Split Hopkinson Pressure Bar Test,” *International Journal of Impact Engineering*, **34**(3), pp. 405–411.
- [136] Warren T. L., and Forrestal M. J., 2009, “Comments on the Effect of Radial Inertia in the Kolsky Bar Test for an Incompressible Material,” *Experimental Mechanics*, **50**(8), pp. 1253–1255.
- [137] Zhang M., Li Q. M., Huang F. L., Wu H. J., and Lu Y. B., 2010, “Inertia-Induced Radial Confinement in an Elastic Tubular Specimen Subjected to Axial Strain Acceleration,” *International Journal of Impact Engineering*, **37**(4), pp. 459–464.
- [138] Song B., Ge Y., Chen W. W., and Weerasooriya T., 2007, “Radial Inertia Effects in Kolsky Bar Testing of Extra-Soft Specimens,” *Experimental Mechanics*, **47**(5), pp. 659–670.
- [139] Song B., Chen W., Ge Y., and Weerasooriya T., 2007, “Dynamic and Quasi-Static Compressive Response of Porcine Muscle,” *Journal of Biomechanics*, **40**, pp. 2999–3005.
- [140] Grote D., Park S., and Zhou M., 2001, “Dynamic Behavior of Concrete at High Strain Rates and Pressures: I. Experimental Characterization,” *International Journal of Impact Engineering*, pp. 869–886.
- [141] Ross C. A., Thompson P. A., and Tedesco J. W., “Split-Hopkinson Pressure-Bar Tests on Concrete and Mortar in Tension and Compression,” *ACI Materials Journal*, **89**, pp. 475–481.
- [142] Malvern L. E., Tang T., Jenkins D. A., and Ross C. A., 1985, “Dynamic Compressive Strength of Cementitious Materials,” pp. 194–199.
- [143] Ross C. A., Jerome D. M., Tedesco J. W., and Hughes M. L., 1996, “Moisture and Strain Rate Effects on Concrete Strength,” *ACI Materials Journal*.
- [144] Tedesco J. W., Ross C. A., and Kuennen S. T., 1993, “Experimental and Numerical Analysis of High Strain Rate Splitting Tensile Tests,” *ACI Materials Journal*, **90**, pp. 162–169.
- [145] Erzar B., and Forquin P., “An Experimental Method to Determine the Tensile Strength of Concrete at High Rates of Strain,” *Experimental Mechanics*, **50**(7), pp. 941–955.
- [146] Brara A., and Klepaczko J. R., 2006, “Experimental Characterization of Concrete in Dynamic Tension,” *Mechanics of Materials*, **38**(3), pp. 253–267.
- [147] Lambert D. E., and Ross C. A., 2000, “Strain Rate Effects on Dynamic Fracture and Strength,” *International Journal of Impact Engineering*, pp. 985–998.
- [148] Li Q. M., and Meng H., 2003, “About the Dynamic Strength Enhancement of Concrete-Like Materials in a Split Hopkinson Pressure Bar Test,” *International Journal of Solids and Structures*, **40**(2), pp. 343–360.

- [149] Zukas J. A., 1980, "Impact Dynamics: Theory and Experiment", US Army Armament R&D Command: Ballistic Research Laboratory.
- [150] Bangash M. Y. H., 1993, *Impact and Explosion*, CRC Press.
- [151] Backman M. E., and Godsmith W., 1978, "The Mechanics of Penetration of Projectiles into Targets," *International Journal of Engineering Science*, **16**(1), pp. 1–99.
- [152] DOD, 1987, "Department of Defense Test Method Standard: V50 Ballistic Test for Armor", MIL-STD-662F.